



**HAL**  
open science

## Adhesion between PTFE films : influence of manufacturing process conditions

Agathe Mocellin

► **To cite this version:**

Agathe Mocellin. Adhesion between PTFE films : influence of manufacturing process conditions. Mechanics of materials [physics.class-ph]. Université Paris-Saclay, 2021. English. NNT : 2021UP-AST112 . tel-03524118

**HAL Id: tel-03524118**

**<https://theses.hal.science/tel-03524118>**

Submitted on 13 Jan 2022

**HAL** is a multi-disciplinary open access archive for the deposit and dissemination of scientific research documents, whether they are published or not. The documents may come from teaching and research institutions in France or abroad, or from public or private research centers.

L'archive ouverte pluridisciplinaire **HAL**, est destinée au dépôt et à la diffusion de documents scientifiques de niveau recherche, publiés ou non, émanant des établissements d'enseignement et de recherche français ou étrangers, des laboratoires publics ou privés.

# Adhesion between PTFE films: influence of manufacturing process conditions

**Thèse de doctorat de l'Université Paris-Saclay**

École doctorale n°579 : Sciences Mécaniques et Energétiques,  
Matériaux et Géosciences (SMEMAG)  
Spécialité de doctorat: Solides, Structures et Matériaux  
Unité de recherche: Université Paris-Saclay, ENS Paris-Saclay, CNRS, LMT -  
Laboratoire de Mécanique et Technologie, 91190, Gif-sur-Yvette, France.  
Réfèrent: : ENS Paris-Saclay

**Thèse présentée et soutenue à Paris-Saclay, le 13 décembre 2021,  
par**

**Agathe MOCELLIN**

## Composition du jury:

<b>Karine Gautier</b> Maître de conférence HdR, LPMT, Université de Haute-Alsace	Rapportrice
<b>Valérie Nassiet</b> Professeur des Universités, LGP, ENI Tarbes	Rapportrice
<b>Elise Lorenceau</b> Directrice de recherche CNRS, LiPhy, Université Grenoble Alpes	Examinatrice
<b>Frédéric Restagno</b> Directeur de recherche CNRS, LPS, Université Paris-Saclay	Président du jury
<b>Jorge Peixinho</b> Chargé de recherche CNRS, PIMM, Arts et Metiers ParisTech, CNAM	Examineur
<b>Nicolas Schmitt</b> Professeur des Universités, LMT, Université Paris-Est Créteil	Directeur
<b>Gilles Régnier</b> Professeur des Universités, PIMM, Arts et Metiers ParisTech, CNAM	Co-directeur
<b>Jean-Yvon Faou</b> Ingénieur de recherche, Saint-Gobain Research Paris	Invité



**Titre : Adhésion entre films de Polytétrafluoroéthylène (PTFE) : influence des conditions de fabrication**

**Mots clés :** Polytétrafluoroéthylène, PTFE, Adhésion, Adhérence, Science des polymères, Mécanique de la rupture

**Résumé long :**

**1. Introduction**

Le polytétrafluoroéthylène (PTFE) est un polymère thermoplastique semi-cristallin ayant une très bonne résistance à la corrosion, une forte stabilité thermique, de très bonnes propriétés d'isolation thermique et un très faible coefficient de friction. Par conséquent, ce matériau est utilisé pour de nombreuses applications; une d'entre elles est la fabrication de films et de tissus enduits de PTFE.

En raison de sa masse molaire élevée et de sa haute viscosité à l'état fondu, les films minces en PTFE sont obtenus par dépôts successifs de dispersions sur une matrice qui est ensuite retirée [Drobny 2009, Ebnesajjad 2000]. Des matériaux composites sont fabriqués en soudant ensemble un tissu pris en sandwich entre deux films. Pour des performances optimales, il est crucial de maîtriser au mieux l'adhésion PTFE-PTFE et PTFE-tissu.

Ce travail porte sur un système modèle : deux films de PTFE sans tissu. L'objectif est de comprendre les mécanismes d'adhésion et d'en déduire une optimisation du soudage des films.

**2. Expérimental : Test de pégosité entre cylindres croisés**

Afin d'évaluer l'adhérence entre deux films de PTFE, un test mécanique s'inspirant du test de pégosité [Creton, Kramer, H. R. Brown, *et al.* 2002] et de la théorie du contact de Hertz [Hertz 1882] entre cylindres croisés a été mis en place. Des supports cylindriques et un système d'attache ont été conçus afin d'être placés à l'intérieur du four équipant le rhéomètre (Anton Paar MCR 502) permettant la mesure et le contrôle simultanés de la force normale et de la température (Fig.1a). Ainsi, une fois les films mis en place sur les supports avec une tension de 2 N, un cycle contrôlé en température et pression en temps est effectué (Fig.1b). A partir des données enregistrées lors de la phase de décollement, un travail "mesuré" est calculé :

$$W_{mes} = \int_0^{U_{max}} \frac{F dU}{\frac{\pi}{4} (a_{haut} + a_{bas})^2} \quad (1)$$

avec  $U$  l'entrefer entre les 2 supports et  $a$  le rayon de la zone collée mesuré a posteriori par microscopie optique.



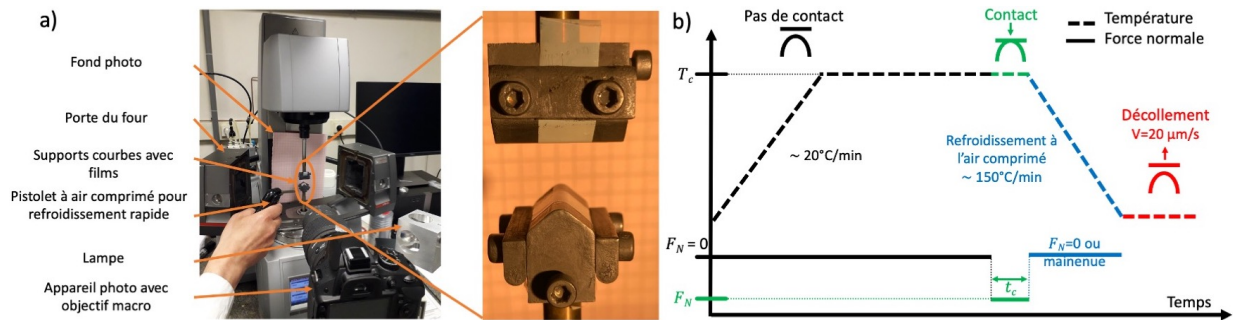


Figure 1: Test de pégo-sité entre cylindres croisés sur rhéomètre. (a) Montage complet et zoom sur les supports avec les films de PTFE. (b) Protocole expérimental : évolution temporelle de la température et de la force normale.

### 3. Résultats et discussion

#### 3.1 Effet de la température sur l'adhésion

Des exemples de la force de décollement en fonction de l'entrefer pour différentes températures de contact  $T_c$  est représentée Fig.2a. Lorsque  $T_c$  augmente, la force maximale de décollement  $F_{max}$  augmente (Fig.2b haut) ainsi que l'entrefer à la rupture. Sur les clichés pris tout au long du décollement pour  $T_c = 375^\circ\text{C}$  (Fig.2a), les films sont étirés et prennent la forme d'un sablier ; cette déformation n'est pas observée pour  $T_c$  inférieure à la fusion. Le rayon de la zone collée augmente avec  $T_c$  au fur et à mesure que le module élastique en tension des films chute (Fig.2b milieu). À partir de l'aire sous la courbe (Fig.2a), le travail mesuré  $W_{mes}$  (Eq.1) est calculé (Fig.2b bas) : lorsque  $T_c$  augmente,  $W_{mes}$  augmente significativement de 325 jusqu'à 340 et  $375^\circ\text{C}$  où un plateau semble être atteint ; ce comportement peut être relié à la progression de la fusion du matériau.

Augmenter la force de contact  $F_N$  permet d'obtenir des  $F_{max}$  plus élevées, des zones de contact plus larges et les  $W_{mes}$  calculés sont plus élevés pour  $T_c$  supérieure à la fusion ; les tendances décrites précédemment sont toujours valides.

#### 3.2 Diffusion de chaînes macromoléculaires

Au-dessus de la fusion, l'interdiffusion des chaînes ou segments macromoléculaires est facilitée : une interphase plus épaisse peut se former et un meilleur ancrage et une meilleure adhésion peuvent ainsi être obtenus ; ces phénomènes sont dépendants du temps [De Gennes 1992]. Expérimentalement, entre  $t_c = 6$  et 600 s, les  $W_{mes}$  sont très proches : la mobilité de la chaîne de PTFE ne semble pas être significative.

Des essais de rhéologie linéaire en cisaillement sont réalisés sur un pseudo-bulk constitué d'un empilement de 10 films de PTFE. Des disques de 2,5 cm de diamètre sont découpés à l'emporte-pièce et placés dans le rhéomètre équipé d'une géométrie plans parallèles. La température est augmentée puis maintenue au-dessus de la fusion. Des balayages en déformation ont préalablement été effectués pour déterminer le régime linéaire viscoélastique. A partir de

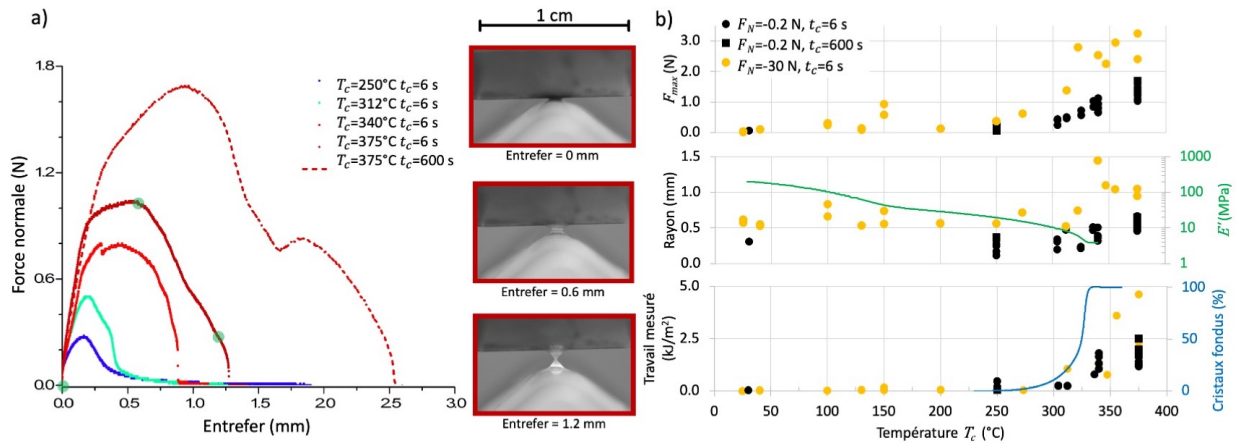


Figure 2: (a) Force de décollement en fonction de l'entrefer pour  $F_N = -0,2$  N et différents  $T_c$  et  $t_c$ . Les images illustrent le comportement du film pour  $t_c = 6$  s et  $T_c = 375^\circ\text{C}$ , les points verts indiquent la position de chaque image sur la courbe de force. (b) Haut : force maximale de décollement  $F_{max}$ , Milieu : rayon moyen de la surface fracturée et module de stockage en tension, Bas : travail mesuré et taux de cristaux fondus, en fonction de  $T_c$  pour différents  $t_c$  et  $F_N$ .

ces échantillons, différents tests sont réalisés.

L'évolution des propriétés mécaniques du matériau est obtenue par superposition temps-température [J. D. Ferry 1980] à partir de balayages en fréquence à différentes températures au-dessus de la fusion. Les résultats ne permettent pas de conclure sur la valeur d'un temps de relaxation : celui-ci est supposé très long. Cependant, des mouvements de portions de chaînes sont attendus à une échelle de temps plus faible. Le suivi temporel de l'évolution du module complexe de cisaillement [Bousmina *et al.* 1998] a permis de mettre en évidence la progression de la cicatrisation aux interfaces sur un empilement de films de PTFE.

### 3.3 Différents mécanismes de rupture au-dessus de la fusion

L'effet de la pression de contact est évalué dans les conditions de meilleure adhésion obtenues précédemment. Pour  $T_c=375^\circ\text{C}$ , différentes  $F_N$  de -0,2 à -40 N conduisant à des pressions de 0,2 à 16 MPa sont explorées pour  $t_c=6$  et 600 s. Un trou peut être formé sur le film inférieur : l'adhésion est suffisante pour conduire à la fracture du film ; ou bien le décollement a lieu à l'interface entre les 2 films. Ces différents modes de rupture sont représentés Fig.3 par des symboles vides en cas de fracture du film ou par des symboles pleins en cas de décollement interfacial. Pour les deux  $t_c$ , la transition entre les 2 modes de rupture se produit autour de 5,5 MPa pour  $t_c=6$  s et autour de 1,3 MPa pour  $t_c=600$  s. Cette pression seuil est plus faible plus  $t_c$  est long.

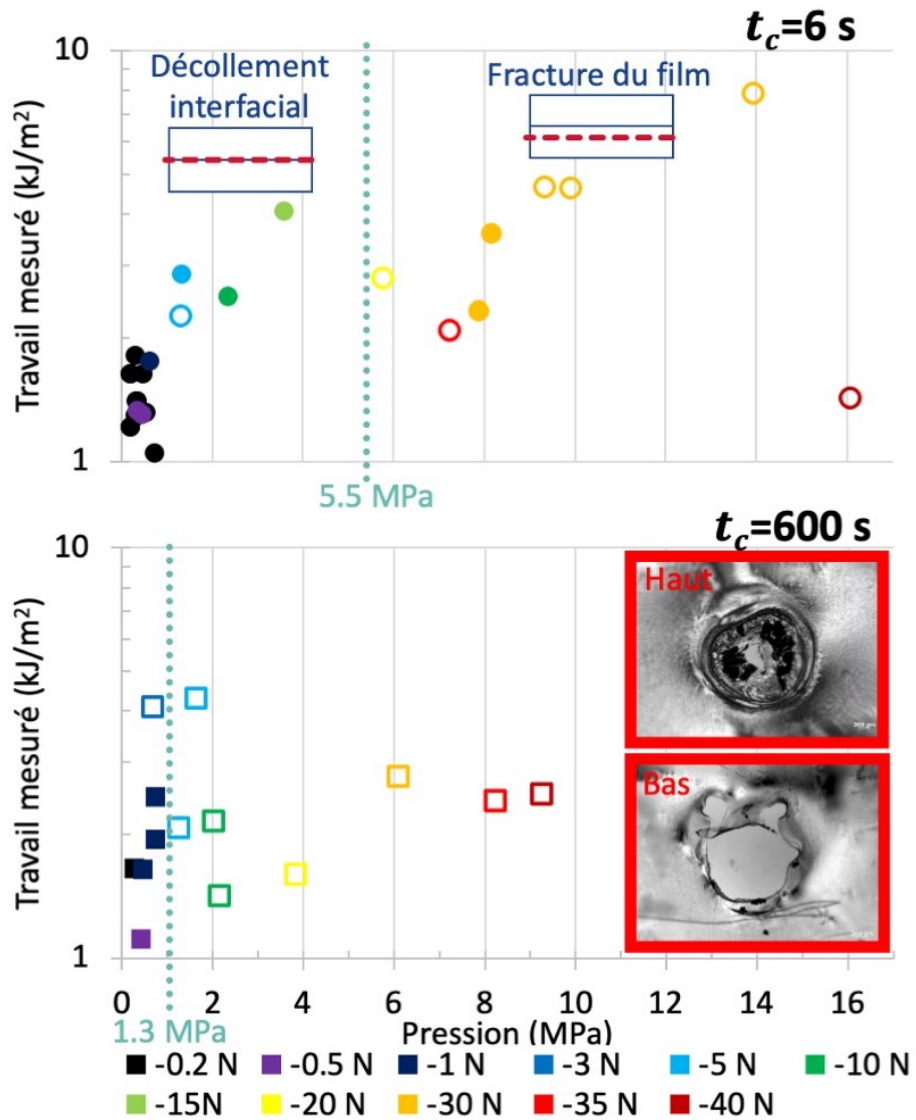


Figure 3: Évolution du travail mesuré en fonction de la pression de contact pour  $t_c = 6$  s (haut) et  $t_c = 600$  s (bas) pour  $T_c = 375^\circ\text{C}$ . Les échantillons troués sont représentés par des symboles ouverts. La pression seuil entre un décollement interfacial et la fracture du film est plus faible pour  $t_c = 600$  s.

#### **4. Conclusion**

Un dispositif expérimental original de pégosité a été développé et a permis l'analyse de l'influence de la température, du temps et de la pression de contact sur les propriétés d'adhésion à l'interface. Le rôle de l'interdiffusion des chaînes dans la phase amorphe dans l'adhésion a été étudié. Une température de contact supérieure à la fusion, facilitant la mobilité des macromolécules, est nécessaire pour obtenir une bonne adhésion. L'augmentation du temps de contact ne montre pas de variation significative de la qualité d'adhésion dans la gamme de temps de contact étudiée. Au-dessus de la fusion, en fonction de la pression de contact, deux modes de rupture sont identifiés. La rupture est réalisée soit via un décollement interfacial soit via une fracture du film. Une pression seuil existe entre ces deux modes de rupture : plus le temps de contact est long, plus la pression seuil est basse.



# Contents

<b>1</b>	<b>Introduction</b>	<b>15</b>
1.1	Polytetrafluoroethylene (PTFE)	17
1.1.1	Discovery	17
1.1.2	Chemical structure	17
1.1.3	Applications	17
1.2	Films manufacturing process	19
1.2.1	Overview of the existing film processes	19
1.2.2	Challenges for the lamination of coated fabrics	22
1.3	Structure of the study	23
<b>2</b>	<b>Adhesion mechanisms between two polymeric materials</b>	<b>25</b>
2.1	Wetting and intimate contact	26
2.1.1	Wetting or thermostatic adsorption	26
2.1.2	Intimate contact quality	28
2.2	Adhesive forces	29
2.3	Interfacial macromolecular diffusion	30
2.3.1	Molecular dynamics	30
2.3.2	Interfacial adhesion strength	35
2.4	Self-adhesion of semi-crystalline polymers	39
<b>3</b>	<b>PTFE films characterization</b>	<b>41</b>
3.1	Materials	42
3.1.1	Raw dispersion	42
3.1.2	Cast films	42
3.2	PTFE: a semi-crystalline polymer	46
3.2.1	Phase diagram	46
3.2.2	Crystalline structure	46
3.2.3	Crystallization kinetics	57
3.3	PTFE cast films mechanical properties	61
3.3.1	Dynamic Mechanical Analysis in tension	61
3.3.2	Uniaxial tensile test	63
3.4	PTFE macro-molecular chains or segments mobility	65
3.4.1	Experimental protocol - Shear rheometry	65
3.4.2	Chain movement: time-temperature superposition	66
3.4.3	Segment movement: progressive healing	68

<b>4</b>	<b>Adherence measurements</b>	<b>73</b>
4.1	Adhesion energy estimation . . . . .	74
4.1.1	Non-adhesive contact – Hertz model . . . . .	74
4.1.2	Adhesive contact – JKR model . . . . .	75
4.2	Theory of fracture and adhesion - short summary . . . . .	78
4.2.1	Semi-crystalline polymers mechanical behavior . . . . .	78
4.2.2	Plane strain, plane stress and different fracture modes . . . . .	78
4.2.3	Energy balance approach . . . . .	80
4.2.4	Stress intensity factor approach . . . . .	81
4.2.5	Relationship between $G$ and $K$ . . . . .	82
4.3	Adherence tests . . . . .	83
4.3.1	Peel tests . . . . .	83
4.3.2	Lap-shear tests . . . . .	84
4.3.3	Tack and pull tests . . . . .	85
4.4	Conclusion . . . . .	86
<b>5</b>	<b>Mechanical adherence tack test between crossed cylinders</b>	<b>87</b>
5.1	Experimental setup . . . . .	88
5.1.1	Motivation . . . . .	88
5.1.2	Setup design . . . . .	88
5.1.3	Experimental protocol . . . . .	90
5.2	Macro-molecular chain movements . . . . .	93
5.2.1	Temperature as a mobility promoter . . . . .	93
5.2.2	Time spent above melting: a mobility enhancement ? . . . . .	98
5.3	Crystallization . . . . .	99
5.3.1	Crystalline content . . . . .	99
5.3.2	Secondary crystallization mechanism . . . . .	99
5.3.3	Crystalline orientation . . . . .	102
5.4	Pressure . . . . .	103
5.4.1	Experimental protocol adjustment - force kept during cooling . . . . .	103
5.4.2	Low and high contact pressures: temperature screening . . . . .	104
5.4.3	Different fracture mechanisms above melting . . . . .	106
<b>6</b>	<b>Towards modelling mechanical adherence tack test</b>	<b>109</b>
6.1	Image analysis . . . . .	110
6.1.1	Scheme of the configuration . . . . .	110
6.1.2	Results . . . . .	111
6.2	Two dimensions model - band approximation . . . . .	113
6.2.1	Kinematics formulation . . . . .	113
6.2.2	Forces estimation . . . . .	114
6.2.3	Energy balance . . . . .	115
6.3	Three dimensions model . . . . .	118
6.3.1	Uniaxial tensile test . . . . .	118
6.3.2	Crossed cylinders tack geometry . . . . .	122
<b>7</b>	<b>Conclusions and perspectives</b>	<b>127</b>
	References . . . . .	138
<b>A</b>	<b>Contact between elastic object: the Hertz theory</b>	<b>139</b>

---

<b>B Flat contact setup</b>	<b>143</b>
B.1 Test of principle . . . . .	143
B.1.1 Welding . . . . .	143
B.1.2 Peeling . . . . .	145
B.2 Welding part design . . . . .	145
B.2.1 Flatness adjustment . . . . .	146
B.2.2 Four points of load application . . . . .	146
B.2.3 Soft intermediate layer . . . . .	150
B.2.4 Small contact area . . . . .	153
<b>C Mechanical adherence tack test - designs</b>	<b>155</b>
<b>D Secondary crystallization morphology visualization by SEM in temperature</b>	<b>161</b>
D.1 Experimental setup . . . . .	161
D.2 Results . . . . .	162
<b>E Image analysis - supplementary</b>	<b>169</b>



# Remerciements

Je voudrais tout d'abord remercier les personnes qui ont accepté de juger mon travail, pour leur temps et pour l'intérêt qu'elles ont montré au sujet de mes recherches: merci aux rapportrices Karine Gautier et Valérie Nassiet d'avoir lu si attentivement mon manuscrit. Merci Elise Lorenceau pour les échanges très intéressants et Frédéric Restagno d'avoir accepté de présider ce jury.

Merci Jorge d'avoir rejoint le navire en cours de route, comme tu le dis, pour encadrer mon travail avec une infinie patience. Merci d'avoir toujours été présent au quotidien et merci pour ton soutien sans faille. Nicolas et Gilles, mon binôme de directeurs de thèse, je tiens à vous remercier pour votre enthousiasme, pour votre investissement et pour toutes vos idées.

Je souhaite également remercier quelqu'un qui n'apparaît pas dans la liste des encadrants: Stéphane, tu fais parti des personnes qui m'ont beaucoup appris.

Cette thèse, je ne l'ai évidemment pas faite toute seule. Au cours de ces trois ans et quelque, j'ai pu collaborer et échanger avec de nombreuses personnes que ce soit au LMT, au PIMM, chez Saint-Gobain ou à l'extérieur. Il est bien sûr compliqué de citer tout le monde, mais quelques-uns ont été d'une aide précieuse. Merci Laurianne pour ta disponibilité et ton aide à dompter ensemble le rhéomètre. Merci Boubou, Xavier et Rémi pour toutes nos discussions, conjectures et plans de montages expérimentaux qui n'ont jamais été conçus mais qui m'ont permis d'alimenter mes réflexions pour aboutir au montage final. Merci Alexandre Tanguy de m'avoir accueillie et épaulée auprès du MEB du LMS à l'Ecole Polytechnique pour imager l'étrange comportement du PTFE en température. Un grand merci à tous les collègues des 2 laboratoires pour leur bonne humeur au quotidien et notamment à mes camarades de bureau. Gabriel, grand frère PTFE, je tiens à te remercier de m'avoir transmis ton savoir et de m'avoir appris à ne pas me perdre entre les différents partenaires.

Je souhaite remercier François et Matthieu chez Saint-Gobain de m'avoir fait confiance pour relever les challenges de ce sujet sur un matériau exotique. Merci à Emmanuelle, Charles et Meghann d'avoir pris la suite toujours attentifs et bienveillants. Merci d'avoir toujours été disponibles, à l'écoute et un très bon relais vers les équipes des usines aux USA, à qui une pandémie m'aura empêché de rendre visite. Jean-Yvon et Myriam, merci de m'avoir si bien encadrée à Saint-Gobain, d'avoir pris autant à coeur le sujet et d'avoir fait le lien entre académique et industriel. Merci à tous les collègues de TMM et plus largement de SGR pour leur accueil chaleureux, leur disponibilité et leur écoute.

Je vous remercie pour la confiance que vous me témoignez en me permettant de contin-

uer mon aventure professionnelle à vos côtés.

Enfin, merci à mes parents, ma famille et mes amis (cette fois je ne vous oublie pas, toutes mes excuses à ceux qui liront cette parenthèse et qui la comprendront). J'ai la chance d'être très bien entourée et rien de tout ce que j'ai réalisé n'aurait été possible sans vous.

Et pour finir, j'aimerais remercier tout particulièrement Pierre-Alain, merci pour tout ton soutien dans ces montagnes russes où nous avons chacun eu notre thèse à mener à bien!

# Introduction

Polytetrafluoroethylene (PTFE) is a thermoplastic semi-crystalline polymer, with excellent chemical and physical properties, employed for numerous applications, especially for manufacturing PTFE films and coated fabrics. Due to their high molecular weight and their high viscosity in the melted state, PTFE thin films are obtained by successive deposition of PTFE dispersions on a substrate which is finally peeled out. Composite materials are manufactured by welding together a fabric sandwiched between two such PTFE films. Therefore, for optimum performance, PTFE-PTFE and PTFE-fabric adhesion (which depends strongly on the manufacturing process conditions) must be controlled.

This work focuses on a model system: two PTFE films without fabrics. The aim is to quantify the adhesion mechanisms and optimize films welding. The role of chain interdiffusion in the amorphous phase and/or co-crystallization of the polymer quasi-crystalline phase in the adhesion is investigated. These mechanisms are sensitive to thermal and mechanical solicitations applied at the interface between the two films, when intimate contact is reached. A specific experimental setup and protocols have been designed to weld PTFE films of low stiffness and perform mechanical adherence tack tests investigating the impact of temperature, contact time and normal pressure on the interfacial adhesive properties.

In this introduction, a presentation of PTFE is made in section 1.1 with its discovery, its chemical structure and its principal applications. The different films manufacturing processes are detailed in section 1.2. A focus is made on cast PTFE films and the main challenges brought during lamination of coated fabrics. Finally, the structure of the manuscript is presented in section 1.3.

**Contents**

---

<b>1.1</b>	<b>Polytetrafluoroethylene (PTFE)</b>	<b>17</b>
1.1.1	Discovery	17
1.1.2	Chemical structure	17
1.1.3	Applications	17
<b>1.2</b>	<b>Films manufacturing process</b>	<b>19</b>
1.2.1	Overview of the existing film processes	19
1.2.2	Challenges for the lamination of coated fabrics	22
<b>1.3</b>	<b>Structure of the study</b>	<b>23</b>

---

## 1.1 Polytetrafluoroethylene (PTFE)

### 1.1.1 Discovery

PTFE was accidentally discovered in 1938 by Roy Plunkett of DuPont de Nemours Company. Plunkett was pursuing studies on a safer and non-inflammable refrigerant liquid based on TetraFluoroEthylene (TFE). By cooling down a compressed TFE sample, he produced a white powder which appeared not to be dissolved in any solvent, acidic or basic. By heating this white powder up to melting, a clear gel is formed without flowing. This turned out to be the first PTFE powder manufacturing. This discovery was then developed in collaboration with the US Army during World War II. The first application of PTFE was for gaskets, packings and liners in the chain of production of the Uranium 235 as no other polymer resists to such critical environment. The first commercialization of PTFE by DuPont de Nemours occurred in 1945 under the brand name Teflon <sup>®</sup>.

### 1.1.2 Chemical structure

PTFE is a semi-crystalline polymer whose chemical structure  $(CF_2-CF_2)_n$  consists of a long carbon chain surrounded by fluorine atoms, as shown in Figure 1.1. Its molecular weight is high, in the order of  $10^7$  g/mol and its melting point is about  $342^\circ\text{C}$ . A huge difference comparatively to "classical" polymers is that PTFE does not melt: its processing is much more difficult. The basic properties of PTFE derive from its specific linear helical molecular configuration of the fluorine and carbon atoms. Both, the carbon-carbon as well as the carbon-fluorine covalent bonds are extraordinary strong (bond enthalpy at 298 K,  $\Delta H_{C-C} = 607$  kJ/mol and  $\Delta H_{C-F} = 536$  kJ/mol) [*Bond dissociation energy table 2021*]. Additionally, the carbon backbone is hermetically shielded by fluorine atoms, thus complicating a chemical attack, making PTFE highly stable and resistant up to high temperature [Neupauer 2014].

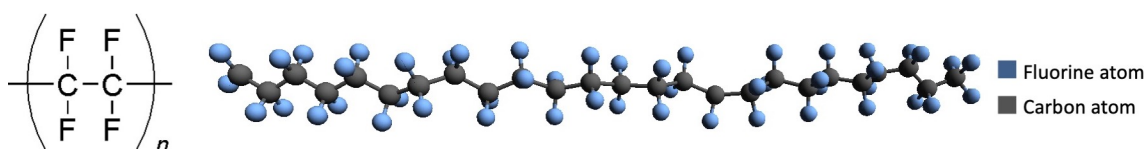


Figure 1.1: PTFE chemical formula and 3D structure.

Further properties like the low surface tension, the low friction coefficient or the excellent stability against temperature and flames are essentially based on the linearity, non-polarity and the high bonding energy on the shielding by fluorine atoms. Some PTFE properties are summarized in Table 1.1 [*Teflon PTFE 2017*].

### 1.1.3 Applications

In our everyday lives, thanks to its hydrophobic behavior and high temperature resistance, PTFE is used as a non-stick coating for pans and other cookware. As it is non-reactive, it is often used in containers and pipework for reactive and corrosive chemicals. When used as a lubricant in slide bearings, PTFE reduces friction, wear and energy consumption of machinery. In the following reference [Neupauer 2014] and in Figure 1.2a [*Saint-Gobain Chemfab - PTFE coated fabrics European brochure 2017*], the basic properties which recommend PTFE since many years for challenging applications under critical

Chemical formula	$(C_2F_4)_n$
Density (amorphous phase)	2.16 g/cm <sup>3</sup>
Molecular weight	10 <sup>7</sup> g/mol
Melting temperature	342°C virgin 327°C sintered
Thermal conductivity	0.25 W/(m.K)
Surface tension in air	25 mJ/m <sup>2</sup>

Table 1.1: PTFE chemical characteristics, at room temperature when not precised [*Teflon PTFE* 2017], [*Polymer data handbook* 1999].

and extreme conditions are summarized: high molecular weight, insolubility, physiological harmless, large range of temperature application, high UV and weathering resistance (no embrittlement by ageing) and very high purity; all of this without any additive.

The focus of this study is on PTFE films and coated fabrics made by Saint-Gobain Performance Plastics company and sold under the brand name Chemfab. These composite materials are made of glass or aramid fabrics and a mono or multilayer PTFE film laminated or not, as depicted in Figure 1.2b. These films are used for many applications through different industries such as building where coated fabrics are used as roofing material for large structures - see Figure 1.3a, aerospace for air-supported antenna protections called radomes - see Figure 1.3b, security with chemical and biological protective suits - see Figure 1.3c. PTFE coated fabrics can also be found in automotive, health, defense, food and beverage industries for components, insulation, packaging, polymer/plastic processing, etc.

**a)**

**Chemical** is about **Reliable containment** and barrier solutions for handling harsh liquids and gases

- Chemically inert
- Excellent barrier properties

**Mechanical** is about **Long lasting and consistent performance** under trying conditions

- Dimensionally stable
- Flexible, thermally weldable
- High tensile and tear strength

**Surface** is about **Higher productivity:** time, materials and energy savings through the low friction & easy release properties

- Non-stick and washable
- Food compliant and hygienic
- Lowest coefficient of friction

**Electrical/RF** is about **Safe operation and reliable performance** through higher RF transparency and insulation properties

- High dielectric strength
- Microwave transparent
- Low electrical losses

**Thermal** is about **Consistent performance** and processing over a wide range of operating temperatures

- Thermally stable from -150 to 260 °C
- Non-flammable/fire resistant
- Excellent heat transfer

**b)**

**CHEMFAB®**

Partner for Performance



Figure 1.2: a) PTFE interesting properties for Saint-Gobain company [*Saint-Gobain Chemfab - PTFE coated fabrics European brochure* 2017], b) Saint-Gobain PTFE coated fabrics and their brand name.

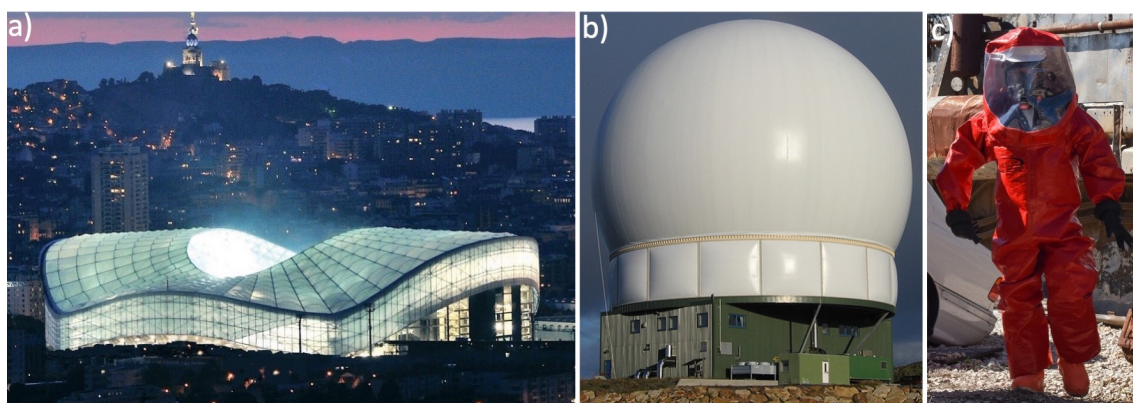


Figure 1.3: a) Stade Vélodrome roof, Marseille, France, 2013, Sheerfill brand [*Saint-Gobain Sheerfill - Interactive location map 2021*], b) A air-supported radome (protective antenna system), Sheergard brand [*Saint-Gobain Sheergard - Ground based radomes brochure 2021*], c) A Onesuit protective suit [*Saint-Gobain Onesuit protection brochure 2021*]. All are Saint-Gobain commercialized products.

## 1.2 Films manufacturing process

### 1.2.1 Overview of the existing film processes

#### PTFE powder and dispersion manufacturing

In 2008, PTFE powders with grains of 1-350  $\mu\text{m}$  were sold \$9/kg [Ebnesajjad 2011]. This high price for a raw polymer product can be explained by the specific fabrication mode since PTFE raw material cannot be produced by melt-processing techniques because of its high viscosity ( $10^9$  to  $10^{11}$  Pa.s at  $380^\circ\text{C}$ ). Consequently, PTFE is obtained by free-radical polymerization mechanism in an aqueous media via addition polymerization of TFE in a batch process. PTFE is produced by suspension polymerization without surfactant to obtain granular resins of about 50 to 100  $\mu\text{m}$  or with a perfluorinated surfactant (emulsion polymerization) to obtain fine powder of about 400 to 800  $\mu\text{m}$  and dispersion products of about 200 to 300 nm [Ebnesajjad 2011].

During emulsion polymerization, the dispersion particles are formed progressively; their genesis is depicted on Figure 1.4. The ribbons consist of lamellae folded upon themselves a given number of times. First, the ribbon is folded once (1), then it folds several times (2) and finally the particle is fully formed (3). Ribbons do not always fold neatly upon themselves: in most cases, the ribbons are tangled (3a). The folding of the thin ribbons is thought to result from the agitation of the aqueous phase during polymerization [Rahl *et al.* 1972].

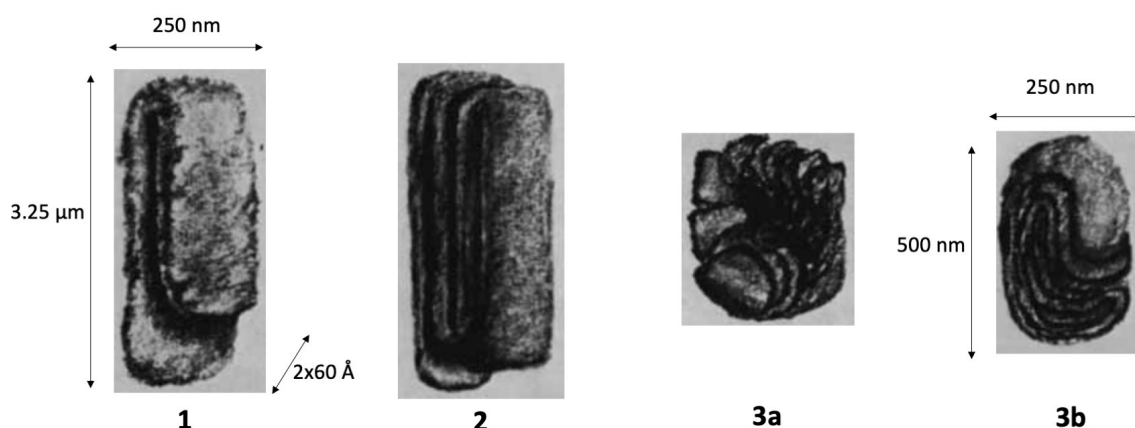


Figure 1.4: Stages in the genesis of PTFE dispersion particles (1. One-fold ribbon, 2. Several-folds ribbon, 3. Fully formed particles) and their typical dimensions [Rahl *et al.* 1972].

### Films manufacturing

The main techniques to manufacture PTFE parts are molding and sintering of granular PTFE, lubricated granular extrusion or dipping in an aqueous dispersion of PTFE. All these techniques start with the same raw material under powder form, with more or less finer particles [Ebnesajjad 2011].

### Compression molding

During compression molding, the granular PTFE powder of larger particle size is compressed into a "billet preform" at ambient temperature with sufficient strength to allow handling. After removal from the mold, the preform is heated above its melting point: it is sintered. During sintering, the particles are coalescing, providing strength and void reduction to reach a homogeneous and strong structure. After cooling, the billets are cut (skived) into wide thin films or sheets of thickness between less than 0.5 and 7 mm, see Figure 1.6 first line.

### Extrusion

PTFE extrusion starts from a fine powder resulting from emulsion polymerization. The mixture between PTFE fine powder and a lubricant is compressed at ambient temperature to form an "extrusion preform". This extrusion preform is then put at the entrance of an extruder. Inside the extruder, the material is melted and then cooled down to exit with the shape given by a die. To manufacture films, a plate can be extruded, calendered to obtain a film of a given thickness, heated to remove lubricant and then sintered, see Figure 1.6 second line.

### Cast films

PTFE aqueous dispersions allow processing of PTFE resin as solution, even if it is insoluble in almost all solvents. Thus, PTFE dispersions are used to coat fabrics, to produce anti-stick and low-friction coatings on metals and other substrates or to manufacture cast films.

To convert a dispersion into a PTFE film, four distinct steps in a coating tower are required, see Figure 1.5:

1. casting onto a supporting surface,

2. drying to remove water,
3. baking to remove the surfactant,
4. sintering to obtain a clear coherent film (optional).

During the drying step, the thickness of the deposited layer is very important: if the deposit is too thick, cracks are appearing, referred to as mudcracking. These defects cannot be eliminated during the sintering step. Thus, each formulation has its critical cracking thickness, below which cracking will not occur in a single application. Typical value under optimum conditions is  $\approx 40 \mu\text{m}$ . It depends mainly on the particle size range, the amount of surfactant used, the solid content and the belt speed [Drobny 2009].

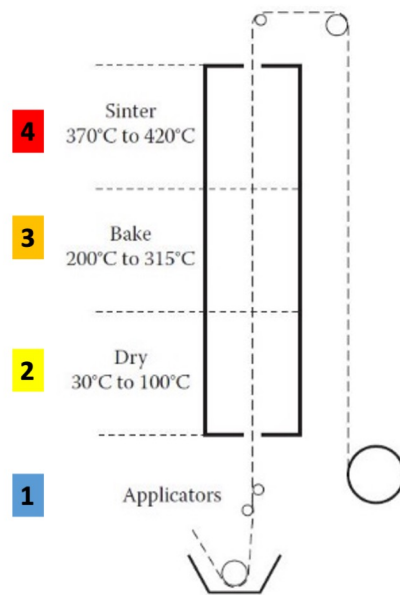


Figure 1.5: PTFE coating tower: 1. casting, 2. drying, 3. baking, 4. sintering [Drobny 2009].

A production machine is built with multiple stages as depicted on Figure 1.6 third line. After a film is sintered, it is recoated in the next stage. At the end of the machine, there is a device designed to strip the finished films from both sides of the belt and to wind them up into rolls. The resulting material has a smooth and sintered side corresponding to the side in contact with the belt and another one sintered or not.

### Fabric coating

PTFE dispersions are used to coat glass and aramid fabrics which can withstand high temperatures required for PTFE sintering without being degraded. As an alternative to perform deposits below the mudcracking thickness, several unsintered layers can be applied, and the coated fabric is then calendered prior to sintering to seal the mud cracks.

Another PTFE films-fabrics adhesion process is based on laminating two substrates having an unsintered PTFE layer on the surface. The two adjacent unsintered layers act as a pressure-sensitive adhesive and, as result of fibrillation under pressure, form a bond strong enough to survive a free sintering (without pressure). After sintering, the bond has the heat resistance of PTFE. This process is suitable for the lamination of coated fabrics as well as for lamination of PTFE cast films with PTFE-coated fabrics [Drobny 2009].

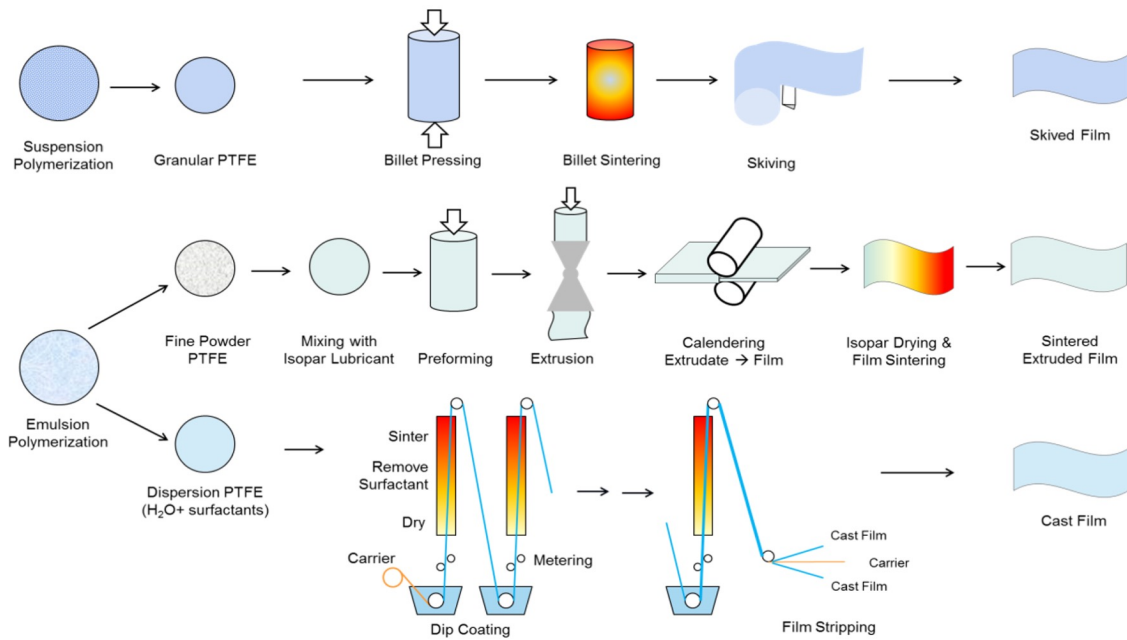


Figure 1.6: Different manufacturing processes of PTFE films used at Saint-Gobain: compression molding, extrusion, casting or dip coating.

### 1.2.2 Challenges for the lamination of coated fabrics

To allow laminated coated fabrics, the longest lifetime in service, the "best" adhesion and adherence properties are required. From the literature review on adhesion mechanisms between polymeric materials exposed in Chapter 2, several factors can impact adhesion quality, such as [W. I. Lee *et al.* 1987, L.-H. Lee 1991b, L.-H. Lee 1991a, Creton and Ciccotti 2016]:

- the wetting quality between adherents,
- the size of the real contact area between adherents,
- the presence and level of intramolecular forces between adherents,
- the occurring and level of macromolecular chain interdiffusion between adherents, which can lead to the formation of an interphase or of a low cohesion layer,
- the ability to dissipate energy during debonding,
- the adhesive chemistry.

For our study on adhesion between two thin PTFE cast films without fabrics, the impact of some of the previously mentioned factors is investigated through a home-made mechanical adherence tack test focusing on the influence of some manufacturing process conditions.

### 1.3 Structure of the study

The goal of this work is to understand and quantify the adhesive properties between two PTFE films in order to optimize the films welding manufacturing processes. Thus, it is essential to understand the commonly accepted adhesion mechanisms at play during polymer/polymer welding (Chapter 2) and to characterize the material of interest - PTFE films (Chapter 3). After a presentation of adherence measurements (Chapter 4), our specific tack test between crossed cylinders is implemented on PTFE films (Chapter 5). Different approaches to evidence and dissociate the different deformation contributions during tack test are discussed (Chapter 6).

The content of each chapter is detailed below.

#### **Chapter 2 - Adhesion mechanisms between two polymeric materials**

The different mechanisms occurring during amorphous polymer self-adhesion at high temperature are reviewed. The progressive collapse of the interface leading to mechanical strength increase happens through wetting and intimate contact, adhesive forces and macro-molecular chain diffusion. A short review provides some insights for semi-crystalline polymers self-adhesion.

#### **Chapter 3 - PTFE films - characterization**

This chapter explores our material of interest: PTFE films. Measurements of their crystallinity, mechanical properties and macro-molecular motions are provided.

#### **Chapter 4 - Adherence measurements**

A review of important concepts for adhesion and fracture mechanics in soft materials is presented through adhesion energy estimation approaches and test methods.

#### **Chapter 5 - Mechanical adherence tack test between crossed cylinders**

In this chapter, our user defined mechanical adherence tack test between crossed cylinders is detailed. The impact of contact temperatures, times and pressures is explored to identify mechanisms which could be responsible for PTFE-PTFE adhesion. According to contact pressure, different fracture modes are highlighted above melting.

#### **Chapter 6 - Towards modelling mechanical adherence tack test**

Using image analysis, the time evolution of some geometric parameters is followed during debonding. Under some assumptions, a first model is introduced to estimate the different energetic contributions and their respective levels. Another modelling method in three dimensions is proposed through a discrete network, which should lead to an estimation of the critical energy release rate.



# Adhesion mechanisms between two polymeric materials

*When two parts of the same polymer material are brought into contact at a high temperature, the macroscopic interface between the parts progressively disappears, while the mechanical strength of the interface increases. This healing process happens with three main stages to be discussed in this chapter: (i) surface approach and rearrangement, (ii) wetting and (iii) diffusion of macromolecules at the interface.*

### Contents

---

<b>2.1</b>	<b>Wetting and intimate contact . . . . .</b>	<b>26</b>
2.1.1	Wetting or thermostatic adsorption . . . . .	26
2.1.2	Intimate contact quality . . . . .	28
<b>2.2</b>	<b>Adhesive forces . . . . .</b>	<b>29</b>
<b>2.3</b>	<b>Interfacial macromolecular diffusion . . . . .</b>	<b>30</b>
2.3.1	Molecular dynamics . . . . .	30
2.3.2	Interfacial adhesion strength . . . . .	35
<b>2.4</b>	<b>Self-adhesion of semi-crystalline polymers . . . . .</b>	<b>39</b>

---

For all welding processes, the healing of the polymer/polymer interface was described by [Wool, Yuan, *et al.* 1989] who identified three main steps: (i) surface rearrangement and surface approach; (ii) wetting and (iii) diffusion. In step (i), the interface has no mechanical properties as two distinct surfaces still exist. In step (ii), the completion of the wetting stage marks the achievement of intimate contact. Potential barriers associated with inhomogeneities or porosities at the interface have disappeared, and molecular chains are free to move across the interface in a process of inter-diffusion also called auto-adhesion (step (iii)) [De Gennes 1980a, Awaja 2016], which leads to the collapse of the interface.

## 2.1 Wetting and intimate contact

Experimentally, the time scale of wetting phenomenon is difficult to quantify and it is also difficult to separate wetting from surface rearrangement. Since the time scale of wetting phenomenon seems shorter than surface rearrangement and molecular diffusion one, steps (i) and (ii) are often gathered into one step called intimate contact [Régnier *et al.* 2016].

Whatever the manufacturing process of polymer or composite parts is, surfaces always present a given roughness. Micro-asperities and micro-valleys as well as more macroscopic surface waves lead to a non-perfect contact between the two parts to assemble. As commonly admitted in thermoplastic welding, intimate contact is the first step in forming a bond between two thermoplastic surfaces that have been brought together under both heat and/or pressure [L.-H. Lee 1991b].

### 2.1.1 Wetting or thermostatic adsorption

Forming an assembly usually requires a liquid-solid contact or molten-solid contact in the case of polymeric materials. When two parts are brought together, the ability of a liquid to stay in contact with a solid surface, resulting from intermolecular interactions is called wetting. A short review is exposed hereafter even if in our study mainly liquid-liquid or solid-solid contacts will be considered.

#### Young and Laplace

When a droplet of a liquid  $L$  with its vapor  $V$  is at rest on a solid surface  $S$ , it takes a configuration minimizing the energy of the system and highlights the liquid-solid interactions. [Young 1805] proposed for this equilibrium state, the vectorial representation depicted in Figure 2.1a.

The equilibrium relation, based on Newton's second law, linking the liquid-solid contact angle  $\theta_{SL}$  to the surface energies liquid-solid, solid-vapor and liquid-vapor ( $\gamma_{LS}$ ,  $\gamma_{SV}$ ,  $\gamma_{LV}$ ) is given by Equation 2.1.

$$\gamma_{LS} + \gamma_{LV} \cos \theta_{SL} - \gamma_{SV} = 0 \quad (2.1)$$

$\gamma_{SV}$  and  $\gamma_{LV}$  are the surface energy (or tension) of solid and liquid phases in contact with vapor.  $\gamma_{LS}$  is the interfacial liquid-solid energy.  $\theta_{SL}$  is the contact angle of the liquid against the solid. If  $\theta_{SL}$  is zero, the liquid propagates freely on the surface and the solid is totally wet.

**Dupré**

When two phases A and B are in intimate contact with each other, an interface with a given interfacial energy,  $\gamma_{AB}$  is present, see Figure 2.1b. When the two phases are separated, this interface will disappear but two new are formed with an energetic cost: the interface between phase A and air ( $\gamma_A$ ) and the interface between phase B and air ( $\gamma_B$ ). The energy per unit of surface required to separate reversibly the two phases in contact is called the **thermodynamic work of adhesion**  $W_A$ , expressed in N/m or J/m<sup>2</sup> and given by Dupré equation [Dupré *et al.* 1869]:

$$W_A = \gamma_A + \gamma_B - \gamma_{AB} \quad (2.2)$$

Note, if the two phases are solid and liquid, the equation 2.2 can be written as

$$W_{SL} = \gamma_{SV} + \gamma_{LV} - \gamma_{LS} \quad (2.3)$$

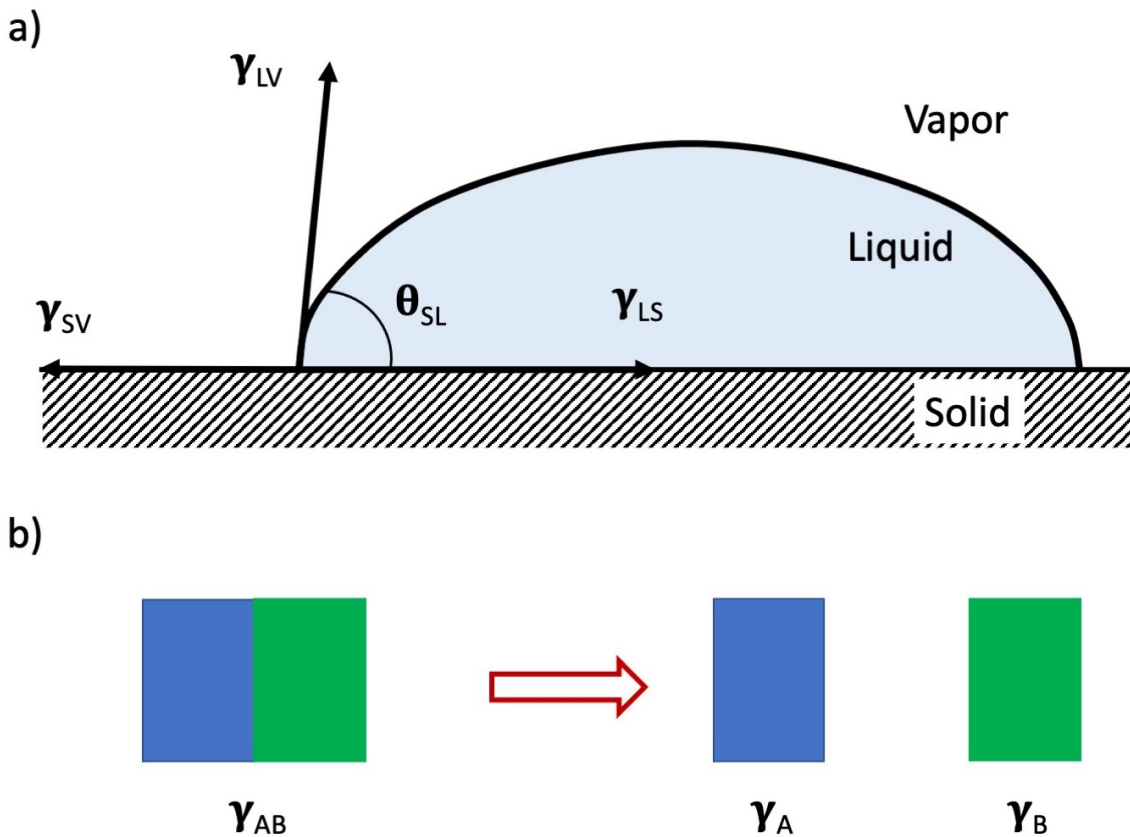


Figure 2.1: a) Vector diagram of the balance adopted by a drop of liquid on a solid. Representation proposed by [Young 1805], b) Separating two phases in contact costs energy: two new interfaces with air are formed (Dupré).

**Measuring thermodynamic work of adhesion**

While the surface tension of the liquid is easy to measure, the other two are more difficult. Combining Young (2.1) and Dupré (2.3) equations in the case of solid-liquid interface gives the Young-Dupré equation:

$$W_{SL} = \gamma_{LV}(1 + \cos \theta_{SL}) \quad (2.4)$$

Thanks to this equation, the work of adhesion can be easily estimated by contact angle measurements.

Experimentally, thanks to pendant drop test, at room temperature, surface tension values in air are comprised between the value for Van der Waals liquid  $\gamma_{VdW-air} \approx 20 \text{ mJ/m}^2$  and for metallic liquid/solids such as mercury  $\gamma_{max-air} \approx 500 \text{ mJ/m}^2$ . Water  $\gamma_{H_2O-air} \approx 72 \text{ mJ/m}^2$  and glycerol  $\gamma_{glycerol-air} \approx 65 \text{ mJ/m}^2$  are commonly used for contact angle measurements [Lange 1999]. For PTFE our material of interest, the work of adhesion is from 18 to 25  $\text{mJ/m}^2$  [Kinloch 1980].

Up to now, only thermodynamics parameters have been considered for wetting assessment but surface roughness also affects wetting and the intimate contact quality. Adhesion on a rough surface will be easier since the effective contact area is larger than for a perfectly flat surface.

### 2.1.2 Intimate contact quality

The quality of the contact can be described through the concept of degree of intimate contact  $D_{ic}$ , introduced by [W. I. Lee *et al.* 1987] and defined as the ratio of the real contact area to the total area of the surfaces to be welded. [W. I. Lee *et al.* 1987] proposed a simplified model of the surface using rectangular elements of the same size. In this very idealized picture, the surface topography is described by its average roughness, that may be attributed to the height  $\alpha$  of rectangles.

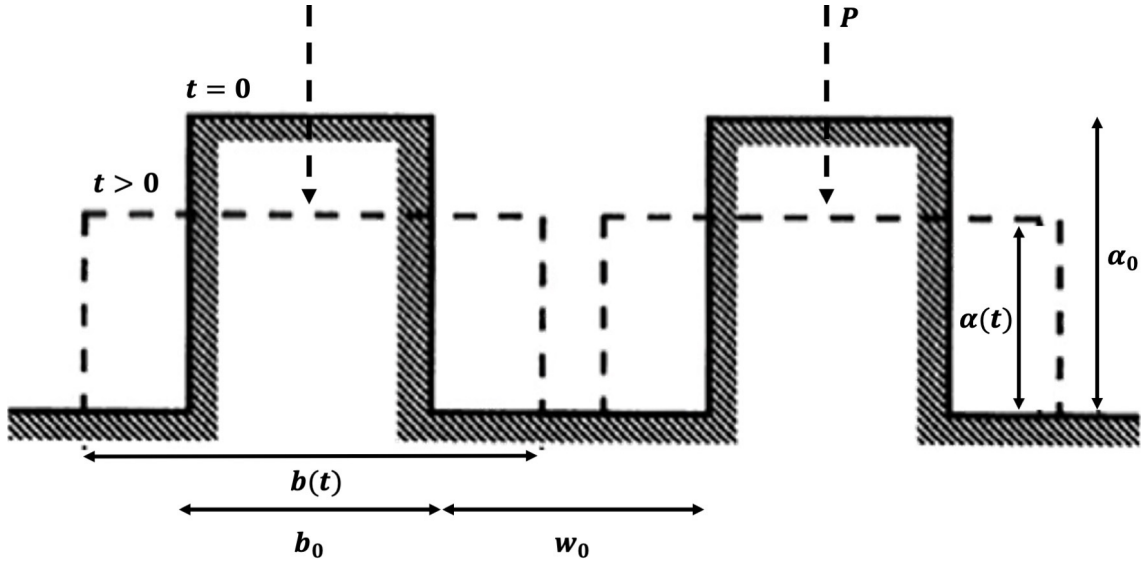


Figure 2.2: Idealization of surface asperities by periodic rectangular elements, before and after squeezing [W. I. Lee *et al.* 1987].

Once the surface topography is obtained experimentally with surface profiler, the main challenge is the prediction of its evolution while submitted to the welding pressure. Using the volume conservation of rectangles and the "squeeze flow" model for a Newtonian fluid, [W. I. Lee *et al.* 1987] obtained in an isothermal case:

$$D_{ic} = \frac{1}{1 + \frac{w_0}{b_0}} \left[ 1 + \frac{5P}{\eta} \left( 1 + \frac{w_0}{b_0} \right) \left( \frac{\alpha_0}{b_0} \right)^2 t \right]^{\frac{1}{5}} \quad (2.5)$$

where  $P$  is the applied pressure and  $\eta$  the viscosity of the molten polymer.

Complete intimate contact is achieved when  $D_{ic}$  becomes unity, so the time required to achieve complete intimate contact can be derived.

Experimentally, [W. I. Lee *et al.* 1987] show that a threshold pressure seems to exist. If the pressure applied is lower, the intimate contact time will be longer; on the other hand, if the pressure is above this threshold, the mechanical properties of the part will not be improved [Wool, Yuan, *et al.* 1989]. This gives the idea that above a given pressure, intimate contact time is negligible compared to other characteristic times such as chain interdiffusion time.

More sophisticated considerations related to adhesion and wetting can be found in [Israelachvili 2011].

## 2.2 Adhesive forces

Interfacial interactions between adherents can help reaching adhesion. When two parts are in contact, different types of forces can be involved such as molecular bonds or intermolecular interactions. These forces act on various distances and energies; a small overview of the different bond length and associated energies is presented on Table 2.1.

Type	Bond length (nm)	Bond energy (kJ/mol)
<b>Chemical bonds</b>		
Covalent	0.15-0.24	60-950
Metallic	0.25-035	100-400
Ionic	0.15-0.3	300-1000
<b>Intermolecular interactions</b>		
Van der Waals forces	0.4-0.5	2-15
Hydrogen bonds	0.26-0.3	10-40

Table 2.1: Orders of magnitude for adhesive forces bond lengths and energies [L.-H. Lee 1991b].

In summary, anchorage (through wetting/intimate contact and adhesive forces) is a preliminary and essential step to the interdiffusion phenomenon. Indeed, the interdiffusion mechanism between two polymers can only take place if the contact between the two parts is sufficient enough [Y. H. Kim *et al.* 1983].

## 2.3 Interfacial macromolecular diffusion

In this part, the focus is on interfaces between identical polymers where identical chains interdiffuse.

### 2.3.1 Molecular dynamics

In this paragraph, the scope is on understanding the different chain motion models and their consequences on the mechanical properties of the material.

#### Chain statistics

In the melt state, linear flexible macromolecular chains adopt Gaussian statistics; their average conformation is described as a random walk, see Figure 2.3. The succession of  $N$  chain section will lead to the following mean square **end-to-end distance**

$$\langle R_0^2 \rangle = Na^2 \quad (2.6)$$

with  $a$  the monomer length.

It has been also demonstrated that the **radius of gyration**  $R_g$  of a Gaussian chain has the same dependence with  $N$ :

$$R_g = aN^{\frac{1}{2}} \quad (2.7)$$

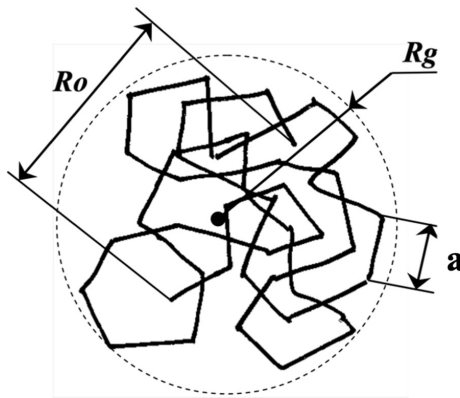


Figure 2.3: Scheme of a single polymer chain conformation

To describe and understand polymers viscoelastic properties, the concept of entanglement is key. For any polymer, a critical molar mass  $M_c$  from which chains starts to entangle can be defined [Berry *et al.* 1968]:

$$M_c = 2M_e \quad (2.8)$$

with  $M_e$  the molar mass between two successive entanglements.

Evaluating the Newtonian viscosity by rheology gives hints of the molar mass. Below the critical molar mass, in the unentangled regime, the experimental viscosity follows a linear relation with molar mass and above  $M_c$ , in the entangled regime, the recorded relationship is to the power 3.4 for linear macromolecules, see Figure 2.4 [Berry *et al.* 1968].

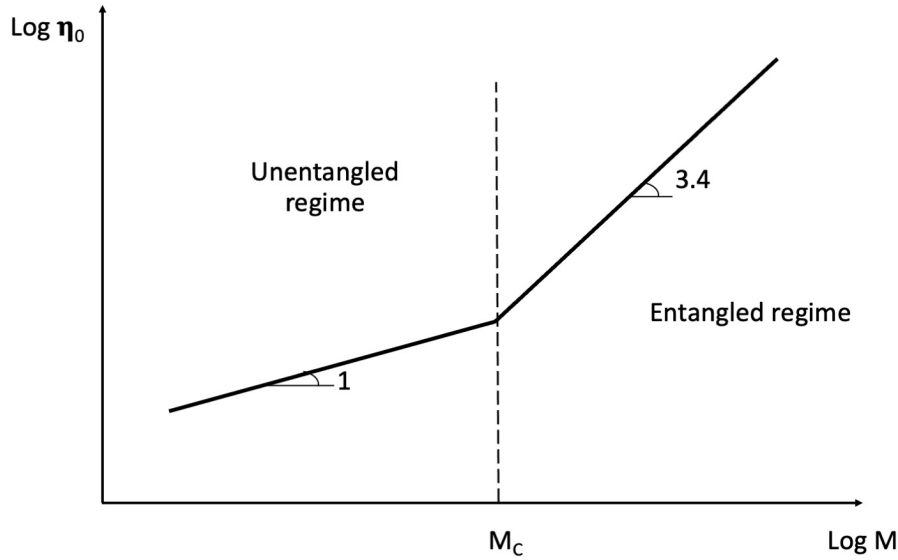


Figure 2.4: Experimental Newtonian viscosity  $\eta_0$  evolution with molar mass  $M$ ; a critical molar mass  $M_c$  marks the transition between unentangled and entangled regimes [Berry *et al.* 1968].

The models exposed here after explain the two regimes of the viscosity evolution with molar mass.

### Rouse model

For  $M < M_c$ , chains are not entangled. While moving, chains can only feel their neighbors through friction. Rouse model (1953) on dilute polymers in a solvent improved by [Zimm 1956] for small chains describes this behavior.

The chain is considered as a succession of  $N$  harmonic springs connecting  $N + 1$  balls. Each spring is a sub-chain long enough to be Gaussian. Interactions between sub-chains are neglected and the force exerted on each sub-chain is composed of [J. D. Ferry 1980]:

- an elastic force, resulting from the reactions of the two adjacent springs,
- a viscous friction force: one of the model predictions is the additivity of the friction coefficients (if  $\xi_0$  is the monomeric friction coefficient, then the overall friction coefficient of the chain is  $\xi = N\xi_0$ ),
- a random force.

Solving the equation leads to  $N$  cooperative modes each one having a relaxation time  $\tau_N$ . The longest internal mode corresponds to the movement of the end-to-end vector with a time:

$$\tau_{Rouse} = \frac{\xi_0}{3\pi^2 k_B T} a^2 N^2 \quad (2.9)$$

with  $k_B$  the Boltzmann constant and  $T$  the temperature.

The Rouse characteristic time is proportional to the square of the chain length  $aN$ . It corresponds to the time for the chain to move of a radius of gyration and for a renewal of the chain conformation. It can be shown that the change of the end-to-end distance  $\Delta R_0$  is of the order of magnitude of  $R_0$  during  $\tau_{Rouse}$ . The diffusion coefficient  $D_N$  corresponding

to a chain displacement of  $\Delta R_0$  is:

$$D_N = \frac{(\Delta R_0)^2}{\tau_{Rouse}} \approx \frac{(R_0)^2}{\tau_{Rouse}} \sim \frac{N}{N^2} \sim \frac{1}{N} \quad (2.10)$$

So, for chains of length  $M < M_c$ , molecules behave according to Rouse regime. The polymer diffusion coefficient is proportional to the inverse of the molar mass:  $D_N \sim M^{-1}$ . Experimentally, the permanent flow viscosity in the melt varies as the molar mass:  $\eta_0 \sim M$ .

## Reptation theory

### Motivation

The previous section dealt with the ideal case of a macromolecular chain isolated in a solvent or of small chains. To interpret the viscoelastic properties of high molecular weight polymer, the notion of entanglement had to be considered [Graessley 1982]. Rouse model assumes that the chain is free and monomers can cross each other. In reality, the chain is surrounded by many other chains. From a static point of view, other chains effect is erased since the chain has a Gaussian conformation. But from a dynamic point of view, this is no longer true: the fact that monomers cannot cross each other must be considered.

In a system of entangled polymers, chain molecular movements can be divided into two categories [Doi *et al.* 1979]:

- Small-scale movements not affecting the entanglements topology. The time scale of these movements is mainly the Rouse relaxation time.
- Large-scale movements changing the topology. The focus will be on these movements obeying another time scale.

### De Gennes and Doi & Edwards theory

The movement of a macromolecule, in concentrated solution or in the melt, is limited by the neighboring chains. To model movements of linear ideal Gaussian chains with  $M > M_c$ , the reptation theory was introduced by de Gennes [De Gennes 1971] and extended by Doi and Edwards [Doi *et al.* 1978, Doi *et al.* 1979].

In the melt, chains can move by Brownian motion, but they cannot cross each other: they are trapped in a network. Between obstacles, chains can move in a wormlike fashion, called reptation. Doi and Edwards [Doi *et al.* 1978, Doi *et al.* 1979] introduced the notion of tube containing the chain as represented in Figure 2.5. Thanks to the tube, the surrounding chain effect imposed by the neighboring monomers through entanglements can be considered: the lateral fluctuations are limited, and the chain movements are restricted along the tube curvilinear length. The tube diameter  $d$  is equal to the distance between two successive entanglements [Edwards 1967]:

$$d \sim aN_e^{\frac{1}{2}} \quad (2.11)$$

with  $a$  the monomer length and  $N_e$  the average number of monomers between entanglements.

The tube diffusion coefficient,  $D_{tube}$ , is given by the Einstein relationship:

$$D_{tube} = \frac{k_B T}{\xi} = \frac{k_B T}{6\pi\eta_1 N a} \quad (2.12)$$

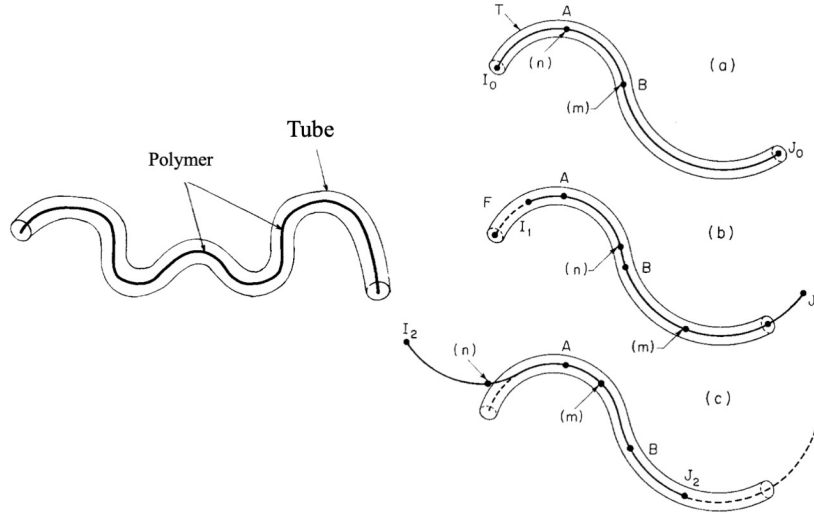


Figure 2.5: Reptation after [De Gennes 1971]; Left: the chain trapped in its tube. Right: (a) to (b) the chain moves along its tube to the right, (b) to (c) the chain moves to the left and exits its original tube.

where  $\xi$  is the friction coefficient and  $\eta_1$  is the local viscosity of the polymer melt. During reptation time  $\tau_{rept}$ , the chain moves over  $L_{tube}$  along the tube:

$$D_{tube}\tau_{rept} = L_{tube}^2 = \left(\frac{N}{N_e}\right)^2 d^2 = \left(\frac{N}{N_e}\right)^2 N_e a^2 \quad (2.13)$$

so:

$$\tau_{rept} = \frac{6\pi\eta_1 a^3 N^3}{k_B T N_e} \quad (2.14)$$

The self-diffusion coefficient  $D_{self}$  can be defined by the time  $\tau_{rept}$  needed for the chain to renew its tube and thus to move from a distance equal to the end-to-end distance  $R_0$ . In fact, the center of gravity of the chain is considered to diffuse over a distance equal to its radius of gyration  $R_g$  during the reptation time.

$$D_{self}\tau_{rept} = R_g^2 = N a^2 D_{self} = \frac{k_B T N_e}{6\pi\eta_1 a N^2} \quad (2.15)$$

**So, the reptation time, relative to the movement of the full chain, varies with  $M^3$ . As  $\eta \sim \tau_{rept}$ , then  $\eta \sim M^3$  according to reptation theory. Experimentally for  $M > M_c$ , the viscosity is found to vary as  $M^{3.4}$  [Berry *et al.* 1968]. The diffusion coefficient representative of the overall mobility of the chain is proportional to  $M^{-2}$ .**

For high molecular weight polymers, the reptation time is very long compared to the inter-entanglement relaxation times. Also, to calculate the reptation time with equation 2.14, local viscosity of the polymer melt  $\eta_1$  must be known as well as the chain geometrical parameters. To our knowledge, this constant is not available in the literature for PTFE, so determining a reptation time using these equations is not possible.

[De Gennes 1971, De Gennes 1980b] also summarizes the different characteristic times associated with polymer chains in a gel – which seems similar to a melt of uncrosslinked chains, see Figure 2.6. At very short times,  $t < \tau_{\text{entanglement}}$ , the motion is restricted to the local Rouse segment. The chain does not feel the constraints of the network and behaves as a Rouse chain in a free space. For  $\tau_{\text{entanglement}} < t < \tau_{\text{Rouse}}$ , the chain starts to feel the topological constraints of the tube and thus the motion of Rouse segments is restricted laterally but free motion is allowed along the curvilinear axis of the tube. However, the defects are not completely adjusted along the whole chain. At  $\tau_{\text{Rouse}} < t < \tau_{\text{rept}}$ , the defects are equilibrated along the total length of the tube and the chains moves as a whole along the fixed tube. The case of  $t \geq \tau_{\text{rept}}$  is governed by a reptational process that allows the chain to completely escape from the initial tube.

Log(chain mean displacement)

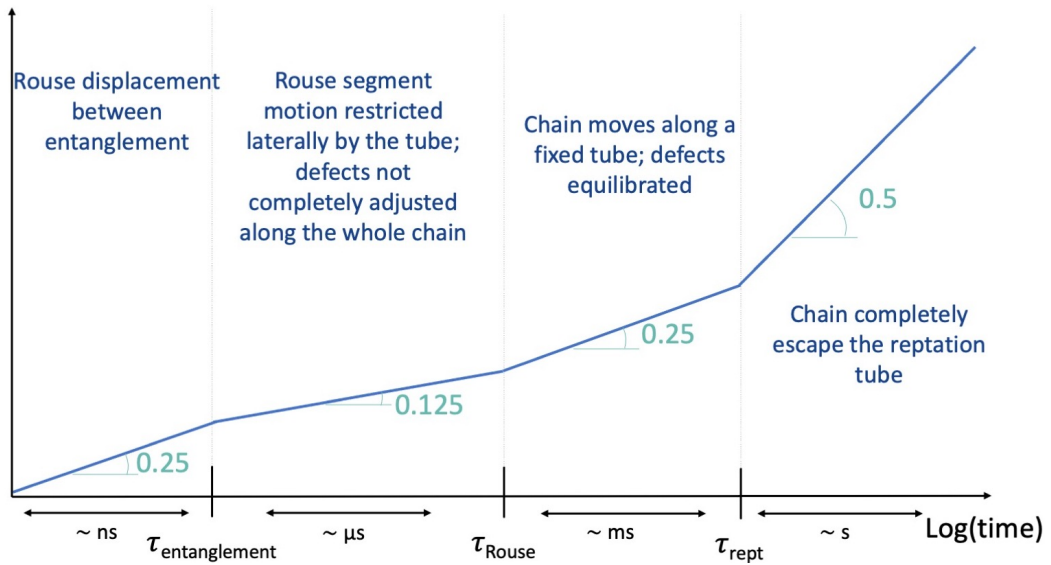


Figure 2.6: Scaling law of the mean chain displacement versus time and associated mechanisms and time scales, reconstructed from [De Gennes 1971, De Gennes 1980b].

### Linear viscoelasticity to quantify macromolecular diffusion

Linear viscoelasticity (LVE) reflects the distribution of relaxation times in a polymer and is therefore strongly correlated to the molecular structure [J. D. Ferry 1980]. Hence, LVE is a powerful tool, which provides fundamental insights about the link between dynamics and polymer structure [Ruymbeke *et al.* 2007].

From linear viscoelastic frequency sweep tests, two characteristic relaxation times can be determined from the terminal relaxation zone, see Figure 2.7. Firstly the number-average relaxation time  $\tau_n$  can be determined from the intersection of the  $G''$  terminal regime with  $G_N^0$ , where  $G_N^0$  is the plateau modulus. Secondly, the intersection frequency  $\omega_w$  of  $G'$  and  $G''$  terminal regimes gives the weight-average terminal relaxation time  $\tau_w = \frac{1}{\omega_w}$ . Therefore, the breadth of relaxation time distribution can be assessed to  $\frac{\tau_w}{\tau_n}$  and varies in the typical range 2 to 3 for nearly monodisperse polymers or polymers with a very narrow molecular mass distribution [J. D. Ferry 1980].

For monodisperse polymers, the reptation time  $\tau_{\text{rept}}$  of tube models is closely linked to

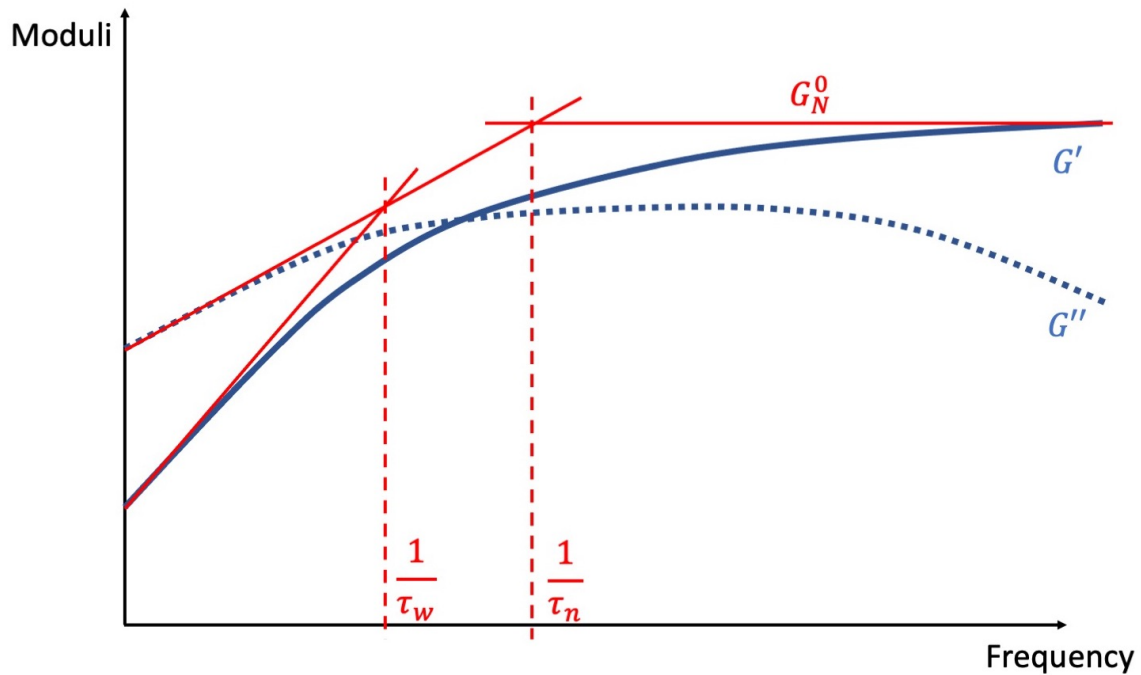


Figure 2.7: Scheme of polymer frequency sweep response (storage modulus  $G'$  - line and loss modulus  $G''$  - dashed line) and the two characteristic relaxation times which can be extracted: the number-average relaxation time  $\tau_n$  and the weight-average terminal relaxation time  $\tau_w$ , adapted from [Régnier *et al.* 2016].

the terminal peak position of  $G''$  [Graessley 1980] and should be intermediate between  $\tau_w$  and  $\tau_n$ . No simple response can be given for polydisperse polymers as obstacles in tube modeling are not really fixed due to smaller chains.

### 2.3.2 Interfacial adhesion strength

When two pieces of the same amorphous polymer material are brought into contact at a temperature above the glass transition temperature, the macroscopic interface between the pieces progressively disappears, whereas the mechanical strength of the interface increases [Jud, Kausch, and Williams 1981, Wool and O'Connor 1981]. This phenomenon is known as "polymer-polymer welding" or "crack healing".

#### Chain inter-diffusion - interphase formation

[De Gennes 1980a] modeled the penetration of chains at the interface, see Figure 2.8. For a highly entangled polymer, the penetration of a chain folded as a hairpin is unlikely (Figure 2.8a): the chain must penetrate by one end (Figure 2.8b). Path AA' corresponds to a random walk of length  $l$ . Points A and A' must be in slices of the same thickness  $e$  above and below the interface. The layer of thickness  $2e$  is the **interphase** where chains are mobile and crossing the interface.

#### Crack healing and polymer-polymer welding

A macroscopic property  $P$ , such as interfacial adhesion strength, can be assumed proportional to the density (or concentration) of links across the interface which is itself

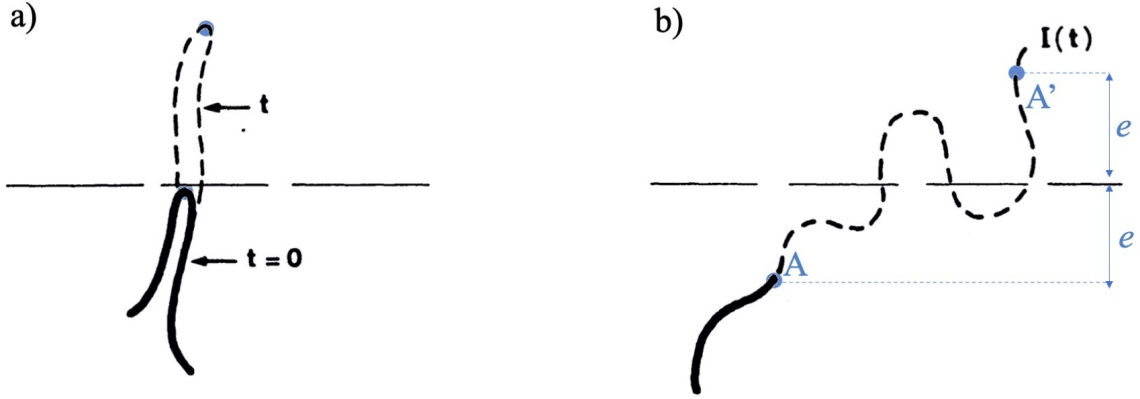


Figure 2.8: Two modes of interdigitation: (a) hairpins (b) chain ends crossing the contact plane. For strongly entangled chains ( $N \gg N_e$ ), process (b) is expected to dominate, adapted from [De Gennes and Brochard-Wyart 1993].

proportional to the time of welding and thus proportional to the time of diffusion.

$$P(t) \sim \left(\frac{t}{\tau_{rept}}\right)^\alpha \quad (2.16)$$

De Gennes [De Gennes 1992] distinguished several cases depending on the time scale and the attraction (through Flory parameter) of both polymers from each side and on the initial configuration of the chain ends at the interface. Only two cases of interest are recalled here.

### Crack healing

Crack healing refers to the development of mechanical strength between **two fractured surfaces of the same sample** brought into contact above the glass transition temperature. Since the two parts result from the fracture of the same initial sample, macromolecules either disentangled or broke through chain scission; resulting in chain ends concentrated at the polymer surface before contact. The diffusion process proceeds in a Rouse-type dynamics. The macroscopic property  $P$ , here the interfacial adhesion strength  $\sigma$  and energy release rate  $G$ , scale in time as

$$\sigma(t) \sim \left(\frac{t}{\tau_{rept}}\right)^{\frac{1}{4}} \quad \text{and} \quad G(t) \sim \left(\frac{t}{\tau_{rept}}\right)^{\frac{1}{8}} \quad (2.17)$$

### Polymer-polymer welding

Polymer-polymer welding consists in bringing together **two surfaces which have not been in contact before**. The chain ends are not initially concentrated at the interface. Before reaching the interface, chain ends have to diffuse in the bulk. In this case, the macroscopic property  $P$ , here the interfacial adhesion strength  $\sigma$  and energy release rate  $G$ , vary in time as

$$\sigma(t) \sim \left(\frac{t}{\tau_{rept}}\right)^{\frac{1}{2}} \quad \text{and} \quad G(t) \sim \left(\frac{t}{\tau_{rept}}\right)^{\frac{1}{4}} \quad (2.18)$$

In both cases (crack healing and polymer-polymer welding), for times larger than the reptation time, the chains are no more bridging chains: they have traveled an average distance larger than their radius of gyration and are losing any interaction with the interface.

Earlier crack healing experiments performed by Kausch and co-workers [Jud and Kausch 1979, Jud, Kausch, and Williams 1981] showed that refracture stress grows as  $t^{\frac{1}{4}}$ . This corresponds to the first case discussed by de Gennes [De Gennes 1992] where the initial fracture generated an excess of chain ends at the initial surfaces before welding. On the other hand, Wool et al. [Wool, Yuan, *et al.* 1989] performed several lap shear experiments on freshly molded samples for polymer-polymer welding. They found that the fracture stress at the welded polymer interface increases with the healing time to the power  $\frac{1}{4}$ , which should not be the case if diffusion of chains in the bulk was first needed. Their analysis focused on the entanglements across the interface and they argued that the scaling law in  $t^{\frac{1}{4}}$  is valid whenever the chains in the deformation region disentangle completely. In the same communication, Wool et al. [Wool, Yuan, *et al.* 1989] give an estimation of the chain length which must have diffuse through the interface to reach full adhesion strength. The interdiffusion of eight times the critical molecular weight, see Equation 2.8, seems to be enough to achieve a "good" adhesion as depicted by the energy release rate reaching a plateau value, see Figure 2.9.

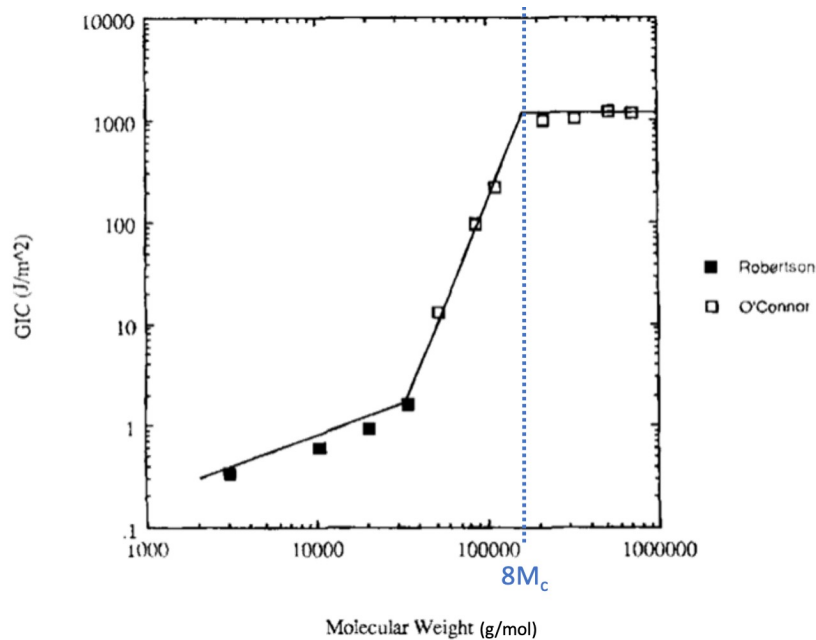


Figure 2.9: Energy release rate  $G_c$  vs molecular weight for polystyrene: eight times the critical molecular mass seems to be enough to reach a "good" adhesion, adapted from [Wool, Yuan, *et al.* 1989].

### Different fracture mechanisms

The mechanisms, kinetics and mechanical strength impact of polymer-polymer interfaces disappearance have been reviewed. Now, a small overview of the different polymer fracture mechanisms is exposed in the case when the number of connectors and the degree of polymerization  $N$  of the connectors are known. Those mechanisms are reviewed by Creton et al. [Creton, Kramer, Hui, *et al.* 1992, Creton, Kramer, H. R. Brown, *et al.* 2002]. Three breaking modes have been highlighted: chain pullout, chain scission and crazing with their respective crack tip stresses -  $\sigma_{pullout}$ ,  $\sigma_{scission}$  and the plastic yield stress  $\sigma_y$ . The breakage mode is determined by the lowest of these three stresses.

### Chain pullout

A chain embedded in the polymer matrix is pulled at one end with a force  $f$  larger than the critical value  $f^* = Nf_{mono}$ , where  $N$  is the degree of polymerization of the polymer and  $f_{mono}$  the static friction force per monomer. The traction stress component normal to the planar interface (assuming that the chains are pulled out normal to the interface) is related to the force  $f$  and the number of chains per unit area of the interface  $\Sigma$ :

$$\sigma_{pullout} = f\Sigma \quad (2.19)$$

Using this model, Xu et al. [Xu *et al.* 1991] have demonstrated that for a sufficiently slow crack growth rate, the critical energy release rate  $G$  is:

$$G_c = \frac{f_{mono}\Sigma N^2 a}{2} \quad (2.20)$$

with  $a$  a statistic unit length.

### Chain scission

For larger values of the degree of polymerization  $N$ , the force required to pull a chain out of the glass,  $f_{mono}N$ , will be higher than the force required to break a main-chain bond  $f_b$ . In this case, the maximum stress that can be sustained by the interface will be independent of  $N$ , and equal to  $\sigma_{scission} = f_b N \Sigma$ . If this interfacial stress is inferior to the crazing stress of both polymers, fracture will occur by simple chain scission and the interface crack will propagate without any significant amount of plastic deformation.

### Crazing

Crazing is a deformation mechanism which can lead to a significant increase in fracture toughness. The energy required to propagate the crack is mainly dissipated by the growth of a craze (corresponding to the plastic zone) at the crack tip. The conditions for the nucleation and growth of crazes in a homogeneous polymeric material have been studied, in particular by [Kramer 1983, Kramer and Berger 1990]. The best current model for craze failure at a crack tip is that originally proposed by Brown [H. R. Brown 1991]. In this model, the craze consists of parallel highly oriented, load-bearing fibril, joined by cross tie fibrils. Those cross tie fibrils have an important effect on the failure mechanism of a craze since they can transfer stress between broken and unbroken fibrils, see Figure 2.10.

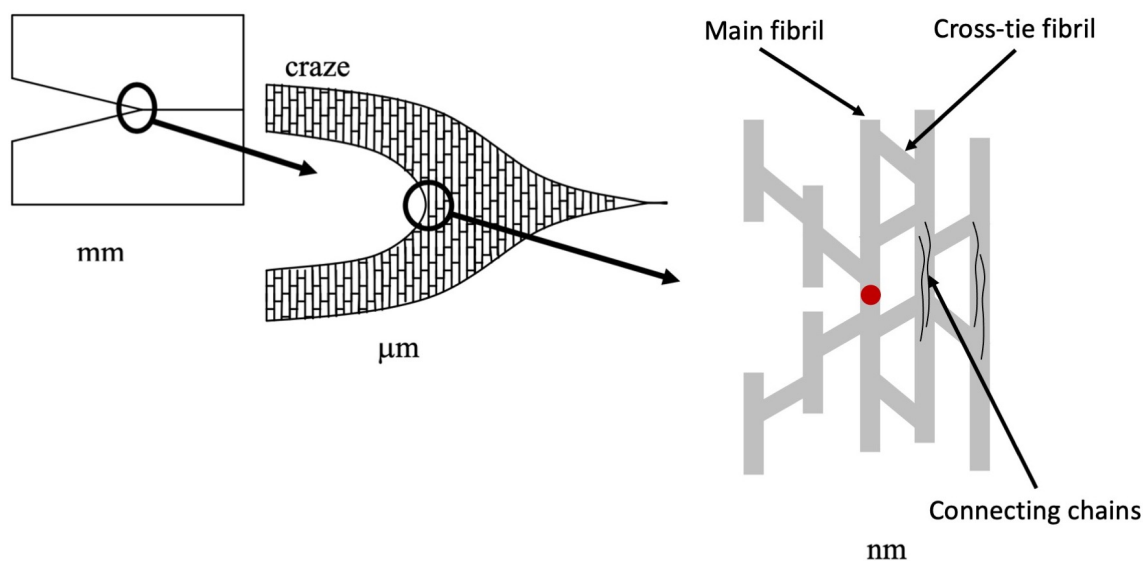


Figure 2.10: Scheme of the various structures at different length scales near the crack tip within the craze, adapted from [Kramer and Berger 1990].

## 2.4 Self-adhesion of semi-crystalline polymers

While diffusion theory applies well for self-adhesion of amorphous polymers, it does not provide a complete explanation for semi-crystalline polymers. Chain mobility of semi-crystalline polymers is reduced due to the presence of crystalline structures and polymer chain inter-diffusion is limited during self-adhesion [Xue, T. A. Tervoort, Rastogi, *et al.* 2000]. Crystallization may also occur simultaneously with inter-diffusion of polymer chains at the interface during self-adhesion of semi-crystalline polymers [Xue, T. A. Tervoort, Rastogi, *et al.* 2000, Lamèthe *et al.* 2005], which will have great influence on the bonding strength development [Yuan *et al.* 1990, Gent, E.-G. Kim, *et al.* 1997].

Several research groups investigated specificities of self-adhesion of semi-crystalline polymers by studying the influence of the temperature [Smith *et al.* 2001], of the chain mobility [Boiko *et al.* 2001], of the morphology [Xue, T. A. Tervoort, and Lemstra 1998] and of the co-crystallization [Xue, T. A. Tervoort, Rastogi, *et al.* 2000, Gent, E.-G. Kim, *et al.* 1997, Bonten *et al.* 2001, Frederix *et al.* 2013]. At a temperature below the melting temperature and in non-isothermal conditions, Smith *et al.* [Smith *et al.* 2001] observed with polypropylene that the solid plate caused a columnar growth in the molten plate, suggesting a certain degree of epitaxy, or at the very least, intimate contact across the interface. At a temperature just above the melting temperature and still in non-isothermal conditions, the columnar region was still observed. The authors argue that the kinetics and temperature dependence of the buildup of strength during fusion bonding of a semi-crystalline polymer just above the melting temperature may not be simply related to self-diffusion in the amorphous phase, but also to co-crystallization. Cho *et al.* [Cho *et al.* 1995] explain that self-bonding of amorphous PEEK films is achieved by crystalline growth after diffusion and entanglement of the polymer chains across the interface. They found that the crystalline growth rate is much higher at higher temperatures, leading to a higher bonding strength. Xue *et al.* [Xue, T. A. Tervoort, Rastogi, *et al.* 2000] showed that co-crystallization over the interface of semi-crystalline polymers could occur due to lamella doubling in size after annealing. Several other authors attributed to co-crystallization an

interfacial reinforcement role in the welding efficiency of semi-crystalline polymers [Gent, E.-G. Kim, *et al.* 1997, Bonten *et al.* 2001, Frederix *et al.* 2013].

Jarrousse [Jarrousse 2004] stressed that the amorphous phase does not seem to play any role in the adhesion below the melting temperature and this whatever the degree of crystallinity of the polymer is. In the case of surfaces brought into contact after equilibrium, i.e. after a preheating time allowing the crystallization or melting process to stabilize, the adhesion becomes measurable only above the melting temperature of the first crystallites, if this fusion is not followed by an immediate recrystallization.

The studies highlight the fact that for semi-crystalline polymers the morphology plays an important role on adhesion. The mechanisms now accepted in the case of amorphous polymers, are applicable to a given extent to semi-crystalline polymers, but are indeed unsatisfactory, since other mechanisms such as co-crystallization, crystalline reorganization or epitaxial growth are expected to impact the surface reinforcement between semi-crystalline polymers. These mechanisms seem to largely influence both the strength and kinetics of adhesion buildup between semi-crystalline polymers, but still more studies on the subject are needed. Moreover, to our knowledge, no studies have been found on this topic on our material of interest, PTFE.

# PTFE films characterization

*This chapter explores our material of interest - PTFE films. Measurements of their crystallinity, mechanical properties and macro-molecular motions are provided; they will be used later to explain PTFE-PTFE adhesion.*

## Contents

---

<b>3.1</b>	<b>Materials</b>	<b>42</b>
3.1.1	Raw dispersion	42
3.1.2	Cast films	42
<b>3.2</b>	<b>PTFE: a semi-crystalline polymer</b>	<b>46</b>
3.2.1	Phase diagram	46
3.2.2	Crystalline structure	46
3.2.3	Crystallization kinetics	57
<b>3.3</b>	<b>PTFE cast films mechanical properties</b>	<b>61</b>
3.3.1	Dynamic Mechanical Analysis in tension	61
3.3.2	Uniaxial tensile test	63
<b>3.4</b>	<b>PTFE macro-molecular chains or segments mobility</b>	<b>65</b>
3.4.1	Experimental protocol - Shear rheometry	65
3.4.2	Chain movement: time-temperature superposition	66
3.4.3	Segment movement: progressive healing	68

---

### 3.1 Materials

The materials of interest are provided by Saint-Gobain High Performance Solutions. They are either raw material bought from other chemical manufacturer supplier - raw dispersion - or materials manufactured by Saint-Gobain from this raw material.

#### 3.1.1 Raw dispersion

The raw dispersion is commercially available. Dispersion consists of water, PTFE particles (around 60% of the wet weight) and organic surfactants (around 6% of the wet weight) giving its white milky aspect as depicted on Figure 3.1a.

When dried and observed by SEM with a thin gold coating, see Figure 3.1b, the dispersion particles size ranges from  $\sim 250$  to  $300$  nm and their shape is similar to the description available in the literature [Rahl *et al.* 1972].

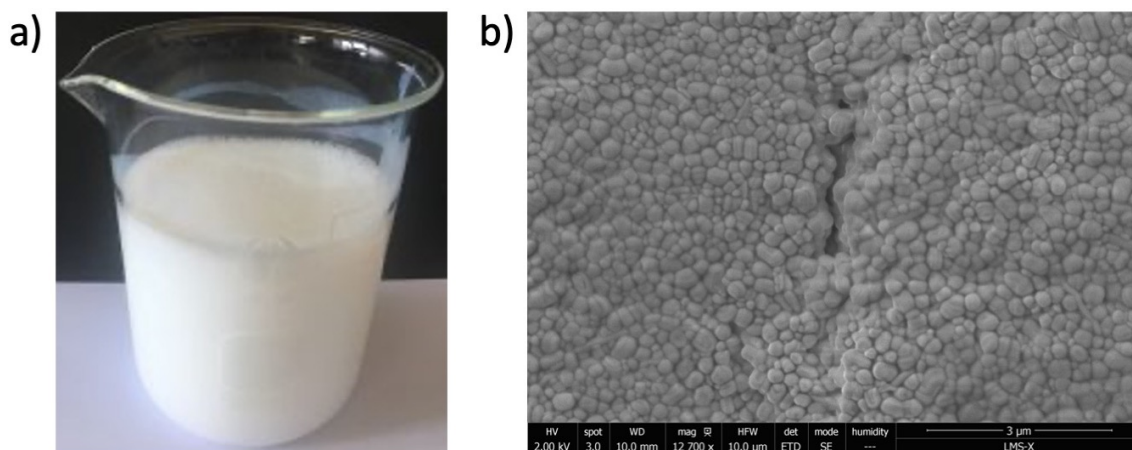


Figure 3.1: PTFE Dispersion a) Picture of PTFE dispersion with milky aspect in a 50 mL beaker, b) SEM image of dried PTFE dispersion at ambient temperature with 1-2 nm gold conductive coating.

#### 3.1.2 Cast films

PTFE cast films are made from dip coating of a matrix into PTFE dispersion (see Figure 1.6 bottom line). Two different samples sold under the reference Chemfilm DF100 delivered in the form of rolls are at our disposal. Cut samples are displayed on Figure 3.3a and b:

- a purple film fully sintered,
- a white film having sintered layers and the one on the top not sintered.

Their typical physical properties as referenced by the manufacturer are depicted on Figure 3.2.

For both samples, the other side of the film was in contact with the matrix used as a carrier for the deposit of the PTFE dispersion, but it has been peeled out. Consequently, three different surface states are obtained, and their topography is imaged by AFM, see Figure 3.3c-f.

### CHEMFILM® Typical Physical Properties\*

Typical Properties	Test Method	Value	Units
<b>Mechanical</b>			
Tensile Strength	ASTM D-882	29.6 (4,300)	MPa (psi)
Elongation	ASTM D-882	400	%
Elastic Modulus	ASTM D-882	413 (60,000)	MPa (psi)
Continuous Service Temperature		-188 to 260 (-400 to 500)	°C (°F)
<b>Electrical</b>			
Dielectric Constant	ASTM D-150	2.0	60-10 <sup>8</sup> Hz
Power/Dissipation	ASTM D-150	<.0001	
Surface Resistivity	ASTM D-257	9x10 <sup>7</sup>	
Volume Resistivity	ASTM D-257	>10 <sup>15</sup>	
Dielectric Strength	ASTM D-149	4200	volts/mil
Surface Arc Resistivity	ASTM D-495	Does not arc	

\*Represent typical performance properties and should not be used for specification purposes

Figure 3.2: PTFE Chemfilm DF100 cast films from Saint-Gobain Performance Plastics typical physical properties from manufacturer [Chemfilm 2021].

An AFM VEECO Multimode-Nanoscope V is used in tapping mode on PTFE films to analyze their topography. From topographical records, the films average roughness can be calculated. The "Flatten" command from Nanoscope Analysis software applied is a filter modifying the data to delete low frequency noise and remove tilt from an image: each line is fit individually to center data, remove tilt and bow. A best least-squares fit polynomial of third order is calculated from each data line and then subtracted out. Each image is then cut in smaller squared zones and only areas without apparent defects are considered to calculate the average roughness. The acquisition parameters are as following:

- scan size: 20  $\mu\text{m}$ ,
- scan speed: 10  $\mu\text{m/s}$ ,
- integral gain 2, proportional gain 4,
- driven signal frequency 250 kHz.

The film sample is stuck on a circular metal support which is then laid on the piezoelectric wedge.

Both samples side in contact with the supporting matrix show similar topography, see Figure 3.3e&f. The two other sides are more contrasted: on the unsintered side of the white film, many deep and regularly spaced fronts are present through the sample. As these fronts are not noticeable on the sintered purple film, they may appear during the drying and baking steps but can't resolve themselves without sintering. These fronts may be a mark of the solvent evaporation fronts. Their orientation is not perfectly normal to the surface; this may be related to the vertical orientation of the film during drying and baking steps. On the two sides not in contact with the supporting matrix, some particles (diameter  $\sim$  250-300 nm) from the original dispersion can be detected.

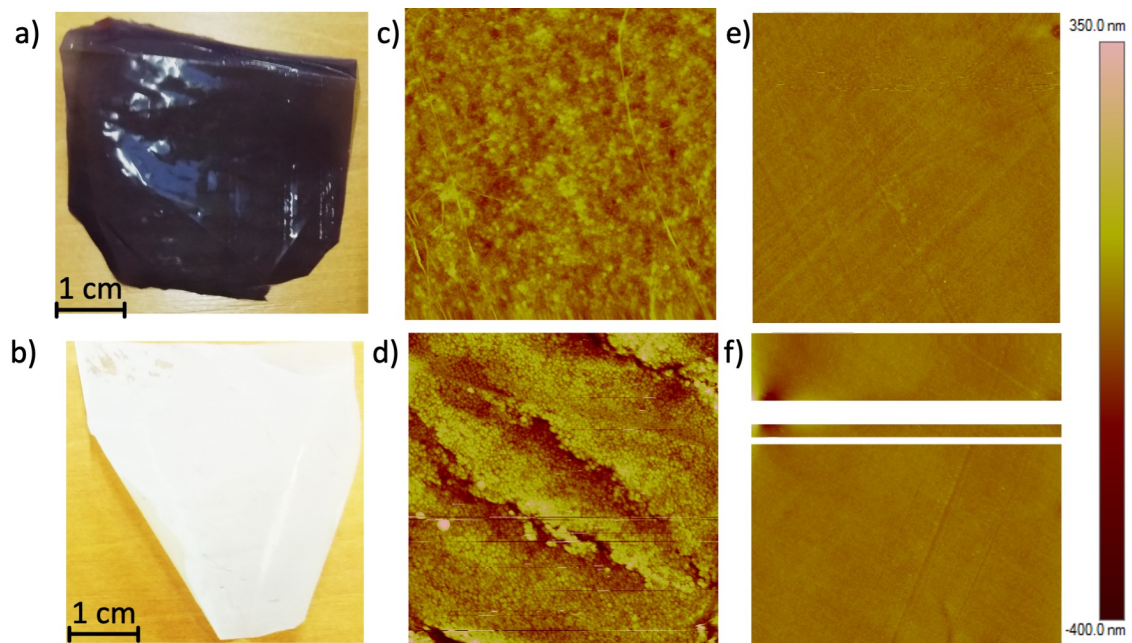


Figure 3.3: PTFE cast films from Saint-Gobain Performance Plastics. First line fully sintered with purple dye films, Second line last layer unsintered without any dye film. a) and b) Pictures. c) to f) topography results from AFM on  $20 \mu\text{m}$  squared zones on both films sides. c) and d): side not in contact with the supporting matrix, dispersion small beads deposit and drying fronts can be seen on the white film surface in d). e) and f): side in contact with the supporting matrix, the topography is homogeneous and quite flat (white areas should not be considered).

---

As expected, the two sides in contact with the supporting matrix have almost the same average roughness of 10 nm: they are the least rough. The white unsintered side where the dispersion particles are still visible is the roughest with an average roughness of about 70 nm, the purple sintered side has a roughness of about 30 nm. When putting in contact two of these surfaces, the real contact area is highly dependent on the topography and on the applied pressure. For our PTFE-PTFE adhesion study, only sintered-sintered interfaces with the smallest roughness will put in contact; this should lead to the best intimate contact conditions.

## 3.2 PTFE: a semi-crystalline polymer

### 3.2.1 Phase diagram

The PTFE chain adopts an helical structure and the polymer crystallizes in an hexagonal crystal arrangement. The helical structure itself is due to lone pair-lone pair repulsion between the fluorine atoms on adjacent  $\text{CF}_2$  units. The helical conformations is a function of the temperature and pressure [Puts *et al.* 2019, Clark 1999].

PTFE may exist in one of four crystal phases (the phase diagram is shown on Figure 3.4) with phase I being the most common followed by phase IV and then phase II. In phase II, the PTFE helix adopts a 13/6 conformation (this means 13  $\text{CF}_2$  units taking part in 6 full rotations about the carbon axis to return the fluorine atoms to the starting coordinates), and it adopts a 15/7 conformation in phase IV. Phases I and IV are the commonly observed crystal phases for PTFE as they occur at atmospheric pressure and ambient temperatures. Phase II is encountered usually at sub-ambient temperatures, while phase III is encountered only at high pressures.

Importantly, the helical structure leads to a stiff, rod-like character to the polymer chain, and as a result, the polymer crystallites are expected to consist of an assemblage of large regions of long, straight and ordered chain packing.

A last crystalline change occurs around 340-350°C during heating of the as-received PTFE (virgin of any previous thermal treatment). The crystalline phase progressively disappears during melting: the material becomes amorphous. When cooling from above melting, the material is crystallizing.

### 3.2.2 Crystalline structure

#### Rigid and mobile amorphous phases

The other important transition occurring in semi-crystalline polymers is the glass transition concerning amorphous phase. For PTFE, the exact temperature of the glass transition has long been discussed [Puts *et al.* 2019]. Using dynamic mechanical analysis (DMA), three transitions can be observed, see Figure 3.5. The  $\gamma$  (around -103°C) and  $\alpha$  (around 116°C) transitions are related to the amorphous phase whereas the  $\beta$  transition characterizes the double transition at ambient temperature [Calleja *et al.* 2013].

The two transitions related to the amorphous phase have been attributed to different structures: the rigid amorphous fraction (RAF) for the  $\alpha$  transition and the mobile amorphous fraction (MAF) for the  $\gamma$  transition, shown in Figure 3.5. The RAF is the part of the amorphous phase closer to the crystalline phase and therefore less mobile than the MAF, farther from the crystals [Calleja *et al.* 2013].

At atmospheric pressure, the two first-order crystal-crystal transitions that occur at 19 and 30°C (see Figure 3.4) should be noticeable. However, by rheology, the differentiation of these crystalline transitions is more difficult since they produce themselves in neighboring temperature zones and are mixed in the  $\beta$  transition peak. Nevertheless, the width and the asymmetry of the  $\beta$  relaxation peak seem to be consistent with the presence of two transitions [Calleja *et al.* 2013].

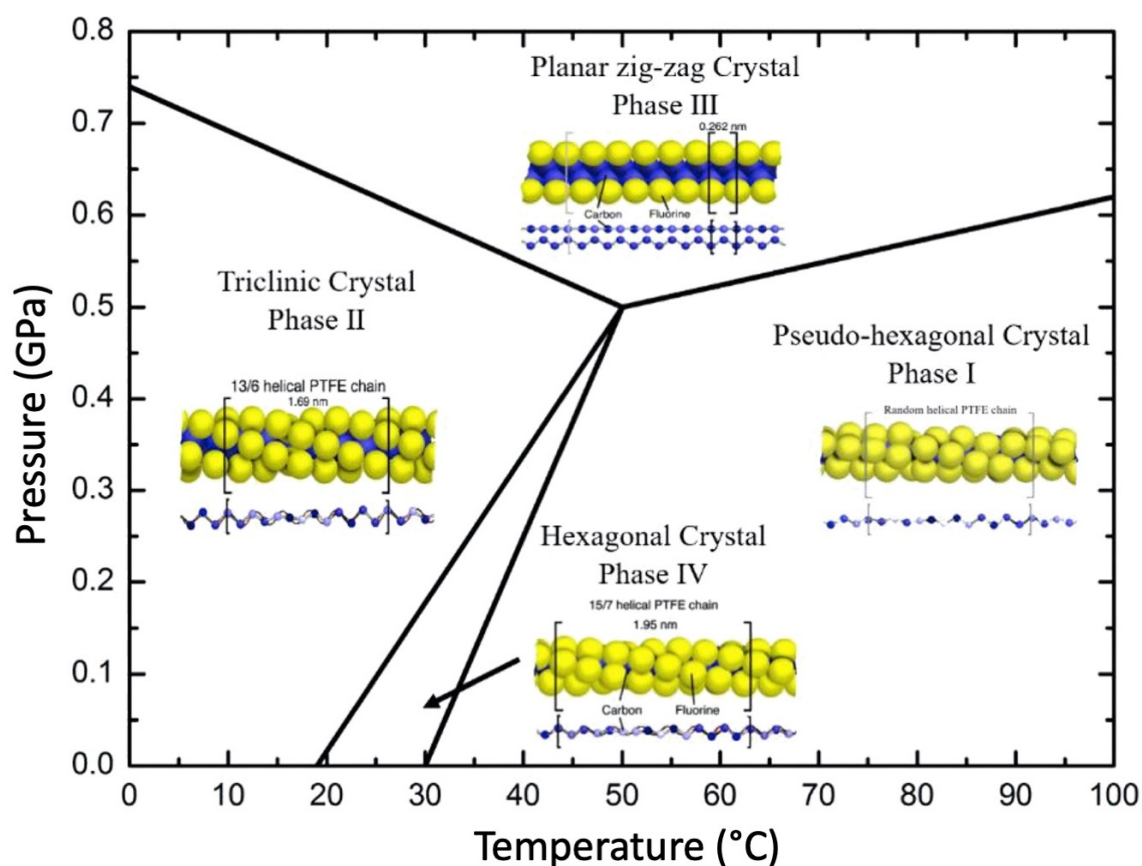


Figure 3.4: Conformation and phase diagram of PTFE [Wu *et al.* 2020, E. N. Brown, Dattelbaum, *et al.* 2007]. The phase transformations (II-IV) and (IV-III) are important as they occur in a small range of temperature close to room temperature and can be triggered by relatively low loadings.

### PTFE lamellae crystals and others

In contrast with most polymers forming spherulite structures, PTFE molecules organize themselves as banded structures, or lamellae, with approximately 10-100  $\mu\text{m}$  length and 0.1 – 1  $\mu\text{m}$  width depending on the hold time, temperature above melting and on the cooling rate of the molten polymer, see Figure 3.6 a and b. These lamellae consist of 20 – 30 nm thick crystalline "slices", which are formed by the folding over and the stacking of crystalline segments and separated by amorphous phases as shown Figure 3.6c.

Due to the high molecular weight (around  $10^7$  g/mol), PTFE chains are very long (about 20  $\mu\text{m}$ ). This limits their mobility and therefore their ability to reorganize at phase changes. This is why it is uncommon to observe PTFE crystals in the form of spherulites since more motion is required to form spherulites than lamellas structures.

Others crystalline structures rearrangements have been reported in the literature such as dendrites (or spindles) and warts appearing during heat treatment above melting [Glaris *et al.* 2013].

Dendrites are filaments completely covering the sample surface, see Figure 3.7a. With increasing annealing time, more and more PTFE particles are elongated to spindle shapes, bound together, and the protrusions grow further to form islands or warts. The slowest the cooling, the largest and more numerous the dendrites [Glaris 2013], which is a proof of

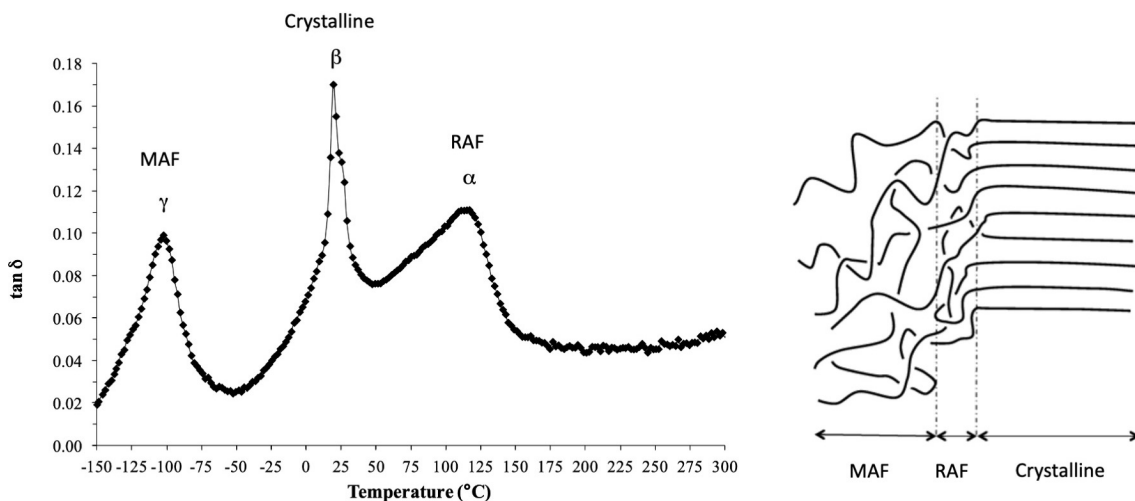


Figure 3.5: PTFE crystalline structure transitions obtained by DMA and corresponding structure scheme in a transition zone [Calleja *et al.* 2013]. Mobile amorphous phase (MAF)  $\gamma$  transition around  $-103^{\circ}\text{C}$ , rigid amorphous phase (RAF)  $\alpha$  transition around  $116^{\circ}\text{C}$ , crystalline phase  $\beta$  transition around  $25^{\circ}\text{C}$ .

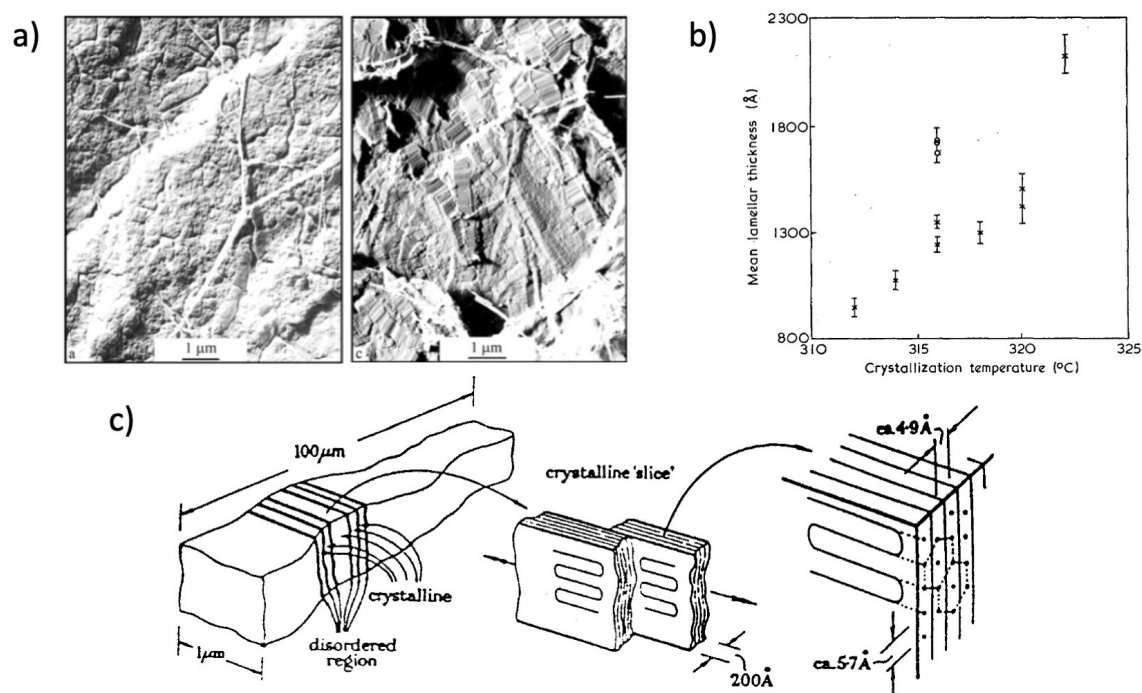


Figure 3.6: PTFE lamellas micrographs and sizes: a) SEM micrographs of sintered PTFE at  $350^{\circ}\text{C}$  for 10 min and quenched into water (left) and of sintered PTFE for 30 min and slow cool (right) [Yang *et al.* 2005], b) Mean crystal thickness as a function of crystallization temperature for 20 min crystallization [Bassett *et al.* 1974], c) Scheme of PTFE lamellas crystalline structure [Ebnesajjad 2000].

their crystalline structure.

Warts are spherical growths distributed over the material surface, their diameter is in the range of  $0.5 - 3 \mu\text{m}$ , see Figure 3.7b. Both time spend above melting [Glaris *et al.* 2013] and cooling rate [Sciuti *et al.* 2017] are impacting warts size. Their origin, suggested by [Glaris *et al.* 2013], may come from relaxation of stresses induced during manufacturing, thus creating features on the material surface. Another hypothesis is given by [Kobayashi *et al.* 2012]: since PTFE has a linear molecular structure, PTFE chains tend to orient themselves normal to the substrate surface during heating because the normal orientation is more stable for a linear molecule, resulting in some protrusions on the surface.

It is interesting to note that these surface features are affecting surface energy and roughness and have consequences on the material wetting properties [Glaris *et al.* 2013].

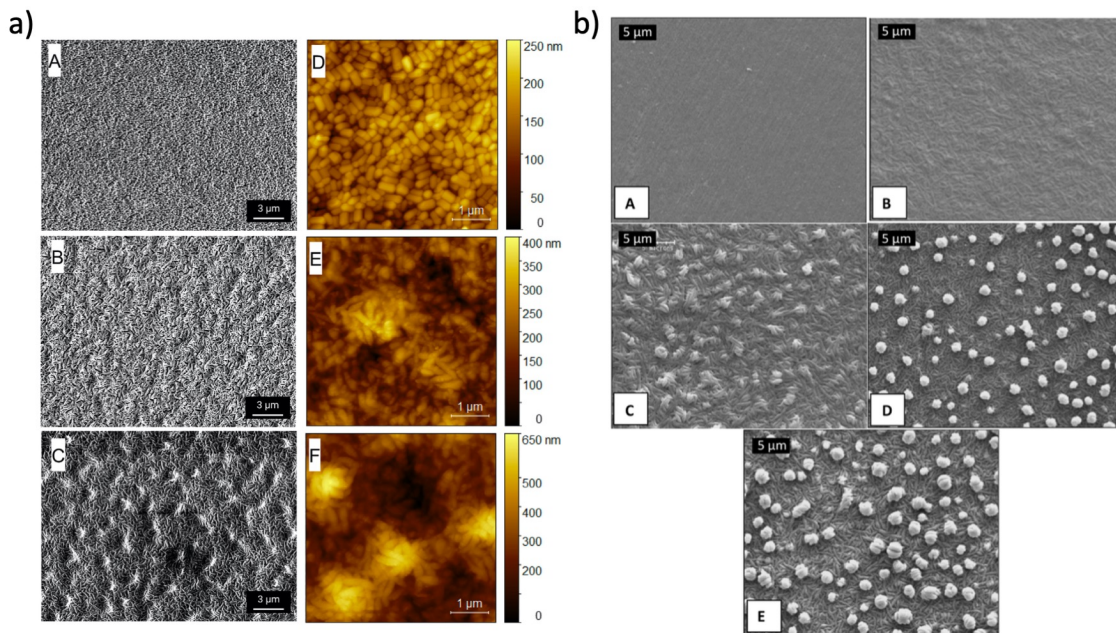


Figure 3.7: a) PTFE dendrites adapted from [Jiang *et al.* 2019]: SEM (first column) and AFM (second column) images of PTFE/PDA coatings on stainless steel without annealing (A, D), with 4 min annealing (B, E) and 8 min annealing (C, F) at  $372^\circ\text{C}$ , b) PTFE warts [Glaris *et al.* 2013]: SEM images of virgin (A) and annealed PTFE samples at  $350^\circ\text{C}$  during B) 10 min; C) 20 min, D) 75 min and E) 120 min.

### Cast films - X-ray measurements

To assess polymer crystalline structures, X-Ray Diffraction measurements can be performed. The general principle of this method is exposed and PTFE cast films are tested to determine if they have a privileged macro-molecular orientation or not.

#### General overview

When in contact with a material, X-rays generate an elastic displacement of the atomic electronic cloud. The induced oscillations leads to the scattering of electromagnetic beams (with the same frequency), referred to as the Rayleigh scattering. For a crystalline lattice, at given angular orientations of the incident beam, scattered beams add up constructively to form a diffraction peak if Bragg's law is followed:

$$2d_{hkl} \sin \Theta = n\lambda \quad (3.1)$$

with  $d_{hkl}$  the lattice spacing between two scattering planes defined by Miller indices  $hkl$ ,  $\Theta$  the Bragg's angle defined between the incident beam and the diffracting crystalline plane,  $n$  an integer and  $\lambda$  the wavelength of the incident beam.

When a monochromatic X-ray beam hits a sample, a scattered signal may be measured and a diffraction pattern, showing the intensity of the signal as function of the angular position  $2\Theta$ , is obtained. Since semi-crystalline polymers consist of periodic micro-structure - the crystalline and amorphous phases - the diffraction pattern appears as a sum of [Chu *et al.* 2001]:

- sharp peaks, corresponding to the coherent diffraction of the crystalline structure,
- an amorphous halo, due to the scattering of entangled macromolecular chains,
- a non coherent scattering background.

From a diffraction pattern, different information can be deduced such as the crystalline content, the size of the crystalline domains and the preferred crystal orientations.

#### Results

Samples are tested using a Philips X'Pert X-ray diffractometer with a copper source (with a generator voltage of 45 kV and a tube current of 40 mA). A first wide scan for  $2\Theta = 5-100^\circ$  on a stack of 10 white cast films is depicted on Figure 3.8a. The most intense peak recorded corresponds to (100) diffraction plane in PTFE crystals [E. N. Brown, P. J. Rae, *et al.* 2008]. A first amorphous halo is superimposed to the (100) peak and a second amorphous halo appears around  $2\Theta = 40^\circ$  [Lebedev *et al.* 2010]. The crystalline ratio of a semi-crystalline material may be related to the ratio between the integrated part of the diffraction signal due to the crystalline phase and the integrated intensity of the whole signal [Hermans *et al.* 1961].

If the material is textured, crystal lattice has a preferred orientation and different amounts of planes diffract according to the orientation of the incident angle  $\Theta$  with respect to the sample orientation  $\Psi$ , see Figure 3.8b. An azimuthal scan is done by varying  $\Psi$  over  $180^\circ$  at  $2\Theta = 18.1^\circ$  corresponding to PTFE diffraction peak (100). A single experimental value is obtained for each  $\Psi$  position. The ratio between the maximum and minimum intensity recorded along  $\Psi$  is close to 1 (data not shown): PTFE cast films are not textured, they don't show any preferential macro-molecular orientation.

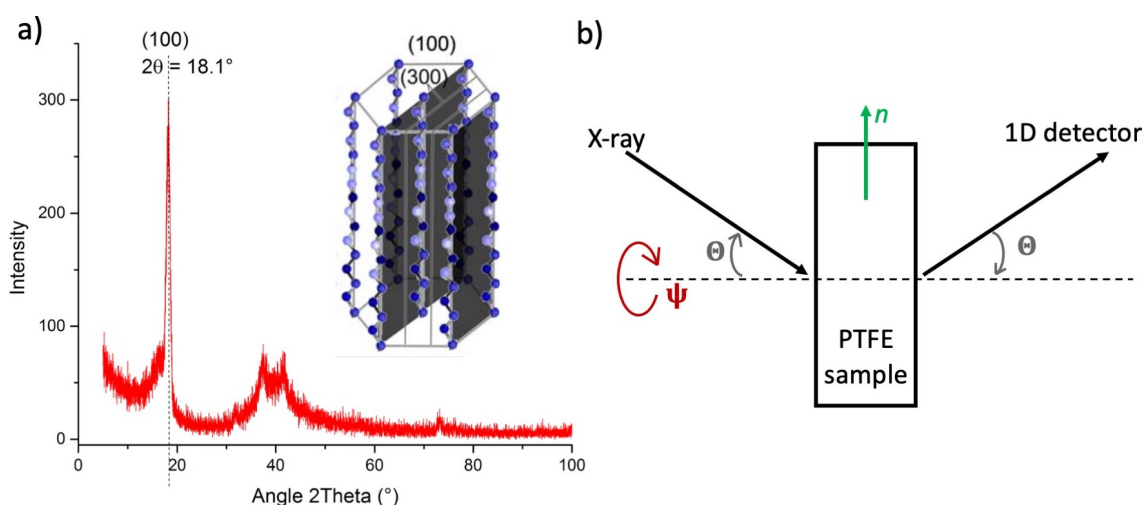


Figure 3.8: a) X-ray diffractogram along  $2\Theta$  for a stack of 10 white PTFE cast films. The peak corresponding to (100) plane is highlighted. Insert: Sketch of the (100) diffraction plane in PTFE crystals taken from [E. N. Brown, P. J. Rae, *et al.* 2008], b) Sketch of the  $\Theta - \Theta$  diffraction setup. The sample is rotated along the horizontal axis to record the diffracted intensity along  $\Psi$ .

### Raw dispersion

The raw dispersion is crystallized upon polymerization: it is made of highly perfect crystals and thus can be considered as a reference for highly crystalline PTFE material. Evaluating its melting enthalpy could give a good approximation of the enthalpy of melting close to the one of a perfectly crystalline PTFE bulk  $\Delta H_f^0$ . In the literature, different values are available for the melting enthalpy of a 100% perfectly crystalline PTFE bulk sample  $\Delta H_f^0$ , some of them are summarized in Table 3.1.

$\Delta H_f^0$ (J/g)	Method	Reference
93 (102)	Clapeyron equation using quenched (or virgin) PTFE	Starkweather <i>et al.</i> 1982
104	Perfluoro-n-alkanes	Starkweather 1986
47-84	Literature to 1980	Starkweather <i>et al.</i> 1982
74	Infrared spectroscopy	Lehnert <i>et al.</i> 1997
69	Raman spectroscopy	Lehnert <i>et al.</i> 1997
82	ASTM D4591	Kerbow <i>et al.</i> 1999

Table 3.1: Table of enthalpy of melting of perfectly crystalline PTFE bulk from literature.

A dried raw dispersion stuck between Kapton tape is analyzed on Philips X'Pert X-ray diffractometer and scanned around  $2\Theta = 15.98-20^\circ$ .

On Figure 3.9, no amorphous halo is superimposed to the (100) peak which is not the case for a white cast film where a halo appears at  $2\Theta = 16.5^\circ$  [Lebedev *et al.* 2010]. Assuming the crystalline content of raw dispersion close to 100% seems valid. Consequently, our own enthalpy of melting of perfectly crystalline PTFE bulk  $\Delta H_f^0$  can be evaluated by DSC Q20

from TA Instruments on  $\sim 5$  mg of raw dried dispersion placed in a standard aluminium pan. Heating and cooling are performed from ambient to  $375^\circ\text{C}$  at  $20^\circ\text{C}/\text{min}$  with a 5 min maintaining time.

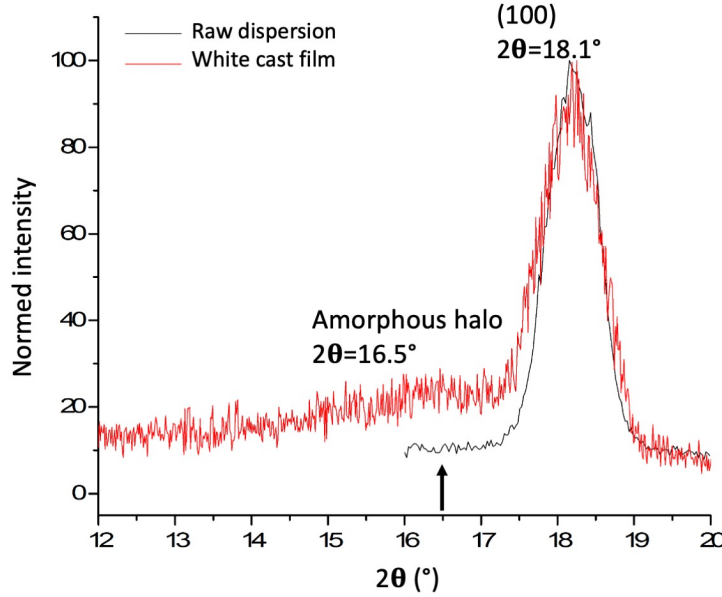


Figure 3.9: X-ray diffractogram along  $2\theta$ . The (100) diffraction plane corresponding to a peak at  $2\theta = 18.1^\circ$  is highlighted. Black: dried raw dispersion ample, red: white cast film sample. No amorphous halo close to  $2\theta = 16.5^\circ$  is present on the dispersion data.

From the whole calorigram on Figure 3.10, the first melting peak is quite narrow and occurs at a higher temperature than the second melting peak. This is due to the high crystallinity of virgin PTFE with large crystal lamellae. The virgin dispersion is crystallized upon polymerization explaining its high degree of perfection. The crystallinity is in the range of 92-98% but will never be reached again after any thermal treatment. The second melting peak is much smaller as recrystallized PTFE is usually around 30 to 50% crystalline [Ebnesajjad 2000].

The integration of the first melting peak shown on Figure 3.11a in red, performed following [Guenoun *et al.* 2020] baseline method, leads to  $\Delta H_f^0 = 84.53 \text{ J/g}$ . In the following, the crystalline content  $\chi$  can be evaluated as:

$$\chi = \frac{\Delta H_f}{\Delta H_f^0} \quad (3.2)$$

with  $\Delta H_f$  the melting enthalpy measured from DSC results as the area below the melting peak following the modified baseline method described by [Guenoun *et al.* 2020] and  $\Delta H_f^0 = 84.53 \text{ J/g}$  the melting enthalpy of a 100% perfectly crystalline bulk sample.

Moreover, the melting peak shape seems to be the superposition of two peaks with different heights which would be the mark of two distinct crystalline structures sizes. Using Origin Software, these two peaks can be decorrelated and fitted with Pseudo-Voigt functions, see Figure 3.11a in blue and black. Their respective peak temperatures ( $T_{m1} = 340^\circ\text{C}$  and  $T_{m2} = 344^\circ\text{C}$ ) and enthalpies are thus obtained. The lamellae thickness can directly

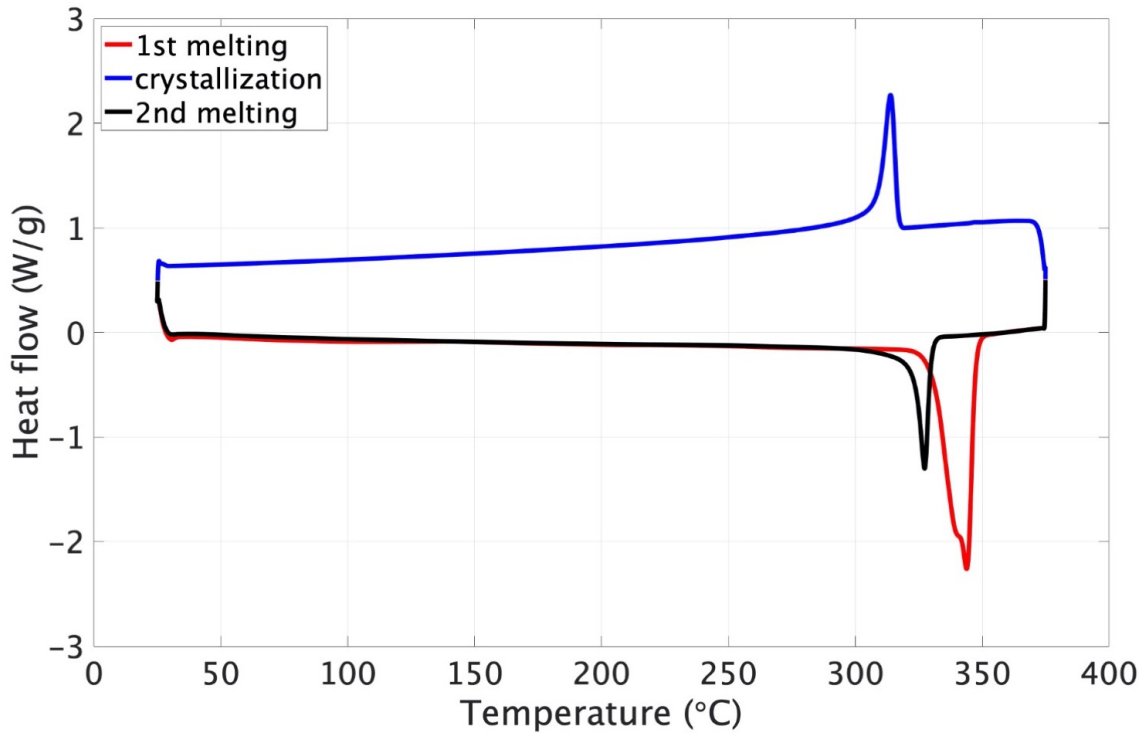


Figure 3.10: DSC calorigram obtained from raw PTFE dispersion with heating/cooling rates of 20°C/min, hold time at 375°C of 300 s. A second heating was performed to melt recrystallized PTFE.

be accessed thanks to Gibbs-Thomson equation [Hoffman *et al.* 1976]:

$$T_m = T_m^0 \left( 1 - \frac{2\sigma_e}{l\Delta H_f} \right) \quad (3.3)$$

where  $T_m$  is the melting temperature of the crystal,  $T_m^0$  is the melting temperature of an infinite crystal,  $\sigma_e$  the end surface free energy,  $\Delta H_f$  the enthalpy of fusion per unit volume of crystal and  $l$  the lamellae thickness.

Assuming the same value of end surface free energy  $\sigma_e$ , the relationship between the two crystalline lamellae thicknesses is  $l_1 \approx 0.3l_2$ . The raw dispersion at our disposal is thus made of folded particles as depicted on Figure 1.4 [Rahl *et al.* 1972] of two different thicknesses and thus different number of folded ribbons. The highest the melting temperature, the largest the crystalline size is as already shown before for different granular PTFE grades, see Figure 3.11b [Bassett *et al.* 1974, L. Ferry *et al.* 1995].

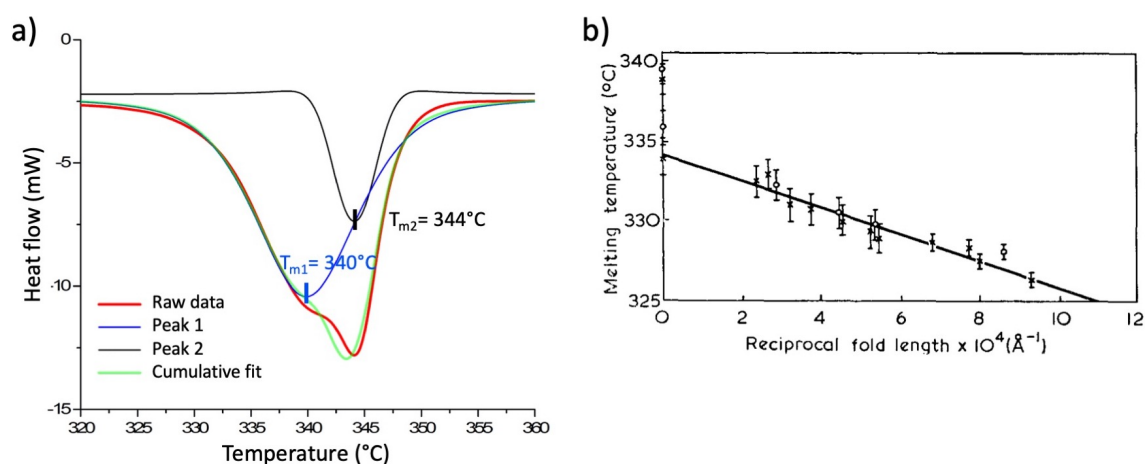


Figure 3.11: a) Melting calorigram for a dried raw dispersion sample obtained by DSC. Red: raw data, black and blue: decorrelated peaks using pseudo-Voigt functions, green: cumulative fit, b) Melting temperature as a function of the reciprocal crystal thickness for different granular PTFE grades [Bassett *et al.* 1974].

### Extruded films - privileged crystalline orientation

Extruded films are made from the process depicted in (see Figure 1.6 middle line). Depending if the films are stretched or not after calendaring, 100  $\mu\text{m}$  thick full or low-density films are obtained. These materials are supposed to have a clear macro-molecular chain privileged orientation in machining direction due to manufacturing process.

To determine if extruded films have a preferential crystalline orientation resulting of molecular chains alignment in a direction which is often the machine or stretching direction used during processing [White *et al.* 1983], Wide Angle X-ray Scattering (WAXS) experiments are performed. Then, the degree of orientation and the percentage of oriented crystallites will be evaluated in both full and low density extruded films, following the method exposed below developed by [Dasgupta 2016].

### Experimental protocol - Wide Angle X-ray Scattering (WAXS)

Extruded films samples are tested using a Xenocs WAXS setup with a micro-focus source  $\text{CuK}\alpha$  providing a X-ray beam of 1.541 Angstrom wave length, previously calibrated with silver behenate following [Huang *et al.* 1993].

The resulting graph from a WAXS experiment is a pole figure. **Pole figure** is a stereographic projection showing the density of crystallographic poles of given planes ( $2\theta$  angle) as a function of orientation ( $\Psi$  angle). If the crystalline orientation is completely random, the poles are scattered all over the stereographic projection. If orientation is present, the poles will tend to be concentrated in given areas within the projection, or in other words a given diffraction ring will show a non-uniform intensity distribution.

Another way of depicting orientation is by quantifying the spread of the intensity distribution on the Debye ring belonging to a specific set of  $hkl$  planes. This is done by measuring the Full Width at Half Maximum (FWHM) of the intensity peak obtained by plotting the intensity along the Debye ring as a function of the angular coordinate  $\Psi$ , see Figure 3.12. The smaller the FWHM, the higher is the **degree of orientation**  $D$  defined as

$$D = \frac{180 - FWHM}{180} \quad (3.4)$$

such that if the oriented crystallites are all parallel to each other then  $D = 1$  while if they are randomly spread over  $180^\circ$  in  $\Psi$  then  $D = 0$ . The  $D$  value allows to compare the degree to which oriented crystallites are aligned in the preferred direction.

To quantify the fraction of oriented crystallites, the baseline intensity on a  $2\Theta$  plot should be determined; ideally this should be zero, but it is never the case since there is always some background intensity due to air scattering. The baseline intensity level is obtained as the intersection of the tangent to the diffraction trace before (100) peak and the peak bisector. The **percentage of oriented crystallites** can be defined as:

$$OC = \frac{A_{oriented}}{A_{oriented} + A_{random}} \times 100 \quad (3.5)$$

with  $A_{random}$  proportional to the number of randomly oriented crystallites and  $A_{oriented}$  representing the number of oriented crystallites, on a plot of the intensity variation along the (100) diffraction ring of a PTFE extruded sample, see Figure 3.12.

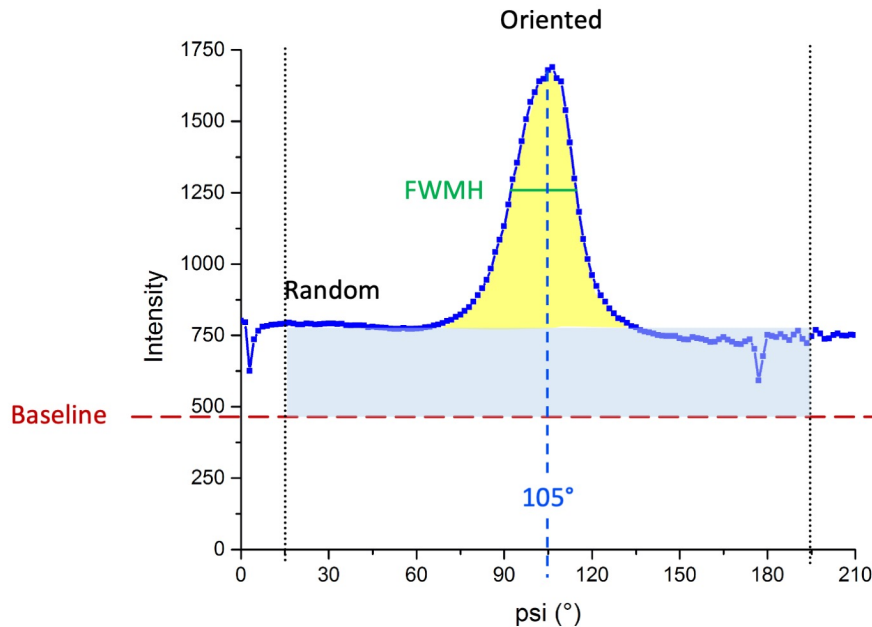


Figure 3.12: Intensity variation along the (100) diffraction ring of a full density PTFE extruded film sample. The full width at middle height (FWMH) in green is used for the degree of orientation determination. The blue shaded area  $A_{random}$  is proportional to the number of randomly oriented crystallites while the yellow shaded area  $A_{oriented}$  represents the number of oriented crystallites.

To take into account the distribution of the oriented crystallites, the **percentage of oriented crystallites in preferred direction** is defined as:

$$OCP = OC \times D \quad (3.6)$$

## Results

Both full density and low density PTFE extruded samples are analyzed by Wide Angle X-Ray Scattering. 2D diffraction pattern or poles figure are obtained as shown on Figure 3.13. The center of the pole figure is not meaningful since it is the image of the source;

moreover, the small uncentered ring on the right side corresponds to a damage on the detector and it should not be considered. The diffraction ring with the highest intensity (at the outside) corresponds to the (100) peak at  $2\Theta = 18.1^\circ$ . Since this ring shows a non-uniform intensity distribution, orientation is present.

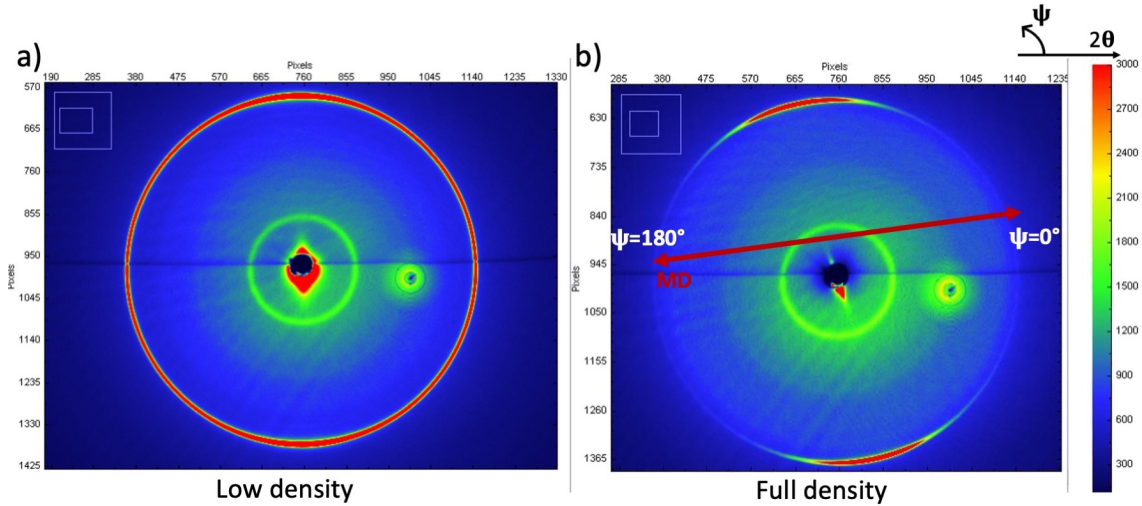


Figure 3.13: Pole figures obtained after WAXS experiment on both a) low density and b) full density PTFE extruded samples. A ring corresponding to the (100) peak at  $2\Theta = 18.1^\circ$  is present with different intensity variation according to  $\Psi$  angle.

Figure 3.12 is a plot of intensity variation along the diffraction ring obtained by integrating the ring cursor along  $2\Theta = 18.1^\circ$ . From this plot, the intensity peak maxima position is at  $\Psi = 105^\circ$ . Since this angle is  $90^\circ$  out of phase with the preferred c-axis direction of the hexagonal unit cells, the direction of orientation is given by the red arrow in Figure 3.13. A small tilt angle of  $5^\circ$  with respect to the machine direction (MD) is observed: it could be the result of some misalignment of the sample with respect to the holder.

As explained above, the baseline intensity is determined and subtracted from the intensity data-points; the new intensity values are plotted. The peak area is computed using a Pseudo-Voigt peak fitting function, also yielded the FWHM value. The total area under the curve in an angular range of  $180^\circ$  centered on the peak maxima (i.e.  $15-195^\circ$  here) is computed by using the integration feature available in OriginLab Software. The degree of orientation, the percentage of oriented crystallites ( $OC$ ) and the percentage of oriented crystallites in preferred direction ( $OCP$ ) are determined using equations 3.4, 3.5, 3.6. Results are summarized in Table 3.2.

	$D$	$OC$ (%)	$OCP$ (%)
<b>Low density</b>	0.86	58	50
<b>Full density</b>	0.87	64	56

Table 3.2: Table of WAXS results for full density and low density PTFE extruded film samples.  $D$ : degree of orientation,  $OC$ : percentage of oriented crystallites,  $OCP$ : percentage of oriented crystallites in preferred direction.

From the pole figures on Figure 3.13 and the quantitative analysis summarized in Table 3.2, crystalline orientation in machine direction is highlighted for both extruded PTFE film samples. The full density sample is the most oriented one globally and in privileged direction. This material will be used to assess the effect of crystalline orientation on the mechanical adherence properties, see section 5.3.3.

### 3.2.3 Crystallization kinetics

#### Differential Scanning Calorimetry

A popular method to study crystallization kinetics is Differential Scanning Calorimetry (DSC) [Parasnis *et al.* 1999] which is a thermal analysis technique measuring the heat energy uptake for a given thermal history. This method is also used to characterize phase transitions: from the heat flow measurement, the transition temperature and the enthalpy associated can be estimated. For semi-crystalline polymers, DSC is widely employed to determine the glass transition, melting and crystallization [Schick 2009].

The DSC method consists in measuring the temperature of the sample and of a reference sample, both placed in a precisely controlled oven. The temperature difference between the sample and the reference is related to the energy released or absorbed by the sample. At constant cooling or heating, the energy change is linked to the specific heat capacity and latent heat of a phase change. When increasing temperature, the melting process results in an endothermic peak in the DSC curve. While decreasing temperature, the crystallization process results in an exothermic peak. In this work, the convention adopted is with endothermic peaks corresponding to negative heat flow values. All peak integration are performed with modified baseline as described by [Guenoun *et al.* 2020].

To perform DSC on PTFE films, films are cut with a punch on 5 mm diameter disks and  $\sim 5$  mg or 3 disks are placed in a standard aluminum pan. Different experiments are performed to study the crystallization dependence with cooling rate:

- A previous work [Guenoun *et al.* 2020] described sintered PTFE powder crystallization kinetics; to verify that our PTFE films made from dispersion are following the same crystallization kinetics, their experiments are reproduced on our white PTFE cast films.

A TA Instruments Q10 is used and the heating and cooling rates are set at 10, 20 or 40°C/min with 5 min maintaining time above melting.

- To reproduce the cooling rate applied with air gun during mechanical adherence tack test, see 5.1.3, a Perkin Elmer Hyper DSC 8500 reaching cooling rates up to 150°C/min is used. The two temperature profiles following the blue curves and the red or green one described on Figure 3.14 are implemented.

#### Primary and secondary crystallization mechanisms

A previous work [Guenoun *et al.* 2020] described sintered PTFE powder crystallization kinetics. To verify that our PTFE cast films are following the same crystallization kinetics, their experiments are reproduced on our materials.

Our results are depicted on Figure 3.15: the crystallization kinetics of our PTFE cast films is in accordance with the observed kinetics for granular powder [Guenoun *et al.* 2020]. Almost independently on the cooling rate, the crystallization temperature onset is estimated at 318°C. Then, the crystalline content increases very rapidly over 5–10°C. At lower temperatures, the crystalline content continues to step up, but much slowly over a

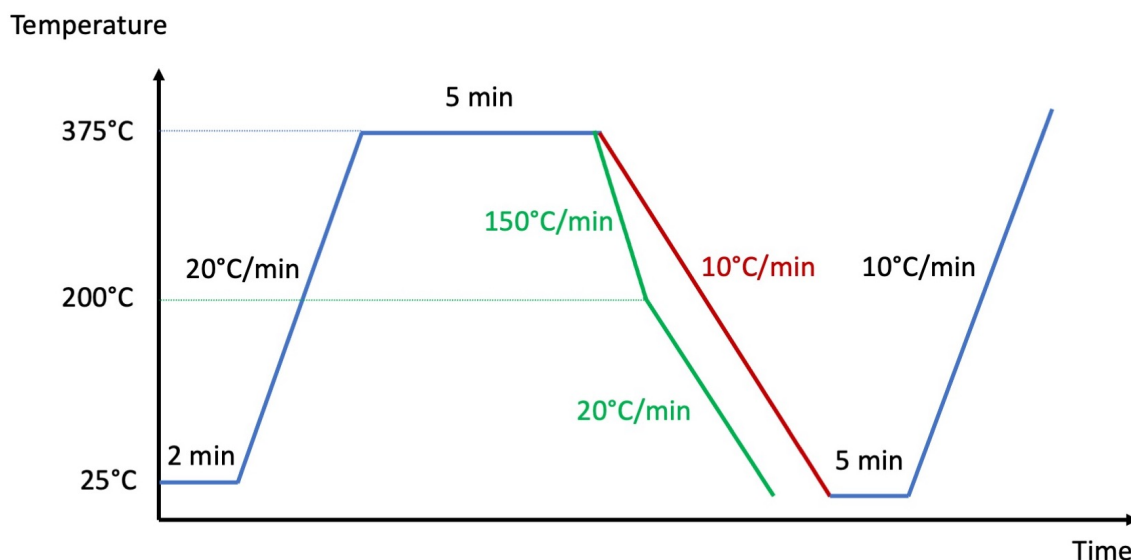


Figure 3.14: Two temperature profiles implemented on Perkin Elmer DSC 8500 to mimic the extremes cooling rates available during mechanical adherence tack test. Both tests are following the blue lines and either the green or red path is taken for cooling.

range of 40-50°C. The marked difference between those two stages suggests two different crystallization mechanisms:

- primary crystallization: 320-310°C
- secondary crystallization: 315-260°C

For all cooling rates, PTFE's secondary crystallization contribution to the crystalline content seems to be independent of the primary crystallization: in the range 315-260°C, all the curves can be superimposed. Hence, the primary crystallization is responsible for the final crystalline content variations obtained after different thermal histories.

Guenoun *et al.* [Guenoun *et al.* 2020] shows that the secondary crystallization induces a reversible isotropic behavior meaning it is the same at cooling and heating. Conversely, the primary crystallization appears to lead to an anisotropic behavior similarly to melting, reminiscent of the initial crystalline orientation.

Moreover, they show that the change of the melting peak at high temperatures is related to the primary crystallization. Therefore, primary crystallization is kinetic dependent in contrast to the secondary crystallization. From a structural point of view, as depicted on Figure 3.11b, the increase of the melting peak temperature towards high temperatures implies a crystalline lamellae thickening [Bassett *et al.* 1974, L. Ferry *et al.* 1995]. Therefore, the broad region of the melting peak at lower temperatures which seems to be related to the secondary crystallization would indicate much smaller crystalline structures. In situ heating and cooling followed by Scanning Electron Microscopy will be performed to try to observe the crystalline structures related to secondary crystallization mechanism, see Appendix D.

Thanks to the knowledge of PTFE films crystallization kinetics, the impact of melted and recrystallized content on the adhesion properties between two PTFE films will be studied by mechanical adherence tack test performed at different temperatures chosen for their specific melted amount and mechanisms, see Section 5.3.2.

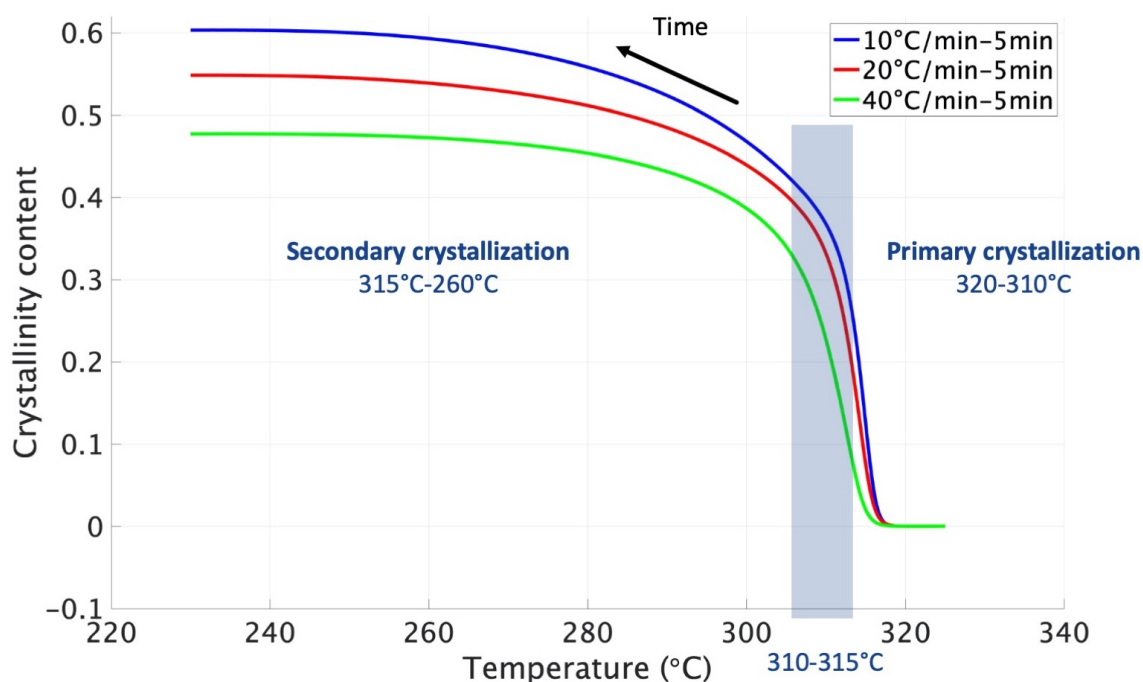


Figure 3.15: Crystalline content  $\chi$  evolution during crystallization for various cooling rates on white PTFE cast films.

### Cooling rate impact on the crystalline content

At 318°C, the molten resin reaches the freeze point and crystallization begins to take place, see Figure 3.15 [Guenoun *et al.* 2020]. Polymer chains, which were randomly distributed in the molten state, begin to pack in an orderly manner. The slower the cool down, the higher the number of crystalline structures as depicted on Figure 3.16 by the increase in melting enthalpy with slower cooling rates [Bosq *et al.* 2013, L. Ferry *et al.* 1995, Canto *et al.* 2011, Bosq *et al.* 2013]. A rapid cooling induces a smaller crystalline content and smaller crystalline structures whereas during a slow cooling, more macro-molecular chain movements and reorganisation is allowed, resulting in a higher crystalline content and larger crystalline structures. Such variations can affect the sample mechanical properties [P. Rae *et al.* 2005, Sperati *et al.* 1961].

Following protocol exposed in Figure 3.14, two cooling rates (10°C/min and 150°C/min) are tested on PTFE films by a Perkin Elmer Hyper DSC 8500. Each test is reproduced twice; the results are gathered on Table 3.3. From these data, the melting peak shift with cooling rate is confirmed on our material from 325°C at 150°C/min to 326°C at 10°C/min cooling rate. From a structural point of view, the increase of the melting peak towards high temperatures is related to a crystalline lamellae thickening [L. Ferry *et al.* 1995]. [Bosq *et al.* 2013] work on PTFE granular powder with a Flash Scanning Calorimetry and browse a large cooling rates range, see Figure 3.16. Converted in K/s, the cooling rates of our experiments are of 0.17 and 2.5K/s; which should correspond to a melting peaks close to 333 and 330°C and an enthalpy of melting close to 72 and 68 J/g [Bosq *et al.* 2013]. Even if the material is not the same and the experiment is not run at the same speed, our melting temperature values vary in the same way while being lower. No confident change in global recrystallized content  $\chi$  can be deduced between 10°C/min and 150°C/min cooling rates. We wonder if such a low variation in global recrystallized content can have some impact

on the adherence properties measured by adherence tack test, see Section 5.3.1.

Cooling rate (°C/min)	$\Delta H_f$ (J/g)	$\chi$ (%)	$T_m$ (°C)
10 (0.17K/s)	41.41	50.5	325.9
	43.69	53.3	326.2
150 (2.5K/s)	36.84	44.9	324.9
	41.62	50.7	324.9

Table 3.3: Enthalpy of melting  $\Delta H_f$ , crystalline content  $\chi$  and melting temperature  $T_m$  for 10°C/min and 150°C/min previous cooling rates measured on Hyper DSC at 10°C/min.

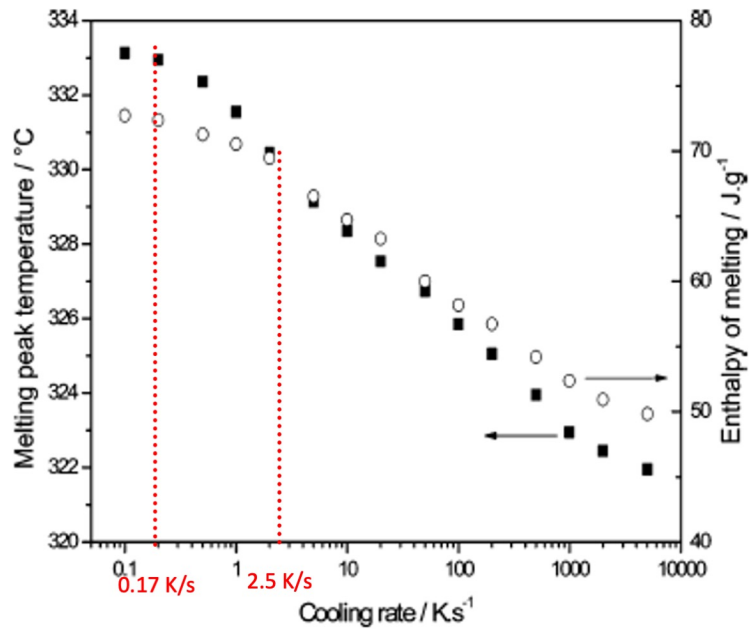


Figure 3.16: Peak temperature (left axis) and enthalpy (right axis) of melting as a function of the previous cooling rate measured on heating by Flash Scanning Calorimetry at 1000K/s on PTFE granular powder [Bosq *et al.* 2013].

### 3.3 PTFE cast films mechanical properties

Different mechanical tests are performed to assess PTFE cast films mechanical properties: classical uniaxial tensile test and dynamic mechanical analysis.

#### 3.3.1 Dynamic Mechanical Analysis in tension

Dynamic mechanical analysis (DMA) is a technique enabling measuring viscoelastic properties of materials. Periodic stress (or strain) is applied to a sample and strain (or stress) is measured. From the amplitude and the phase lag of the response, storage and loss modulus are obtained. Amplitude and frequency of the applied load can be varied to scan material properties. Dynamic mechanical thermal analysis (DMTA) also allows to vary the temperature along the test. This test is widely used to characterize the viscoelastic behavior of polymers [J. D. Ferry 1980].

#### Experimental protocol

DMTA in tension experiments are performed on white cast films cut with a punch to reach a constant width of 10 mm. The DMA in film tension mode is recording force and displacement all along a test, from which the stiffness is calculated. Then, the modulus is obtained as the stiffness multiplied by a geometric factor clamp and geometry dependent [TA Instruments 2021]. The sample length is chosen as small as possible but still easy to manipulate by hand: around 11 mm, leading to a minimum modulus value measurable close to 5 MPa [TA Instruments 2021]. Before any test, a pre-load of 0.1 N is imposed. With these parameters, different tests are performed:

- **amplitude strain sweep** tests to determine the linear visco-elastic range (LVE) [Mishra 2021],
- **temperature sweep** tests in LVE at different frequencies in order to assess the material properties evolution in tension from 25°C to 375°C at a constant heating rate of 3°C/min.

#### Results

##### Evolution of modulus with temperature

Temperature sweep tests from 25 to 350°C at a heating rate of 3°C/min are performed at frequencies of 1, 2, 4, 8 and 10 Hz and at strains in the LVE [Mishra 2021]. Figure 3.17a shows the evolution of the storage and loss modulus and damping factor with temperature.

With temperature increase, both the storage and loss modulus decrease; a factor of at least 100 MPa is still present between storage and loss modulus, the elastic behavior remains dominant. Around 70 to 150°C, for all frequencies, the data seems noisy: an explanation could be an unstable material configuration due to thermal changes not yet homogeneous; decreasing the heating rate could help to fix this issue. Focusing on the  $\tan \delta$  curve, a peak is noticed between 60 and 180°C associated to the relaxation of the PTFE rigid amorphous phase (RAF), see Figure 3.5 [Calleja *et al.* 2013]. With increasing frequency, the curves shift towards higher temperatures.

##### Arrhenius dependence

The evolution of the temperatures taken at the maximum of the  $\alpha$  relaxation peak can

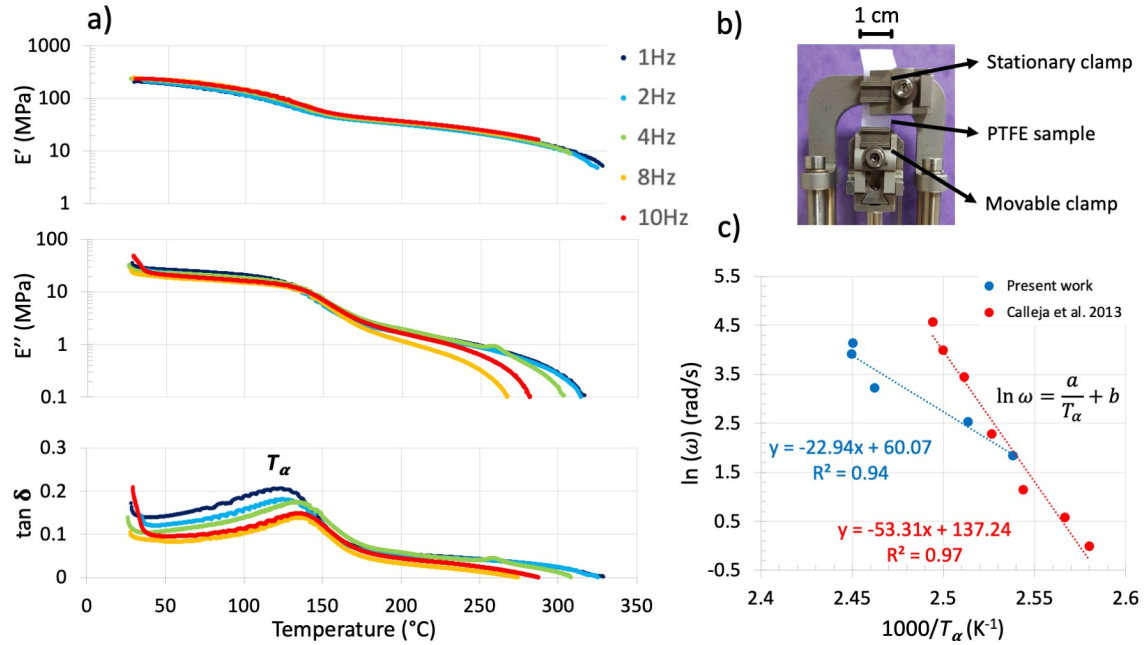


Figure 3.17: a) Storage ( $E'$ ) and loss ( $E''$ ) modulus and damping factor ( $\tan \delta$ ) obtained from temperature sweep tests for different frequencies (1, 2, 4, 8, 10 Hz). The  $\alpha$  transition peak temperature ( $T_\alpha$ ) is shifted towards high temperatures as the frequency increases, b) DMA clamps for film testing in tension, c) Arrhenius dependence of frequency as a function of temperature  $T_\alpha$  [Calleja *et al.* 2013].

be described using the model proposed initially by [Glasstone *et al.* 1941] to detail the effect of the temperature on the macro-molecular chain segment diffusion phenomena:

$$\omega = A \exp\left(\frac{E_a}{RT}\right) \quad (3.7)$$

with  $A$  the pre-exponential factor (rad/s),  $E_a$  the activation energy (kJ/mol),  $\omega$  the frequency (rad/s),  $R$  the gas constant equal to 8.32 (J/mol/K) and  $T$  is the absolute temperature at which the maximum of  $\tan \delta$  is observed for the corresponding frequency. In other words, from this Arrhenius equation, an apparent activation energy can be calculated from the plot of  $\omega$  versus the inverse of the temperature taken at the maximum of each corresponding peak, see Figure 3.17c. The red data points correspond to previous tests in torsion made on thick PTFE sheet (1 mm thick) [Calleja *et al.* 2013]; blue data points are from the present tests on PTFE films performed in tension. For our material, an activation energy of **191 kJ/mol** is obtained whereas [Calleja *et al.* 2013] obtained 444 kJ/mol for the same transition which is in the same order of magnitude than the value proposed for the characterization of PTFE from dielectric spectroscopy [Sauer *et al.* 1996]. This significant variation of more than 200 kJ/mol in the activation energies could be explained by the different manufacturing processes (granular PTFE powder and dispersion) and by the different solicitation (tension versus torsion).

### 3.3.2 Uniaxial tensile test

#### Experimental protocol

Uniaxial tensile tests are performed on white PTFE cast films in order to determine the Young modulus, the yield strength and to select the appropriate behavior law. Rectangular samples of 10 mm width are cut with a punch and placed between the clamps of uniaxial machine with a gauge length ( $L_G$ ) of 20 mm. After placing the film, a pre-load of 0.1 N is imposed at 5 mm/min before any experiment. Then, two different tests are run:

- **Tensile tests until fracture**

The mechanical behaviour of films placed in machining (MD) and transverse (TD) directions are tested until rupture at 50 mm/min on an Instron 4301 equipped with a 100 N load cell and small compressed air clamps.

In addition, a Shimadzu Ag-X equipped with a 1 kN load cell is used to have a better estimation of Young modulus thanks to a higher sampling rate.

- **Cyclic loading-unloading tests**

To obtain an overview of the elastic and plastic contributions during material deformation, cyclic loading-unloading tests at 20 mm/min are run on the Shimadzu Ag-X apparatus equipped with a 1 kN load cell. Three different displacement increments are implemented: 0.2 mm, 10 mm and 20 mm each of them is repeated five times with an unloading limit in 0.5 N in force.

At least two tests are run in each configuration. No significant variation is recorded and only one curve is depicted as example in the following figures.

#### Results

The results are analyzed in terms of planar stress  $\sigma^*$  defined as:

$$\sigma^* = h\sigma \quad (3.8)$$

with  $h$  the film thickness and  $\sigma$  the stress tensor usually employed in mechanics.

Under incompressibility assumption, the planar true stress in tensile direction expresses as:

$$\sigma_{yy}^{*,true} = \frac{F_y \sqrt{\lambda_{yy}}}{w_0} \quad (3.9)$$

with  $\lambda_{yy}$  the stretch in the tensile direction,  $F_y$  the recorded force in the tensile direction and  $w_0$  the initial film width.

First, the influence of the manufacturing direction is assessed: uniaxial tests until rupture are performed twice in machining (MD) and transverse direction (TD); only one of each is shown on Figure 3.18b in black and blue. No significant change is observed according to orientation: PTFE films have a mechanical isotropic behaviour.

Looking at the evolution of the stress, the global behaviour can be qualified of strain hardening. First, up to 1.05 stretch, an elastic regime is observed: on cyclic test shown in Figure 3.19 insert, the hysteresis areas are small and may be due to the imposed condition of the next loading starting once a 0.5 N force is reached. The material unloading is not perfect but maintaining a low force outside the load cell noise range is necessary. In this elastic regime, a PTFE film Young modulus value can be estimated at  $E = 315$  MPa. Then, the stress continues to increase but with a lower slope to finally exhibit some localization instability around 1.8 stretch as depicted on pictures in Figure 3.18a: whatever the vertical position, the sample width is almost constant excepted for 1.8 stretch. Until a stretch of

3, a plastic plateau is exhibited with a plane true stress value around 0.5 N/mm. Finally, the stress increases rapidly until rupture.

From the experimental data, a simplified behavior law between planar true stress and stretch in tensile direction is identified. The chosen model is depicted in Figure 3.18b in red:

- for stretches up to 2.2, a logarithmic law is fitted

$$\sigma_{yy}^{*,true}(t) = 0.28 \times \ln(\lambda_{yy}(t)) + 0.25 \quad \text{for } \lambda_{yy} < 2.2 \quad (3.10)$$

- for stretches larger than 2.2, a power two law is fitted

$$\sigma_{yy}^{*,true}(t) = 0.08 \times [\lambda_{yy}(t) - 2]^2 + 0.47 \quad \text{for } \lambda_{yy} > 2.2 \quad (3.11)$$

with  $\sigma_{yy}^{*,true} = \frac{F_y \sqrt{\lambda_{yy}}}{w_0}$  the true stress under incompressibility assumption and  $\lambda_{yy}$  the stretch in the tensile direction.

This behaviour law will be further used to model PTFE films mechanical response in Chapter 6.

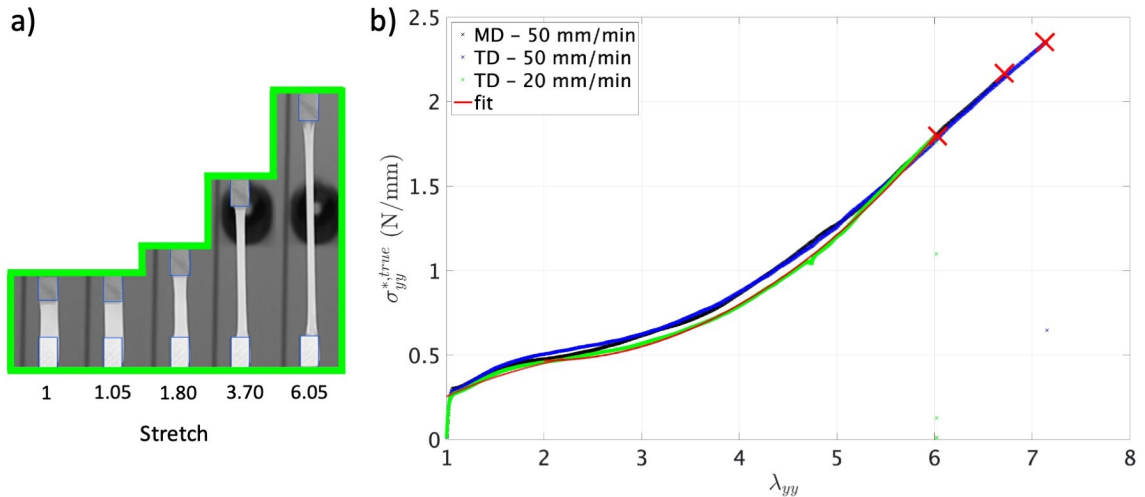


Figure 3.18: a) Pictures taken during tensile test, a localization instability seems to appear at a stretch of 1.8: the section is no more constant all along the sample, b) True plane stress ( $\sigma_{yy}^{*,true}$ ) versus stretch  $\lambda_{yy}$  curves obtained on 2 test directions under incompressibility assumption: machine (MD) and transverse (TD) - no significant variation is observed. The red crosses indicate the rupture. Our simplified behavior law is depicted in red.

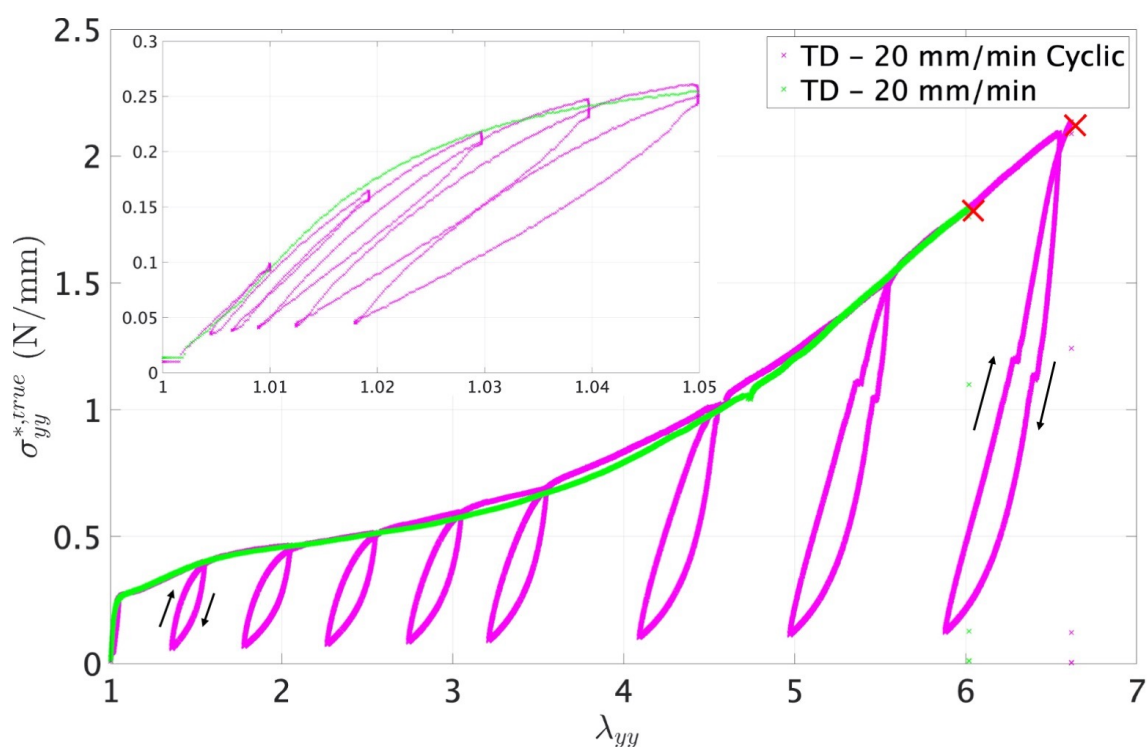


Figure 3.19: Stress-stretch curves in transverse direction until rupture and with cyclic loading/unloading. Up to a stretch of 1.05, the behaviour can be considered as purely elastic as highlighted in the insert. The red crosses indicate the rupture.

### 3.4 PTFE macro-molecular chains or segments mobility

Rheology is a tool used to characterize macro-molecular chain or segment diffusion by applying an oscillatory strain to the test material and registering the resulting stress. The time evolution of the viscoelastic parameters of the material can be monitored. In the present work, rheometry is performed on Anton Paar MCR502 equipped with a CTD 450 oven.

#### 3.4.1 Experimental protocol - Shear rheometry

All rheometry experiments are performed on a pseudo-bulk made from at least 10-films stack. 2.5 cm diameter disks cut with a punch are placed in the rheometer equipped with parallel plate geometry and the temperature is increased above melting and maintained for a given time. From this pseudo-bulk sample, different tests are performed:

- **amplitude strain sweep** to determine the limit of the Linear ViscoElastic regime (LVE) corresponding to the range in which the frequency sweep test can be carried out without destroying the structure of the sample. In the LVE region, the storage shear modulus  $G'$  has a constant value called plateau value.
- **frequency sweep** tests at different temperatures above melting to describe the time-temperature dependent behavior of the sample in the LVE regime.
- **dynamic time sweep** tests in LVE regime to follow the healing process across the polymer/polymer interfaces.

The temperature dependant mechanical properties of LVE materials can be obtained from

superposition and shifting of the frequency sweeps curves [J. D. Ferry 1980].

### 3.4.2 Chain movement: time-temperature superposition

In order to determine the appropriate working strain for the frequency tests, strain sweeps from 0.02 to 200% are performed after 10 min hold time at the maximum and minimum temperatures (330 and 375°C) and frequencies (0.1 and 100 rad/s) of interest. The working strain should be in the LVE range, on the common plateau to all recorded curves. On Figure 3.20a, the LVE range seems larger for the smallest frequency up to  $\sim 10\%$  strain. Time-temperature experiments are run at 1% strain following the experimental protocol depicted on Figure 3.20b. The sample is sintered for 1h30 at 375°C with a normal force of  $\sim 10$  N corresponding to a pressure of about 500 Pa. From this "pseudo-bulk" sample, frequency sweep tests are performed at different temperatures above and close to melting. Between each temperature step from 365 to 330°C, 10 min temperature settling time while keeping pressure is prescribed. In Figure 3.20b, the time-evolution of temperature, normal force and gap through the different temperature stages is presented. It can be seen that the gap decreases as temperature decreases. Since the zero gap initialisation has been done at room temperature, the gap values given at high temperatures are not accurate: they are the sum of the sample and plates dilatation.

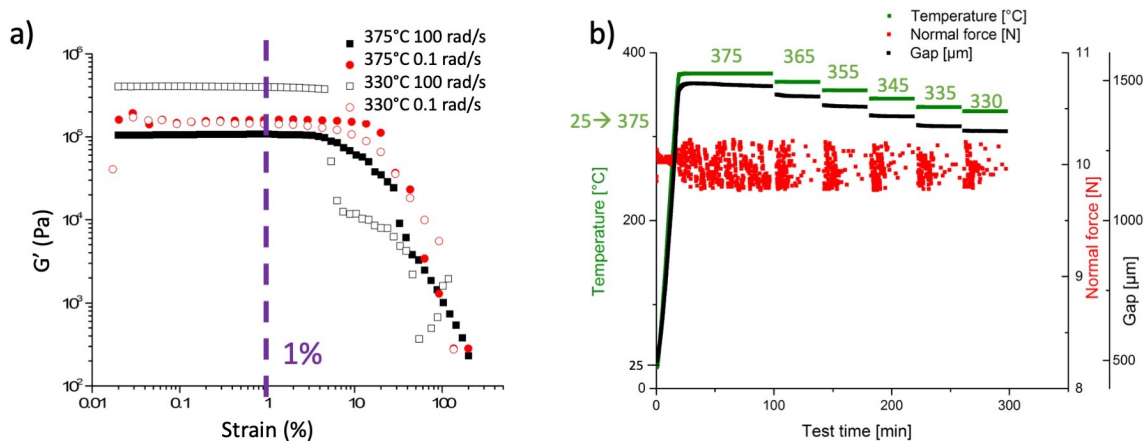


Figure 3.20: a) Linear ViscoElastic range determination by strain sweep at extreme temperatures and frequencies of interest. The chosen strain is 1%. b) Time-Temperature Superposition experimental protocol from film stack to a pseudo-bulk: temperature and normal force are controlled, gap is free. (i) Heating from 25 to 375°C with 10 N normal force, (ii) Relaxation at 375°C for 90 min with 10 N normal force: the material is now considered as a pseudo-bulk, (iii) frequency sweep at 375°C with 10 N normal force, (iv) 10 min relaxation followed by frequency sweep still with 10 N normal force at various temperatures (365, 355, 345, 335, 330°C).

From the method in Figure 3.20b, storage and loss modulus at different temperatures are obtained. Thanks to time-temperature superposition principle and RepTate Software [Boudara *et al.* 2020], the recorded curves are shifted and the master curve in Figure 3.21a is obtained. The storage modulus is almost constant at a value of  $\sim 0.5$  MPa with a small increase with increasing frequency; the loss modulus is decreasing with frequency and it is in the range 0.05 to 0.02 MPa. Both storage and loss moduli decrease with decreasing temperature. Here, there is no crossover of the storage and loss modulus, the reptation

time is assumed very large.

In literature, relatively few data concerning PTFE rheological properties in temperature are available. To check the validity of our measurement, [T. Tervoort *et al.* 2000] storage modulus data at 380°C are reproduced on Figure 3.21a. Their values overlap what we obtained but their slope is steeper; this could be explained by the molecular mass difference  $1.2 \times 10^6$  g/mol for [T. Tervoort *et al.* 2000] and around  $10^7$  g/mol for our material.

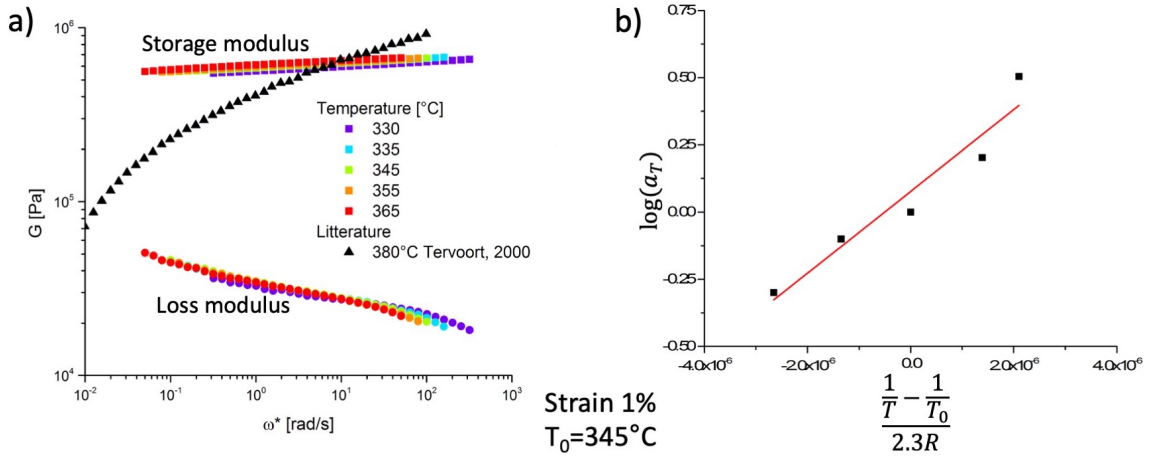


Figure 3.21: a) Storage and loss moduli results from frequency sweeps at different temperatures on PTFE films stack shifted thanks to time-temperature sweeps and comparison to literature data [T. Tervoort *et al.* 2000], b) Activation energy determination following Arrhenius dependence from time-temperature shift factors.

For thermally activated relaxation process, such as polymer relaxation above melting, Arrhenius law is used to describe its process:

$$\log a_T = \frac{E_{a,TTS}}{2.3R} \left( \frac{1}{T} - \frac{1}{T_0} \right) \quad (3.12)$$

with  $E_{a,TTS}$  the activation energy,  $R$  the gas constant,  $T_0$  the reference temperature and  $a_T$  the shift factors used to build Time-Temperature superposition master curve.

From our experimental data, the activation energy can be computed (Figure 3.21b), leading to a value of 152 kJ/mol. In Section 3.3.1, an activation energy has already been obtained by DMA in tension:  $E_{a,DMA} = 191$  kJ/mol. These two values cannot be compared since their are not obtained in the same temperature range nor on the same sample (1 film or a 10 films stack). Moreover, the sollicitation modes are not the same in tension for DMA and in shear for rheology.

Since a whole macro-molecular chain movement is not expected, we wonder what the possible mechanisms responsible for adhesion at our time scale could be:

- either a small length of chain movement could be enough to ensure interfacial adhesion: [Wool, Yuan, *et al.* 1989] showed that the interdiffusion of eight times the critical molecular weight seems to be enough to achieve a "good" adhesion, see Figure 2.9,
- and/or interfacial co-crystallization may have a predominant impact.

The first hypothesis of small length chain movements is explored in the next paragraph.

### 3.4.3 Segment movement: progressive healing

To test chain segments motion which could play a role in the adhesion between two PTFE films, the time evolution of healing on film stacks is followed on a PTFE films stack as shown by [Bousmina *et al.* 1998] on a polystyrene/polystyrene assembly. The complex shear modulus should increase with time following one of the power law predicted by the literature for macromolecular chains or segments motion, summarized on Figure 2.6.

#### Experimental protocol

Strain sweeps are performed on 10 layers stack of white (sintered/unsintered interfaces) and purple (sintered/sintered interfaces) films at a frequency of 0.1 rad/s after a 1 min soak time at 375°C, see Figure 3.22a&b.

The evolution of storage and loss modulus with strain is reproduced on Figure 3.22c. Recorded signal is noisy for the sample at the lowest strains in red, the rheometer limit range seems to be reached; this part cannot be used. Between the different tested samples, the storage modulus varies of more than one decade. This can be explained by the different normal forces applied (see Figure 3.22c) the higher the normal force, the better the recorded signal quality and the higher the storage modulus. This emphasizes the importance of normal force-controlled experiments. This highest normal force (45 N) is chosen for the following tests.

On the strain sweep with controlled normal force at 45 N, torque is also recorded. According to Anton Paar technical support, for good oscillatory measurements, the optimum torque range is comprised between 10 and 90% of the instrument maximum torque (230 mNm for a MCR 502 [AntonPaar 2011]) leading to a range comprised between 23 and 207 mNm. Taking this in consideration, the minimum strain in linear viscoelastic range allowing a torque of around 20 mNm is 0.2%; this value is chosen for further rheological experiments on PTFE films stack.

Rheological experiments on stack or healing tests are performed according to the experimental procedure depicted on Figure 3.23. Rheometer temperature is increased up to 375°C and the measurement starts at a frequency of 0.1 rad/s, with a normal force of 45 N imposed at a strain of 0.2%. Such a high normal force is applied to ensure the best intimate contact conditions through the highest possible real contact area. Complex shear modulus evolution is monitored with time; points are recorded in a logarithmic ramp from 1 to 300 s per point for 4 h or in a discrete way. Different sample configurations are tested:

- using the same sample all along measurement for 4 h or changing sample for each point to avoid history consequences,
- films stacks pressed (8 MPa for 30 s, with Gibrite thermopress at ambient temperature) or not,
- samples kept in vacuum for 8 h or not.

To estimate bulk values, after the full method described before, the sample is cooled back to room temperature still between rheometer plates and the same test is reproduced.

#### Results

Figure 3.24a shows the time evolution of the complex shear modulus for 10 layers PTFE films stack with sintered/unsintered interface (white cast films). The complex shear modulus of a bulk sample is estimated around 1.7 MPa (the light green curve sample is tested a second time to give the dark green curve). In the explored time range, all the curves tend to this asymptotic value without reaching it. The sample in cyan was pressed

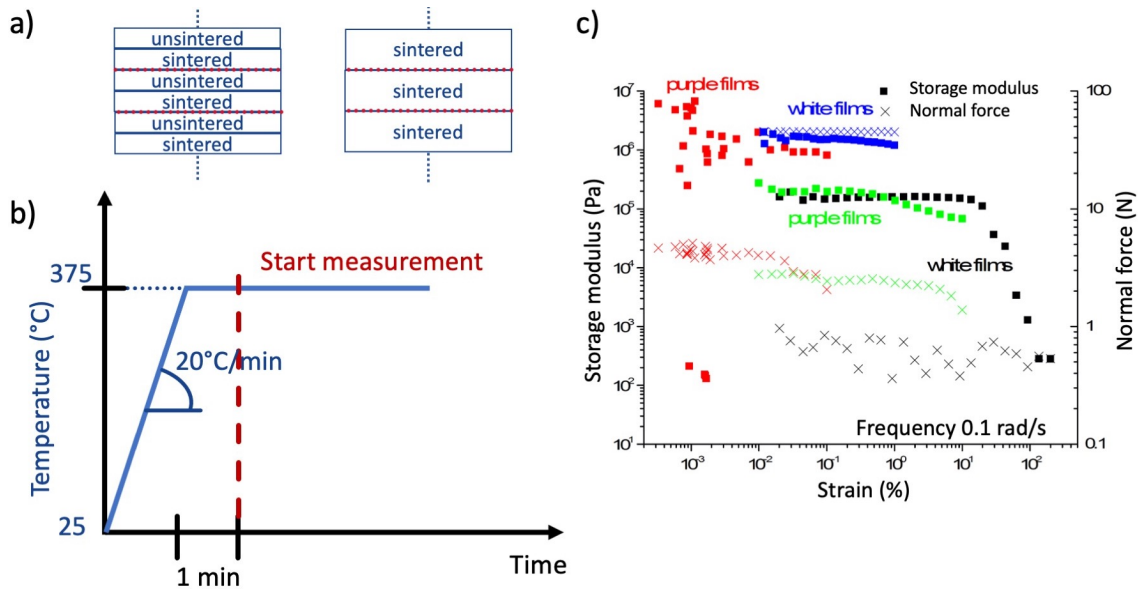


Figure 3.22: a) Different PTFE film stacks and the interfaces in contact (red dotted line), b) Experimental temperature protocol before the start of strain sweep on PTFE films stacks, c) Evolution of storage modulus and normal force with strain on different experiments. Normal force importance chose to be kept at 45 N, strain 0.2% smallest and torque still in range.

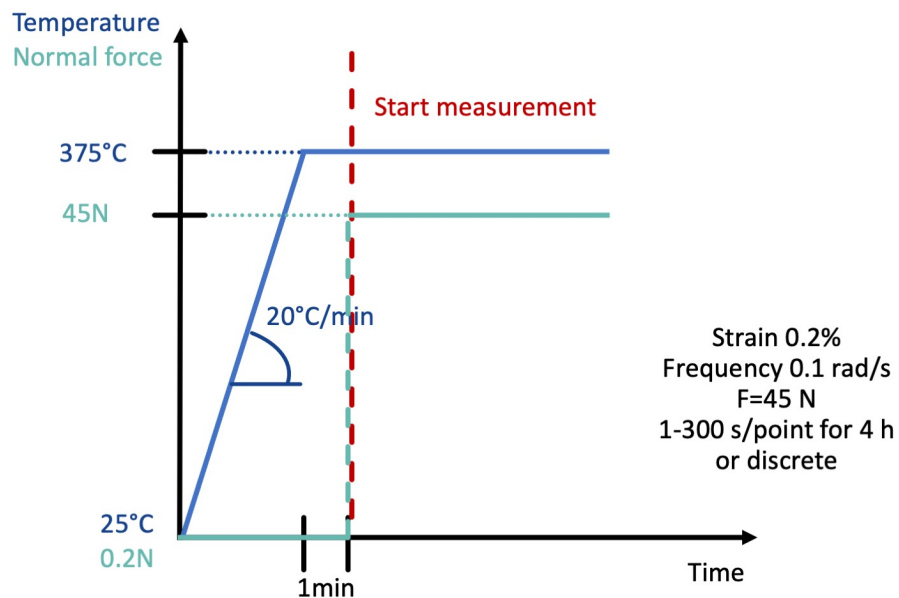


Figure 3.23: Experimental protocol for healing test on PTFE films stacks: temperature and normal force evolution.

and put under vacuum before testing, no clear change seems to result from this treatment. No clear power law with time can be deduced from the experiments made on stacks with sintered/unsintered layers for 10 or even 20 layers; reproducibility is difficult to obtain. This may be due to the unsintered layer which is easy to damage by contact with any other material.

For fully sintered stacks, less data dispersion is observed, see Figure 3.24b. Also, the complex shear modulus of a fully sintered stack bulk sample seems higher than the one for a stack with sintered/unsintered interfaces. Large square data points in dark blue on Figure 3.24b correspond to a sample put for 8 h under vacuum before any measurement; this treatment does not seem to impact the recorded value and we hope it allows to trap less air between layers than before. Moreover, the results on sintered/sintered stacks for continuous measurements show two clear slopes in two different time ranges: from 40 to 100 s the increase of the modulus is steeper.

Whatever the interface nature is, performing discrete or continuous measurement show no clear change. Changing the sample after each measure point is not modifying the material response (data not shown). Consequently, the impact of the previous measurements on the material healing in progress seems negligible. For all the tests run, the complex shear modulus increases over more than 2 time decades with slopes in the range of 0.05 to 0.18 Pa/s.

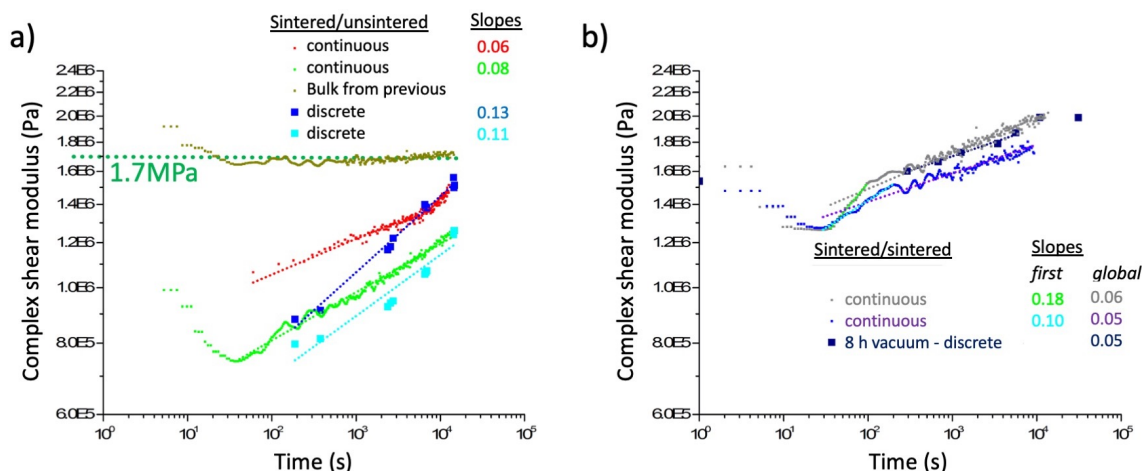


Figure 3.24: Time evolution of the complex shear modulus for 10 layers PTFE films stack with a) sintered/unsintered interface (white films) and b) sintered/sintered interfaces (purple films).

In order to have a visual evaluation of the healing progress, a low voltage scanning electron microscope Hitachi 4800 II is used to observe PTFE samples. Low voltage SEM gives good resolution on polymers without any conductive coating on the surface. PTFE films stacks are cryofractured to access the bulk material with limited reorganization of the macromolecules on the splitted surface [Bunn *et al.* 1958]. The resulting images give information on the quality and intensity of healing in progress, see Figure 3.25. The stack with sintered/sintered interfaces is the one with the steeper modulus increase with time but the different layers are still present on the splitted surface: holes are homogeneously distributed in lines spaced of one film thickness. However, healing seems of good quality on the sintered/unsintered stack: only defects are visible on left of the picture between the second and third layers from the bottom.

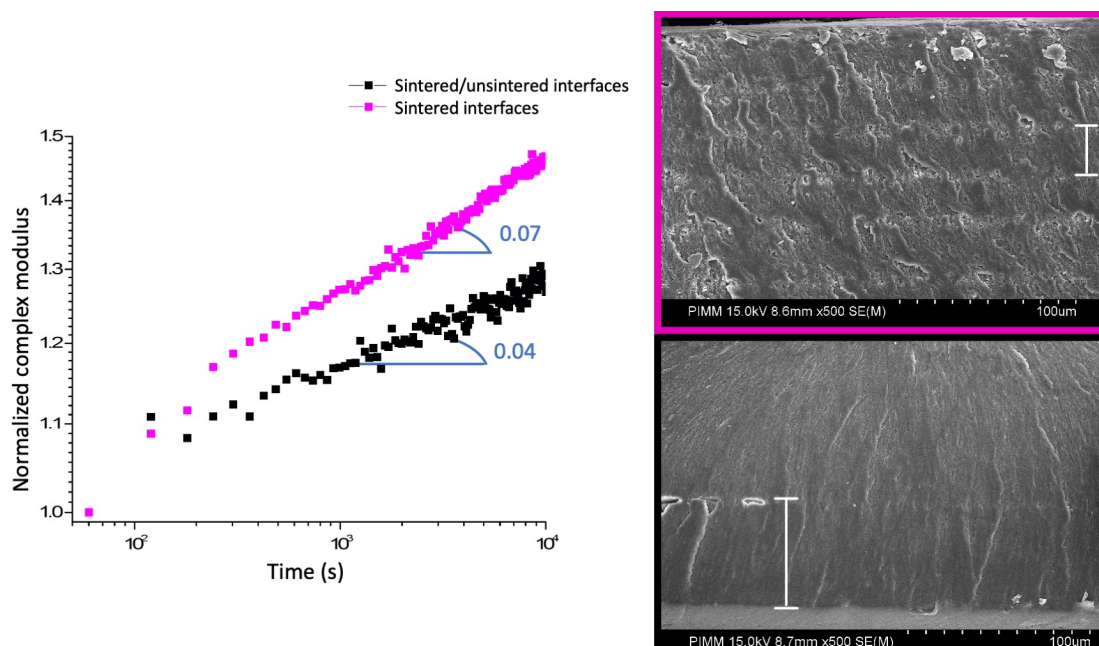


Figure 3.25: Time evolution of the complex shear modulus for 10 layers PTFE films stack with sintered/unsintered (in black) and sintered/sintered (in purple) interfaces. On the right, SEM pictures the previous samples cryofractured after healing: for the sample with sintered interfaces the layers are still noticeable.

To conclude, from the dynamic time sweep experiments, an increase of the modulus with time has been highlighted and healing has been visually observed on a cryofractured sample. However, the chain segment motion at play could not be identified to one described in the literature (Figure 2.6), since no clear exponents can be determined. Both small length of chain motion and interfacial co-crystallization are possible mechanisms responsible for PTFE-PTFE adhesion.



# Adherence measurements

*In this chapter, important results from literature for the understanding of mechanical adherence testing and adhesion are summarized.*

## Contents

---

<b>4.1</b>	<b>Adhesion energy estimation . . . . .</b>	<b>74</b>
4.1.1	Non-adhesive contact – Hertz model . . . . .	74
4.1.2	Adhesive contact – JKR model . . . . .	75
<b>4.2</b>	<b>Theory of fracture and adhesion - short summary . . . . .</b>	<b>78</b>
4.2.1	Semi-crystalline polymers mechanical behavior . . . . .	78
4.2.2	Plane strain, plane stress and different fracture modes . . . . .	78
4.2.3	Energy balance approach . . . . .	80
4.2.4	Stress intensity factor approach . . . . .	81
4.2.5	Relationship between $G$ and $K$ . . . . .	82
<b>4.3</b>	<b>Adherence tests . . . . .</b>	<b>83</b>
4.3.1	Peel tests . . . . .	83
4.3.2	Lap-shear tests . . . . .	84
4.3.3	Tack and pull tests . . . . .	85
<b>4.4</b>	<b>Conclusion . . . . .</b>	<b>86</b>

---

In Chapter 2, the focus was on the mechanisms at play during interface formation. Only the term **adhesion** term has been used to describe this bonding step characterized by the value of Dupré reversible thermodynamic work of adhesion  $W_A$ . When talking about interfacial strength and weld fracture (mechanisms and measurements), the term **adherence** is most appropriate and the associated value is the strain energy release rate or toughness  $G$ .

## 4.1 Adhesion energy estimation

In our study, a home-made probe tack test is implemented. To estimate the adhesion energy or work of debonding from probe tack test, the theory of contact between two solids of the specific test geometry must be understood; some of them are exposed here after.

### 4.1.1 Non-adhesive contact – Hertz model

Using a strictly mechanical analysis, Hertz has developed a model of the non-adhesive contact between two spheres of radius  $R_1$  and  $R_2$  or between a plane and a sphere of radius  $R$ , for which the two objects can be separated without apparition of adhesive forces [Hertz 1882]. Theoretically, the contact area of two spheres is a point. As a result, when the two bodies are subject to a normal force, the pressure between two curved surfaces should be infinite which will cause immediate yielding of both surfaces. However, a small contact area is created through elastic deformation, thereby considerably limiting the stresses. These contact stresses are called Hertz contact stresses. The Hertz theory is valid under some assumptions:

- the strains are small and within the elastic limits of the materials,
- the surface of contact has a radius  $a \ll R$ ,
- the surfaces are frictionless,
- there are no adhesive forces between the two surfaces.

Let consider the case of a sphere of radius  $R$ , with Young's modulus  $E_1$  and Poisson ratio  $\nu_1$ , and a plane made of a material of Young's modulus  $E_2$  and Poisson ratio  $\nu_2$ . If no pressure  $P$ , or normal force  $F$  is applied, the contact is made only on a single point. Upon increasing of the normal force  $F$  between the two objects, by increasing the indentation  $\delta$ , the contact area is then a circle of radius  $a$ , see Figure 4.1. The contact profile between the two objects can be approximated by a paraboloid, so that in scaling law,  $z \sim \frac{x^2}{R}$ , leading to

$$a \sim \sqrt{R\delta} \quad (4.1)$$

The characteristic strain  $\epsilon$  on the penetration depth is  $\epsilon \sim \frac{\delta}{a}$ . So, the elastic energy for the Hertz contact  $W_{el}$  can be expressed as  $W_{el} \sim E^* \epsilon^2 V$  with  $V \sim a^3$  the volume of the deformed zone, giving  $W_{el} \sim E^* a \delta^2$  with  $E^*$  the reduced modulus of the system ( $E^* = \frac{E_1}{1-\nu_1^2} + \frac{E_2}{1-\nu_2^2}$ ). By replacing  $a$  with equation 4.1,

$$W_{el} \sim E^* \delta^{\frac{5}{2}} R^{\frac{1}{2}} \quad (4.2)$$

The total energy of the system is then  $W_{tot} \sim -F\delta + W_{el}$ . At equilibrium,  $\frac{\partial W_{tot}}{\partial \delta} = 0$ . The force is then  $F \sim \frac{\partial W_{el}}{\partial \delta}$

$$F \sim E^* \delta^{\frac{3}{2}} R^{\frac{1}{2}} \quad (4.3)$$

The exact calculation can be found in Appendix A.

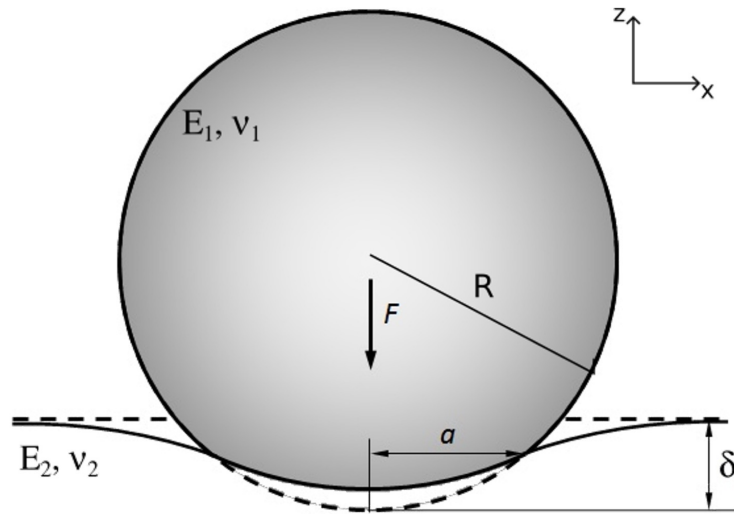


Figure 4.1: The Hertz situation: contact of an elastic sphere with an elastic half-space. Adapted from wikipedia.

#### 4.1.2 Adhesive contact – JKR model

Roberts and Kendall showed experimentally that for systems of two rubber spheres or two glass spheres, the contact area at low loads were considerably larger than what was predicted by the Hertz theory. Along with Johnson [Johnson *et al.* 1971], they expanded the Hertz theory to include the effect of surface energy in the contact between soft elastic spheres, which is detailed here. The range of the surface forces is negligible as compared to the gap between the surfaces outside the contact zone and traction forces are encountered at the periphery of the contact.

In this theory, the adhesive equilibrium is reached in two steps, see Figure 4.2:

- a non-adhesive contact is achieved under the Hertz load,
- a rigid vertical displacement is applied to all contact points to achieve, at constant contact radius, the load and indentation depth at equilibrium.

Johnson, Kendall and Roberts [Johnson *et al.* 1971] developed the theory for adhesive contacts based on an energetic point of view. They consider the case of a sphere of radius  $R$ , with a Young's modulus  $E_1$  and a Poisson ratio  $\nu_1$ , and a plane made of a material of Young's modulus  $E_2$  and a Poisson ratio  $\nu_2$ . They state that the contact radius  $a$  between the objects is a function of the total energy of the system  $W_{tot}$ , and that at equilibrium the total energy should be minimal.

This total energy of the system is made of three terms: the stored elastic energy  $W_{el}$ , the mechanical energy in the applied load  $W_m$  and the surface energy  $W_s$ :

$$W_{tot} = W_{el} + W_m + W_s \quad (4.4)$$

When adhesive forces are present, the same contact area  $\pi a^2$  is obtained with an applied force  $F < F_H$  where  $F_H$  is the force predicted by Hertz for this value of  $a$ . For calculation, the elastic energy  $W_{el}$  can be separated in two contributions: a Hertzian compression phase (path between O and A in Figure 4.3b, with energy  $W_H$ ) where the surface forces are zero ( $W_A = 0$ ), followed by a decompression at constant contact radius  $a$  (between A and B Figure 4.3b, with energy  $W_B$ ) where  $W_A$  has a finite value.

$$W_{el} = W_H - W_B \quad (4.5)$$

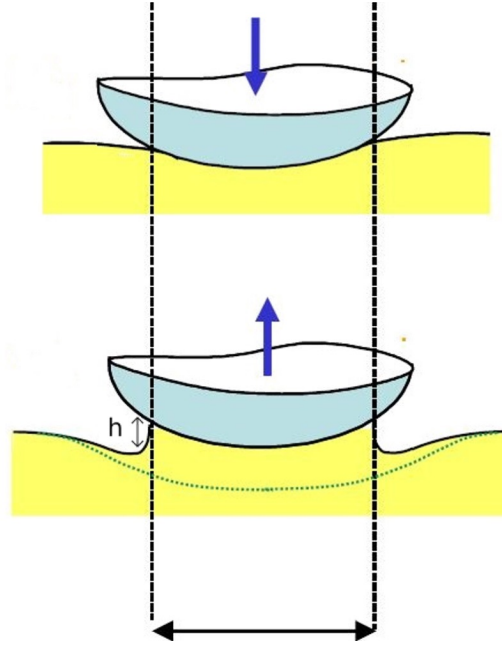


Figure 4.2: Two steps to reach an adhesive equilibrium: Top - Hertzian contact, Bottom - vertical body displacement at constant contact radius  $a$ . Adapted from Antoine Chateau-minois Master 2 MAGIS Course.

During the compression, Hertz theory predicts

$$W_H = \int_0^{\delta_H} F d\delta = \frac{2}{5} \frac{F_H^{\frac{5}{3}}}{K^{\frac{2}{3}} R^{\frac{1}{3}}} \quad (4.6)$$

with  $K = \frac{4}{3} \left( \frac{1}{E_1^*} + \frac{1}{E_2^*} \right)$ , with the reduced modulus  $E_i^* = \frac{E_i}{1-\nu_i^2}$

During the decompression with constant radius  $a$ , the force goes from  $F_H$  to  $F_1$ . Since the radius is constant, the force-indentation relation is given by the Boussinesq theory [Boussinesq 1885]:

$$\delta = \frac{2}{3} \frac{F}{K a_1} \quad (4.7)$$

In that case, the elastic energy  $W_B$  is then given by

$$W_B = \int_{\delta_H}^{\delta_1} F d\delta = \frac{1}{3K^{\frac{2}{3}} R^{\frac{1}{3}}} \frac{F_H^2 - F_1^2}{F_H^{\frac{1}{3}}} \quad (4.8)$$

Finally, using equation 4.5, the total elastic energy  $W_{el}$  is

$$W_{el} = \frac{1}{3K^{\frac{2}{3}} R^{\frac{1}{3}}} \left( \frac{1}{15} F_H^{\frac{5}{3}} + \frac{1}{3} F_1^2 F_H^{-\frac{1}{3}} \right) \quad (4.9)$$

The mechanical potential energy is given by

$$W_m = -F_1 \delta_1 = \frac{-F_1}{3K^{\frac{2}{3}} R^{\frac{1}{3}}} \left( \frac{1}{3} F_H^{\frac{2}{3}} + \frac{2}{3} F_1 F_H^{-\frac{1}{3}} \right) \quad (4.10)$$

Last, the surface energy  $W_s$  is expressed as a function of the thermodynamic work of adhesion  $W_A$

$$W_s = -W_A \pi a_1^2 = -W_A \pi \left( \frac{R F_H}{K} \right)^{\frac{2}{3}} \quad (4.11)$$

The minimization of the total energy  $\frac{dW_{tot}}{da_1} = \frac{dW_{tot}}{dF_H} = 0$  and its stability  $\frac{d^2W_{tot}}{dF_H^2} = 0$  gives the apparent Hertz load acting between two elastic bodies of surface energy  $W_A$  which is bigger than the applied load  $F_1$

$$F_H = F_1 + 3W_A\pi R + \sqrt{6W_A\pi R F_1 + (3W_A\pi R)^2} \quad (4.12)$$

Note here that in the case where  $W_A = 0$ , the previous equation gives  $F_H = F_1$  and  $a^3 = \frac{RF_1}{K}$ : the JKR theory includes the Hertz theory. Also, at zero applied load  $F_H = 0$  (during a compression phase), the contact radius has a finite value  $a^3 = \frac{6\pi W_A R^2}{K}$ . When the applied load is made negative, during a traction phase, the contact radius decreases and finally falls to zero for a minimal load also called the pull-out force

$$F_{pull-out} = -\frac{3}{2}W_A\pi R \quad (4.13)$$

which is independent of the materials properties.

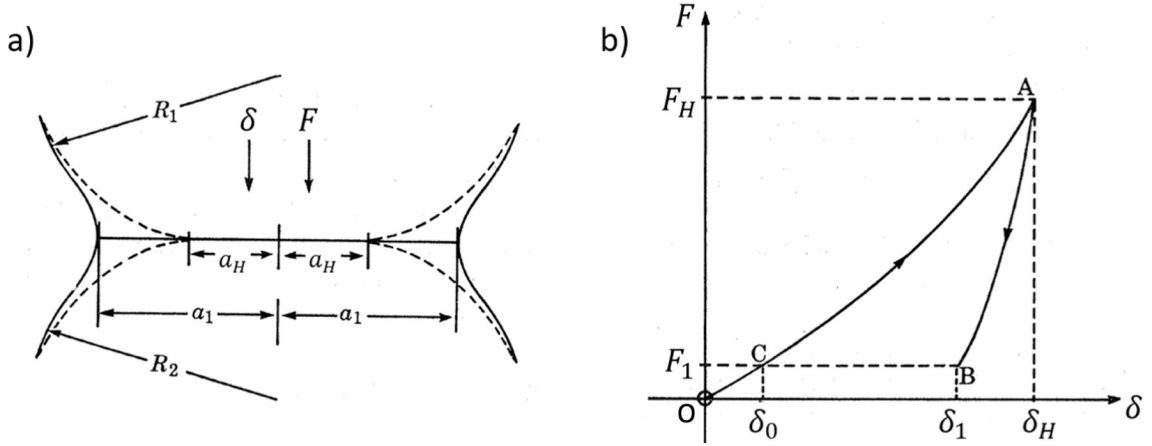


Figure 4.3: The contact between two elastic solids both in the presence (contact radius  $a_1$ ) and absence (contact radius  $a_H$ ) of surface forces. a) shows the contact between two convex bodies of radii  $R_1$  and  $R_2$  under a normal load of  $F$ ;  $\delta$  is the elastic displacement. b) represents the load-displacement relation for the contacting surfaces. Point A is the Hertz stress with  $a = a_1$  and  $F = F_H$ ; Point B the actual stress (Johnson 1958) with  $a = a_1$  and  $F = F_1$  and point C the Hertz stress with  $a = a_H$  and  $F = F_H$  [Johnson *et al.* 1971].

## 4.2 Theory of fracture and adhesion - short summary

Fracture mechanics is the field of mechanics concerned with the study of the propagation of a crack inside a material creating two new interfaces. When describing the rupture of an interface, the common framework is Linear Elastic Fracture Mechanics (LEFM) based on the hypothesis that during the crack propagation, the surrounding bulk materials remain linearly elastic everywhere except in a tiny region around the crack tip called the fracture process zone.

In this section, the fracture behaviour of polymers is briefly summarized in order to build the theoretical background needed for the study of polymer adhesion. We introduce some general theoretical concepts which are useful to interpret the adhesion test used in our study.

### 4.2.1 Semi-crystalline polymers mechanical behavior

The mechanical response of all polymers is characterized by an elastic part, an anelastic part and a plastic part, the relative magnitude of which depends on the total strain. At low strains the elastic and the anelastic components dominate while above the yield stress  $\sigma_Y$ , the plastic component dominates.

The plastic deformation of semi-crystalline polymers is complex since they can be assimilated to composite materials with very specific tie molecules between the crystalline domains. The typical mechanical response of a ductile semi-crystalline polymer to a tensile test is summarized in Figure 4.4 in blue. At low strains under  $\epsilon_Y$ , a nearly elastic deformation is observed, where the strain  $\epsilon$  is nearly proportional to the applied stress  $\sigma$ . This regime is characterized by an apparent slope  $E$ , which is generally defined as the Young's modulus, neglecting the anelasticity. For higher levels of strain, the deformation becomes plastic and preferential orientation can be induced in the sample. The maximum of the stress strain curve is called the yield stress  $\sigma_Y$ . The cold drawing appearing after the yield point comes from the rearrangement of the chains in a characteristic and complex manner, beginning with necking in the sample. A neck is a narrowing of a portion of the stressed material to a smaller cross section. The necked region grows, at the expense of the material at either end, eventually consuming the entire specimen. When the plastically deformed and oriented part has extended to the whole sample being tested, a hardening can occur until breakage of the material.

Moreover, for semi-crystalline polymers two other cases should be considered. If the amorphous portion is rubbery, then the polymer will tend to have a low modulus, and the extension to break will be very large, see Figure 4.4 in black. If the amorphous portion is glassy, the polymer will behave much more like a brittle plastic, see Figure 4.4 in green.

### 4.2.2 Plane strain, plane stress and different fracture modes

Before presenting the two crack propagation approaches, the two limit cases of stress and strain relevant to the fracture of material are briefly recalled as well as the different modes of loading encountered.

There are two limit cases of stress distribution particularly relevant to the fracture of materials. One is plane stress which is obtained in deformed thin sheets as shown in Figure 4.5a. In a thin body, the stress through the thickness ( $\sigma_z$ ) cannot vary appreciably due to the thin section. Because there can be no stresses normal to a free surface,  $\sigma_z = 0$  throughout the section, a biaxial state of stress results, called plane stress condition.

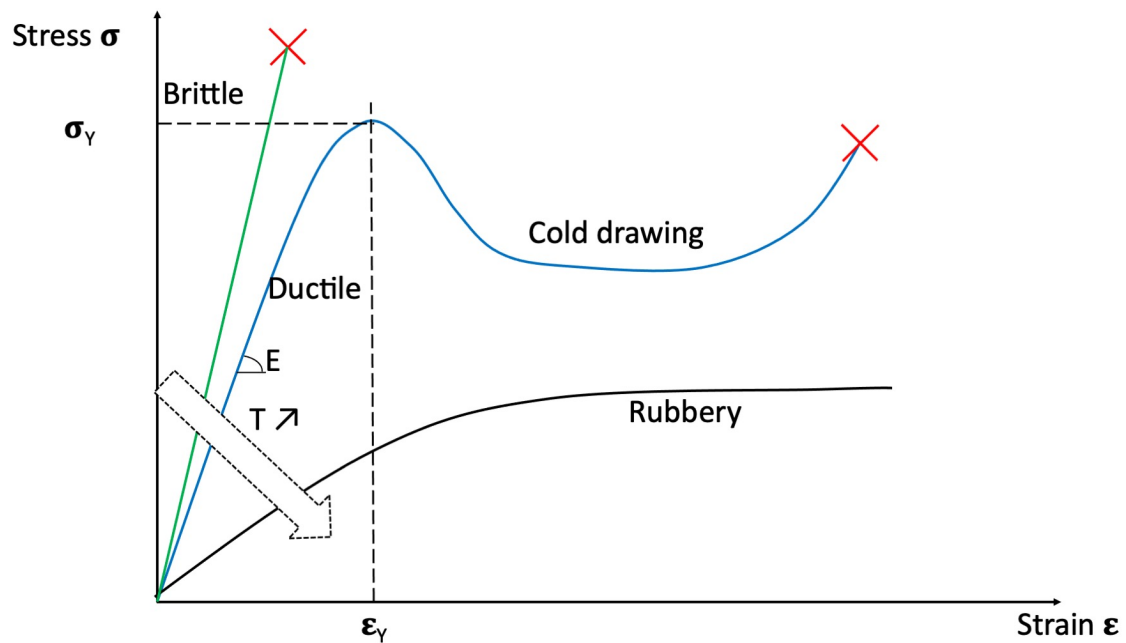


Figure 4.4: Schematic stress strain curves for semi-crystalline polymers. Blue: ductile behavior, Green: brittle behavior, Black: rubbery behavior. The red cross depicts the sample fracture point.

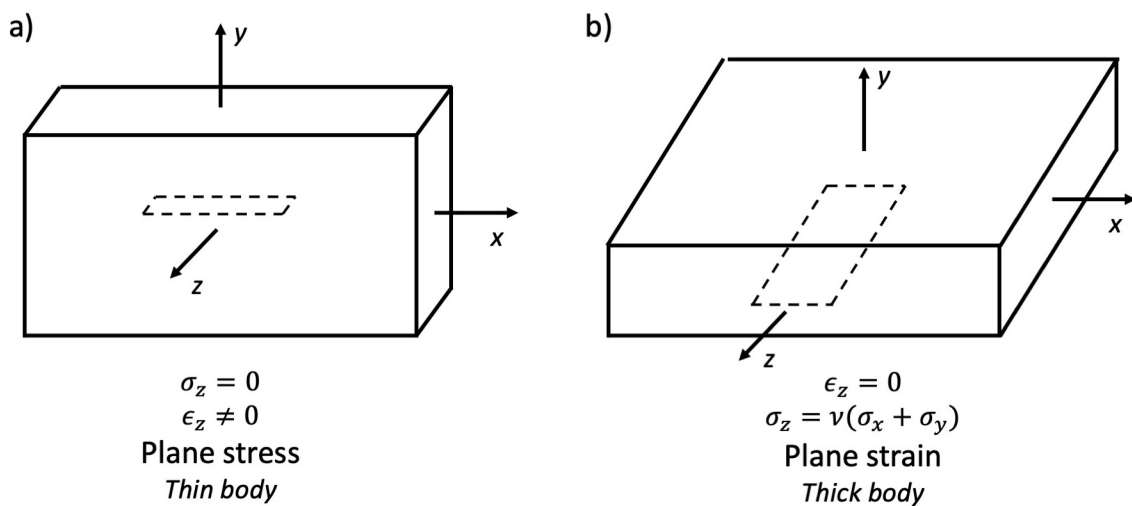


Figure 4.5: Schematic representation of a) plane stress and b) plane strain.

Another situation is the case where one of the three principal strains is equal to zero. This is often encountered in constrained conditions around crack tips in relatively thick sheets. In a thick body, the material is constrained in the  $z$  direction due to the thickness of the cross section and  $\epsilon_z = 0$ , resulting in a plane strain condition. Due to Poisson's effect, a stress,  $\sigma_z$ , is developed in the  $z$  direction.

A crack in a solid may be loaded in three different modes represented in Figure 4.6. The following discussion will then mainly be focused on a mode I loading, which is the situation encountered in our work.

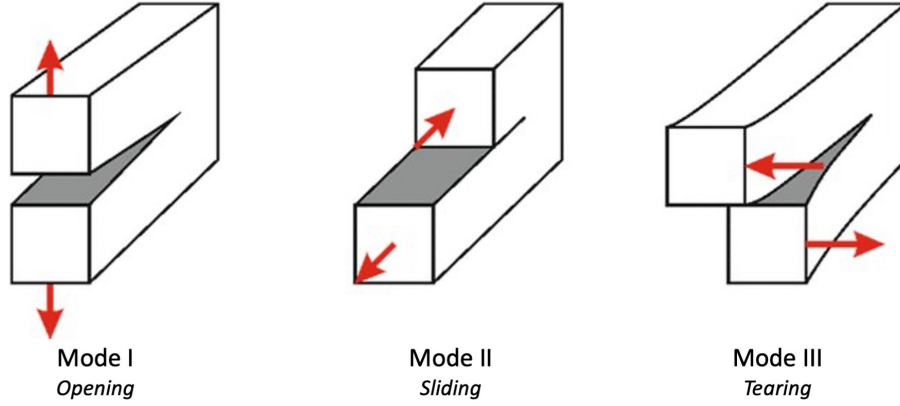


Figure 4.6: Three modes of loading. Adapted from [Preiß 2018].

### 4.2.3 Energy balance approach

In 1921, Griffith [Griffith 1921] adopted an energetic approach to characterize the unstable crack propagation in linear-elastic brittle solids. Invoking the first law of thermodynamics, he stated that a flaw becomes unstable, and thus fracture occurs, when the strain energy change that results from an increment of crack growth is sufficient to overcome the surface energy of the material: the work of external forces  $W_{ext}$  is converted in elastically stored energy  $U_{el}$  and in the Dupré's adhesion energy ( $W_A$ , see equation 2.2). The energy created when the interfacial crack propagates is called the strain energy release rate defined as a energy density ( $G$  in  $\text{J}/\text{m}^2$  or  $\text{N}/\text{m}$ ). It corresponds to the energy dissipated when the crack front of width  $w$  propagates on a length  $a$  creating a new surface of area  $A = w \times a$ . The strain energy release rate is defined by the balance equation 4.14:

$$G = -\frac{dU}{dA} = \frac{dW_{ext}}{dA} - \frac{dU_{el}}{dA} = W_A \quad (4.14)$$

where  $U$  is the potential energy available for crack growth.

For the simple case of a thin infinite plate with a crack of length  $2a$  perpendicular to the tensile load, the energy release rate  $G$  becomes:

$$G = \frac{\pi\sigma^2a}{E} \quad (4.15)$$

with  $\sigma$  the applied stress,  $a$  half the crack length, and  $E$  the Young's modulus, which for the case of plane strain should be divided by the plate stiffness factor  $(1 - \nu^2)$ .

When the stress at fracture  $\sigma_f$  is reached, the energy release rate value is  $G = G_c$  called the critical energy release rate. Thus, the criterion for crack propagation expresses as:

$$G \geq G_c \quad (4.16)$$

In 1956, Irwin [Irwin 1956] extended the work of Griffith by expanding theories to ductile materials by including the energy dissipated by local plastic flow in the process zone. Consequently, the energy required to break an established interface has two main contributions:

- a thermodynamic term - Dupré work of adhesion  $W_A$  describing the separation of the molecules at the interface from surface, see definition 2.1.1,
- a dissipative factor  $\phi$  - the energy required to deform the adhesive and substrate, which depends on the debonding speed and temperature.

So, the strain energy release rate can be expressed as [Maugis *et al.* 1978]:

$$G = W_A[1 + \phi(V, T)] \quad (4.17)$$

In the case of structural adhesives which are quite brittle, the total bond strength depends on  $W_A$  more than on dissipative properties. For relatively tough materials such as rubbers and Pressure Sensitive Adhesives's (PSA), the viscoelastic dependance is much more important than  $W_A$ .

The scheme on Figure 4.7 synthesize the different adhesion sources and the order of magnitude of the energy release rate associated.

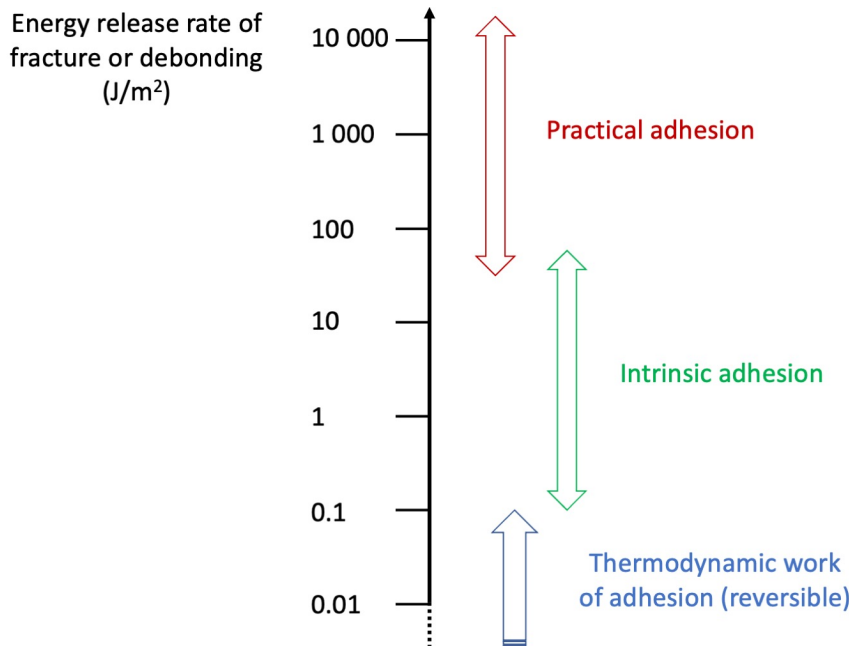


Figure 4.7: Some orders of magnitude of energy release rate of fracture or debonding. Inspired from David Dillard American Adhesion Society short course 2021.

#### 4.2.4 Stress intensity factor approach

In the case of a sharp crack of length  $2a$  in a uniformly stressed infinite sheet Westergaard [Westergaard 1939] has developed stress-function solutions which relate the local concentration of stresses at the crack tip to the applied far-field stress  $\sigma_0$ .

For regions close to the crack tip, the solution takes the form:

$$\sigma_{ij} = \sigma_0 \sqrt{\frac{a}{2r}} f_{ij}(\theta) \quad (4.18)$$

where  $\sigma_{ij}$  are the components of the stress tensor at a point  $r, \theta$  in polar coordinates and  $f_{ij}$  are functions that depend on the crack geometry and loading conditions.

Irwin [Irwin 1957] finds a method of calculating the amount of energy available for fracture in terms of the asymptotic stress and displacement fields around a crack front in a linear elastic solid. This asymptotic expression for the stress field in mode I loading is related to the stress intensity factor  $K_I$  following:

$$\sigma_{ij} = \frac{K_I}{\sqrt{2\pi r}} f_{ij}(\theta) \quad (4.19)$$

From equation 4.19, it is obvious that close to the crack tip ( $r \rightarrow 0$ ), the stress goes to infinity, hence it is necessary to have a reasonable local fracture criterion. Irwin postulated that the following condition,  $K_I \geq K_{Ic}$ , is a good failure criterion. This criterion has the advantage of being independent of the detailed geometry of the sample far away from the crack tip. Any far-field loading situation would result in the same stress distribution but different intensities reflected by  $K$ .

Since the stresses at the crack tip are singular then the yield criterion is clearly exceeded in some zone near the crack tip region. However, if this zone is assumed to be small, the elastic stress field will not be greatly disturbed.

#### 4.2.5 Relationship between $G$ and $K$

In the case of LFEM, a simple relationship exists between  $G$  and  $K$  given in mode I by:

$$G_I = \frac{K_I^2}{E} \quad \text{for plane stress} \quad (4.20)$$

$$G_I = \frac{K_I^2}{E} (1 - \nu^2) \quad \text{for plane strain} \quad (4.21)$$

### 4.3 Adherence tests

When performing adherence tests, the energy required to stretch the bulk material should be considered. Thus, when estimating the macroscopic work  $W_{meas}$  from the experimental curve, the value measured is a combination of the work to propagate the interfacial crack and deform the bulk material between  $t = 0$  and  $t$ :

$$W_{meas} = W_{debonding} + W_{bulk} \quad (4.22)$$

$$W_{meas} = \int_{t=0}^t G dA + \int_{t=0}^t \Pi_{bulk} \times V \quad (4.23)$$

We will talk about interfacial work of debonding  $W_{debonding}$  to designate the work provided only to separate the two interfaces and  $W_{bulk}$  to designate the bulk deformation contribution (with  $\Pi_{bulk}$  a volume energy density in the bulk material).

To characterize the adherence of different materials on polymers or of polymers on themselves, several tests can be implemented [Anderson 2017]. In the following, some elements that help estimate the macroscopic work of adhesion are presented assuming materials are purely linear elastic. Thus, it does not consider viscoelastic or plastic dissipation or non-linear behavior. To compare results from different test configurations, the easiest way is to evaluate their macroscopic work of adhesion  $W_{meas}$ .

#### 4.3.1 Peel tests

Peel tests (Figure 4.8a) are the most used tests to characterize adhesion between a thin strip of material and a surface in steady state. A constant displacement speed  $V$  is imposed at the free arm end and the resulting force is measured. In these tests, some parameters must be controlled to extract a "geometry-independent" adhesion - or strictly speaking adherence - energy.

As the adhesive or peeled material rheology depends on time and temperature, the displacement speed  $V$  applied at the free arm end must be controlled as well as the test temperature; the resulting force is recorded. As reported in the literature (for example by [Kinloch *et al.* 1994]), the peel energy depends on the opening mode of the crack through the peel angle imposed (pure tension  $\theta = 90^\circ$ , pure shear  $\theta = 0^\circ$  or intermediate mode for other angles). It also depends on the deformation of the material at the crack tip and in the peeled free arm. To prevent the contribution of the deformation of the peeled free arm, a flexible but stiff backing can be applied on the other side of the peeled layer to limit stretching in the traction direction. In this case, considering zero bending stiffness and an infinitely rigid string, the macroscopic work of adhesion is given by the Rivlin equation [Rivlin 1997]:

$$W_A = W_{meas} = \frac{F}{b}(1 - \cos \theta) \quad (4.24)$$

with  $F$  the steady state peel force recorded and  $b$  the sample width, see Figure 4.8b.

If it is not possible to prevent stretching of the free arm, the stored elastic energy can be taken into account and the expression of the macroscopic work of adhesion is given by the Kendall equation [Kendall 1975]:

$$W_{meas} = \frac{F}{b}(1 - \cos \theta) + \frac{F^2}{2b^2 E h} \quad (4.25)$$

with  $E$  the Young modulus,  $b$  the width of the peel band and  $h$  the thickness of the peel band.

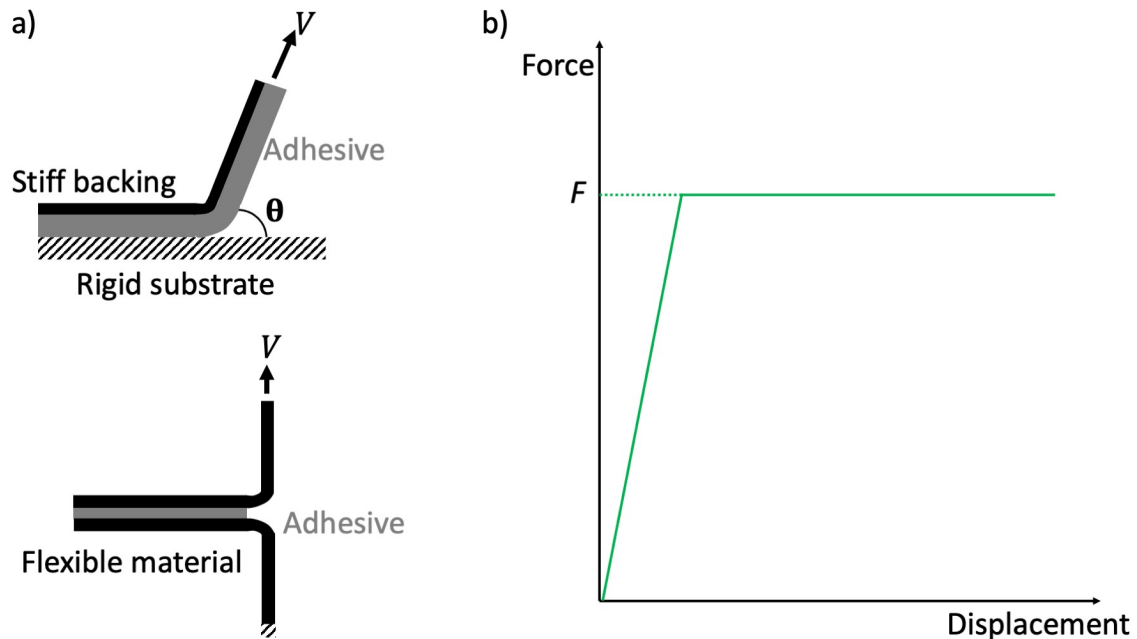


Figure 4.8: a) Top: Peel test configuration - A finite displacement speed  $V$  is applied on the free arm of the peel material with a constant peel angle  $\theta$ . Bottom: T-Peel test configuration - A finite displacement speed  $V$  is applied on the upper free arm while the free arm of the bottom part is fixed. b) Scheme of the force versus displacement recorded data,  $F$  is the steady-state force.

### T-peel tests

T-peel tests (Figure 4.8a bottom) are used to peel two flexible substrates from each other. One substrate sticks up and the other sticks down while the bonded area sticks out horizontally, so that the entire setup forms a "T" shape. Flexion of the unpeeled part is a source of error and often occurs when one of the materials do not bend easily. Note that the two materials can be glued directly together or using another adhesive. T-peel tests are a specific case of controlled angle peel test where  $\theta$  is  $180^\circ$  and thus the previous Kendall equation 4.25 applies with an additional correction to consider the elongation of the second material involved:

$$W_{meas} = \frac{2F}{b} + \frac{F^2}{b^2 E h} \quad (4.26)$$

### 4.3.2 Lap-shear tests

Lap-shear tests (Figure 4.9) can be used to mimic the separation of two flexible materials or of a flexible material from a rigid substrate under shear. A constant displacement speed  $V$  is applied at a controlled temperature.

In the case where one is peeling a soft material from a rigid substrate, extending the equation 4.25 to peel at  $0^\circ$  gives the macroscopic work of adhesion:

$$W_{meas} = \frac{F^2}{2b^2 E h} \quad (4.27)$$

In the case of the lap-shear between two soft materials of modulus  $E_1$  and  $E_2$  and respective thickness  $h_1$  and  $h_2$  a corrective term must be applied to consider the bending

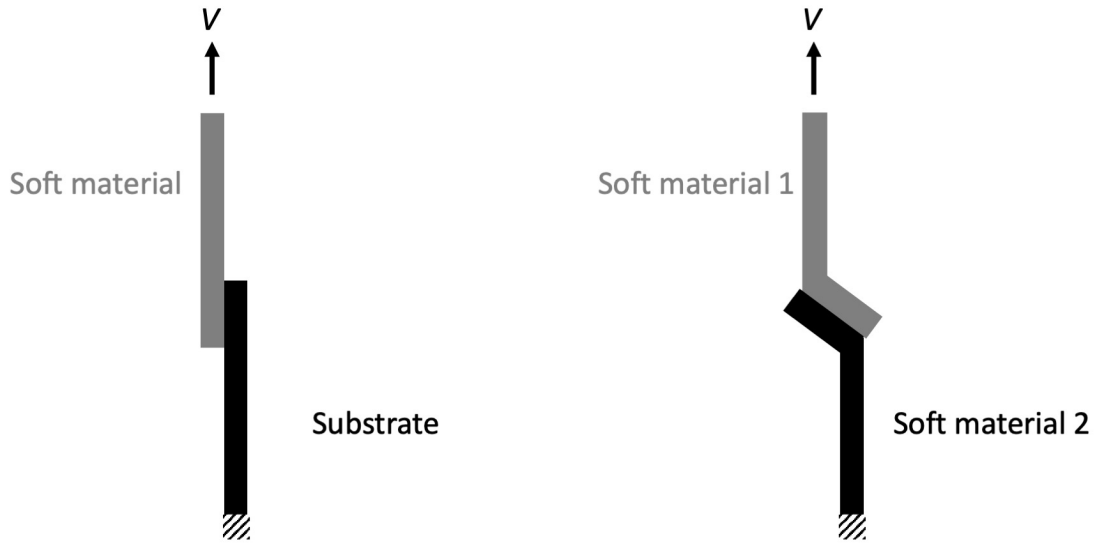


Figure 4.9: Lap-shear test configurations. A finite displacement speed  $V$  is applied on the upper free arm while the free arm of the bottom part is fixed.

of the overlap region. This expression of the macroscopic adhesion energy was found experimentally by Kendall [Kendall 1975].

$$W_{meas} = \frac{F^2}{b^2 E_1 h_1} \left( \frac{1}{E_1 h_1} - \frac{1}{E_1 h_1 + E_2 h_2} \right) \quad (4.28)$$

### 4.3.3 Tack and pull tests

In the previous tests, the peel force is measured during a steady state propagation of the delamination front; the initiation is most of the time disregarded. Tack and pull tests are focusing also on the initiation of the interfacial crack.

Usually tack test is used to designate a test where the contact and the separation of the interface are performed in the same experiments while the pull tests look only at the separation of an existing interface. In the tack test, the contact parameters such as time, temperature and pressure can be controlled. An adhesive layer is first compressed between a flat ended cylindrical probe of radius  $a$  and a hard substrate. After a set contact time, the probe is removed from the surface at a constant velocity  $V$  and the load  $F$  is measured as a function of time or distance, as illustrated in Figure 4.10 left. The advantage of the probe test is the application of a well-defined displacement field to the deformable adhesive since all parts of the measuring instrument have a negligible bending stiffness. Moreover, a well-defined strain history can be applied to the adhesive before debonding.

The result of a probe test is a force versus displacement curve. This curve is usually transformed into a nominal stress versus nominal strain curve (figure 4.10 right), which is obtained by normalizing the force by the maximal area of contact  $A_{max}$  during the compression stage (linked to the probe radius  $a$ ) and the displacement  $\Delta h$  normalizes by

the initial layer thickness  $h_0$  defines a nominal strain  $\epsilon$ :

$$\sigma_N = \frac{F}{A_{max}} \quad (4.29)$$

$$\epsilon = \frac{h - h_0}{h_0} \quad (4.30)$$

Because the debonding mechanism of a soft confined adhesive layer is usually complex and is not a simple propagation of an axisymmetric crack from the edge toward the center, data from probe tests cannot be easily compared in a quantitative way to a model or to a simulation [Creton and Ciccotti 2016].

However, the shape of the stress-strain curve reveals details about the deformation mechanisms. Four main parameters can be extracted from the curve:

- the peak stress  $\sigma_{max}$ ,
- the maximum extension  $\epsilon_{max}$ ,
- the plateau stress  $\sigma_P$ ,
- the work of debonding  $W_{meas} = h_0 \int_0^{\epsilon_{max}} \sigma_N d\epsilon$ , which is the area under the loading curve multiplied by  $h_0$ ; it quantifies the dissipative processes in the bulk during the traction phase, which are the adhesive properties of the sample and the stored and/or dissipated energy by material deformation.

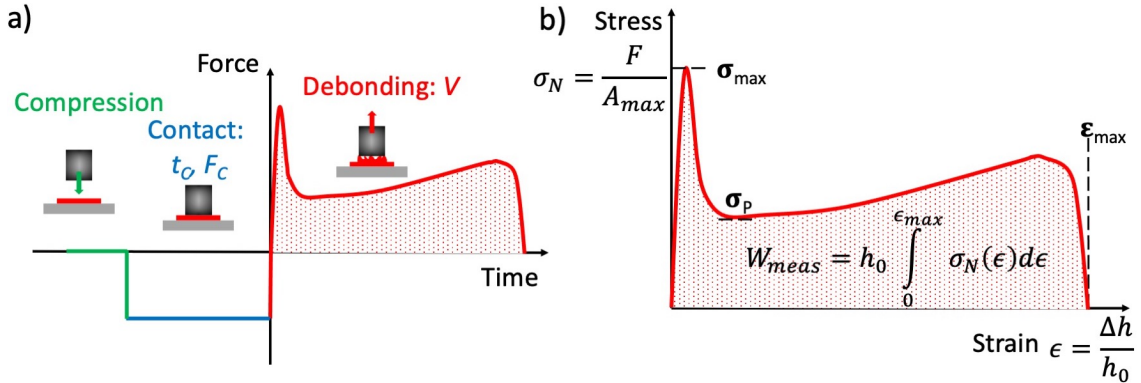


Figure 4.10: a) Schematic of a probe test used to test adhesion of soft materials, b) Normalized force-displacement curve typically obtained for a probe test and definition of the main parameters that can be extracted from it. Adapted from [Creton and Ciccotti 2016].

The nominal stress-strain curve obtained from the test can be compared for different materials and different test conditions providing significantly more information than the simple value of the peel force extracted from a traditional peeling test.

#### 4.4 Conclusion

The adherence tests review made above is not exhaustive, many other tests can be found in literature and tests can even be designed to model a specific application. As long as the deformation of the materials involved in these tests is monitored at different length scales and considered, an adhesion energy release rate independent of the test geometry could be estimated.

In our study, a user defined test, which is a combination between the JKR experiment and the probe tack test, will be implemented and detailed in the next chapter.

# Mechanical adherence tack test between crossed cylinders

*In this chapter, our mechanical adherence tack test between crossed cylinders is presented. The mechanisms that could be responsible for PTFE-PTFE adhesion are tested and discussed.*

## Contents

---

<b>5.1</b>	<b>Experimental setup</b>	<b>88</b>
5.1.1	Motivation	88
5.1.2	Setup design	88
5.1.3	Experimental protocol	90
<b>5.2</b>	<b>Macro-molecular chain movements</b>	<b>93</b>
5.2.1	Temperature as a mobility promoter	93
5.2.2	Time spent above melting: a mobility enhancement ?	98
<b>5.3</b>	<b>Crystallization</b>	<b>99</b>
5.3.1	Crystalline content	99
5.3.2	Secondary crystallization mechanism	99
5.3.3	Crystalline orientation	102
<b>5.4</b>	<b>Pressure</b>	<b>103</b>
5.4.1	Experimental protocol adjustment - force kept during cooling	103
5.4.2	Low and high contact pressures: temperature screening	104
5.4.3	Different fracture mechanisms above melting	106

---

## 5.1 Experimental setup

### 5.1.1 Motivation

All the adherence tests exposed in chapter 4 could be implemented to characterize the adherence between two thin PTFE cast films. However, some properties are restrictive such as the films high elongation up to 400 % [Chemfilm 2021]. To perform peeling tests or lap-shear tests, a flexible but stiff backing should be glued on PTFE films. Its role is to prevent the contribution of the deformation of the peeled free arm by limiting stretching in the traction direction. The chosen backing and glue should resist to temperatures up to PTFE melting ( $\sim 327^\circ\text{C}$ ) without any degradation. Moreover, succeeding in making the glue deposit perfectly homogeneous and flat is challenging; due to the low film thickness, changes in apparent surface roughness may appear. Appendix B shows some preliminary peeling tests, flat and large welding configurations focusing on PTFE composite films made of a polyimide matrix coated with fluorinated ethylene propylene and PTFE as an outside layer.

Consequently, the stiff baking strategy has not been chosen; the proposed approach is to reduce the bonded size to obtain limited film deformation. Experiments such as the probe tack test or Hertz or JKR tests deal with smaller bonded areas than peeling or lap-shear tests by putting in contact a probe on a surface. The choice of the probe geometry is important: a flat punch is not wanted for the reason exposed above, a sphere could be suitable but the films attachment on the sphere surface without any folds seems difficult. Hence, using cylinders appears more convenient since films could be easily wrapped around them. Such cylinders have already been implemented on the surface force apparatus (SFA) in a crossed configuration to study adhesion, friction and fracture between two substrates [Israelachvili and Adams 1976, Luengo *et al.* 1998, Maeda 2002, McGuiggan *et al.* 2007]. Other authors even implemented crossed cylinders geometry outside of a SFA [Suzuki *et al.* 2007, Sakasegawa *et al.* 2009]. From a geometrical point of view, a crossed cylinders configuration is equivalent to sphere-plane or sphere-sphere contact described by Hertz theory since the contact area is a disk, see Section 4.1.1.

The mechanical adherence tack test geometry selected is a crossed cylinders configuration where films are mechanically locked by metallic plates screwed on each cylinder side. This test is implemented on the Anton Paar MCR 502 rheometer allowing a precise measurement of both force (0 to 50 N) and displacement ( $\pm 1\ \mu\text{m}$ ) and equipped with a CTD450 oven with a temperature range from  $-150^\circ\text{C}$  to  $450^\circ\text{C}$  [AntonPaar 2011].

### 5.1.2 Setup design

#### From Hertz theory

##### Sizing

Following Hertz theory described in Section 4.1.1 and the equations given in Appendix A, a specific tack test geometry between crossed cylinders is designed.

Some specifications are required for our experimental setup, such as:

- the explored pressure range, from 5 to 100 MPa in order to scan the whole range used by the process,
- the contact area radius  $a$ , between 100 and 500  $\mu\text{m}$ , allowing eye and optical microscopy identification,
- the maximum load, 50 N is the maximum sustainable by the rheometer [AntonPaar 2011]; for safety reasons, a 45 N limit is chosen.

As a first approach, the film soft layer of low thickness is neglected. A pure steel/steel contact is considered with Young modulus  $E_{steel} = 200$  GPa and Poisson's ratio  $\nu_{steel} = 0.3$  [materials no date]. Following equations in Appendix A (A.4 and A.6), the pressure distribution in the contact zone (equation A.2) is calculated for three cylinder radii and given forces such as satisfying the specifications mentioned above, see Figure 5.1.

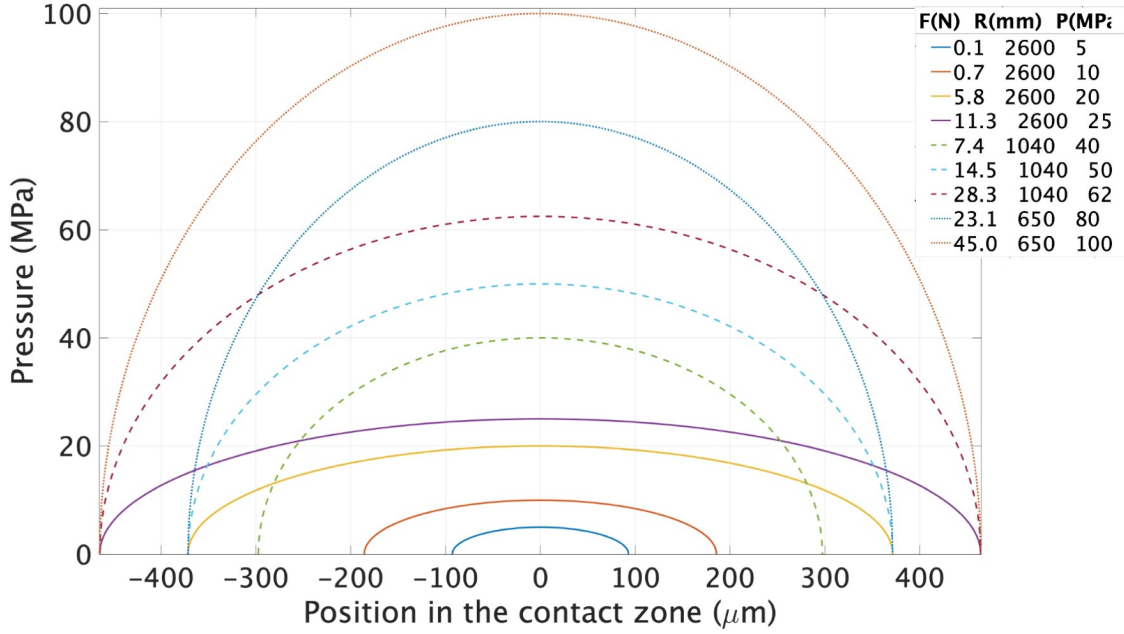


Figure 5.1: Pressure distribution in the contact zone according to Hertz theory between crossed cylinders (equivalent to sphere-plane configuration) for three different sphere radii of curvatures  $R$ . Line:  $R = 2600$  mm, dashes:  $R = 1040$  mm, dots:  $R = 650$  mm.

Three curved supports with curvature radii of 650 mm, 1040 mm and 2600 mm have been manufactured by Vuichard company by electrical discharge machining wire cutting allowing an average roughness lower than  $0.2 \mu\text{m}$  on the metallic part close to the contact zone. This low roughness is specified to limit as much as possible mechanical anchorage between PTFE and metal, especially above melting.

The designs for the whole setup (curved support and maintaining plates) are available in Appendix C Figures C.1, C.2 and C.3 for the  $R = 650$  mm configuration.

### First test

A first test is performed following the experimental protocol exposed hereafter, see Section 5.1.3. Parameters are chosen such as the "best welding" is likely to occur: two white cast films are put in contact for  $t_c = 60$  s at  $T_c = 375^\circ\text{C}$  with a normal force  $F_N = 10$  N, supposed to reach a pressure at the center zone of 60 MPa and a radius of the contact zone  $a = 280 \mu\text{m}$  according to the Hertz calculation presented here above.

During this test, debonding is not occurring; films are deforming and no interfacial fracture happens, see Figure 5.2. Moreover, the debonding force peak is saturating at 50 N which is the rheometer load cell limit, see Figure 5.2. The welded zone in this experiment seems to be a square of 10 mm side length corresponding to the total width of the support; the curvature seems too large to have any effect. Since PTFE elastic modulus is way smaller than the steel one considered for our setup design here above, PTFE films can

deform under compression and maybe compensate the support curvature; leading to a configuration close to a flat squared punch.

Consequently, a new design, where debonding in such conditions can happen, has to be proposed.

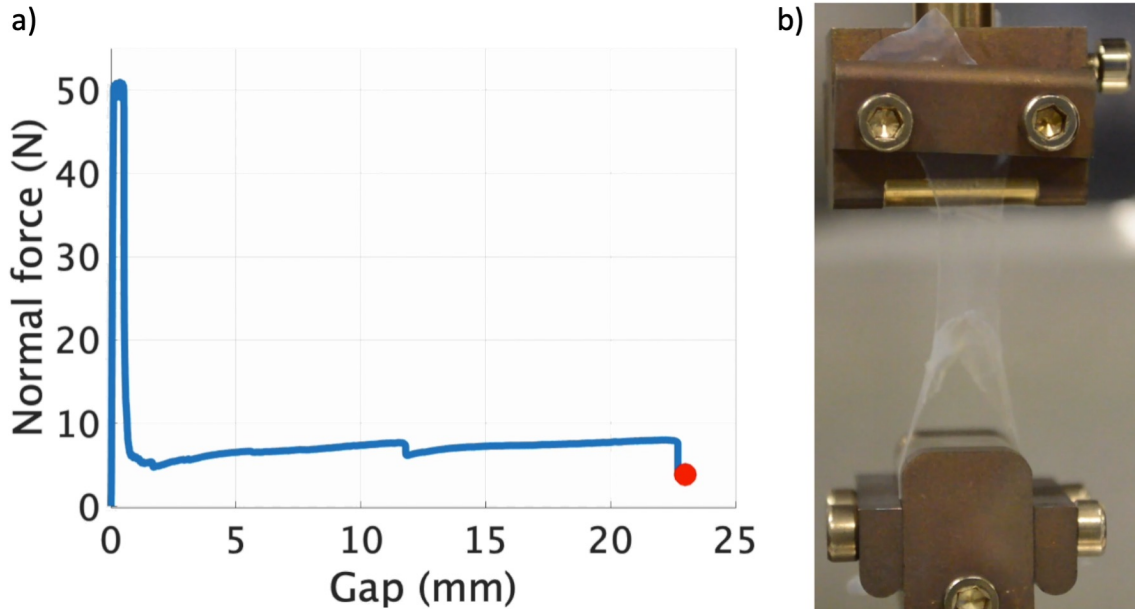


Figure 5.2: Mechanical adherence tack test with sintered-sintered sides in contact. a) Normal force evolution during debonding for two white PTFE cast films welded at  $T_c = 375^\circ\text{C}$  during  $t_c = 60$  s under  $F_N = 10$  N contact normal force. b) Debonding is not occurring, the films are deforming.

### New design

The new design consists on a sharp curvature of  $R = 2.5$  mm, see Figure 5.3b. By decreasing the contact size, the peak force during debonding should decrease and less film deformation should occur. This new design does not obey Hertz contact theory: the pressure cannot be estimated a priori. Visualizing and measuring the contact zone size a posteriori could give hints about the pressure imposed during welding. The design of this new curved support is available in Appendix C Figure C.4.

### 5.1.3 Experimental protocol

Dry lubricant (molybdenum di-sulfur in suspension in acetone) is sprayed on the two curved supports designed in the previous section to ensure the least adhesion between PTFE films and steel supports. After two hours waiting for solvent evaporation, the supports are cleaned with a soft cloth to remove the possible lubricant agglomerates and inhomogeneities.

Then, the supports are set in a crossed configuration on an Anton Paar MCR 502 (or 302) rheometer thanks to a PP08 upper shaft (parallel plate of 8 mm diameter, commercially available) and an on-demand lower shaft equipped with a thermocouple. A black picture background is put behind and a camera Nikon D3200 equipped with a macro lens (Sigma

EX DG Macro 105 mm) is placed in front of the setup. For a better video recording quality, a lamp is directed towards the contact zone, see Figure 5.3a.

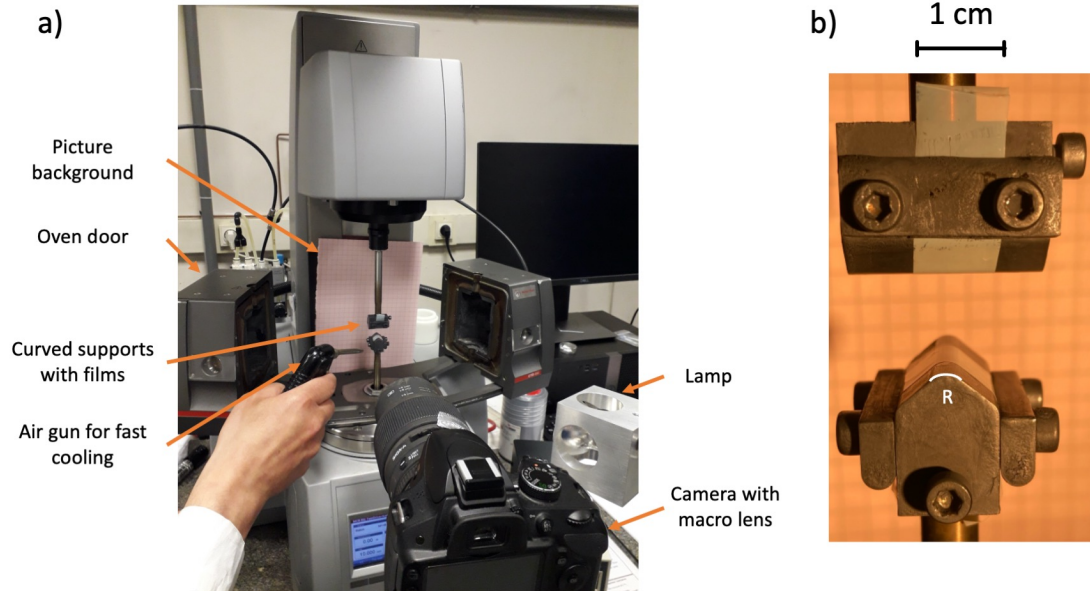


Figure 5.3: Mechanical adherence tack test between crossed curved surfaces implemented on a rheometer. a) Whole setup, b) Zoom on the new design supports with PTFE white cast film as mounted,  $R = 2.5$  mm is the support radius of curvature.

The zero gap initialization is performed at the bonding temperature. After the setup cooled down to room temperature, two white PTFE cast films cut with a punch in a rectangular shape of 10 per 100 mm are mounted such that their sintered sides will be in contact, see Figure 5.3b. As mentioned in [Wan and Dillard 2003] and [Wan and Kogut 2005] who modeled the delamination of a thin flat elastic circular membrane from a rigid punch, the membrane initial tension is an important parameter to control in order to obtain reproducible results during debonding. With the help of a paperclip and a 5 N spring balance, see Figure 5.4a, a tension of 2 N is imposed on each film. This value is in the material elastic domain, see Section 3.3.2 and close to the values used during the welding process in the plant. As expected, regulating the film initial tension improves the results reproducibility, see Figure 5.4b but some variations in term of curve shape, maximum force or maximum gap can still occur. All along this chapter, no average between reproduced tests is calculated: all the extracted raw data are shown.

Once the oven is closed, an automatic force and temperature controlled sequence is launched on the rheometer software, see Figure 5.5. Without any contact, the temperature is increased until the desired bonding temperature  $T_c$  and a five minutes soak time is set to ensure a uniform temperature. Then, contact is realized by imposing a given compressive normal force  $F_N$  for a given contact time  $t_c$  as depicted by the green step on Figure 5.5. After bonding, the oven is open and fast cooling is achieved with an air gun while the compressive normal force is either kept or fixed to 0 N. Back to room temperature, the debonding step recorded by the camera starts: the upper shaft moves at a constant speed of  $V = 20 \mu\text{m/s}$  towards the top; force and gap values are saved every 0.04 s corresponding to the camera frame rate of 25 fps until weld breakage. Films are carefully unmounted and

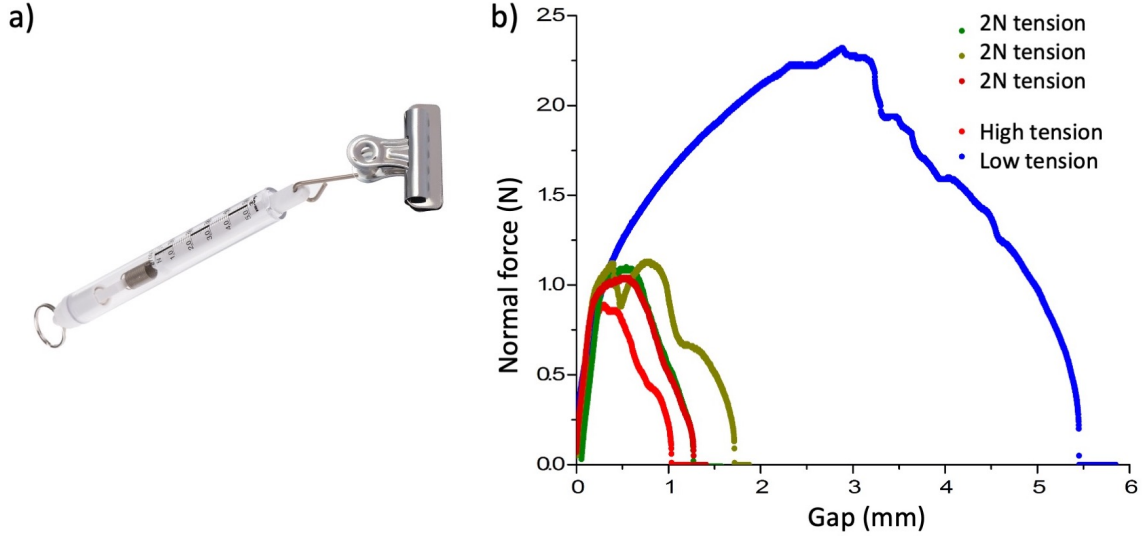


Figure 5.4: Mechanical adherence tack test - film tension control. a) Spring balance and paperclip used to impose a 2 N tension on PTFE cast films mounted on curved supports, b) Experimental evidence of reproducibility enhancement during debonding by film initial tension control. Contact parameters:  $R=2.5$  mm,  $F_N = 0.2$  N,  $t_c = 6$  s,  $T_c = 375^\circ\text{C}$ .

stored for further microscopic examination. An optical microscope - Zeiss Axio Imager 2 - is used in reflective light to obtain magnified images of PTFE films fractured surfaces. It allows to measure the size of the contact zone and estimate the minimum pressure applied during bonding.

From the values recorded during debonding, a typical debonding curve (Figure 4.10b [Creton and Ciccotti 2016]) can be plotted; our main analyze parameters are:

- the peak force  $F_{max}$
- the maximum gap  $U_{max}$  between the two films,
- the radii of top and bottom fractured surfaces measured by optical microscopy  $a_{top}$  and  $a_{bottom}$ ,
- the measured work or macroscopic work of adhesion  $W_{meas}$  per unit area, corresponding to the area below the force versus gap curve normed by the average contact size area:

$$W_{meas} = \frac{\int_0^{U_{max}} F dU}{\frac{\pi}{4}(a_{top} + a_{bottom})^2} \quad (5.1)$$

This protocol is implemented to explore the effect of contact temperature, contact time and pressure on the adhesive properties between two PTFE cast films and to identify the involved mechanisms.

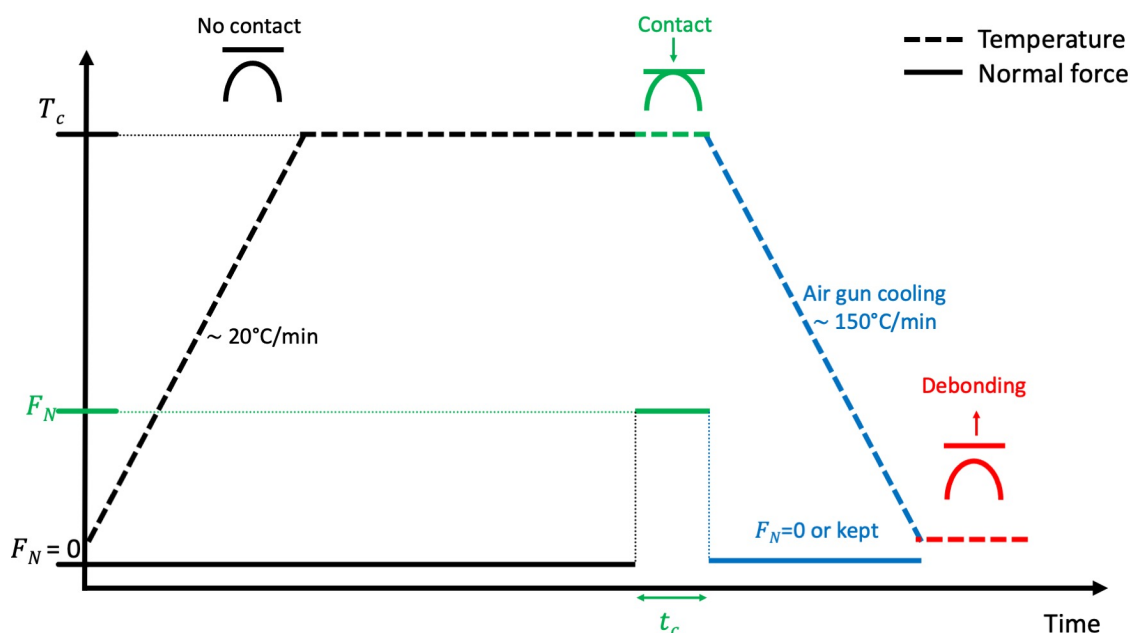


Figure 5.5: Mechanical adherence tack test between crossed cylinders experimental protocol: temperature (top curve) and normal force (bottom curve) time evolution.

## 5.2 Macro-molecular chain movements

Macro-molecular chain interdiffusion forming an interphase between the two polymeric materials in contact is a physical mechanism responsible for polymer-polymer adhesion enhancement [De Gennes 1992]. Depending on the applied temperature, the macro-molecular chain mobility can be triggered: close to the melt, more mobility is allowed. The interphase formation between two PTFE films is also time dependant: PTFE macro-molecular chain diffusion characteristic time have been identified long but chain segments motions are expected at smaller time scales, see Section 3.4.

### 5.2.1 Temperature as a mobility promoter

White PTFE cast films are tested on our custom mechanical adherence tack test setup. Bonding is performed for  $t_c = 6$  s with  $F_N = 0.2$  N at various temperatures from 250 to 375°C. During cooling, the normal force is set to zero such that contact is kept without any more pressure applied.

An illustration of the debonding force versus gap for different bonding temperatures is depicted on Figure 5.6. When the contact temperature increases, the maximum debonding force increases (see Figure 5.7 filled circles) as well as the gap at break. On the pictures taken all along debonding at  $T_c = 375^\circ\text{C}$ , the films are stretched and forming a sand-glass shape. At  $T_c = 250^\circ\text{C}$ , the pictures reveals no significant deformation. Thus, the adhesion obtained at 375°C bonding temperature is better.

Looking at the fractured surface micrographs obtained by optical microscopy in Figure 5.8a, whatever the contact temperature is, the circular contact zone is detected: films become transparent in this area since the unsintered PTFE layer is deposited on the metallic support. At bonding temperatures above melting, the stretched area outside the contact zone is quite large and folds seem to appear at the outside edge. The fractured surface

shape is close to an asymmetric cone out of plane. Considering the short depth of field, the chosen focus is on the edge of the largest contact zone circle.

The evolution of the fractured surface radii measured by optical microscopy with bonding temperature is depicted on Figure 5.9 for both the top (filled symbols) and bottom (empty symbols) films. Without considering the films (only pure steel), Hertz theory (see Equation A.6) predicts in these experimental conditions a contact size radius of  $\sim 12 \mu\text{m}$ ; the measured radii are in the order of  $400 \mu\text{m}$ . This discrepancy could be due to the film acting as a soft intermediate layer thus more able to deform and not considered is Hertz model. Both films contact sizes (top and bottom) are expected equal but from the measurements, the bottom contact size is always larger than the top one. This could be explained by the effect of gravity and measurements uncertainties. With contact temperature  $T_c$  increase, the contact size radius increases: the films are more able to deform at high temperatures since their modulus is falling, see section 3.3.1.

From the area below the force versus gap curves in Figure 5.6, the measured work or macroscopic work of adhesion can be calculated: results are depicted on Figure 5.10. With bonding temperature increase, the measured work  $W_{meas}$ , see Equation 5.1, increases significantly from  $325^\circ\text{C}$  up to  $340$  and  $375^\circ\text{C}$  where a plateau seems to be reached. This behaviour can be related to the melting in progress: the percentage of melted crystallites depicted on Figure 5.10 bottom is obtained from a step by step integration of the second melting peak in black on Figure 3.10 performed on raw dispersion. The global crystalline content is supposed to depend on the crystallization cooling speed; however, for the range of cooling speed achievable with our setup, almost no variation is expected, see Figure 3.16. Thus, the highest the area below the force versus gap curve, the highest the measured work: increasing contact temperature induces an improvement of PTFE-PTFE films adhesion quality. However, the measured work is a combination of the work to propagate the interfacial crack and the work to deform the bulk material. As depicted by the pictures on Figure 5.6 the level of deformation is highly dependent on the bonding temperature: comparing the raw measured work to assess PTFE adhesive properties is a delicate issue.

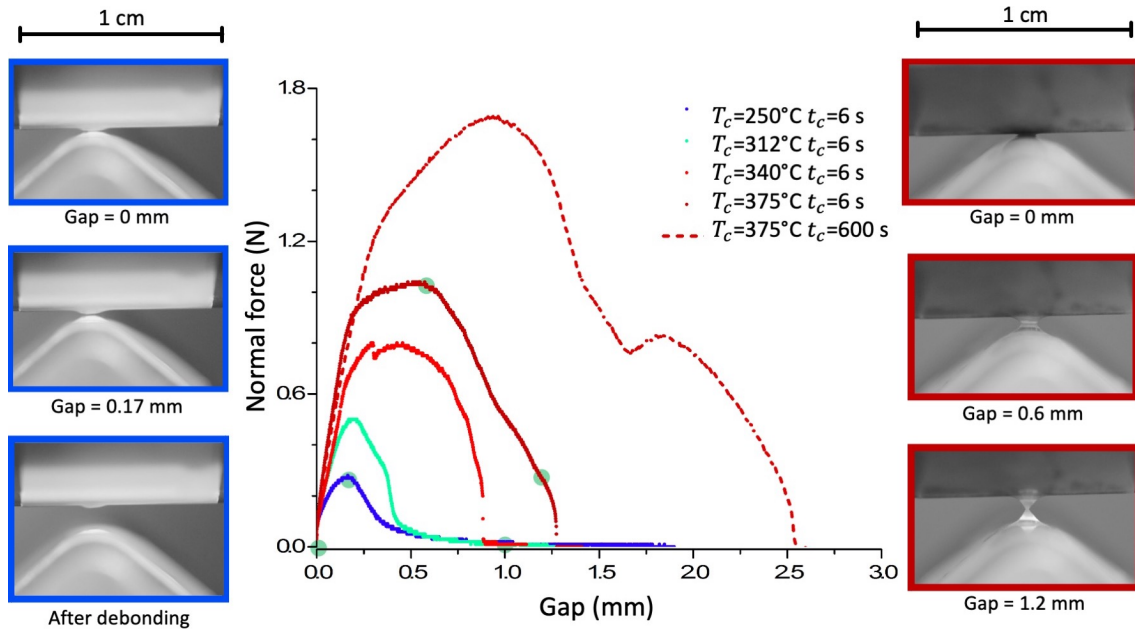


Figure 5.6: Debonding force versus gap for  $F_N = 0.2$  N bonding normal force and for different bonding temperatures  $T_c$  and contact times  $t_c$ : 250, 312, 340 & 375°C - continuous lines for 6 s contact time and in dotted line, 600 s contact time at 375°C; the setup used has a radius of curvature  $R=2.5$  mm. Pictures illustrates the film behaviour for 6 s contact time at 250 and 375°C at different gaps, big green dots indicate the pictures position on the force versus gap curves.

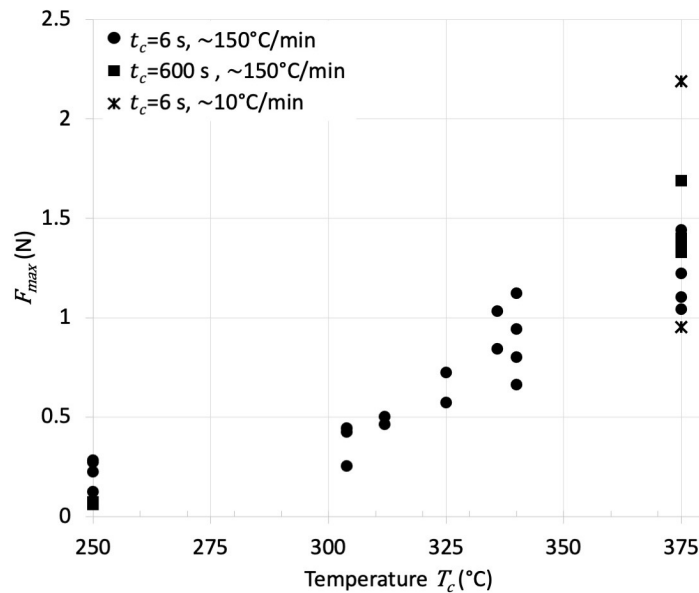


Figure 5.7: Maximum force during debonding evolution with bonding temperature  $T_c$  for  $t_c = 6$  s (circles) and  $t_c = 600$  s (squares) contact time with air gun cooling ( $\sim 150^\circ\text{C}/\text{min}$ , filled symbols). The slow cool conditions (stars) corresponds to  $t_c = 6$  s and cooling at  $10^\circ\text{C}/\text{min}$ . The bonding normal force is always  $F_N = 0.2$  N and the setup used has a radius of curvature  $R=2.5$  mm.

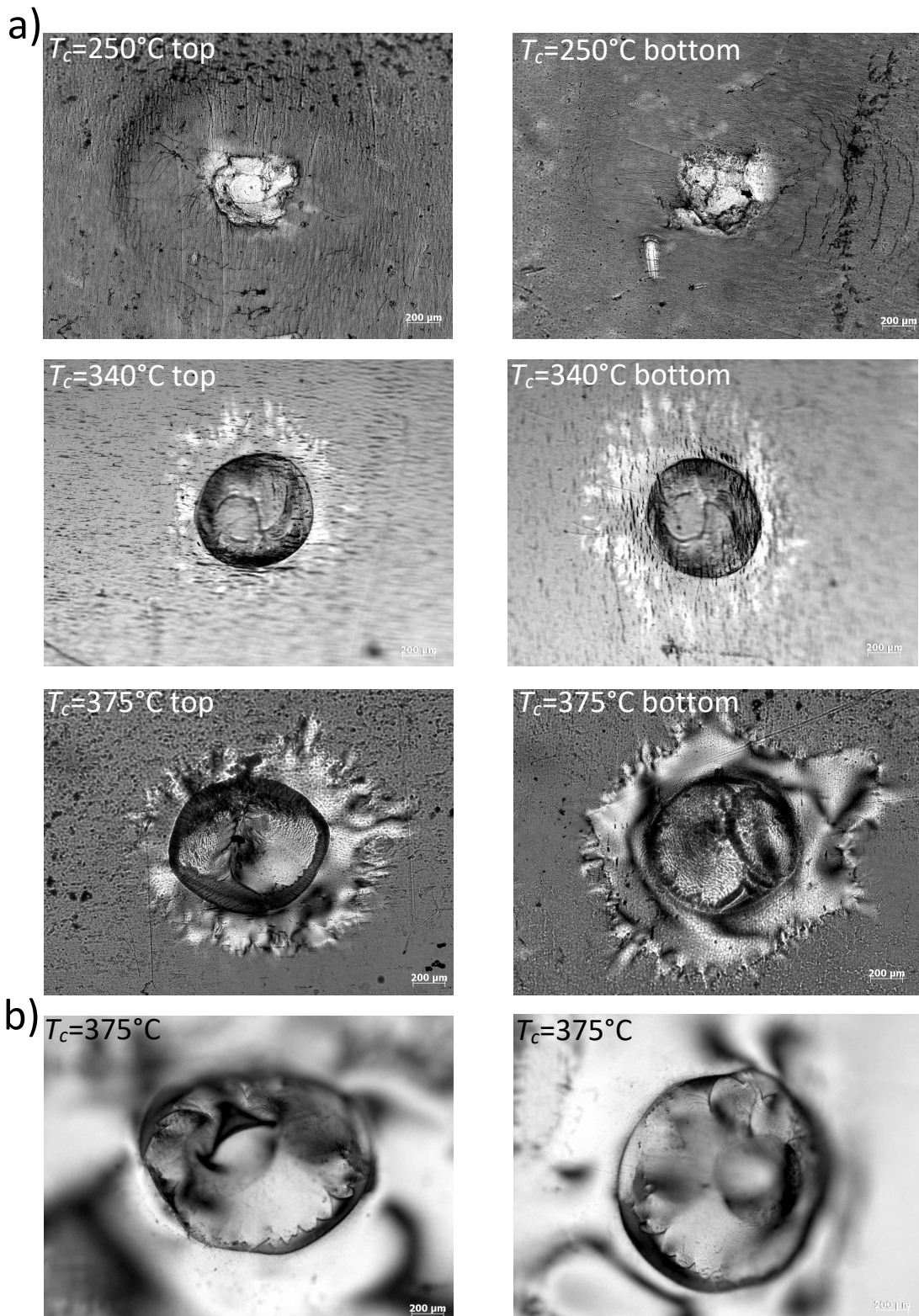


Figure 5.8: Optical micrographs of the fractured surfaces for various bonding temperatures  $T_c$ . First column top film, second column bottom film. a)  $t_c = 6$  s, b)  $t_c = 600$  s. The bonding normal force is always  $F_N = 0.2$  N and the setup used has a radius of curvature  $R=2.5$  mm. The contact area can be approximated by a disk.

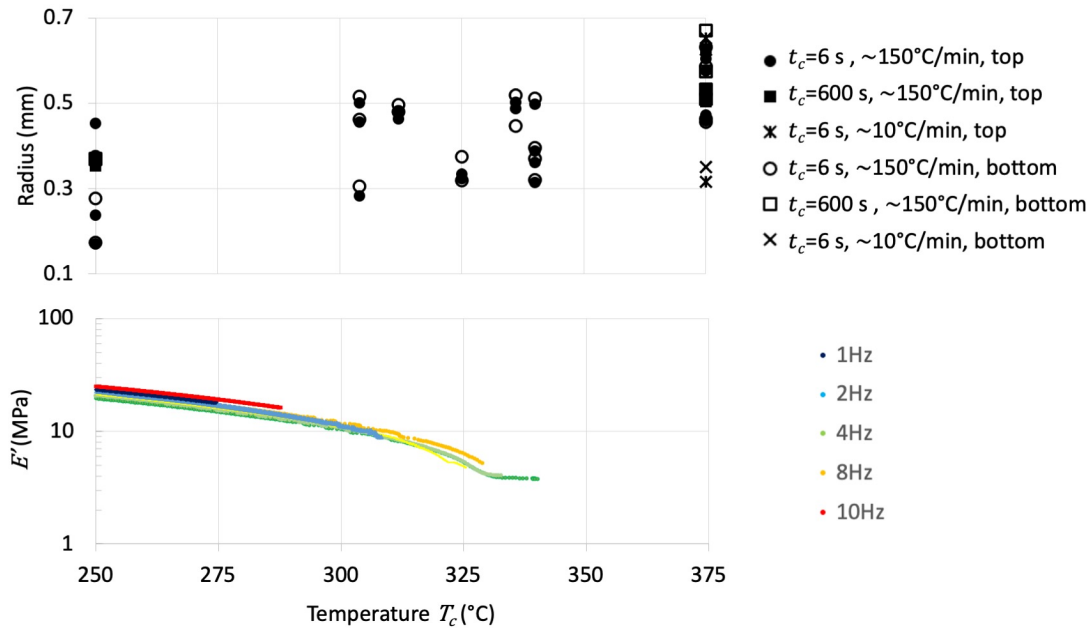


Figure 5.9: Top: fractured surface radius evolution with bonding temperature for  $t_c = 6$  s (circles) and  $t_c = 600$  s (squares). Rapid cooling ( $\sim 150^\circ\text{C}/\text{min}$ ) is performed with air gun and the slow cool conditions (stars) corresponds to  $t_c = 6$  s and cooling at  $10^\circ\text{C}/\text{min}$ . Filled symbols correspond to the top film and empty symbols to the bottom film. The bonding normal force is always  $F_N = 0.2$  N and the setup used has a radius of curvature  $R=2.5$  mm. Bottom: storage modulus evolution with temperature obtained by DMA in tension.

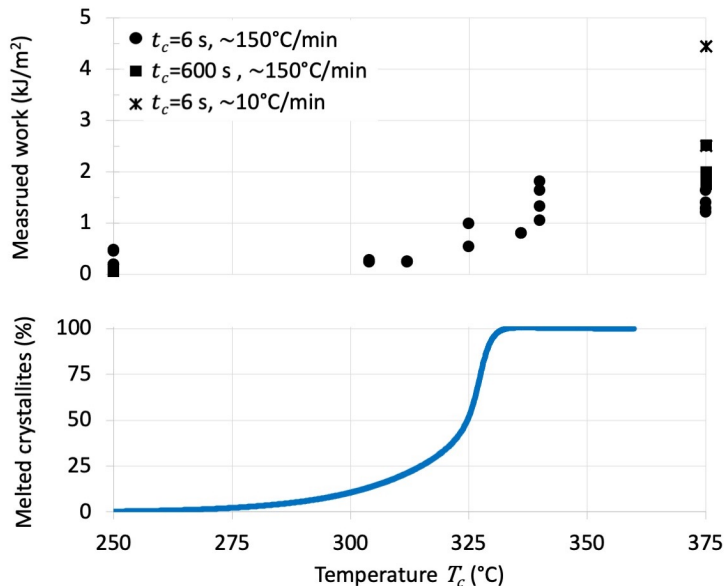


Figure 5.10: Measured work (top) and crystalline amount melted (bottom) evolution with bonding temperature  $T_c$  for  $t_c = 6$  s (circles) and  $t_c = 600$  s (squares) contact time. Rapid cooling ( $\sim 150^\circ\text{C}/\text{min}$ ) is performed with air gun and the slow cool conditions (stars) corresponds to  $t_c = 6$  s and cooling at  $10^\circ\text{C}/\text{min}$ . The bonding normal force is always  $F_N = 0.2$  N and the setup used has a radius of curvature  $R=2.5$  mm.

### 5.2.2 Time spent above melting: a mobility enhancement ?

Increasing the contact time above melting should allow more macro-molecular chain or segment motions and thus a larger interphase thickness between the two films leading to a better anchorage and adhesion. Mechanical adherence tack tests are performed as in the previous section at 250 and 375°C bonding temperatures  $T_c$  with  $t_c = 600$  s contact time. No significant change is expected between  $t_c = 6$  and  $t_c = 600$  s at  $T_c = 250^\circ\text{C}$ .

The debonding force versus gap curves for both times are depicted in Figure 5.6 in dark red for  $T_c = 375^\circ\text{C}$ . Both the gap at break and the area below the curve are increased; the curve shape also changes: a shoulder appears after the maximum force as if a peeling plateau would be reached.

Looking at the fractured surface micrographs obtained by optical microscopy, see Figure 5.8, for both contact times above melting, the fractured surface shape is close to an asymmetric cone out of plane. As indicated by the large unfocused areas, the cone height is greater for the longest contact time; its value is almost double for  $t_c = 600$  s as shown by the values of the gap at debonding in Figure 5.6.

The results of the maximum force at debonding (Figure 5.7), fracture surface radius (Figure 5.9) and measured work (Figure 5.10) are depicted by squared symbols for  $t_c = 600$  s. None of these analyze parameters show notable change for  $t_c = 600$  s at  $T_c = 375^\circ\text{C}$ .

Consequently, in this range of contact time ( $t_c = 6$  and 600 s), PTFE macro-molecular chain segment mobility, which could have an impact on the adhesive properties, is not significant. As shown in section 3.4, the macro-molecular chain diffusion characteristic time is very long but chain segments motions are expected at smaller time scales; healing experiments performed up to  $10^4$  s give hints of such motions.

## 5.3 Crystallization

In semi-crystalline polymers, when interfacial chain diffusion is incomplete, crystallites constituted of chains from each side of the interface can be formed through the interface during cooling [Xue, T. A. Tervoort, Rastogi, *et al.* 2000]. This phenomenon known as co-crystallization phenomenon takes part in interface consolidation [Yuan *et al.* 1990, Gent, E.-G. Kim, *et al.* 1997]. In the following, the impact of the crystalline content, the crystallization mechanism and the macromolecular chain orientation is investigated.

### 5.3.1 Crystalline content

The previous mechanical adherence tack tests performed for  $t_c = 6$  s at  $T_c = 375^\circ\text{C}$  with a rapid cooling thanks to an air gun leading to a cooling rate from 375 down to  $200^\circ\text{C}$  (where all the recrystallization already happen, see Figure 3.15) close to  $150^\circ\text{C}/\text{min}$  are compared with slow cooling rate experiments where the oven closed and a cooling rate of  $10^\circ\text{C}/\text{min}$  is imposed. The slowest the cooling, the highest the crystalline content should be since more time and more motion is allowed for the macro-molecules to rearrange in crystallites [Bosq *et al.* 2013].

Slow cooling rate results are depicted by stars symbols on Figures 5.7, 5.9 and 5.10. Whatever the cooling rate is, both maximum force and fractured surface radii show no significant variation; the measured work appears slightly higher in slow cooling conditions. To know if this trend is in the range of experimental errors or not, Dynamic Scanning Calorimetry experiments are performed at the two cooling rates to assess the corresponding change in global recrystallized amount, see Section 3.2.3. No significant change in global recrystallized content  $\chi$  can be deduced between  $10^\circ\text{C}/\text{min}$  and  $150^\circ\text{C}/\text{min}$  cooling rates. If there is a variation in global recrystallized content, it is too low to be detected; therefore it could have some impact on the adherence properties but they are not enhanced by our experiments. Choosing two cooling rates with a larger gap could help investigating this hypothesis since the recrystallized amount would have more distant values, see Figure 3.16.

### 5.3.2 Secondary crystallization mechanism

Two crystallization mechanisms have been identified and discussed in section 3.2.3 for PTFE. Here, the scope is on investigating the impact on the secondary crystallization content on PTFE adhesion properties. On the previous tests performed with ambient debonding, different bonding temperatures  $T_c$  were tested among them: 250, 304 and  $312^\circ\text{C}$ , see Figure 5.10. On Figure 3.15, these temperatures respectively correspond to different secondary crystallites amount melted: respectively, 0,  $\sim 50$  and close to 100%. These temperatures are superimposed with the material progressive melting, thus to conclude on the effect of secondary crystallites on adhesion, melting and crystallinity must be decorrelated.

In this aim, mechanical adherence tack test are performed for  $t_c = 6$  s at  $T_c = 312^\circ\text{C}$ , temperature at which all secondary crystals are melted, and **debonding at various temperatures**, obtained with the oven closed and slow cooling rates (lower than  $10^\circ\text{C}/\text{min}$ ):

- **$312^\circ\text{C}$**  no recrystallization at all,
- **$304^\circ\text{C}$**  half secondary crystallization content is recrystallized,
- **$250^\circ\text{C}$**  all secondary crystallization content is recrystallized.

Thus, a good adhesion is expected at a debonding temperature of  $250^\circ\text{C}$ .

These experiments are implemented on the curved supports of radius  $R=650$  mm since the recorded force signal is too low with  $R=2.5$  mm setup in the conditions where the highest adhesion is expected, see Figure 5.11. During cooling the normal force is set to zero such as contact is kept but no more pressure is applied.

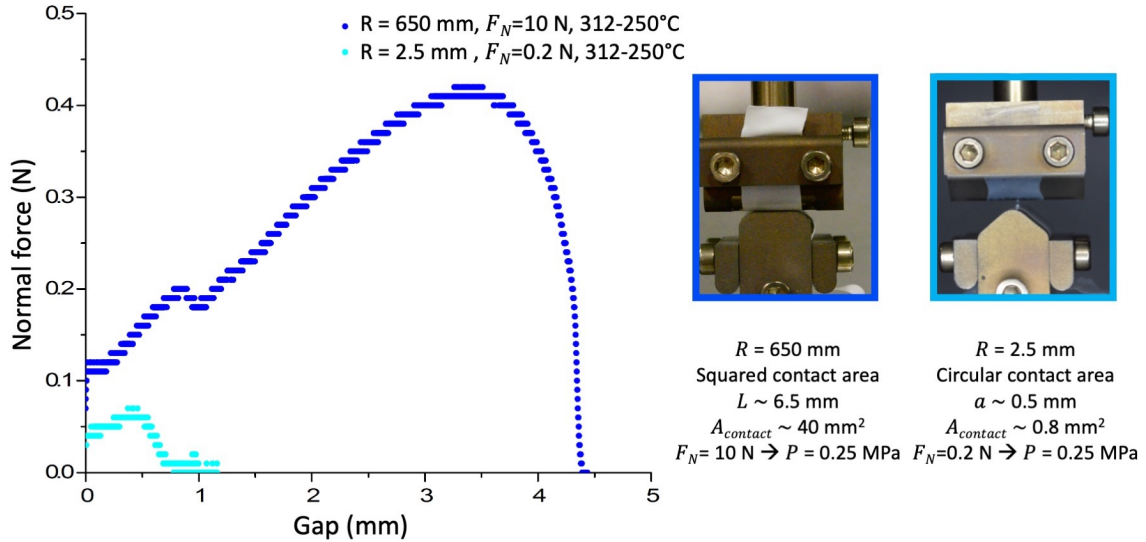


Figure 5.11: Two curved supports geometries available. In conditions such as the estimated pressure is in the same range ( $R=650$  mm  $F_N = 10$  N,  $R=2.5$  mm  $F_N = 0.2$  N), for  $t_c = 6$  s,  $T_c = 312^\circ\text{C}$  and  $T_{debonding} = 250^\circ\text{C}$  where the highest adhesion is expected, the recorded force signal is too close to the sensor limit for the small contact area setup in light blue.

The evolution of the force versus gap during debonding is depicted on Figure 5.12 left for the three debonding temperatures. Whatever the debonding temperature is, the maximum force is of the same order around 0.45 N. When decreasing the debonding temperature, the gap at break and the area below the curve decrease, see Figure 5.12. Between 250 and 312°C, PTFE cast films have a storage modulus in tension falling from 25 to 8 MPa as measured before by Dynamic Mechanical Analysis, see Section 3.3.1 and Figure 5.12 right last line. Since the film mechanical properties in tension are varying in the temperature range of interest, the recorded response contains both film stretching and interfacial strength change due to different recrystallization amount.

To conclude, no clear signature of the impact of the secondary crystallization amount on adhesion is detected in this experiment.

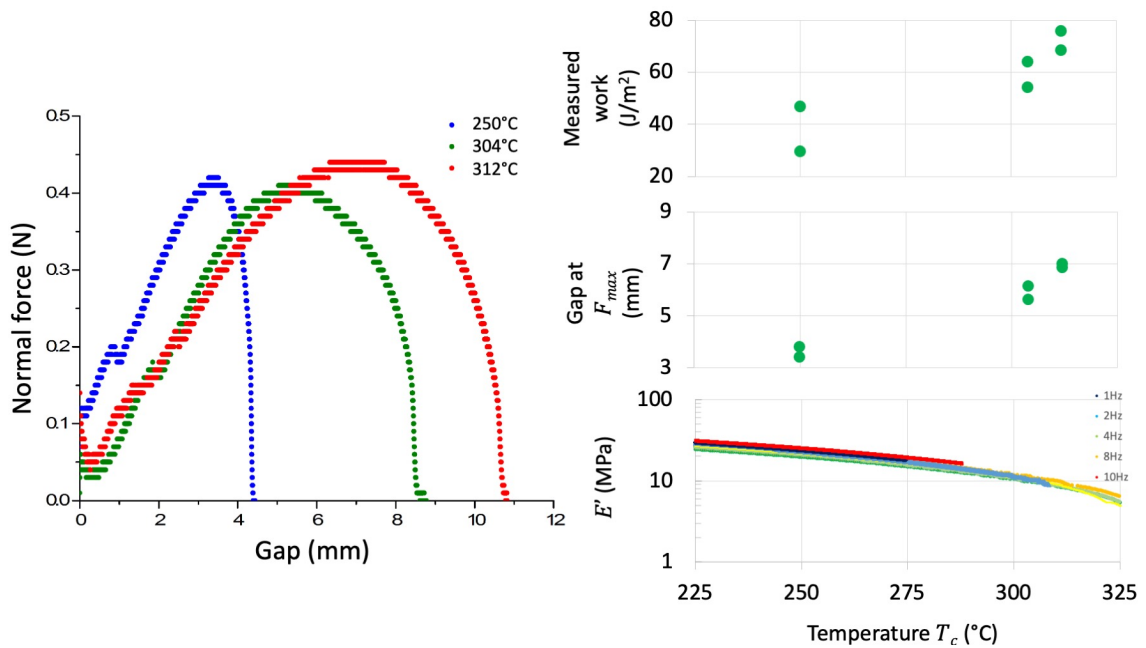


Figure 5.12: Debonding in temperature results for  $t_c = 6$  s contact time at  $T_c = 312^\circ\text{C}$  to investigate the impact of secondary crystallization mechanism on the adhesion properties. The R=650 mm setup is used with  $F_N = 10$  N. Left: force versus gap for 3 debonding temperatures (250, 304 &  $312^\circ\text{C}$ ) obtained for slow cooling rates (lower than  $10^\circ\text{C}/\text{min}$ ), right: measured work and gap at maximum force evolution with debonding temperature as well as storage modulus evolution with temperature obtained by DMA in tension.

### 5.3.3 Crystalline orientation

As shown in Section 3.2.2, full density extruded PTFE films have a clear crystalline privileged orientation in the machining direction. When mounting samples on the tack curved supports, two configurations can be set up: either crystallites from both films in a parallel or in perpendicular orientation. To create an interfacial crystalline structure in between the two films during the bonding step, more energy may be needed for the rearrangement of the perpendicular configuration since the crystalline orientation is  $90^\circ$  between each films. With the same bonding parameters, the adhesion should be less important in the perpendicular configuration than in the parallel one.

Two samples of full density extruded PTFE films are tested on our home-made mechanical adherence tack test setup with curved supports of radius 650 mm in each configuration. The film initial tension is not controlled. Bonding is performed for  $t_c = 1$  min with  $F_N = 10$  N at  $T_c = 312^\circ\text{C}$ . During air gun cooling the normal force is set to zero such as contact is kept but no more pressure is applied. By performing the bonding at  $T_c = 312^\circ\text{C}$ , a partial mobility of the crystalline structure is allowed: only secondary crystals should be melted and consequently, no high bonding is expected.

The resulting debonding curve of the force versus gap is shown on Figure 5.13 as well as pictures taken all along the test for one representative sample in each configuration. In the parallel configuration, debonding occurs at a gap close to 5 mm whereas for the perpendicular orientation, debonding is not possible up to the maximum gap of 25 mm: films are stretched and no interfacial fracture propagates. This result is not in accordance with the above hypothesis and expected result. An explanation could be the change in the mechanical properties of the film due to the material structure anisotropy.

Concluding on the adherence properties relative to different crystalline orientations in this experiment is not possible: changes in the mechanical properties, mainly stretching, resulting from the material structure anisotropy are dominant.

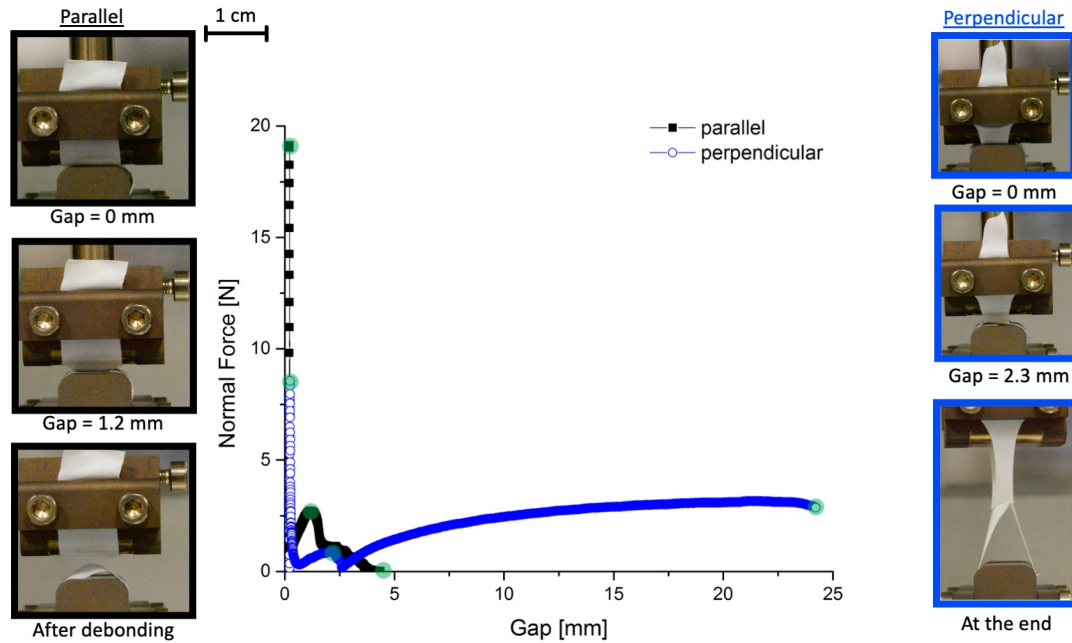


Figure 5.13: Full density PTFE extruded film mechanical adherence tack test  $R = 650$  mm,  $F_N = 10$  N,  $t_c = 1$  min,  $T_c = 312^\circ\text{C}$  parallel and perpendicular crystalline orientation, cooling performed with air gun. For both orientation, pictures on the sides depict film behaviour all along testing; big green dots indicate the pictures position on the force versus gap curves. Note that the film initial tension is not controlled in these experiments.

## 5.4 Pressure

In the previous sections, experiments were performed to investigate the mechanisms which could be involved in polymer/polymer adhesion: macro-molecular chain diffusion and co-crystallization. In this section, the pressure effect is explored in the "best" welding conditions where the contact force is kept during cooling to insure intimate contact quality and bonding is achieved at a temperature above melting.

### 5.4.1 Experimental protocol adjustment - force kept during cooling

All the mechanical adherence tack tests results exposed until now were implemented with a zero normal force imposed during cooling such that the films stay in contact but not under compression. To check if the intimate contact quality is affected or not by the gap increase during cooling or if debonding is initiated during cooling, experiments are implemented at  $T_c = 375^\circ\text{C}$  and  $F_N = 0.2$  N kept during cooling. Results are depicted with diamonds symbols when normal force is maintained during cooling and circles when it is not on Figures 5.14, 5.15, 5.16. The maximum force, the fractured surface radius and the measured work are in the same range whatever the normal force is kept or not during cooling (see black circles vs grey diamonds).

Assuming that the contact is well maintained when imposing zero normal force during cooling seems valid. By precaution, the next experiments are performed by keeping the force during cooling.

### 5.4.2 Low and high contact pressures: temperature screening

Until now, only  $F_N = 0.2$  N has been applied between PTFE films, leading to a minimum pressure below 1 MPa, see Figure 5.15 black and grey points. It should be kept in mind that the pressure estimated here is a lower bound: contact normal force is normalized by the largest contact area observed on the fractured surfaces by optical microscopy. Moreover, due to the crossed cylinders geometry, the pressure distribution is not constant in the contact zone; a maximum is reached at the center and decreasing progressively towards the border similarly to the Hertz pressure distribution on Figure 5.1. To evaluate the impact of contact pressure on the adhesive properties, mechanical adherence tack tests are performed with  $F_N = 30$  N leading to a minimum pressure close to 10 MPa; between the two experimental series, an order of magnitude difference in pressure is present.

The maximum force during debonding evolution with bonding temperature is plotted on Figure 5.14: it is almost constant until  $T_c = 250^\circ\text{C}$  and then increasing more rapidly than for  $F_N = 0.2$  N. The fractured surface average radius is larger than for  $F_N = 0.2$  N, see Figure 5.15: more deformation occurs under high load and thus, the contact zone is larger; the contact zone size increases with melting previously mentioned is still noticeable. Consequently, the minimum pressure is around 20 MPa before  $T_c = 312^\circ\text{C}$  and then it falls between 8 to 10 MPa, which is still higher than the pressure obtained with  $F_N = 0.2$  N. The calculated measured work is depicted on Figure 5.16: with bonding temperature increase, the measured work is increasing significantly from  $312^\circ\text{C}$  up to  $340$  and  $375^\circ\text{C}$  where a plateau value seems to be reached. This behaviour could be related to the melting in progress. Specifically, the rapid rise in the percentage of melted crystallites and measured work between  $275$  and  $340^\circ\text{C}$  appears correlated, see Figure 5.16. Thus, increasing contact temperature induces a significant improvement of PTFE-PTFE films adhesion quality in the range of contact normal force tested.

With  $F_N = 30$  N, the untested temperature range from  $25$  to  $250^\circ\text{C}$  has been explored: as expected, no significant change is recorded in this range; the maximum force during debonding, the fractured surface radius and the measured work are all constant at low values. Almost no adhesion is noticed in this temperature range below melting.

Clearly, pressure plays a significant role in the quality of adhesion. Now, let's look at extreme pressure case and its effects above melting.

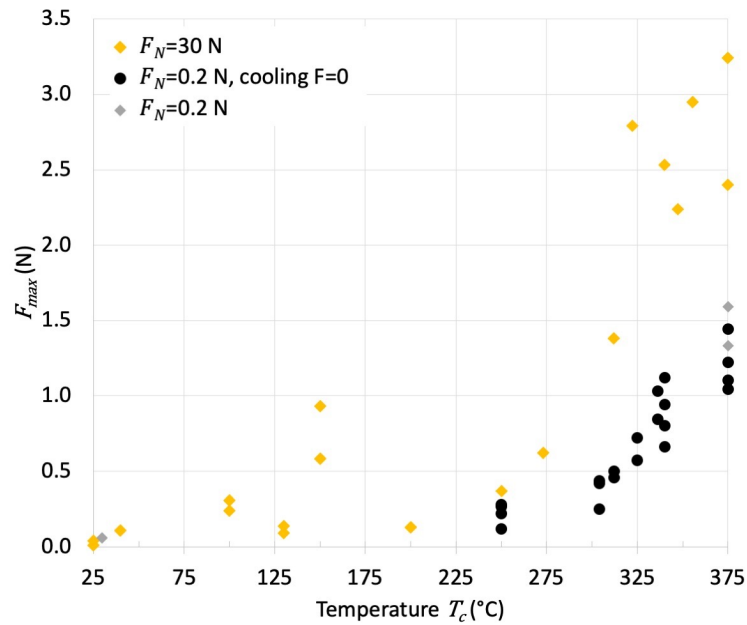


Figure 5.14: Maximum force during debonding evolution with bonding temperature  $T_c$  for  $t_c = 6$  s and various bonding normal force conditions: in diamond normal force kept during cooling, in circle normal force set to zero during cooling, in yellow  $F_N = 30$  N, in black and grey  $F_N = 0.2$  N. The setup used is  $R=2.5$  mm.

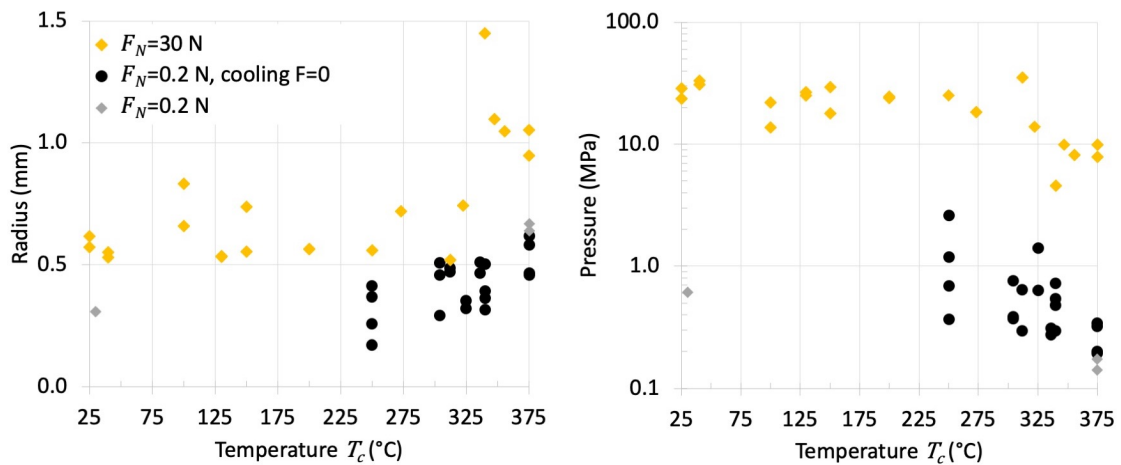


Figure 5.15: Fractured surface average radius (left) and minimum pressure (right) evolution with bonding temperature  $T_c$  for  $t_c = 6$  s and various bonding normal force conditions: in diamond normal force kept during cooling, in circle normal force set to zero during cooling, in yellow  $F_N = 30$  N, in black and grey  $F_N = 0.2$  N. The setup used is  $R=2.5$  mm.

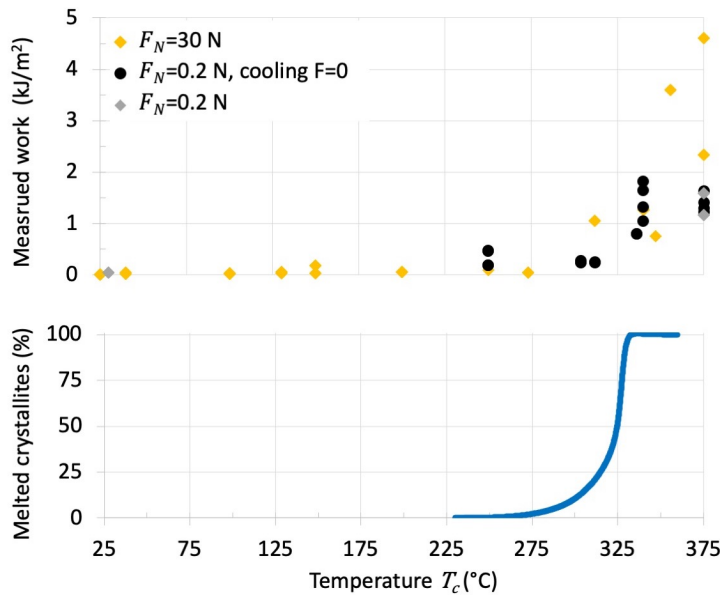


Figure 5.16: Measured work (top) and crystalline amount melted (bottom) evolution with bonding temperature  $T_c$  for  $t_c = 6$  s and various bonding normal force conditions: in diamond normal force kept during cooling, in circle normal force set to zero during cooling, in yellow  $F_N = 30$  N, in black and grey  $F_N = 0.2$  N. The setup used is  $R=2.5$  mm.

### 5.4.3 Different fracture mechanisms above melting

From the experiments discussed here above, the best adhesion is obtained for bonding temperatures above melting. Here, the scope is on performing pressure screening in the "best" welding conditions. At  $T_c = 375^\circ\text{C}$ , different normal forces ranging from 0.2 to 40 N leading to pressures from 0.2 to 16 MPa are explored for contact times of 6 and 600 s.

An example of the debonding force versus gap evolution as well as the fractured surfaces micrographs is depicted in Figure 5.17 for  $F_N = 35$  N at  $T_c = 375^\circ\text{C}$  for 6 (in black) and 600 s (in red). In this case, a hole appears on the bottom film (sometimes on the top one or on both films too): the bonding is good enough to lead to film fracture; others samples do not fractured with holes but with an interfacial debonding mechanism. These different fracture mechanisms are shown on Figure 5.18 by empty symbols in case of film fracture or filled symbols for interfacial debonding mechanism. For both contact times, a transition between interfacial debonding and film fracture occurs around 5.5 MPa for  $t_c = 6$  s and around 1.3 MPa for  $t_c = 600$  s. This threshold pressure between interfacial debonding and film fracture mechanisms is lower for the longest contact time.

Increasing the contact time allows more chain ends mobility and so more macromolecular chain or segments interfacial diffusion, the ability to form crystalline structures at the interface should be enhanced even if our experiments did not give any proof. Increasing the contact pressure and time could lead to a localized thickness decrease and consequently a possible easier film breakage dependent on pressure level and contact time. To assess this hypothesis, performing real local thickness measurement during contact step along an experiment could be helpful. This means instrumenting the small remaining space inside oven with devices sustaining temperatures up to  $400^\circ\text{C}$  and allowing a measurement resolution up to  $1\ \mu\text{m}$ .

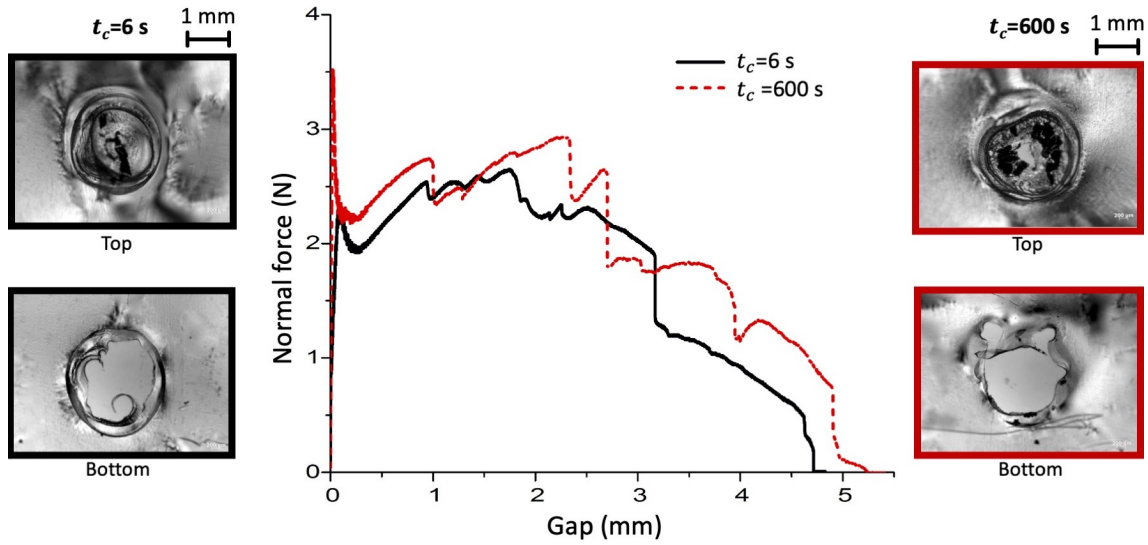


Figure 5.17: Debonding force versus gap for  $F_N = 35\text{ N}$  at  $T_c = 375^\circ\text{C}$  and 6 s (black) or 600 s (red) contact times  $t_c$ . Pictures are films fractured surfaces micrographs: holes are visible on the bottom one, film failure conditions are reached. The setup used is  $R = 2.5\text{ mm}$ .

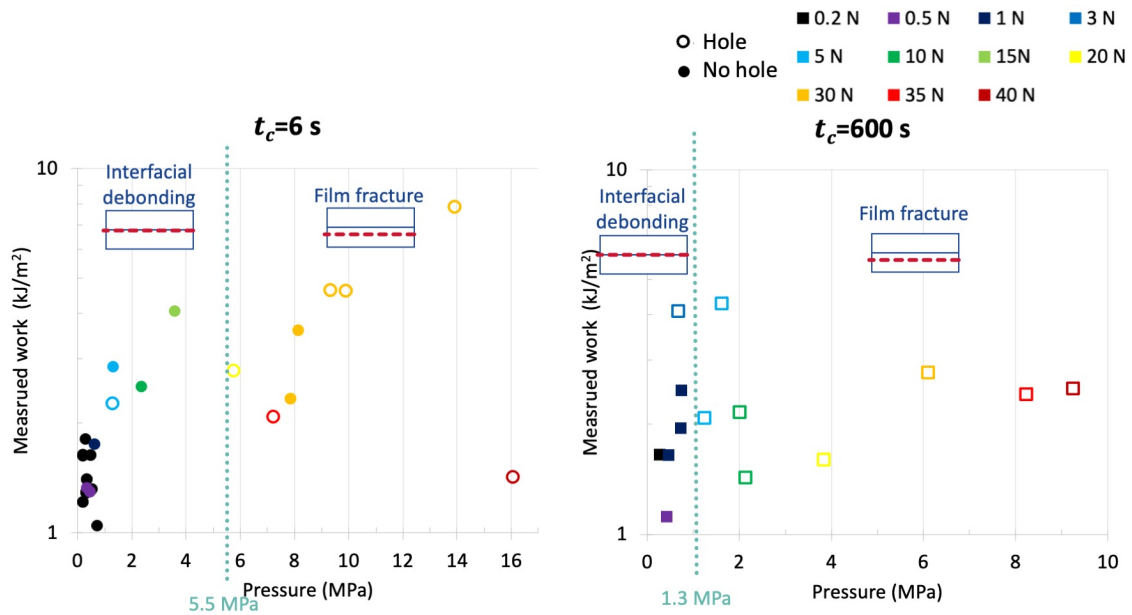


Figure 5.18: Measured work evolution with applied pressure for  $t_c = 6\text{ s}$  (left) and  $t_c = 600\text{ s}$  (right). Various normal force  $F_N$  are applied from 0.2 to 40 N in blue to red, leading to various estimated pressures from 0 to 16 MPa. Samples with hole on the fractured surfaces are depicted by open symbols. The threshold pressure between interfacial debonding and film fracture is lower for  $t_c = 600\text{ s}$ . The setup used is  $R = 2.5\text{ mm}$ .



# Towards modelling mechanical adherence tack test

*Using image analysis, the time evolution of some geometric parameters is monitored during debonding. Under some assumptions, a model is introduced to estimate the different energetic contributions. Another modelling method in three dimensions is proposed through a discrete network, which leads to an estimation of the critical energy release rate.*

### Contents

---

<b>6.1</b>	<b>Image analysis</b>	<b>110</b>
6.1.1	Scheme of the configuration	110
6.1.2	Results	111
<b>6.2</b>	<b>Two dimensions model - band approximation</b>	<b>113</b>
6.2.1	Kinematics formulation	113
6.2.2	Forces estimation	114
6.2.3	Energy balance	115
<b>6.3</b>	<b>Three dimensions model</b>	<b>118</b>
6.3.1	Uniaxial tensile test	118
6.3.2	Crossed cylinders tack geometry	122

---

All along this chapter, focus is on the debonding step of one example mechanical adherence tack test experiment performed with bonding at  $375^{\circ}\text{C}$  for 6 s under 0.2 N normal force corresponding to the dark red continuous line curve depicted on Figure 5.6. In such bonding conditions, a "good" welding and measurable film deformation occur.

## 6.1 Image analysis

### 6.1.1 Scheme of the configuration

A schematic of the mechanical tack test setup is shown on Figure 6.1. PTFE films are represented as a thick blue line. During film debonding, the bottom shaft is fixed and the upper shaft moves towards the top at a constant speed of  $V = 20 \mu\text{m/s}$ ; the vertical force  $F_{exp}$  is recorded as well as the gap  $U = 2\delta$ . In "good" welding conditions, films are deforming taking a sand-glass shape. To follow film deformation, some geometrical parameters can be monitored by image analysis with MatLab program such as:

- the radius of the welded zone  $a$ : half of the horizontal distance between points B on the right and left sides,
- the distance  $R$  of point D to the vertical axis: half of the horizontal distance between points D on the right and left sides,
- the angle  $\theta$  between the horizontal axis and the straight line BD (the blue dotted line on Figure 6.1 right) approximated by the mean angle between right and left sides.

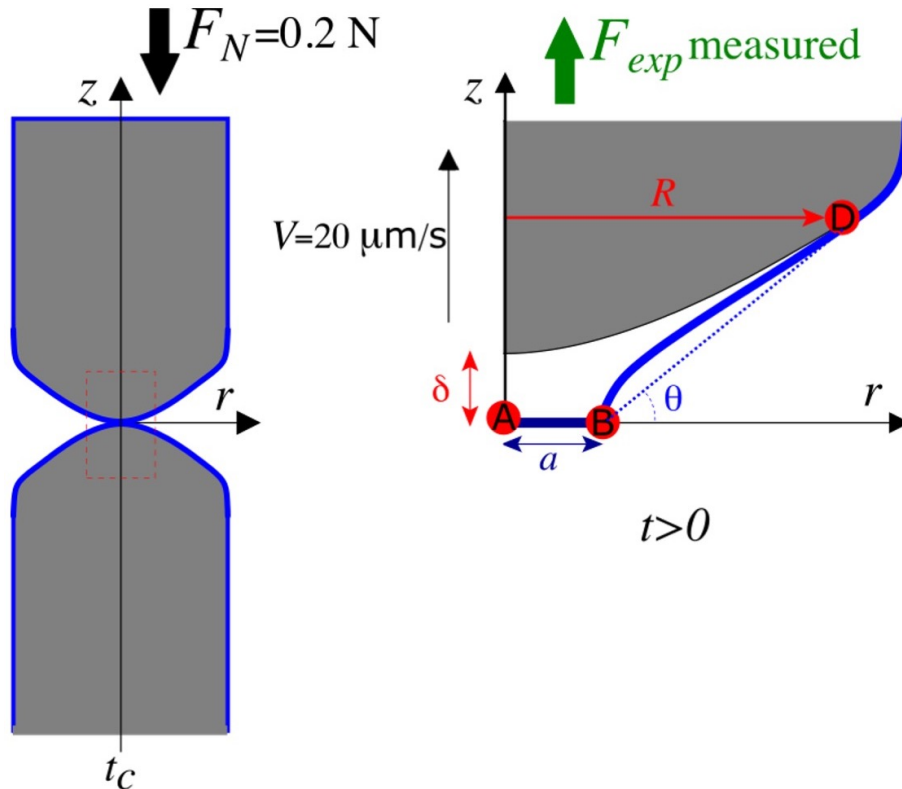


Figure 6.1: Schematic of mechanical adherence tack test axisymmetric geometry; films are represented as thick blue lines. Left: during contact and bonding. Right: magnification of the top-half right adhesive contact in a deformed configuration for  $t > 0$ .

### 6.1.2 Results

Pictures in Figure 6.3 are taken from the test video recording during debonding with a camera Nikon D3200 equipped with a macro lens (Sigma EX DG Macro 105 mm) leading to image size of 1920 by 1080 pixels. Since the camera focus is made on the center of the top support before bonding, only the top half of the configuration can be safely exploited by image analysis. Moreover, the top support horizontal is slightly misaligned with the camera horizontal axis. Before any analysis of the raw video recording, the misalignment is corrected by a full image rotation. The achieved resolution is one pixel for  $14 \mu\text{m}$ .

Points B and D are automatically detected through edge grey level detection; their raw coordinates in horizontal  $r$  and vertical  $z$  directions are registered and depicted on Figure 6.2 for both the top left and right sides.

On Figure 6.2 left, focusing on point D coordinates, left and right sides coordinates in purple and yellow are well superimposed: the correction of the misalignment of the top support horizontal to the camera horizontal axis is effective. The vertical displacement speed of point D corresponds to the imposed speed  $V = 20 \mu\text{m/s}$  but point B vertical speed is two times lower around  $10 \mu\text{m/s}$ . This means that the film is deformed between point B and D as depicted on Figure 6.3.

From Figure 6.2 right, the decrease of the size of the welded zone (point B horizontal coordinates in blue and red) is not occurring exactly at the same time and at the same speed on both sides: it starts first on the right side (in blue) and it is more rapid on this side.

For the clarity of the analysis, the evolution of points B and D coordinates in pixels with time is fitted with order one polynomials as shown on Figure 6.2 with lines.

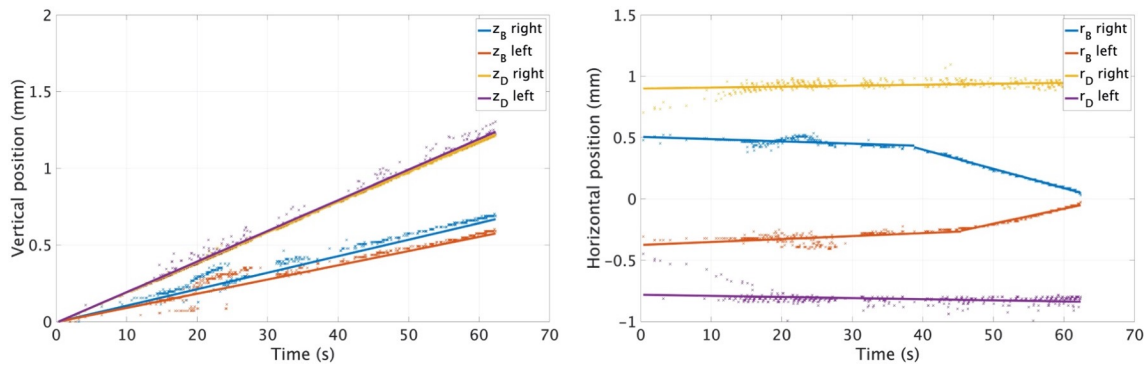


Figure 6.2: Time evolution of the raw coordinates of B and D points both on the top right and left sides obtained from image analysis. Left: Vertical coordinates; point D speed is  $20 \mu\text{m/s}$  corresponding to the imposed vertical speed and point B speed is close to  $10 \mu\text{m/s}$ . Right: Horizontal coordinates, the welded area size decreases.

The geometrical parameters of interest calculated from the fitted coordinates are depicted on Figure 6.3. The distance  $R$  of point D to the vertical axis almost constant around 0.8 mm. The angle  $\theta$  between the horizontal and the film increases and reaches a plateau value around  $40^\circ$  when debonding is initiated after 38 s as shown by the radius of the welded zone  $a$  decrease. The average radius of contact zone measured by optical microscopy on the fractured surface is  $457 \mu\text{m}$  and the maximum radius of the welded zone obtained by image analysis is 0.44 mm: the two measurements are in accordance with a relative error of 3.8%. The maximum recorded force happens close to the time when debonding starts  $t_d$ , this is confirmed by other experiments analysis, see Appendix E.

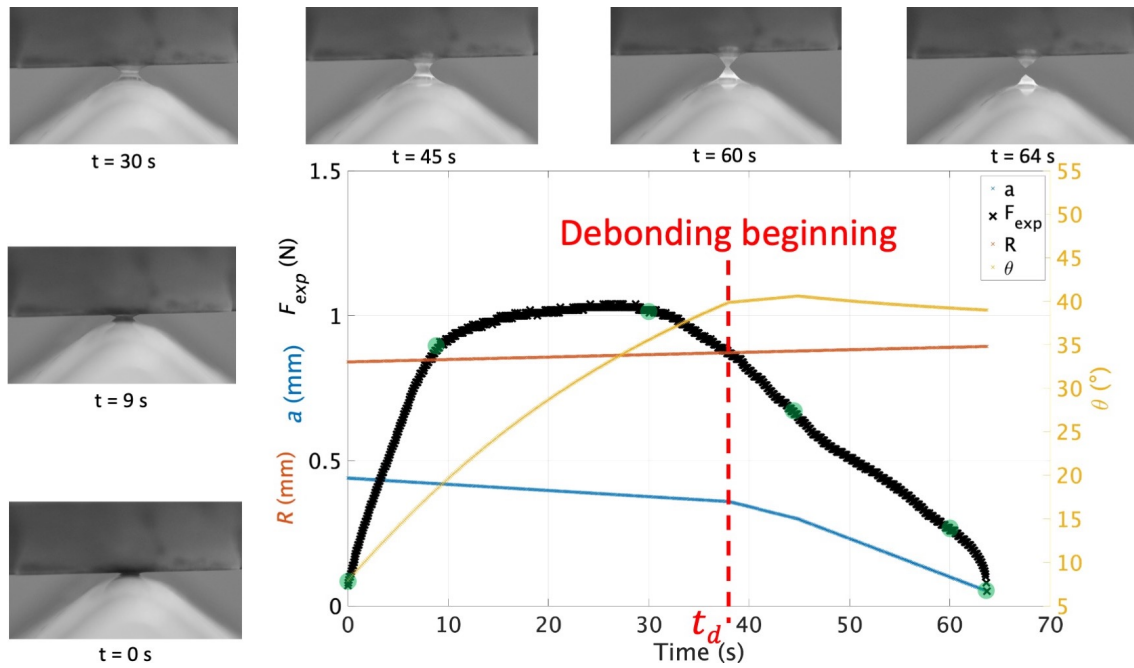


Figure 6.3: Experimental results: time evolution of the measured debonding force  $F_{exp}$  and pictures showing the deformation of the two films and their debonding (green points on the black force curve); Image analysis results: time evolution of the radius of the welded zone  $a$ , the contact point  $R$  between film and support and the mean angle  $\theta$  between the film arm and the horizontal axis.

Other kinematics values can be deduced from image analysis such as the arm length  $L$  and its corresponding stretch ratio; time evolution of the arm length BD recorded by image analysis is shown on Figure 6.4 left for both right and left sides of the upper part. The length BD is calculated as a straight line between points B and D fitted coordinates. The initial arm length  $L(t = 0)$  is difficult to evaluate precisely; since point D is moving, on the zone where point B coordinates is almost constant, the arm length is not constant. A shift in arm length values appears between left and right sides after the start of debonding; this can be explained by the debonding first initiated on the right side. Anyway, the overall trend of increasing arm length is well followed by each side with an arm length growth rate increasing after the beginning of the debonding.

From these data, an average stretch ratio in arm direction can be calculated as  $\lambda(t) = \frac{L(t)}{L(t=0)}$ , results are depicted in Figure 6.4 right, keeping in mind that the stretch ratio is not uniform in the arm as the cross-section changes from B to D. At maximum, the stretch in the arm direction  $\lambda$  is lower than 3 and thus always depicted by our experimentally identified behaviour law in Section 3.3.2.

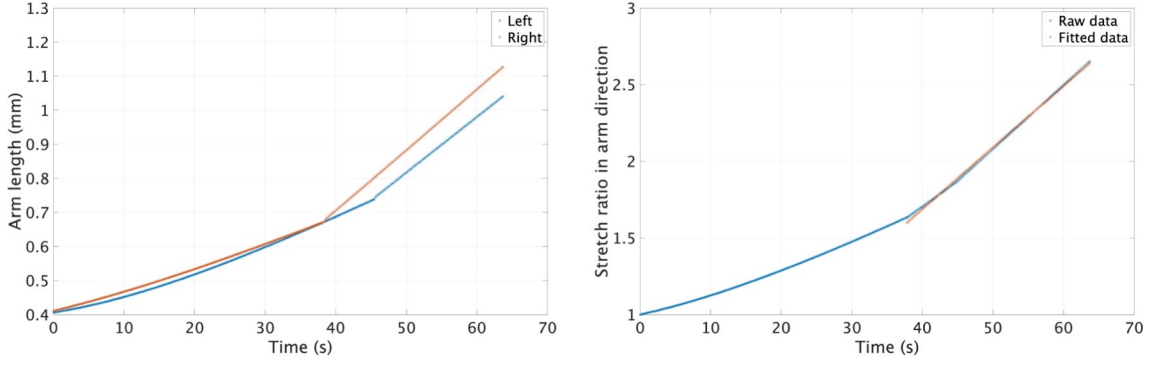


Figure 6.4: Left: Time evolution of the arm length for both right (in red) and left (in blue) sides on the upper part - line approximation between B and D points, Right: time evolution of the mean stretch ratio in arm direction  $\lambda(t) = \frac{L(t)}{L(t=0)}$  in blue and its fitted data for the debonding part in red.

## 6.2 Two dimensions model - band approximation

In this section a first model is exposed: the film curvature between points B and D in Figure 6.1 is not considered since the film arm is approximated by a straight band. Thus, the angle between the film and horizontal axis  $\theta(r, t) = \theta(t)$  is constant along the peeling arm.

### 6.2.1 Kinematics formulation

The considered geometry focuses on the upper film. It is made of a planar film and points A, B and D are thus line segments of width  $w$  as defined below, see Figure 6.5. Point A at  $z = 0$  is fixed, point B remains at  $z = 0$  and point D is a free end. The upper film is bonded to the lower film along AB remaining horizontal during the loading. At time  $t$ , the length of the welded part AB is  $a(t)$  and the peeling arm BD length is  $L(t)$ . The later is tilted of an angle  $\theta(t)$ . The width of the peeling arm is  $w(r, t) = w(t) = \pi a(t)$ . The cone shape is described as a plane: this made our modelling very simplified and thus only used to capture some features. The thickness of the film under loading  $h(t)$  is considered thin and the film mass is neglected.

At the end line in D, a tensile force  $\vec{F}(t) = F(t)\vec{k}(t)$  is applied in the direction of the peeling arm axis,  $F(t)$  being the magnitude of the load and  $\vec{k}(t)$  the unit vector in the arm axis direction  $\vec{k} = \cos\theta(t)\vec{i} + \sin\theta(t)\vec{j}$ . The vertical component of  $F_z(t) = \vec{F}(t) \cdot \vec{z} = \frac{F_{exp}}{2}$  is the half of the external load applied.

At  $t = 0$  the part AB is pre-stressed with an internal normal force  $F_0$ . At line B, the peeling arm applies the tilted force  $\vec{F}(t)$ . The vertical component  $F_z(t)$  contributes to the debonding of the interface between the two films and the horizontal component  $F_r(t)$  stretches the part AB. **Only  $F_z(t)$  is measured during the test.  $F_r(t)$  remains unknown or deduced as shown in Section 6.2.2.** Bending effects are neglected and stresses are considered uniform all along the film.

In this model, a vertical displacement  $U$  is prescribed on the top with speed  $V = \frac{1}{2}V_{exp}$  due to symmetry. During time increment  $dt$ , the contact edge line D moves by an increment of  $d\vec{u}$ :

$$d\vec{u} = du_r\vec{i} + du_z\vec{j} \quad (6.1)$$

where  $\vec{i}$  and  $\vec{j}$  are unit vectors.

The vertical displacement increment is  $\delta = du_z = \frac{1}{2}dU_{exp}$ . The horizontal increment  $du_r$  is not controlled but can be estimated knowing  $\theta(t)$  and  $d\theta$ .

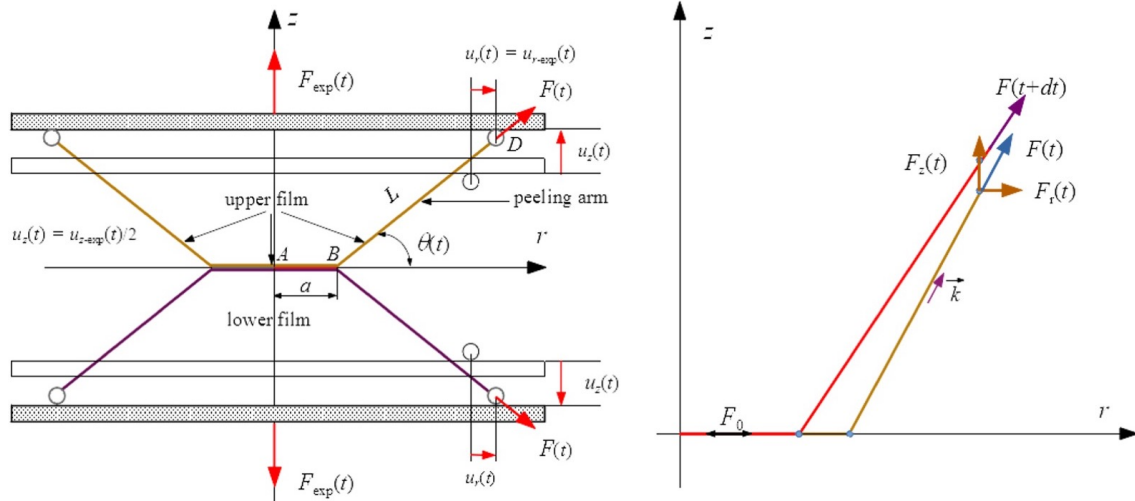


Figure 6.5: Notations. Left: global configuration, lengths and displacements, Right: forces.

## 6.2.2 Forces estimation

### Estimation

For times  $t > 0$ , neglecting the pre-stretch of the part  $AB$ , the forces applied in the peeling arm  $BD$  and the welded part  $AB$  are respectively

$$F(t) = \frac{F_{exp}(t)}{2 \sin \theta(t)} \quad ; \quad F_r(t) = \frac{F_{exp}}{2 \tan \theta(t)} \quad (6.2)$$

### Application to an experiment

On Figure 6.6 left, both force contributions — in arm direction in blue and in horizontal direction in red — are plotted along with half of the experimental force recorded in vertical direction. A good shape correlation is noticeable between experimental force and the estimated ones with equation (6.2). Both force contributions are following the same tendency; they are shifted vertically of a constant value  $\cos(\theta)$  depicted on Figure 6.6 right.

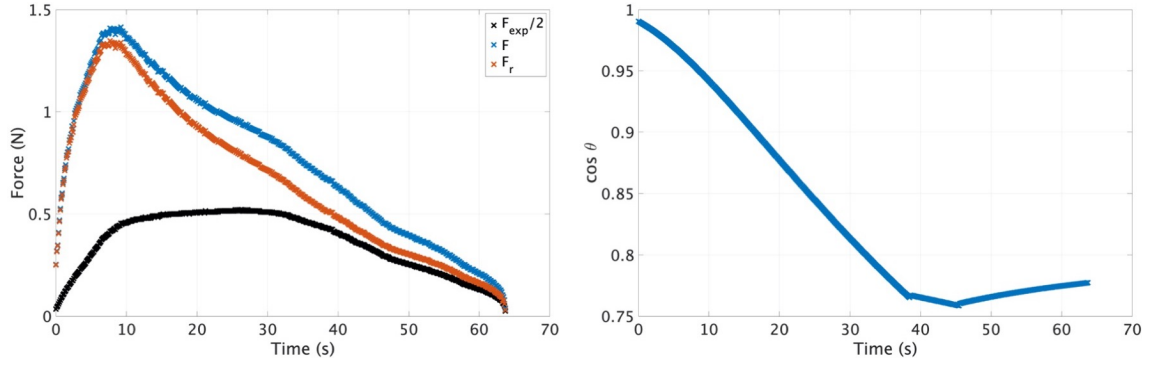


Figure 6.6: Left: Time evolution of the forces following equations (6.2), Right: Time evolution of the  $\cos \theta$  factor between the forces.

### 6.2.3 Energy balance

Focus will be only on the part where peeling is already initiated - the radius of the welded zone  $a$  clearly decreases, after  $t_d = 38$  s on Figure 6.3.

#### Modelling

The elementary energy balance on one side top and bottom (right or left) of the configuration depicted on Figure 6.1 must apply during the time increment  $dt$

$$\delta W_{ext} = 2\delta U_{1arm} + \delta U_{weld} + \delta W_{adh} \quad (6.3)$$

with :

- $\delta W_{ext}$  the elementary work done by the external force  $F(t)$  at point  $D$  between  $t$  and  $t + dt$

$$\delta W_{ext} = 2\vec{F}d\vec{u} = 2F_z du_z + 2F_r du_r = \delta W_{ext,z} + \delta W_{ext,r} \quad (6.4)$$

The first term on the right of Equation (6.4) is known experimentally: half of the surface increment under the experimental curve force versus gap. Considering that line D is very remote at a static position, the entire second term vanishes.

$$\delta W_{ext} = \frac{F_{exp}}{2} dU_{exp} \quad (6.5)$$

- $\delta U_{1arm}$  the energy stored and/or dissipated in one arm between  $t$  and  $t+dt$ : calculated from the energy density per unit volume  $e_v$  (area below stress-stretch curve) coming from the material behavior law identified in Section 3.3.2, see Figure 6.7 top line.

$$\delta U_{1arm} = hwL[e_v(t+dt) - e_v(t)] \quad (6.6)$$

- $\delta U_{weld}$  the energy stored and/or dissipated in the welded zone between  $t$  and  $t + dt$ : From equation 6.2, the nominal stress in horizontal direction can be calculated as  $\sigma_r = \frac{F_r}{2hw}$ . Using our experimentally identified behavior law Figure 3.18, the stretch in the welded zone can be deduced from the stress value, see Figure 6.7 bottom line. Then, the energy density corresponding to each stretch at each time step  $e_{v,weld}$  is used for calculation.

$$\delta U_{weld} = 2hwa[e_{v,weld}(t+dt) - e_{v,weld}(t)] \quad (6.7)$$

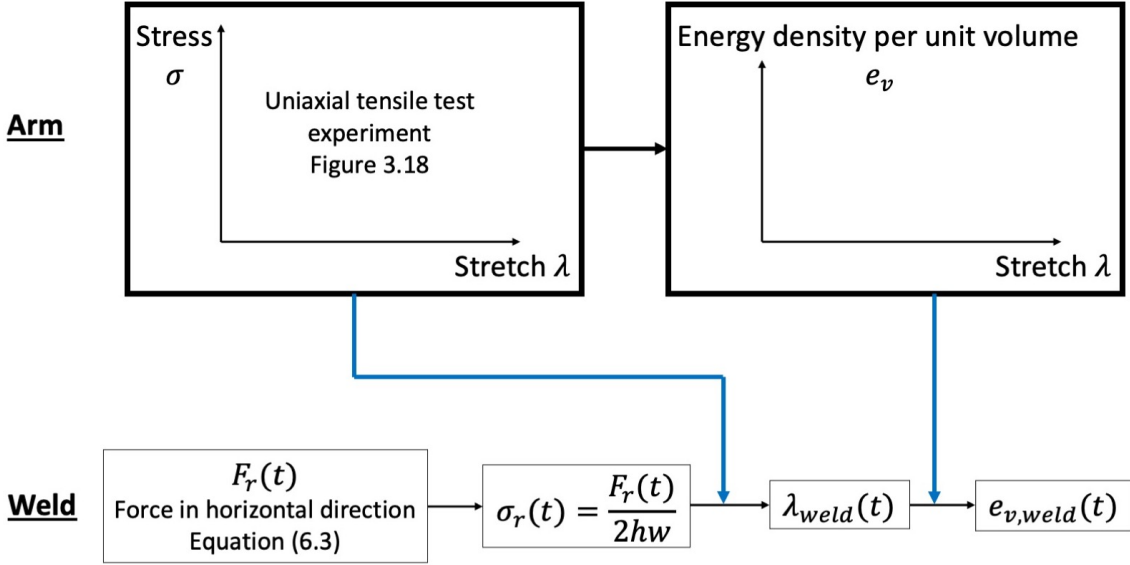


Figure 6.7: Scheme of the determination of the energy density in the film arm (top line) and weld zone (bottom line).

- $\delta W_{adh}$  the work of adhesion at the debonding interface  
In conclusion, combining (6.3) with (6.5), (6.6) and (6.7):

$$\delta W_{adh} = \delta W_{ext} - 2\delta U_{1arm} - \delta U_{weld} \quad (6.8)$$

For all the time increments we are interested in, starting at  $t_d$  the time at which debonding propagates:

$$W_{adh} = \sum_{t_d}^{t_{end}} \delta W_{adh} = \sum_{t_d}^{t_{end}} \delta W_{ext} - 2 \sum_{t_d}^{t_{end}} \delta U_{1arm} - \sum_{t_d}^{t_{end}} \delta U_{weld} \quad (6.9)$$

### Application to an experiment

In chapter 5, to characterize adherence from mechanical tack test, measured work defined as the area below the force versus gap curve is calculated whatever the debonding is initiated or not. For the experiment taken as an example in this chapter, the measured work value obtained is  $W_{meas} = 0.92$  mJ. Here, only half of the configuration is modelled, leading to  $W_{meas,1side} = 0.46$  mJ or  $700$  J/m<sup>2</sup>. This value takes into account the energy required to stretch the bulk material. The final aim is to evaluate the "real" proportion of the macroscopic measured work dissipated for interfacial crack propagation called interfacial work of debonding  $W_{debonding}$ .

The previously exposed energy balance is applied to the example experiment after the start of debonding. The film width  $w(t)$  is adjusted to be close to the "real" contact size corresponding to the area where peeling occurs: it is half of the perimeter of the bonded zone  $w(t) = \pi a(t)$ . Results are depicted in Figure 6.8. During debonding, the main energy contribution comes from the work of the external force in blue  $W_{ext} = 0.131$  mJ; the energy stored and/or dissipated in two film arms in red is two orders of magnitude lower  $2U_{1arm} = 6.2 \times 10^{-3}$  mJ. The energy stored and/or dissipated in the welded zone in yellow is negligible since the stretch in the bonded zone is almost constant.

Using equation (6.9), the interfacial work of debonding is depicted in purple:

$$W_{adh} = 0.125 \text{ mJ} \text{ and } W_{adh,surf} = \frac{W_{adh}}{a_{max}} = 205 \text{ J/m}^2.$$

To conclude, the main contribution of the work of adhesion once debonding is initiated comes from the work of the outside force. For the whole mechanical tack test, around 70% of the measured energy is stored and/or dissipated by film stretching before and during fracture propagation. The remaining 30% are really used to separate the two welded films.

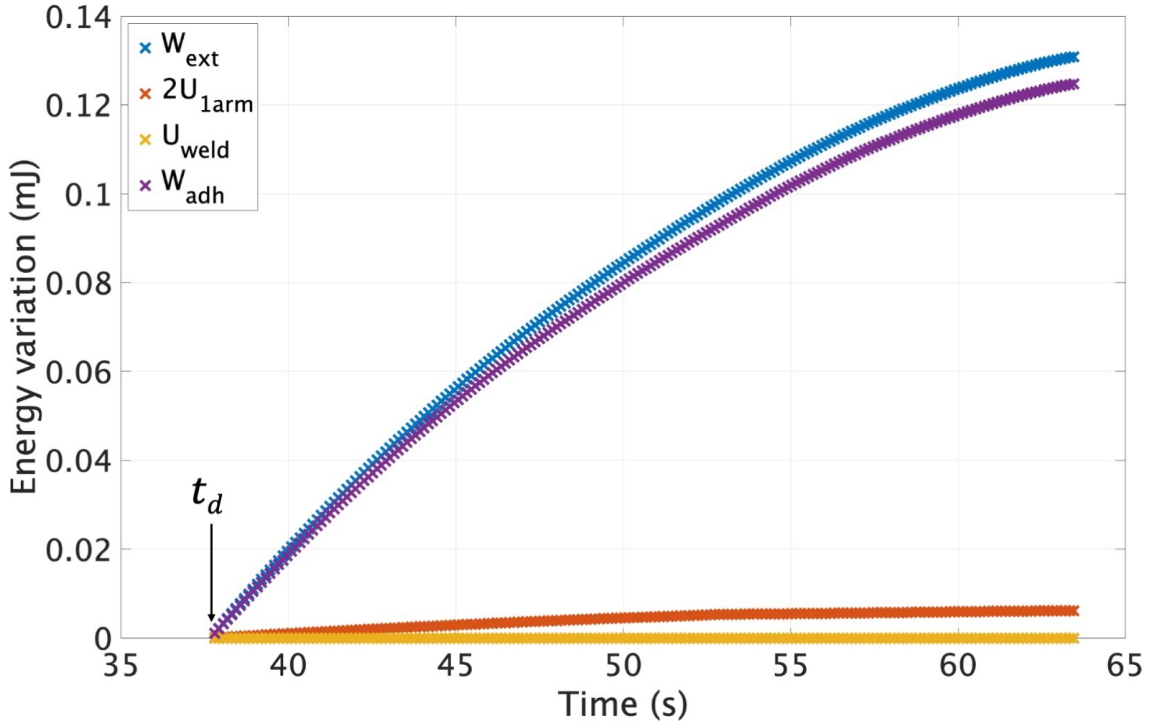


Figure 6.8: Cumulative energy variations calculated from previous equations (6.8). The zero is set at the time where debonding starts  $t_d = 38$  s, estimated by image analysis, see Figure 6.3.

This first model gives a rough estimation of the debonding work. However, the initial film tension highlighted on Figure 5.4 as a parameter with a huge impact on the measured work is not an input of this model. Also, the characteristic sand-glass shape is not considered in this model since the film is approximated by a planar film. All of this could lead to huge value imprecisions.

### 6.3 Three dimensions model

The three dimensions model is based on the lattice spring method extensively described in literature [Hrennikoff 1941, Pan *et al.* 2018] used to characterize membranes behavior [Wright 1965]. This approach, which takes into account non linearities both from the material and the geometry, is an alternative to finite elements methods. In this work, a simplified method is implemented.

A discrete network based on regular triangular elements is used to map the film surface: only thickness integrated quantities are used. Equilateral triangles are made of an assembly of deformable bars sustained to normal loads only; each bar is articulated at its ends at points localized at hexagons centers (see Figure 6.9). Each hexagon area links the bars loads at the hexagon center and the stress tensor in an equivalent continuous medium.

The following section exposes a two dimensions problem: the case of a uniaxial tensile test, to understand how to calibrate the material experimental behavior law considering the discrete network. Then, the crossed cylinders tack test geometry is implemented and the three dimensions sand-glass films deformed shape is reproduced. The initial film tension, highlighted on Figure 5.4 as a parameter with a huge impact on the measured work, is an input of this model.

#### 6.3.1 Uniaxial tensile test

First, a uniaxial tensile test in  $y$  direction is implemented. The force is calibrated to fit as well as possible the experimental data from tensile test made on samples. A geometric factor is determined to account for the chosen nodes and bonds network discretization.

##### Force calibration

Initially, the film surface is modeled with a regular triangular nodes network (in green on Figure 6.9a) corresponding to a regular hexagonal network where the apothem is half of a bond length  $\frac{l_0}{2}$  (in black on Figure 6.9). Half of the angle between two neighbouring bonds has a value  $\theta_i = \frac{\pi}{6}$ .

Considering an elementary bond for example from point  $O(0,0)$  the origin to point  $A_i$  of coordinates  $(X_i, Y_i) = (l_0 \sin \theta_i, l_0 \cos \theta_i)$ , in the deformed state, Figure 6.9b,  $A_i$  coordinates express as  $(x_i, y_i) = (\lambda_{xx} X_i, \lambda_{yy} Y_i)$ .

The stretch in bond direction  $\vec{n}_i$ , corresponding to the stretch of the elementary bond  $OA_i$  with  $l_i = \lambda_i l_0$ , is then:

$$\lambda_i = \frac{1}{2} \sqrt{\lambda_{xx}^2 + 2\lambda_{yy}^2} \quad (6.10)$$

with  $\lambda_{xx}$  and  $\lambda_{yy}$  the stretches of equivalent continuous medium.

The deformed angle  $\Theta_i$ , characterizing the rotation of the elementary bond  $OA_i$ , changes to:

$$\Theta_i = \arctan \left( \frac{\sqrt{3} \lambda_{xx}}{3 \lambda_{yy}} \right) \quad (6.11)$$

Around one node at the surface of one black hexagon, the simulated planar stress tensor (see Section 3.3.2 for the definition of planar stress), expresses as:

$$\sigma^{*,\text{simu}} = \frac{3 f_i l_i}{2 S} \vec{n}_i \otimes \vec{n}_i \quad (6.12)$$

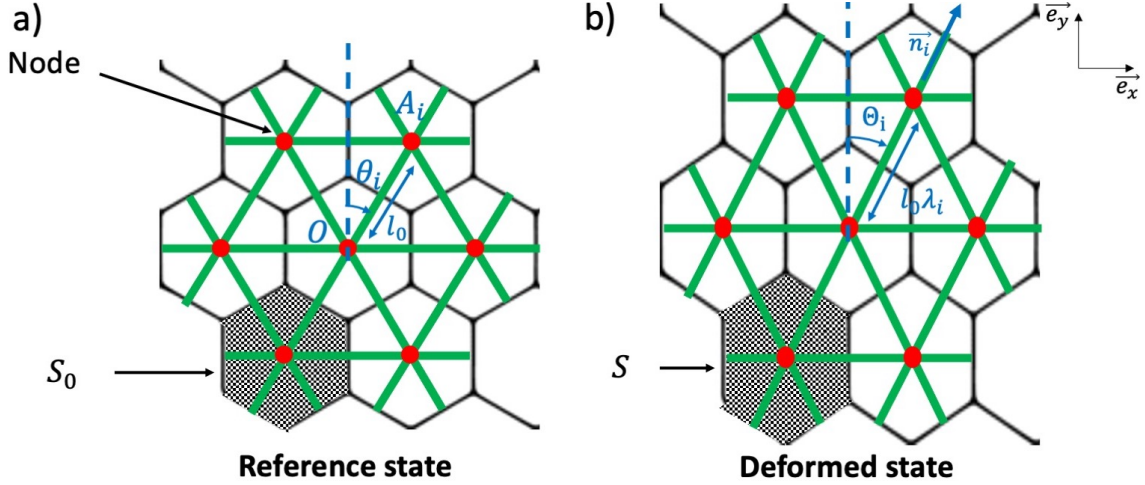


Figure 6.9: Triangular nodes network in a) reference and b) deformed state. Nodes are depicted by red dots and bonds by green lines. Notation is introduced.

$$\sigma^{*,\text{simu}} = \frac{3 f_i l_i}{2 S} \vec{n}_i \otimes \vec{n}_i \quad (6.13)$$

with  $\otimes$  the tensor product,  $f_i$  the norm of the force along one bond,  $\vec{x}_i = \frac{l_i}{2} \vec{n}_i$  the half inter-nodes vector,  $S = \lambda_{xx} \lambda_{yy} S_0$  the area of one deformed hexagon and  $S_0$  the area of an undeformed hexagon  $S_0 = 2\sqrt{3} \left(\frac{l_0}{2}\right)^2$ .

In the traction direction  $y$ , the stress component is

$$\sigma_{yy}^{*,\text{simu}} = \frac{3 f_i l_i}{2 S} \cos^2 \Theta_i \quad (6.14)$$

From the experimental behaviour law  $\sigma_{yy}^{*,\text{exp}}$ , identified in Section 3.3.2, should be equal to the value obtained by simulation  $\sigma_{yy}^{*,\text{simu}}$  for  $\lambda_{yy}^{\text{exp}} = \lambda_{yy}^{\text{simu}}$ . Consequently, the norm of the force along each bond is:

$$f_i = \frac{2 S \sigma_{yy}^{*,\text{exp}}}{3 l_i \cos^2 \Theta_i} \quad (6.15)$$

The same approach could be used to determine the other stress tensor components.

Under incompressibility assumption,  $\lambda_{xx} = \frac{1}{\sqrt{\lambda_{yy}}}$ , the force per bond  $f_i$  can be expressed as a function of the bond stretch  $\lambda_i$  thanks to Equation 6.15, with  $\sigma_{yy}^{*,\text{exp}}$  from the experimental behaviour law previously identified in Figure 3.18. Figure 6.10 shows its evolution for  $\lambda_{yy}$  varying from 1 to 4. For  $\lambda_i$  larger than 2.8, the second branch of the material experimental behaviour law is reached: the slope increases steeply. According to the slope sign, the strain is either stable (positive slope) or unstable (negative slope) leading to a strain localization as suggested by Figure 3.18 at 1.8 stretch where the section does not seem constant along the sample.

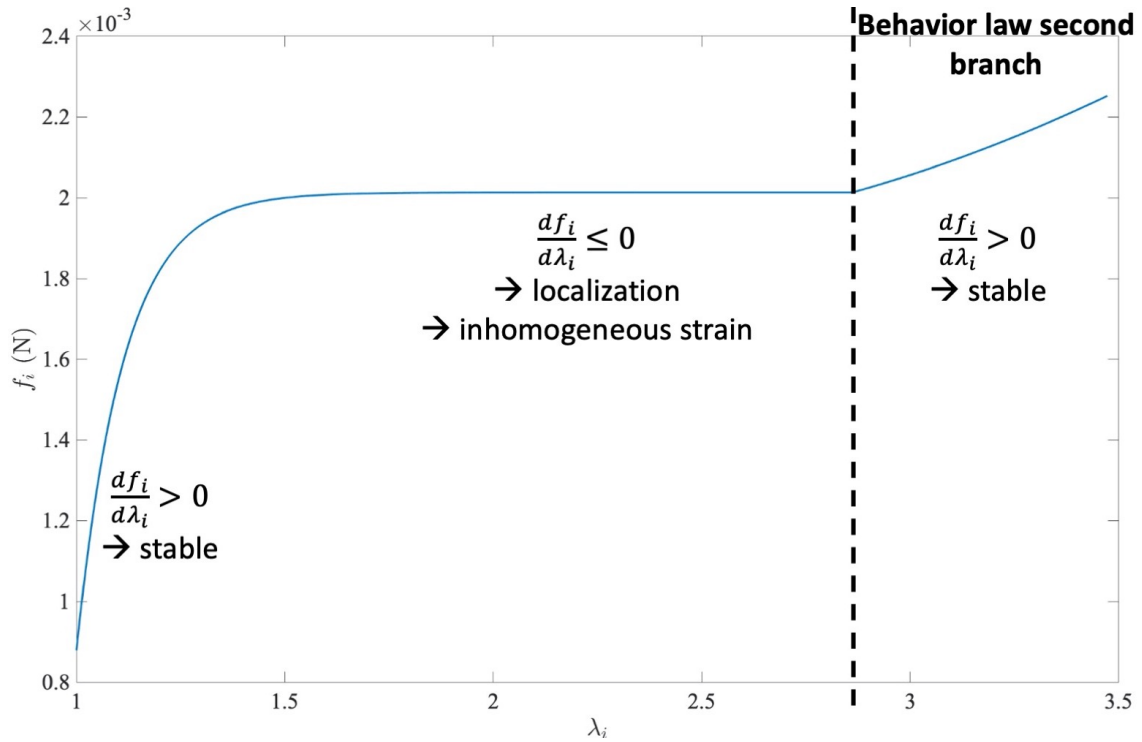


Figure 6.10: Force in a bond  $f_i$  as a function of the bond stretch  $\lambda_i$  under incompressibility assumption. Different regimes are highlighted leading to stable or unstable strains.

## Results

A quarter of the tensile test sample is modeled with initial dimensions  $L_x = 10$  mm and  $L_y = 1$  mm. A vertical displacement in  $y$  direction is imposed with an increment  $d\delta = 0.1$  mm. Figure 6.11a shows the force per bond level in the sample at different stretches values: horizontal bonds carry almost no load. A virtual cut is realized at a height  $y_{cut}$  and the resulting vertical force component  $F_y$  is depicted on Figure 6.11b for various initial bond lengths and  $\lambda_{yy} = 1.19$ . The resulting force is constant whatever the cut height is. Small force variations are observed when decreasing the initial bond length: between 1.43 and 1.47 N for initial bond lengths divided up to 8.

Under different assumptions, the planar stress in tensile direction evolution with tensile stretch can be plotted, see Figure 6.12. For an incompressible material ( $\lambda_{xx} = \lambda_{zz} = \frac{1}{\lambda_{yy}}$ ), both the theoretical result coming from the discrete modelling and the experimental result are depicted. The theoretical modelling is in good agreement with the experiment even if it is overestimated between 1.5 and 3 stretch values. However, in a simplified configuration with oedometric hypothesis ( $\lambda_{xx} = 1$ ), both the theoretical and simulated results are superimposed. In the following, the theoretical incompressible case is kept.

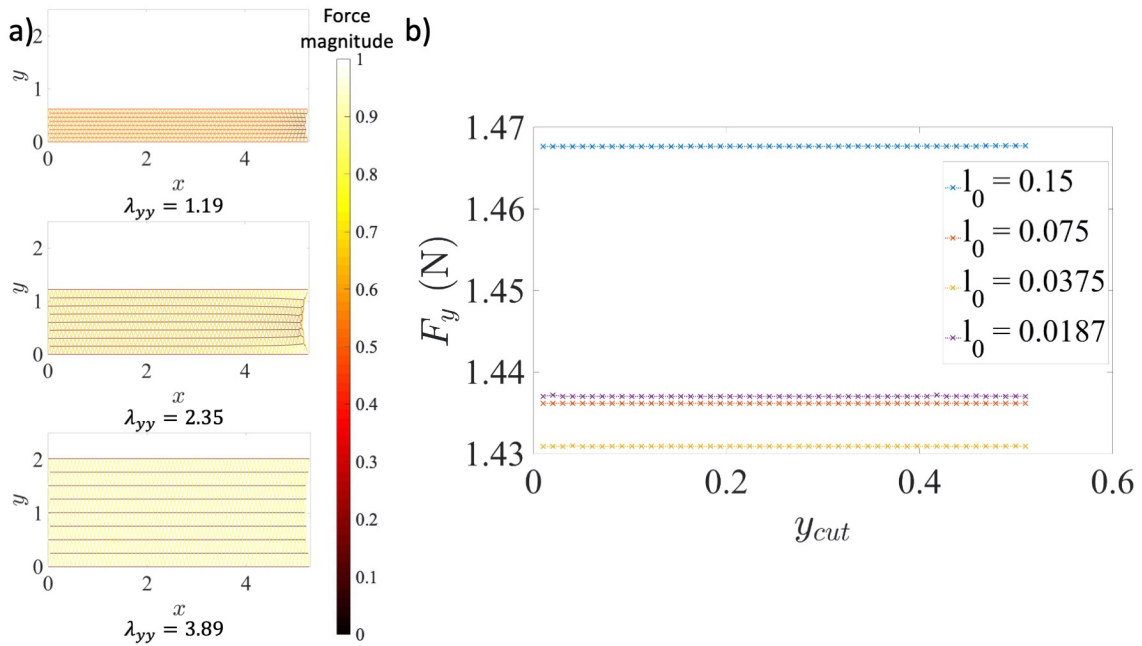


Figure 6.11: a) Normalized force magnitude per bond for different stretches along tensile test for initial bond length  $l_0 = 0.075$ . Only a quarter of the sample is depicted. b) Vertical force along y-axis  $F_y$  as a function of the virtual cut position  $y_{cut}$  for various initial bond lengths  $l_0$  and  $\lambda_{yy} = 1.19$ .

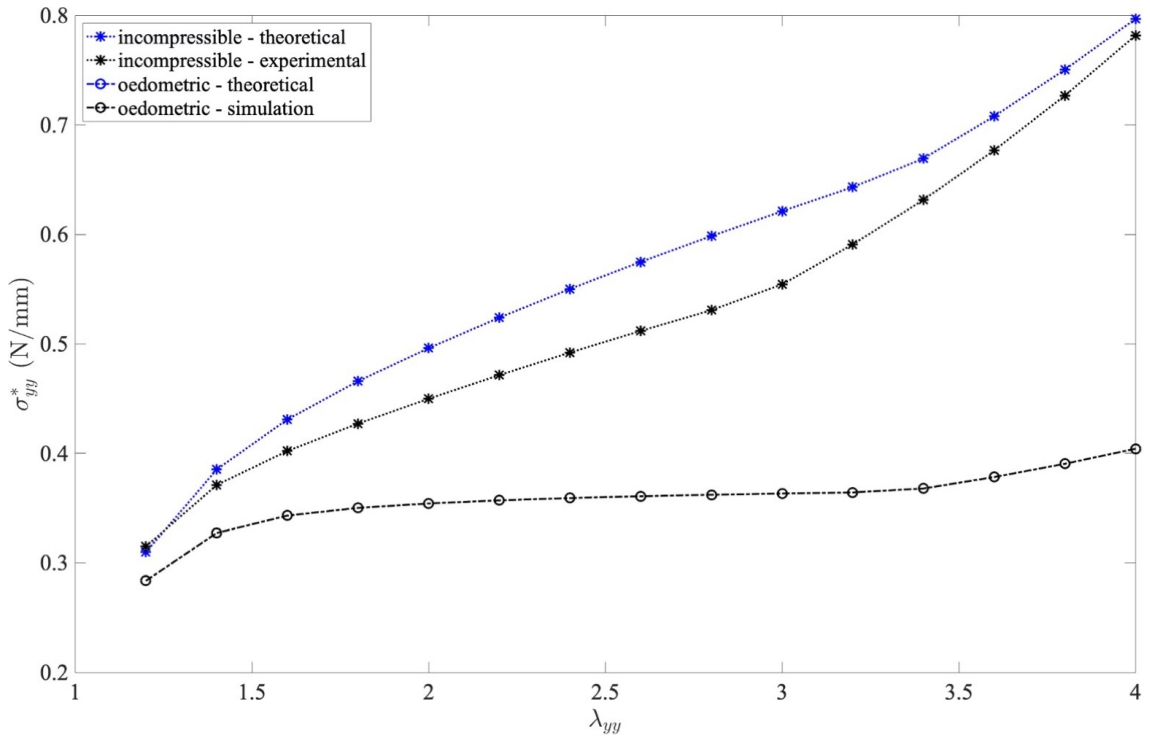


Figure 6.12: Planar stress in tensile direction  $\sigma_{yy}^*$  as a function of tensile stretch  $\lambda_{yy}$  for various hypothesis: incompressibility or oedometric case, theoretical, experimental or simulated results for  $l_0 = 0.075$  mm.

### 6.3.2 Crossed cylinders tack geometry

Films are folded around the cylinders in crossed geometry such that the film-cylinder contact is considered as non-slip. During the simulation of the tack test, it is assumed that both cylinder vertical position vary at a constant speed. The welded area is a disc rigidly fixed in the plane  $z = 0$ . By exploiting the symmetries, only one film is modeled (the top one) and a quarter is described, see Figure 6.13 in red.

To be as close as possible to the experimental test taken as an example all along this chapter, the following lengths are chosen:

- the cylinders radius of curvature:  $R_{cylinder} = 2.5$  mm,
- the quarter of the crossed cylinder geometry modeled lengths in both  $x$  and  $y$  directions:  $L_x = L_y = 1.5$  mm, chosen larger than  $R_{max}$  from image analysis on Figure 6.3,
- the bonded radius,  $a = 0.4$  mm, corresponding to the mean value when no debonding is occurring before  $t_d = 38$  s on Figure 6.3.

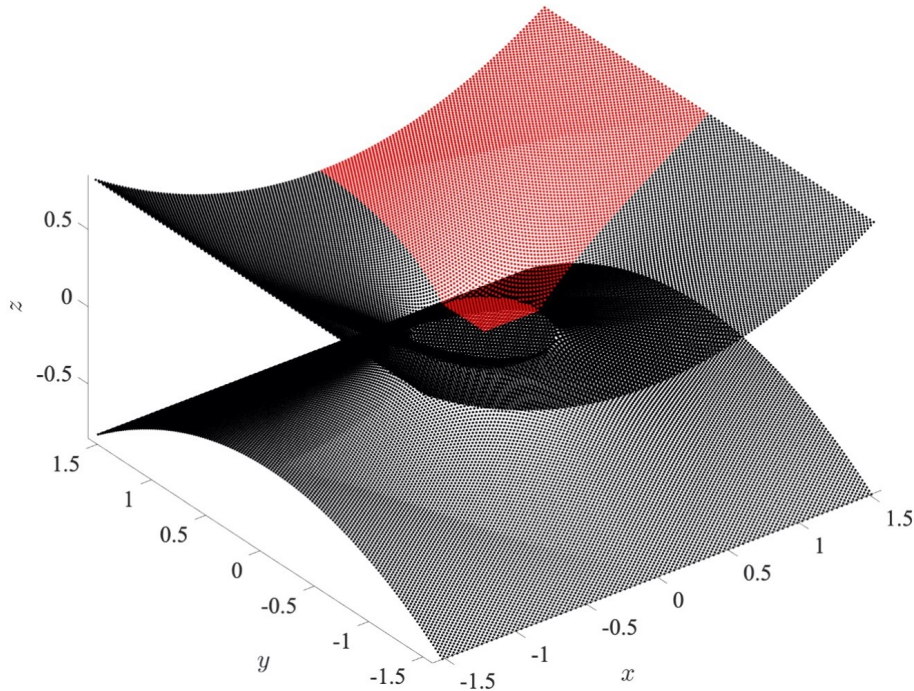


Figure 6.13: Three dimensions model whole configuration in a deformed state. Due to symmetries, only the red zone is modelled.

#### Initial state

Initially, the upper film is anisotropically pre-stretched on the cylinder with  $\lambda_{xx} = 1.025$ , close to the 2 N load experimentally imposed with the spring balance, see Figure 5.4; the bottom film is stretched the same way along  $y$ . The opposite edges to the welded zone are fixed on the cylinder. All along vertical displacement increment, the contact zone with the cylinder is self-determined from a contact condition.

### Traction example

The first part of the crossed cylinders tack experiment is simulated: the contact zone size  $a$  is constant while the gap between the top cylinder and the welded zone increases by steps of 0.05 mm. The nodes and bonds geometries are exposed on Figure 6.14 for various displacements  $\delta$  along  $z$ . All along the test, the bonds sustaining the highest load are located at the foot of the welded zone. The characteristic sand-glass deformed shape outside the contact zone observed experimentally is reproduced and both its height and radius seem to increase with the gap.

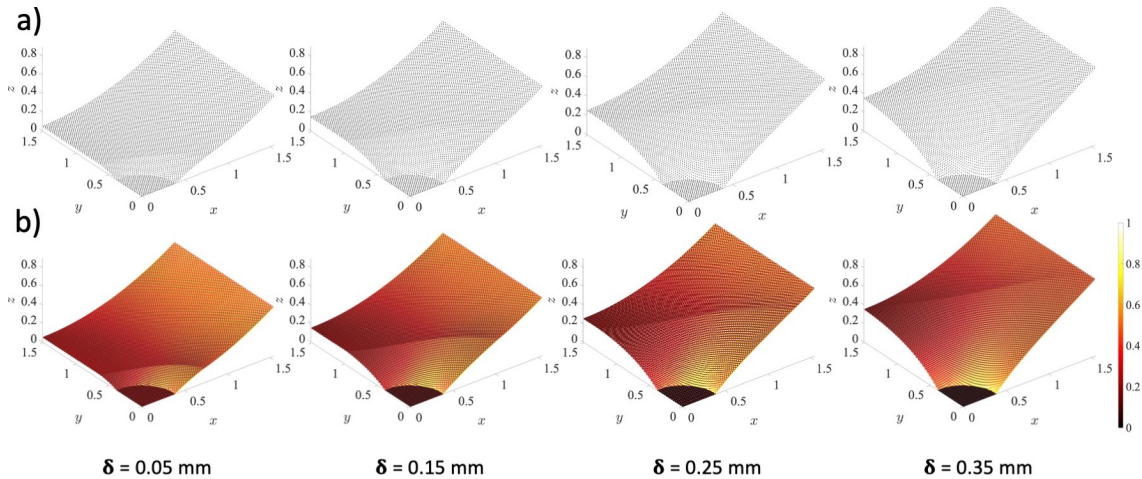


Figure 6.14: 3D view of a) Nodes geometry and b) force along each bond during displacement increase along the vertical direction  $z$ . The color represents the tensile load level in each bond.

For the last step corresponding to a vertical displacement of 0.35 mm, the two dimensions stress and strain tensors components are mapped, see Figure 6.15. For each component, the highest value is located in the component direction close to the welded area: the configuration is thus still axisymmetric. The stress in the radial direction is almost uniform: we are in a peeling situation with constant load but changing angle.

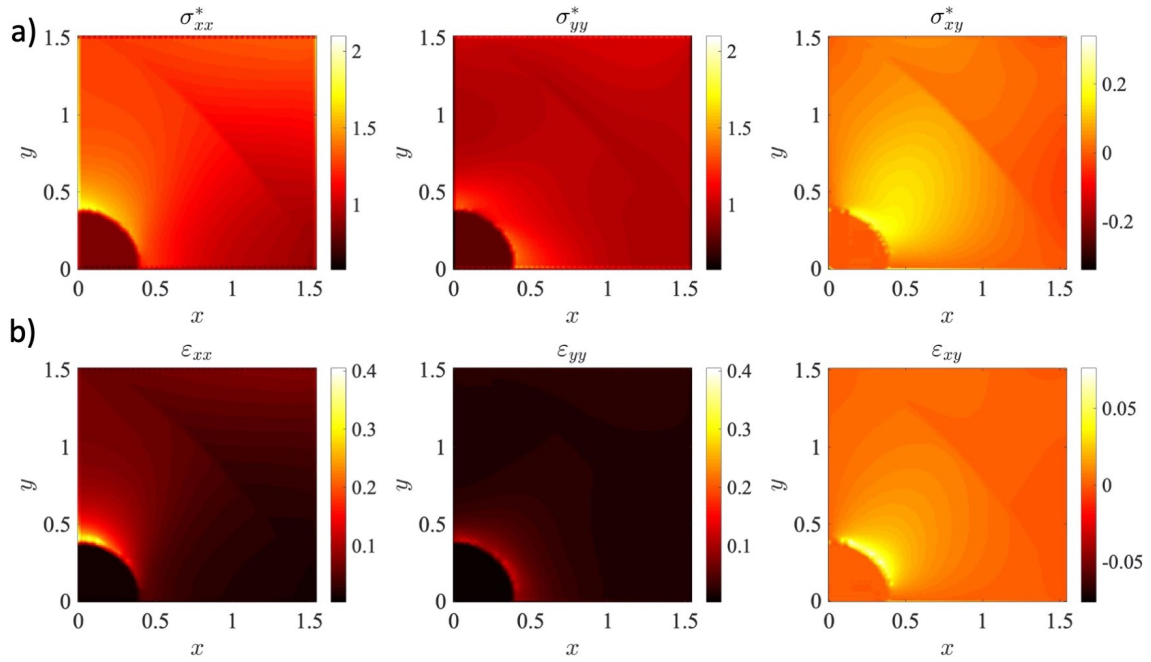


Figure 6.15: 2D projection of a) stress and b) strain 2D-tensors components for  $\delta = 0.35$  mm.

### Constant bonded size

Thanks to the geometric factor determination exposed in section 6.3.1, the force during debonding in crossed cylinders tack test can be simulated for the first stage where the bonded size is constant, see Figure 6.16. The obtained force is slightly varying with the initial bond length  $l_0$  (curves in red and blue,  $l_0$  distinct of a factor 2) and with the gap increment  $d\delta$  (curves in red and yellow,  $d\delta$  divided by 5). At the end, from  $\delta$  larger than 0.27 mm, the simulated force is overestimated. If the initial bonded size  $a$  is divided by two, the simulated force is also almost divided by two (compare the red curves crosses and circles on Figure 6.16). By doubling the initial stretch value  $\lambda_{xx}$ , the force response is slightly higher (red curves crosses and stars).

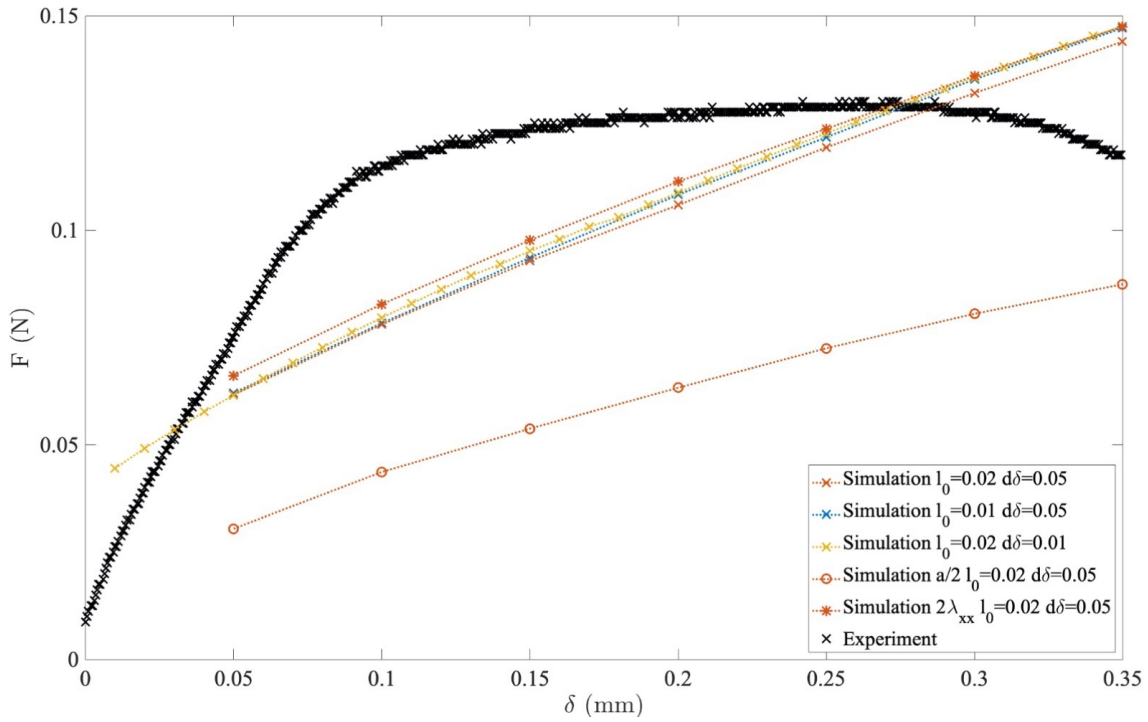


Figure 6.16: Force versus gap evolution for an eighth of the experimental configuration (in black) and obtained by simulation for various initial bond lengths  $l_0$  and gap increments  $d\delta$ . The impact of the contact zone size  $a$  and initial stretch  $\lambda_{xx}$  is illustrated.

### Debonding

The bonded size decrease will be implemented through energy release rate  $G$  variation already defined in Chapter 4:

$$G = -\frac{dW}{dA} \quad (6.16)$$

with  $W(t) = W(\delta(t), A(t)) = \int_0^{\delta(t)} F d\delta$  the work of the simulated force, and  $A(t) = \frac{\pi a(t)^2}{4}$  the corresponding bonded area.

Following the chart in Figure 6.17, the debonding part of the tack test can be simulated. From the debonding start point, when the simulated force in the constant bonded size zone is equal to the experimental one, at each gap increment  $d\delta$ , the radius of the welded zone decreases  $a(t + dt) = a(t) - da$ , so that  $\frac{dW}{dA} = G$ . The force in the new state can thus be deduced, as well as all along debonding. The critical energy release rate used for the simulation  $G$  is adjusted all along debonding so that the simulated and experimental force versus gap curves are as close as possible. This study is still ongoing and this algorithm has to be implemented.

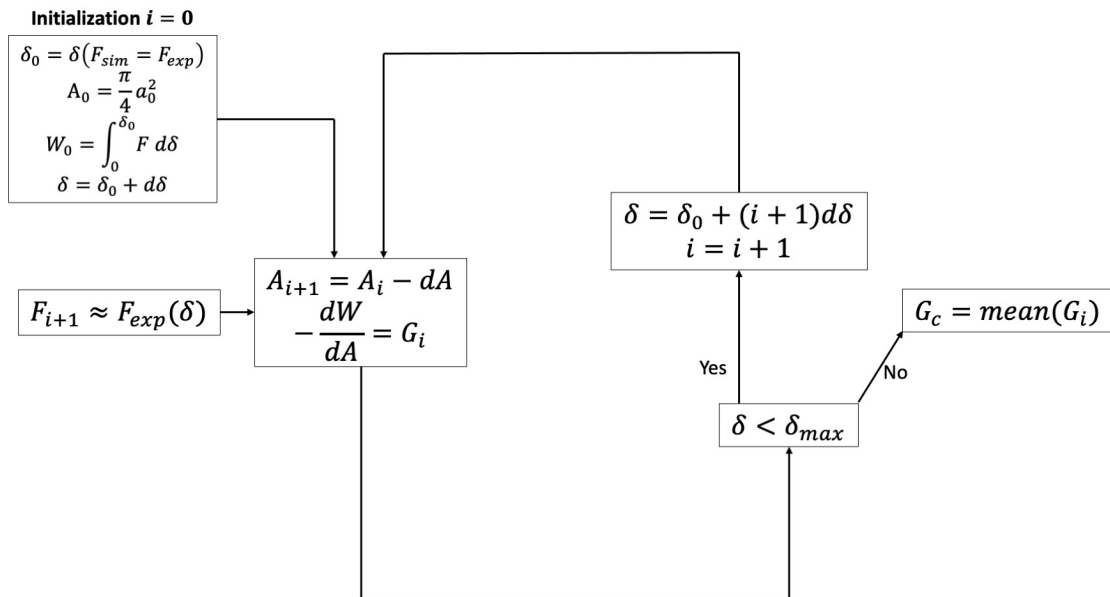


Figure 6.17: Chart of the algorithm to be implemented to evaluate the critical energy release rate  $G_c$  during crossed cylinders tack test experiment debonding phase.

# Conclusions and perspectives

By welding together a fabric sandwiched between two PTFE cast films, composite materials are manufactured. For optimum performance, PTFE-PTFE and PTFE-fabric adhesion, which depends strongly on the manufacturing process conditions, must be controlled. The present study focused on a model system: two PTFE films without fabrics. To understand and quantify their adhesive properties, a specific experimental setup and protocols have been designed. Mechanical adherence tack tests between crossed cylinders have been performed to investigate the impact of temperature, contact time and normal pressure.

The different steps leading to adhesion between two pieces of the same amorphous polymer material above the glass transition temperature have been identified from literature. Once intimate contact is reached - after surface rearrangement, surface approach and wetting - interfacial macromolecular diffusion can occur. Different chain motion dynamics has been reviewed: Rouse model for small-scale movements and reptation theory for large-scale movements. All these mechanisms are involved in the formation of an interphase inducing the progressive collapse of the interface between the two pieces, whereas mechanical strength is improved.

For semi-crystalline polymers, chain mobility is reduced due to the presence of crystalline structures and thus polymer chain inter-diffusion is limited. The mechanisms accepted in the case of amorphous polymers, are applicable to a given extent, but are indeed unsatisfactory, since other mechanisms such as co-crystallization, crystalline reorganization or epitaxial growth are supposed to impact the interfacial reinforcement. These mechanisms are expected to largely influence both the strength and kinetics of adhesion buildup between semi-crystalline polymers.

The role of chain inter-diffusion in the amorphous phase and co-crystallization of the polymer quasi-crystalline phase in the adhesion between two PTFE films has been investigated.

While contact temperature is rising, the amount of melted crystallites increases and thus macro-molecular chain mobility is enhanced until reaching melting. A contact temperature

higher than melting has been highlighted as a necessary condition to obtain good adhesion. However, increasing the contact time shows no significant variation in adhesion quality in the range studied. This result differs from what has been reported for amorphous polymers such as polystyrene [Zeng *et al.* 2006] and polybutadiene [Jarrousse 2004]. By shear rheology, the order of magnitude of the macro-molecular chain diffusion characteristic time has been estimated long but chain segments motions predicted at smaller time scales seems sufficient to create a good adhesion.

Both the crystalline content, crystallization mechanisms - primary or secondary - as well as the crystalline orientation have been explored without any satisfying result due to either device limitation or changes in the material mechanical response superimposed to the expected phenomenon.

Different fracture mechanisms have been highlighted above melting according to the contact pressure: the weld fracture is either non destructive through interfacial debonding or destructive resulting in a hole. The threshold pressure between interfacial and film failure mechanisms can be determined: the longer contact time, the lower the threshold pressure.

By image analysis of crossed cylinders adherence tack tests above melting, a better understanding of film deformation and debonding kinetics has been acquired. First, large film deformation occurs while the contact zone size remains constant and the measured vertical force increases; then, the contact zone size decreases and debonding happens.

Films mechanical behaviour in tension has been characterized both in temperature by DMA and at ambient temperature by uniaxial tensile test until rupture. From ambient to melting temperature, the storage modulus falls of more than one decade in MPa. The films mechanical response at room temperature has been identified from uniaxial tensile test: the evolution of the planar stress versus stretch is modeled first with a logarithm and for larger stretches with a power 2 law. This experimental behaviour law is an input of the models developed to dissociate the different energetic contributions during a crossed cylinders tack test. Both models exposed are based on the energy balance approach of fracture mechanics introduced by Griffith in 1921 [Griffith 1921]. The first model approximates the film by a planar band without any initial tension: the main energetic contribution comes from the work of the outside force. The second model considers the three-dimensions shape of the deformed film through a discrete network. The film initial tension is an input parameter and the material response is integrated through the lattice spring method. After calibration of the experimental behaviour law to the network, the first zone of the debonding curve where the contact zone size is constant has been reproduced. The final aim is to estimate a most accurate adhesive energetic value than the experimentally recorded measured work, such as the energy release rate. This work is still in progress and a method to reproduce the second part of the debonding force curve when fracture propagates is proposed.

To go further on the understanding of PTFE-PTFE adhesion, different perspectives can be considered:

The crossed cylinders mechanical adherence tack test geometry could be used further to explore more parameters.

The impact of the crystalline content could be assessed if a faster cooling could be achieved: performing an in situ quenching with liquid nitrogen is an additional option commercially available on some rheometers. The unsintered material surface state has not been tested during this work: changes in the adhesive behaviour are expected since this material has

---

a higher roughness than the sintered one and thus the contact quality is no more similar. However, identifying the weakest interface where failure occurs is challenging: it could either be between the two unsintered sides in contact or between the sintered and unsintered layers of each film.

All the mechanical adherence tack test presented were performed at a constant speed of  $20 \mu\text{m/s}$ : varying the debonding speed could allow to explore the material viscoelastic response [Kaelble 1964, Gent and Petrich 1969, Gibert *et al.* 1999]. The measured work is maybe not maximum at the speed chosen but little variation is expected since PTFE mechanical behaviour has been shown almost constant above melting.

Moreover, all the exposed results do not take in consideration the changes induced by various thermal treatments (temperatures and times) on the film mechanical properties. Performing uniaxial tensile tests until rupture on samples with different thermal histories could help improving the confidence given to these results.

When increasing the contact pressure and time, the local film thickness can decrease and lead to a possible easier film breakage. To assess this hypothesis, performing real local thickness measurement during contact step along an experiment could be helpful. This means instrumenting the small remaining space inside oven with devices sustaining temperatures up to  $400^\circ\text{C}$  and allowing a measurement resolution up to  $1 \mu\text{m}$ ; not sure a laser sheet would fill all these specifications.

The impact of crystalline structures on the interfacial adhesive properties has been examined. The evolution of PTFE secondary crystallization microstructure has been investigated by SEM equipped with an in-situ heating stage. However, several equipment limitations were highlighted and using an AFM in temperature could maybe help visualizing the secondary crystals.

The proposed three-dimensions model has been partially tested on only one experimental result. To check its accuracy and limitations, a more systematic analyze of crossed cylinders tack experiments should be performed. Moreover, since film thickness is neglected, using a finite element modelling method could help considering this last dimension and its inhomogeneous variations.

We believe that all the results given about PTFE-PTFE films adhesion could be extended to PTFE-fabric-PTFE composite materials with porous enough or woven fabrics with large holes. The consideration of fabrics should open other broad and interesting questions on PTFE-fabric adhesion and the different improvement levers available such as surface treatments or compatibility layers made of less viscous and more mobile polymers.



# References

- Anderson, T. L. (2017). *Fracture mechanics: fundamentals and applications*. CRC press.
- AntonPaar (2011). *Instruction Manual MCR Series*.
- Awaja, F. (2016). “Autohesion of polymers”. en. In: *Polymer* 97, pages 387–407. ISSN: 00323861. DOI: [10.1016/j.polymer.2016.05.043](https://doi.org/10.1016/j.polymer.2016.05.043). (Visited on 12/06/2017).
- Barthel, E. (2008). “Adhesive elastic contacts: JKR and more”. In: *Journal of Physics D: Applied Physics* 41.16, page 163001.
- Bassett, D. C. and R. Davitt (1974). “On crystallization phenomena in polytetrafluoroethylene”. In: *Polymer* 15.11, pages 721–728.
- Berry, G. C. and T. Fox (1968). “The viscosity of polymers and their concentrated solutions”. en. In: *Fortschritte der Hochpolymeren-Forschung*. Volume 5/3. Series Title: Advances in Polymer Science. Berlin/Heidelberg: Springer-Verlag, pages 261–357. ISBN: 978-3-540-04032-3. DOI: [10.1007/BFb0050985](https://doi.org/10.1007/BFb0050985).
- Boiko, Y. M., G. Guérin, V. A. Marikhin, and R. E. Prud’homme (2001). “Healing of interfaces of amorphous and semi-crystalline poly (ethylene terephthalate) in the vicinity of the glass transition temperature”. In: *Polymer* 42.21, pages 8695–8702.
- Bond dissociation energy table* (2021). URL: <https://labs.chem.ucsb.edu/zakarian/armen/11---bonddissociationenergy.pdf>.
- Bonten, C. and E. Schmachtenberg (2001). “A new hypothesis to describe the mechanisms acting in a welded joint of semicrystalline thermoplastics”. In: *Polymer Engineering & Science* 41.3, pages 475–483.
- Bosq, N., N. Guigo, E. Zhuravlev, and N. Sbirrazzuoli (2013). “Nonisothermal Crystallization of Polytetrafluoroethylene in a Wide Range of Cooling Rates”. en. In: *The Journal of Physical Chemistry B* 117.12, pages 3407–3415. ISSN: 1520-6106, 1520-5207. DOI: [10.1021/jp311196g](https://doi.org/10.1021/jp311196g).
- Boudara, V. A. H., D. J. Read, and J. Ramírez (2020). “REPTATE rheology software: Toolkit for the analysis of theories and experiments”. en. In: *Journal of Rheology* 64.3, pages 709–722. ISSN: 0148-6055, 1520-8516. DOI: [10.1122/8.0000002](https://doi.org/10.1122/8.0000002).
- Bousmina, M., H. Qiu, M. Grmela, and J. E. Klemberg-Sapieha (1998). “Diffusion at Polymer/Polymer Interfaces Probed by Rheological Tools”. en. In: *Macromolecules* 31.23, pages 8273–8280. ISSN: 0024-9297, 1520-5835. DOI: [10.1021/ma980562r](https://doi.org/10.1021/ma980562r).
- Boussinesq, J. (1885). *Application des potentiels à l’étude de l’équilibre et du mouvement des solides élastiques*. Gauthier-Villars. Volume 4.
- Brown, E. N., D. M. Dattelbaum, D. W. Brown, P. J. Rae, and B. Clausen (2007). “A new strain path to inducing phase transitions in semi-crystalline polymers”. en. In: *Polymer* 48.9, pages 2531–2536. ISSN: 00323861. DOI: [10.1016/j.polymer.2007.03.031](https://doi.org/10.1016/j.polymer.2007.03.031).
- Brown, E. N., P. J. Rae, D. M. Dattelbaum, B. Clausen, and D. W. Brown (2008). “In-situ Measurement of Crystalline Lattice Strains in Polytetrafluoroethylene”. en. In:

- Experimental Mechanics* 48.1, pages 119–131. ISSN: 0014-4851, 1741-2765. DOI: 10.1007/s11340-007-9075-3.
- Brown, H. R. (1991). “A molecular interpretation of the toughness of glassy polymers”. en. In: *Macromolecules* 24.10, pages 2752–2756. ISSN: 0024-9297, 1520-5835. DOI: 10.1021/ma00010a018.
- Bunn, C. W., A. J. Cobbold, and R. P. Palmer (1958). “The fine structure of polytetrafluoroethylene”. In: *Journal of Polymer Science Part A: Polymer Chemistry* 28.117, pages 365–376.
- Calleja, G., A. Jourdan, B. Ameduri, and J.-P. Habas (2013). “Where is the glass transition temperature of poly (tetrafluoroethylene)? A new approach by dynamic rheometry and mechanical tests”. In: *European Polymer Journal* 49.8, pages 2214–2222.
- Canto, R. B., N. Schmitt, J. De Carvalho, and R. Billardon (2011). “Experimental identification of the deformation mechanisms during sintering of cold compacted polytetrafluoroethylene powders”. en. In: *Polymer Engineering & Science* 51.11, pages 2220–2235. ISSN: 00323888. DOI: 10.1002/pen.21994.
- Chemfilm, S.-G. (2021). *DF100 and Type C/CD*. URL: [https://www.films.saint-gobain.com/sites/imdf.specialtyfilms.com/files/specialty\\_films\\_chemfilm\\_cast\\_film\\_73867\\_0\\_0.pdf](https://www.films.saint-gobain.com/sites/imdf.specialtyfilms.com/files/specialty_films_chemfilm_cast_film_73867_0_0.pdf). (accessed: 06.23.2021).
- Cho, B.-R. and J. L. Kardos (1995). “Consolidation and self-bonding in poly(ether ether ketone) (PEEK)”. en. In: *Journal of Applied Polymer Science* 56.11, pages 1435–1454. ISSN: 00218995, 10974628. DOI: 10.1002/app.1995.070561106.
- Chu, B. and B. S. Hsiao (2001). “Small-Angle X-ray Scattering of Polymers”. en. In: *Chemical Reviews* 101.6, pages 1727–1762. ISSN: 0009-2665, 1520-6890. DOI: 10.1021/cr9900376.
- Clark, E. (1999). “The molecular conformations of polytetrafluoroethylene: forms II and IV”. en. In: *Polymer* 40.16, pages 4659–4665. ISSN: 00323861. DOI: 10.1016/S0032-3861(99)00109-3.
- Creton, C. and M. Ciccotti (2016). “Fracture and adhesion of soft materials: a review”. In: *Reports on Progress in Physics* 79.4, page 046601. ISSN: 0034-4885, 1361-6633. DOI: 10.1088/0034-4885/79/4/046601.
- Creton, C., E. J. Kramer, H. R. Brown, and C.-Y. Hui (2002). “Adhesion and Fracture of Interfaces Between Immiscible Polymers: from the Molecular to the Continuum Scal”. In: *Molecular Simulation Fracture Gel Theory*. Berlin, Heidelberg: Springer Berlin Heidelberg, pages 53–136. ISBN: 978-3-540-45141-9. DOI: 10.1007/3-540-45141-2\_2.
- Creton, C., E. J. Kramer, C. Y. Hui, and H. R. Brown (1992). “Failure mechanisms of polymer interfaces reinforced with block copolymers”. en. In: *Macromolecules* 25.12, pages 3075–3088. ISSN: 0024-9297, 1520-5835. DOI: 10.1021/ma00038a010.
- Dasgupta, N. (2016). “PTFE Orientation by X-Ray Diffraction”. en. In: *Saint-Gobain Internal report*.
- De Gennes, P.-G. (1971). “Reptation of a Polymer Chain in the Presence of Fixed Obstacles”. en. In: *The Journal of Chemical Physics* 55.2, pages 572–579.
- (1980a). “Comptes Rendus de l’Académie des Sciences, Paris. 1980”. In: *B291* 219.
- (1980b). “Dynamics of fluctuations and spinodal decomposition in polymer blends”. en. In: *The Journal of Chemical Physics* 72.9, pages 4756–4763. ISSN: 0021-9606, 1089-7690. DOI: 10.1063/1.439809.
- (1992). “Mechanical Properties of Polymer Interfaces”. In: *Physics of Polymer Surfaces and Interfaces*. Butterworth-Heinemann; Manning Publications Co. London: Sanchez, I.C., Fitzpatrick, L.E., page 55.

- De Gennes, P.-G. and F. Brochard-Wyart (1993). “Rheology at interfaces”. In: *The Interfacial Interactions in Polymeric Composites*. Springer, pages 61–80.
- Doi, M. and S. F. Edwards (1979). “Dynamics of concentrated polymer systems. Part 4.—Rheological properties”. In: *Journal of the Chemical Society, Faraday Transactions 2: Molecular and Chemical Physics* 75.0. Publisher: The Royal Society of Chemistry, pages 38–54. ISSN: 0300-9238. DOI: [10.1039/F29797500038](https://doi.org/10.1039/F29797500038).
- Doi, M. and S. F. Edwards (1978). “Dynamics of rod-like macromolecules in concentrated solution. Part 2”. In: *Journal of the Chemical Society, Faraday Transactions 2: Molecular and Chemical Physics* 74.0. Publisher: The Royal Society of Chemistry, pages 918–932. ISSN: 0300-9238. DOI: [10.1039/F29787400918](https://doi.org/10.1039/F29787400918).
- Drobny, J. G. (2009). *Technology of fluoropolymers*. 2nd ed. OCLC: ocn154683820. Boca Raton: CRC Press. ISBN: 978-1-4200-6317-2.
- Dupré, A. and P. Dupré (1869). *Théorie mécanique de la chaleur*. Gauthier-Villars.
- Ebnesajjad, S. (2000). *Fluoroplastics vol. 1: Non-Melt Processible Fluoroplastics the Definitive User’s Guide and Databook*. Inc. Norwich. 19. NY: Williams Andrew.
- (2011). *4 Introduction to Fluoropolymers*. Elsevier. Applied Plastics Engineering Handbook.
- Edwards, S. F. (1967). “The statistical mechanics of polymerized material”. en. In: *Proceedings of the Physical Society* 92.1, pages 9–16. ISSN: 0370-1328. DOI: [10.1088/0370-1328/92/1/303](https://doi.org/10.1088/0370-1328/92/1/303).
- Ferry, J. D. (1980). *Viscoelastic properties of polymers*. John Wiley & Sons. ISBN: 0-471-04894-1.
- Ferry, L., G. Vigier, R. Vassoille, and J. L. Bessede (1995). “Study of polytetrafluoroethylene crystallization”. In: *Acta polymerica* 46.4, pages 300–306.
- Frederix, C., P. Beauchene, R. Seguela, and J. Lefebvre (2013). “Kinetics of the non-isothermal fusion-welding of unlike ethylene copolymers over a wide crystallinity range”. en. In: *Polymer* 54.11, pages 2755–2763. ISSN: 00323861. DOI: [10.1016/j.polymer.2013.03.038](https://doi.org/10.1016/j.polymer.2013.03.038).
- Gent, A., E.-G. Kim, and P. Ye (1997). “Autohesion of Crosslinked Polyethylene”. In: *Journal of Polymer Science Part B - Polymer Physics* 35.4, pages 615–622.
- Gent, A. and R. Petrich (1969). “Adhesion of viscoelastic materials to rigid substrates”. In: *Proceedings of the Royal Society of London. A. Mathematical and Physical Sciences* 310.1502, pages 433–448.
- Gibert, F., A. Allal, G. Marin, and C. Derail (1999). “Effect of the rheological properties of industrial hot-melt and pressure-sensitive adhesives on the peel behavior”. In: *Journal of adhesion science and technology* 13.9. Publisher: Taylor & Francis, pages 1029–1044. ISSN: 0169-4243.
- Glaris, P. (2013). “Ingénierie de surface de matériaux composites pour l’aéronautique: chimie et topographie de surface, une aide au démoulage?” fr. PhD thesis.
- Glaris, P., J.-F. Coulon, M. Dorget, and F. Poncin-Epaillard (2013). “Thermal annealing as a new simple method for PTFE texturing”. en. In: *Polymer* 54.21, pages 5858–5864. ISSN: 00323861. DOI: [10.1016/j.polymer.2013.08.011](https://doi.org/10.1016/j.polymer.2013.08.011).
- Glasstone, S., K. J. Laidler, and H. Eyring (1941). *The theory of rate processes; the kinetics of chemical reactions, viscosity, diffusion and electrochemical phenomena*. Technical report. McGraw-Hill Book Company,
- Graessley, W. W. (1980). “Some phenomenological consequences of the Doi–Edwards theory of viscoelasticity”. en. In: *Journal of Polymer Science: Polymer Physics Edition* 18.1, pages 27–34. ISSN: 00981273, 15429385. DOI: [10.1002/pol.1980.180180103](https://doi.org/10.1002/pol.1980.180180103).

- Graessley, W. W. (1982). “Entangled linear, branched and network polymer systems — Molecular theories”. In: *Synthesis and Degradation Rheology and Extrusion*. Berlin, Heidelberg: Springer Berlin Heidelberg, pages 67–117. ISBN: 978-3-540-39483-9.
- Griffith, A. A. (1921). “VI The phenomena of rupture and flow in solids”. In: *Philosophical transactions of the royal society of London*. Series A 221.582-593, pages 163–198.
- Guenoun, G., J.-Y. Faou, G. Régnier, N. Schmitt, and S. Roux (2019). “Thermal cycling of cold-pressed PTFE compacts: Reversible and irreversible behavior”. en. In: *Polymer Testing* 75, pages 99–106. ISSN: 01429418. DOI: [10.1016/j.polymertesting.2019.01.018](https://doi.org/10.1016/j.polymertesting.2019.01.018).
- (2020). “PTFE crystallization mechanisms: Insight from calorimetric and dilatometric experiments”. en. In: *Polymer*, page 122333. ISSN: 00323861. DOI: [10.1016/j.polymer.2020.122333](https://doi.org/10.1016/j.polymer.2020.122333).
- Hermans, P. H. and A. Weidinger (1961). “On the determination of the crystalline fraction of polyethylenes from X-ray diffraction.” en. In: *Die Makromolekulare Chemie* 44.1, pages 24–36. ISSN: 0025116X, 0025116X. DOI: [10.1002/macp.1961.020440103](https://doi.org/10.1002/macp.1961.020440103).
- Hertz, H. (1882). “Über die Berührung fester elastischer Körper”. In: *Journal für die reine und angewandte Mathematik* 92, pages 156–171.
- Hoffman, J. D., G. T. Davis, and J. I. Lauritzen (1976). “The rate of crystallization of linear polymers with chain folding”. In: *Treatise on solid state chemistry*. Springer, pages 497–614.
- Hrennikoff, A. (1941). “Solution of problems of elasticity by the framework method”. In.
- Huang, T. C., H. Toraya, T. N. Blanton, and Y. Wu (1993). “X-ray powder diffraction analysis of silver behenate, a possible low-angle diffraction standard”. en. In: *Journal of Applied Crystallography* 26.2, pages 180–184. ISSN: 00218898. DOI: [10.1107/S0021889892009762](https://doi.org/10.1107/S0021889892009762).
- Irwin, G. R. (1957). “Analysis of stresses and strains near the end of a crack traversing a plate”. In.
- Irwin, G. R. (1956). *Onset of fast crack propagation in high strength steel and aluminum alloys*. Technical report. Naval Research Lab Washington DC.
- Israelachvili, J. N. (2011). *Intermolecular and surface forces*. Academic press.
- Israelachvili, J. N. and G. Adams (1976). “Direct measurement of long range forces between two mica surfaces in aqueous KNO<sub>3</sub> solutions”. In: *Nature* 262.5571, pages 774–776.
- Jarrousse, G. (2004). “Self adhesion of semi-crystalline polymers between their glass transition temperature and their melting temperature”. PhD Thesis. Université Pierre et Marie Curie-Paris VI.
- Jiang, Y., D. Choudhury, M. Brownell, A. Nair, J. A. Goss, and M. Zou (2019). “The effects of annealing conditions on the wear of PDA/PTFE coatings”. en. In: *Applied Surface Science* 481, pages 723–735. ISSN: 01694332. DOI: [10.1016/j.apsusc.2019.03.076](https://doi.org/10.1016/j.apsusc.2019.03.076).
- Johnson, K. L. (1987). *Contact mechanics*. Cambridge university press.
- Johnson, K. L., K. Kendall, and A. Roberts (1971). “Surface energy and the contact of elastic solids”. In: *Proc. R. Soc. Lond. A* 324.1558, pages 301–313.
- Jud, K. and H. Kausch (1979). “Load transfer through chain molecules after interpenetration at interfaces”. en. In: *Polymer Bulletin* 1.10. ISSN: 0170-0839, 1436-2449. DOI: [10.1007/BF00255445](https://doi.org/10.1007/BF00255445).
- Jud, K., H. Kausch, and J. G. Williams (1981). “Fracture mechanics studies of crack healing and welding of polymers”. In: *Journal of materials science* 16.1, pages 204–210.

- Kaelble, D. (1964). "Theory and analysis of peel adhesion: Rate-temperature dependence of viscoelastic interlayers". en. In: *Journal of Colloid Science* 19.5, pages 413–424. ISSN: 00958522. DOI: [10.1016/0095-8522\(64\)90041-8](https://doi.org/10.1016/0095-8522(64)90041-8).
- Kendall, K. (1975). "Thin-film peeling-the elastic term". en. In: *Journal of Physics D: Applied Physics* 8.13, pages 1449–1452. ISSN: 0022-3727, 1361-6463. DOI: [10.1088/0022-3727/8/13/005](https://doi.org/10.1088/0022-3727/8/13/005).
- Kerbow, D. and C. Sperati (1999). In *Polymer Handbook*, ; Brandrup, J.; Immergut, EH; Grulke, EA, Eds.
- Kim, Y. H. and R. P. Wool (1983). "A theory of healing at a polymer-polymer interface". In: *Macromolecules* 16.7, pages 1115–1120.
- Kinloch, A. J. (1980). "The science of adhesion". en. In: *Journal of materials science* 15.9, pages 2141–2166.
- Kinloch, A. J., C. C. Lau, and J. G. Williams (1994). "The peeling of flexible laminates". In: *International Journal of Fracture* 66.1, pages 45–70.
- Kobayashi, E., K. K. Okudaira, and T. Okajima (2012). "Effects of annealing on the molecular orientation in polytetrafluoroethylene thin films: Effects of annealing on the molecular orientation in PTFE thin films". en. In: *Surface and Interface Analysis* 44.6, pages 740–743. ISSN: 01422421. DOI: [10.1002/sia.4895](https://doi.org/10.1002/sia.4895).
- Kramer, E. J. (1983). "Microscopic and molecular fundamentals of crazing". en. In: *Crazing in polymers*. Springer, Berlin, Heidelberg, pages 1–56.
- Kramer, E. J. and L. L. Berger (1990). "Fundamental processes of craze growth and fracture". en. In: *Crazing in Polymers Vol. 2*. Edited by H. Kausch. Volume 91/92. Series Title: Advances in Polymer Science. Berlin, Heidelberg: Springer Berlin Heidelberg, pages 1–68. ISBN: 978-3-540-51306-3. DOI: [10.1007/BFb0018018](https://doi.org/10.1007/BFb0018018).
- Lam  the, J.-F., P. Beauch  ne, and L. L  ger (2005). "Polymer dynamics applied to PEEK matrix composite welding". en. In: *Aerospace Science and Technology* 9.3, pages 233–240. ISSN: 12709638. DOI: [10.1016/j.ast.2005.01.008](https://doi.org/10.1016/j.ast.2005.01.008). (Visited on 05/07/2018).
- Lange, N. A. (1999). *Lange's handbook of chemistry*. en. Edited by J. A. Dean. 15. ed. McGraw-Hill handbooks. New York, NY: McGraw-Hill. ISBN: 978-0-07-016384-3.
- Lebedev, Y. A., Y. M. Korolev, V. M. Polikarpov, L. N. Ignat'eva, and E. M. Antipov (2010). "X-ray powder diffraction study of polytetrafluoroethylene". en. In: *Crystallography Reports* 55.4, pages 609–614. ISSN: 1063-7745, 1562-689X. DOI: [10.1134/S1063774510040127](https://doi.org/10.1134/S1063774510040127).
- Lee, L.-H., editor (1991a). *Adhesive Bonding*. en. Boston, MA: Springer US. ISBN: 978-1-4757-9008-5 978-1-4757-9006-1. DOI: [10.1007/978-1-4757-9006-1](https://doi.org/10.1007/978-1-4757-9006-1). (Visited on 06/03/2021).
- editor (1991b). *Fundamentals of Adhesion*. en. Boston, MA: Springer US. ISBN: 978-1-4899-2075-1 978-1-4899-2073-7. DOI: [10.1007/978-1-4899-2073-7](https://doi.org/10.1007/978-1-4899-2073-7).
- Lee, W. I. and G. S. Springer (1987). "A model of the manufacturing process of thermoplastic matrix composites". In: *Journal of composite materials* 21.11, pages 1017–1055.
- Lehnert, R., P. Hendra, N. Everall, and N. Clayden (1997). "Comparative quantitative study on the crystallinity of poly(tetrafluoroethylene) including Raman, infra-red and 19F nuclear magnetic resonance spectroscopy". In: *Polymer* 38.7, pages 1521–1535.
- Luengo, G., J. Pan, M. Heuberger, and J. N. Israelachvili (1998). "Temperature and Time Effects on the "Adhesion Dynamics" of Poly(butyl methacrylate) (PBMA) Surfaces". en. In: *Langmuir* 14.14, pages 3873–3881. ISSN: 0743-7463, 1520-5827. DOI: [10.1021/1a971304a](https://doi.org/10.1021/1a971304a).

- Maeda, N. (2002). “Adhesion and Friction Mechanisms of Polymer-on-Polymer Surfaces”. en. In: *Science* 297.5580, pages 379–382. ISSN: 00368075, 10959203. DOI: [10.1126/science.1072378](https://doi.org/10.1126/science.1072378).
- Marthelot, J. (2016). “Rupture et délamination de films minces”. fr. PhD thesis.
- materials, A. (no date). *Stainless steel*. URL: <https://www.azom.com/properties.aspx?ArticleID=863>. (accessed: 06.24.2021).
- Maugis, D. and M. Barquins (1978). “Fracture mechanics and the adherence of viscoelastic bodies”. en. In: *Journal of Physics D: Applied Physics* 11.14, pages 1989–2023. ISSN: 0022-3727, 1361-6463. DOI: [10.1088/0022-3727/11/14/011](https://doi.org/10.1088/0022-3727/11/14/011).
- McGuiggan, P. M., J. S. Wallace, D. T. Smith, I. Sridhar, Z. W. Zheng, and K. L. Johnson (2007). “Contact mechanics of layered elastic materials: experiment and theory”. In: *Journal of Physics D: Applied Physics* 40.19, pages 5984–5994. ISSN: 0022-3727, 1361-6463. DOI: [10.1088/0022-3727/40/19/031](https://doi.org/10.1088/0022-3727/40/19/031).
- Mishra, D. (2021). *Experimental assessment of adhesion properties between two PTFE films*. Technical report. Master 2 thesis, ENSAM Paris.
- Neupauer, A. (2014). *Introduction into the processing of PTFE resins*. Technical report. pro-K Fluoropolymergroup.
- Omega - Cartridge Heaters (2019). URL: [https://www.omega.fr/heaters/pdf/CSS\\_CSH.pdf](https://www.omega.fr/heaters/pdf/CSS_CSH.pdf).
- Pan, Z., R. Ma, D. Wang, and A. Chen (2018). “A review of lattice type model in fracture mechanics: theory, applications, and perspectives”. en. In: *Engineering Fracture Mechanics* 190, pages 382–409. ISSN: 00137944. DOI: [10.1016/j.engfracmech.2017.12.037](https://doi.org/10.1016/j.engfracmech.2017.12.037). URL: <https://linkinghub.elsevier.com/retrieve/pii/S0013794417308391>.
- Parasnis, N. and K. Ramani (1999). “Non-isothermal crystallization of UHMWPE”. In: *Journal of thermal analysis and calorimetry* 55.3, pages 709–719.
- Polymer data handbook* (1999). Oxford university press. Mark, James E.
- Preiß, E. (Jan. 2018). “Fracture Toughness of Freestanding Metallic Thin Films Studied by Bulge Testing”. PhD thesis.
- Putts, G. J., P. Crouse, and B. M. Ameduri (2019). “Polytetrafluoroethylene: Synthesis and Characterization of the Original Extreme Polymer”. en. In: *Chemical Reviews* 119.3, pages 1763–1805. ISSN: 0009-2665, 1520-6890. DOI: [10.1021/acs.chemrev.8b00458](https://doi.org/10.1021/acs.chemrev.8b00458).
- Rae, P. and E. Brown (2005). “The properties of poly(tetrafluoroethylene) (PTFE) in tension”. en. In: *Polymer* 46.19, pages 8128–8140. ISSN: 00323861. DOI: [10.1016/j.polymer.2005.06.120](https://doi.org/10.1016/j.polymer.2005.06.120).
- Rahl, F. J., M. A. Evanco, R. J. Fredericks, and A. C. Reimschuessel (1972). “Studies of the morphology of emulsion-grade polytetrafluoroethylene”. In: *Journal of Polymer Science Part B: Polymer Physics* 10.7, pages 1337–1349.
- Régnier, G. and S. Le Corre (2016). “Modeling of Thermoplastic Welding”. In: *Heat Transfer in Polymer Composite Materials Forming Processes*. ISTE Wiley. London & Hoboken: N. Boyard, pages 235–263.
- Rivlin, R. S. (1997). “The Effective Work of Adhesion”. en. In: *Collected Papers of R.S. Rivlin*. Edited by G. I. Barenblatt and D. D. Joseph. New York, NY: Springer New York, pages 2611–2614. ISBN: 978-1-4612-7530-5 978-1-4612-2416-7. DOI: [10.1007/978-1-4612-2416-7\\_179](https://doi.org/10.1007/978-1-4612-2416-7_179).
- Ruymbeke, E. van, C.-Y. Liu, and C. Bailly (2007). “Quantitative tube model predictions for the linear viscoelasticity of linear polymers”. en. In: page 82.

- Saint-Gobain Chemfab - PTFE coated fabrics European brochure* (2017). English. URL: [https://www.chemfab.com/sites/imdf.chemfab.com/files/chemfab\\_top\\_30\\_brochure\\_eu.pdf](https://www.chemfab.com/sites/imdf.chemfab.com/files/chemfab_top_30_brochure_eu.pdf) (visited on 12/27/2017).
- Saint-Gobain Onesuit protection brochure* (2021). English. URL: [https://www.onesuitprotection.com/sites/imdf.onesuitprotection.com/files/onesuit\\_web\\_0.pdf](https://www.onesuitprotection.com/sites/imdf.onesuitprotection.com/files/onesuit_web_0.pdf).
- Saint-Gobain Sheerfill - Interactive location map* (2021). English. URL: <https://www.sheerfill.com/resources/sheerfill-locations>.
- Saint-Gobain Sheergard - Ground based radomes brochure* (2021). English. URL: <https://www.sheergard.com/sites/imdf.sheergard.com/files/ground-based-radomes-brochure.pdf>.
- Sakasegawa, D. and A. Suzuki (Sept. 2009). “Adhesion curves between two viscoelastic materials by a point-contact method in a crossed-cylinder geometry”. en. In: *Journal of Polymer Science Part B: Polymer Physics* 47.18, pages 1778–1788. ISSN: 08876266, 10990488. DOI: 10.1002/polb.21781.
- Sauer, B. B., P. Avakian, and H. W. Starkweather Jr (1996). “Cooperative relaxations in semicrystalline fluoropolymers studied by thermally stimulated currents and ac dielectric”. In: *Journal of Polymer Science Part B: Polymer Physics* 34.3, pages 517–526.
- Schick, C. (2009). “Differential scanning calorimetry (DSC) of semicrystalline polymers”. en. In: *Analytical and Bioanalytical Chemistry* 395.6, pages 1589–1611. ISSN: 1618-2642, 1618-2650. DOI: 10.1007/s00216-009-3169-y.
- Sciuti, V. F., C. C. Melo, L. B. Canto, and R. B. Canto (2017). “Influence of Surface Crystalline Structures on DSC Analysis of PTFE”. In: *Materials Research* 20.5, pages 1350–1359. ISSN: 1980-5373, 1516-1439. DOI: 10.1590/1980-5373-mr-2017-0326.
- Smith, G. D., C. J. Plummer, P.-E. Bourban, and J.-A. E. Manson (2001). “Non-isothermal fusion bonding of polypropylene”. In: *Polymer* 42.14, pages 6247–6257.
- Sperati, C. A. and H. W. Starkweather (1961). “Fluorine-containing polymers. II. Polytetrafluoroethylene”. In: *Fortschritte Der Hochpolymeren-Forschung*. Springer, pages 465–495.
- Starkweather, H. W. (1986). “Melting and crystalline transitions in normal perfluoroalkanes and poly(tetrafluoroethylene)”. en. In: *Macromolecules* 19.4, pages 1131–1134. ISSN: 0024-9297, 1520-5835. DOI: 10.1021/ma00158a034.
- Starkweather, H. W., P. Zoller, G. A. Jones, and A. J. Vega (1982). “The heat of fusion of polytetrafluoroethylene”. en. In: *Journal of Polymer Science: Polymer Physics Edition* 20.4, pages 751–761. ISSN: 00981273, 15429385. DOI: 10.1002/pol.1982.180200416.
- Suzuki, A., T. Sato, D. Sakasegawa, H. Sawada, and M. Goto (2007). “Adhesion properties of swollen hydrogels evaluated by a point-contact method”. en. In: *Journal of Applied Polymer Science* 105.6, pages 3729–3738. ISSN: 00218995, 10974628. DOI: 10.1002/app.26434.
- TA Instruments, W. L. (2021). *Dynamic Mechanical Analysis Basic Theory & Applications Training - 2018*. URL: <http://www-cs-faculty.stanford.edu/~uno/abcde.html>. (accessed: 06.22.2021).
- Teflon PTFE* (2017). Technical report (302) 479-7731. Du Pont.
- Tervoort, T., J. Visjager, B. Graf, and P. Smith (2000). “Melt-Processable Poly(tetrafluoroethylene)”. In: *Macromolecules* 33.17, pages 6460–6465.
- Wan, K.-T. and D. A. Dillard (2003). “Adhesion of a flat punch adhered to a thin prestressed membrane”. en. In: *The Journal of Adhesion* 79.2, pages 123–140. ISSN: 0021-8464, 1545-5823. DOI: 10.1080/00218460309573.

- Wan, K.-T. and L. Kogut (2005). “The coupling effect of interfacial adhesion and tensile residual stress on a thin membrane adhered to a flat punch”. In: *Journal of Micromechanics and Microengineering* 15.4, page 778.
- Westergaard, H. M. (1939). “Bearing Pressures and Cracks: Bearing Pressures Through a Slightly Waved Surface or Through a Nearly Flat Part of a Cylinder, and Related Problems of Cracks”. In.
- White, J. L. and J. E. Spruiell (1983). “The specification of orientation and its development in polymer processing”. en. In: *Polymer Engineering and Science* 23.5, pages 247–256. ISSN: 0032-3888, 1548-2634. DOI: [10.1002/pen.760230503](https://doi.org/10.1002/pen.760230503).
- Wool, R. P. and K. M. O’Connor (1981). “A theory crack healing in polymers”. en. In: *Journal of Applied Physics* 52.10, pages 5953–5963. ISSN: 0021-8979, 1089-7550. DOI: [10.1063/1.328526](https://doi.org/10.1063/1.328526).
- Wool, R. P., B.-L. Yuan, and O. J. McGarel (1989). “Welding of polymer interfaces”. In: *Polymer Engineering & Science* 29.19, pages 1340–1367.
- Wright, D. T. (1965). “Membrane forces and buckling in reticulated shells”. In: *Journal of the structural division* 91.1, pages 173–201.
- Wu, J., H. Wang, B. Feng, Y. Li, S. Wu, Q. Yin, Z. Yu, and J. Huang (2020). “The effect of temperature-induced phase transition of PTFE on the dynamic mechanical behavior and impact-induced initiation characteristics of Al/PTFE”. In: *Polymer Testing* 91, page 106835. ISSN: 0142-9418. DOI: <https://doi.org/10.1016/j.polymertesting.2020.106835>.
- Xu, D.-B., C.-Y. Hui, E. Kramer, and C. Creton (1991). “A micromechanical model of crack growth along polymer interfaces”. en. In: *Mechanics of Materials* 11.3, pages 257–268. ISSN: 01676636. DOI: [10.1016/0167-6636\(91\)90007-M](https://doi.org/10.1016/0167-6636(91)90007-M).
- Xue, Y.-Q., T. A. Tervoort, and P. J. Lemstra (1998). “Welding behavior of semicrystalline polymers. 1. The effect of nonequilibrium chain conformations on autoadhesion of UHMWPE”. In: *Macromolecules* 31.9.
- Xue, Y.-Q., T. A. Tervoort, S. Rastogi, and J. Lemstra (2000). “Welding Behavior of Semicrystalline Polymers. 2. Effect of Cococrystallization on Autoadhesion”. en. In: *Macromolecules* 33.19, pages 7084–7087. ISSN: 0024-9297, 1520-5835. DOI: [10.1021/ma000754y](https://doi.org/10.1021/ma000754y).
- Yang, J., K. L. Petersen, R. A. Williams, P. H. Geil, T. C. Long, and P. Xu (2005). “Morphology evolution in PTFE as a function of melt time and temperature I: high molecular weight single- and multi-molecule folded chain single crystals and band structures”. In: *Chinese journal of polymer science* 23.02, pages 123–135.
- Young, T. (1805). *An assay on the cohesion of fluids*. Philos. Technical report. TR Soc., 95: 65–87.
- Yuan, B.-L. and R. P. Wool (1990). “Strength development at incompatible semicrystalline polymer interfaces”. en. In: *Polymer Engineering and Science* 30.22, pages 1454–1464. ISSN: 0032-3888, 1548-2634. DOI: [10.1002/pen.760302206](https://doi.org/10.1002/pen.760302206).
- Zeng, H., N. Maeda, N. Chen, M. Tirrell, and J. Israelachvili (2006). “Adhesion and Friction of Polystyrene Surfaces around  $T_g$ ”. en. In: *Macromolecules* 39.6, pages 2350–2363. ISSN: 0024-9297, 1520-5835. DOI: [10.1021/ma052207o](https://doi.org/10.1021/ma052207o).
- Zimm, B. H. (1956). “Dynamics of Polymer Molecules in Dilute Solution: Viscoelasticity, Flow Birefringence and Dielectric Loss”. en. In: *The Journal of Chemical Physics* 24.2, pages 269–278. ISSN: 0021-9606, 1089-7690. DOI: [10.1063/1.1742462](https://doi.org/10.1063/1.1742462).

# Contact between elastic object: the Hertz theory

In this appendix, the exact calculation for the Hertz theory is detailed.

Let consider the case of a sphere of radius  $R$ , with a Young's modulus  $E_1$  and a Poisson ratio  $\nu_1$ , and a plane made of a material of Young's modulus  $E_2$  and a Poisson ratio  $\nu_2$ . If no pressure  $P$ , or normal force  $F_H$  is applied, the contact is made only on a single point. Upon increasing of the normal force  $F_H$  between the two objects, by increasing the indentation  $\delta$ , the contact area is then a disk of radius  $a$ . Because of the angular symmetry, we choose a circular coordinate system  $(r, z)$ , see Figure A.1.

In Figure A.1, the distance  $OH$  is defined as the interpenetration depth  $OH = \delta$ . Near the  $z$ -axis, the distance between  $M$  (of coordinate  $z_1$ ) and  $N$  (of coordinate  $z_2$ ), two points on the undeformed surfaces of each object, taken vertically from each other, is given by  $z_1 + z_2 = \frac{r^2}{2R}$ . The non-interpenetrability of the sphere and the plane induces a sum of the deformations of the two objects in contact

$$u(z) = u_1(z_1) + u_2(z_2) = \delta - (z_1 + z_2) = \delta - \frac{r^2}{2R} \quad (\text{A.1})$$

The deformation  $u(z)$  depends on the pressure distribution. If we assume that the pressure distribution on the contact area is represented by the coordinate of a half-sphere of radius  $a$  constructed on the surface of contact, then the pressure distribution is given by

$$p(r) = p_0 \sqrt{1 - \frac{r^2}{a^2}} \quad (\text{A.2})$$

And it is shown in [Johnson 1987] that

$$u_z = \frac{\pi p_0}{4aE^*} (2a^2 - r^2) \quad (\text{A.3})$$

with  $E^* = \frac{E}{1-\nu^2}$  the reduced modulus. By combining equations A.1 and A.3, for  $r = 0$ ,  $u_z = \frac{\pi p_0 a}{2E^*} = \delta$

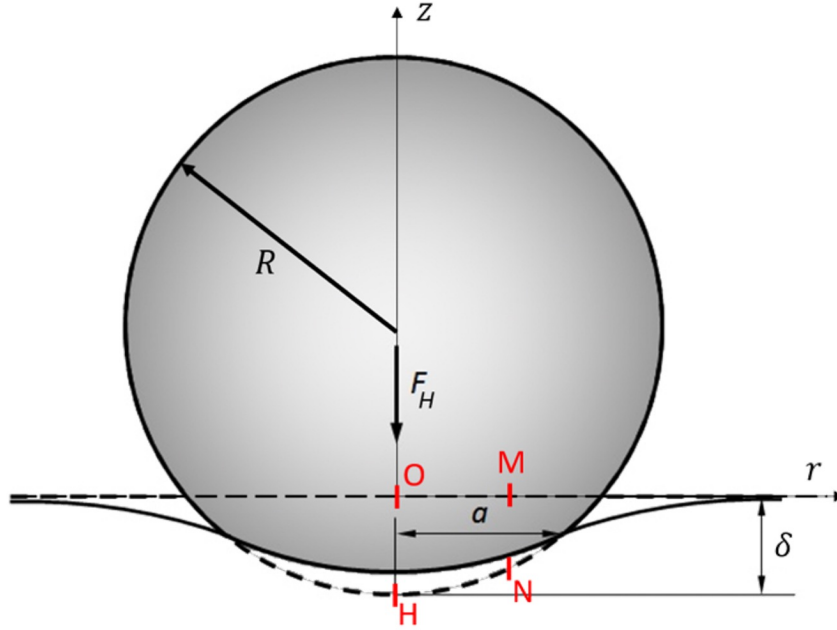


Figure A.1: Contact of an elastic sphere with an elastic half-space. Adapted from Wikipedia.

And for  $r = a$ ,  $u_z = \frac{\pi p_0 a}{4E^*} = \delta - \frac{a^2}{2R}$

$$a = \frac{\pi p_0 R}{2E^*} \quad (\text{A.4})$$

And finally,

$$\delta_H = \frac{a^2}{R} \quad (\text{A.5})$$

The total force acting between the solids is then,  $F = \int_0^a 2\pi r p(r) dr = \frac{2}{3} p_0 \pi a^2$

$$F_H = \frac{4}{3} \frac{E^* a^3}{R} \quad (\text{A.6})$$

The pressure repartition profile in the case of a Hertz contact between two elastic solids is then parabolic, as shown on Figure A.2. The maximum pressure occurring at the center of the contact zone is then  $p_0 = \frac{1}{\pi} \sqrt[3]{\frac{6FE^{*2}}{R^2}}$  and the corresponding contact area size is  $a = \sqrt[3]{\frac{3RF}{4E^*}}$ .

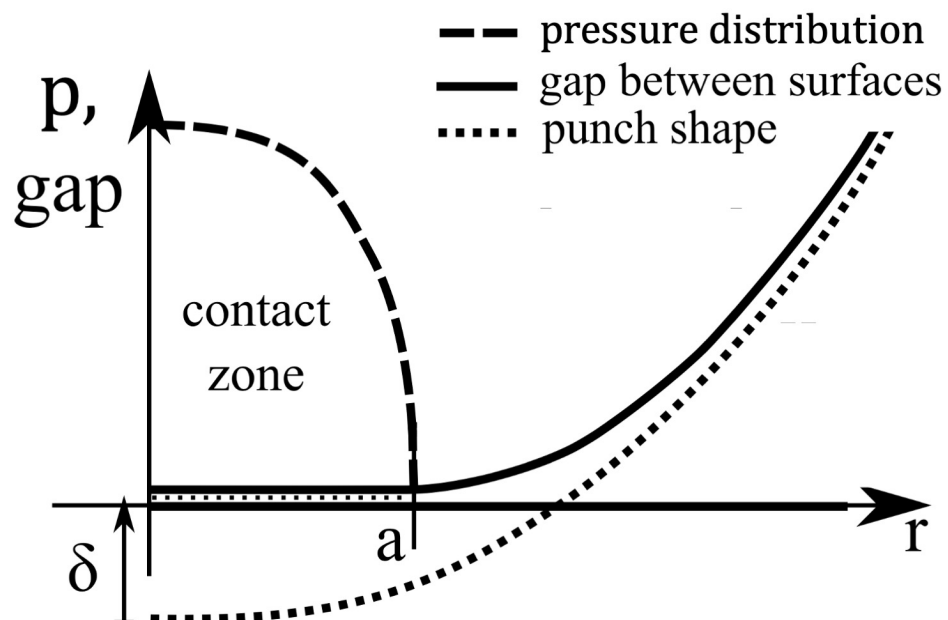


Figure A.2: The Hertz contact between two elastic solids. Pressure, gap between surfaces and punch shape distributions. The pressure is maximum at the center of the contact zone. Adapted from [Barthel 2008].



# Flat contact setup

## B.1 Test of principle

### B.1.1 Welding

#### Experimental setup

To realize a first approximate welding, sintered PTFE films deposited on both sides of a polyimide matrix are used. Two pieces of 20 cm long and 15 cm wide are cut and put in contact between two steel plates (15 cm long, 10 cm wide and 1.5 cm thick). This sandwich is placed into the oven on a steel cylinder linked to the fixed down jack as depicted on Figure B.1a. The oven has a fixed thermocouple (pilotage) to control the temperature evolution; it is placed at the high of the plates on a side. To follow the temperature evolution, other thermocouples were set at different places: in air just above the top plate (haut), on the cylinder below the plate (bas), outside the oven near the jack and the cooling cell (verin bas). The following thermal cycle is implemented: a ramp at 4°C/min from room temperature to 375°C, a plateau of 30 min at 375°C and then a cooling ramp at 2°C/min. Both imposed thermal cycle and measured one at the "pilotage" thermocouple are in good agreement, see Figure B.1b. The temperature measured at different locations are similar and close to the cooling cell is well regularized not exceeding 35°C, see Figure B.1c.

#### Results

After a night cooling, the sandwich is taken out of the oven and opened; the assembly on Figure B.2 is obtained. By hand, when applying a moderate force, it is not possible to separate the two films; the welding seems good even if it is clearly not homogeneous (air bubbles are present) as depicted by the color pattern.

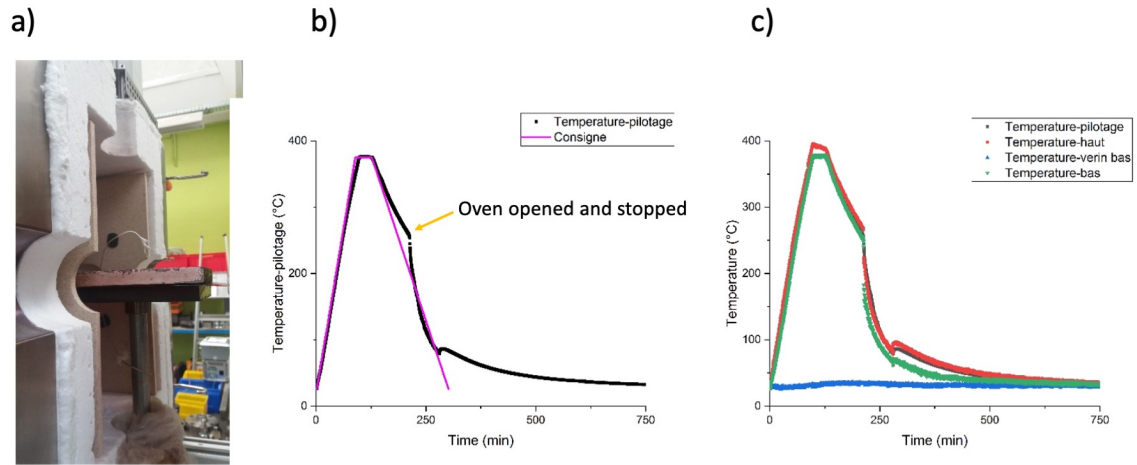


Figure B.1: a) Experimental welding setup, b) Imposed (pink) and measured (black) thermal cycle, c) Temperature measured at different locations.

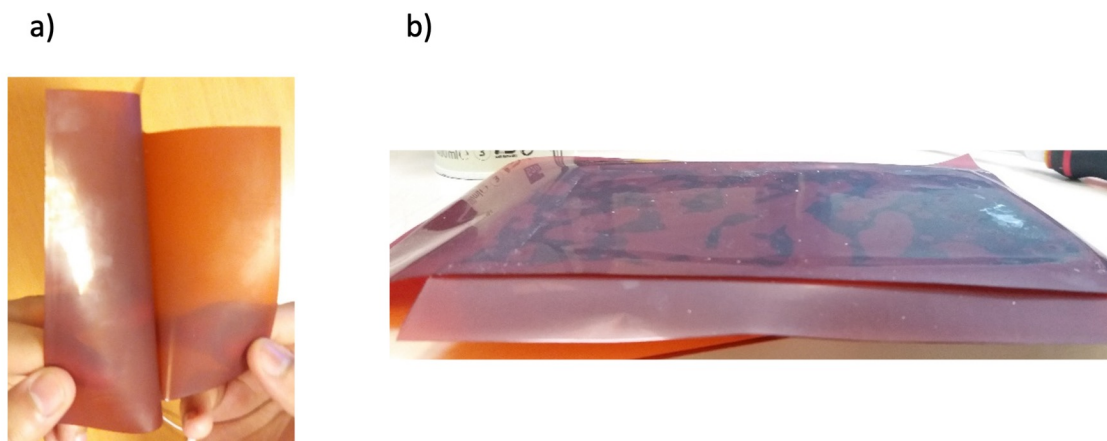


Figure B.2: Welding results: a) films can resist a moderate hand delamination, b) many welding defects are present at the interface.

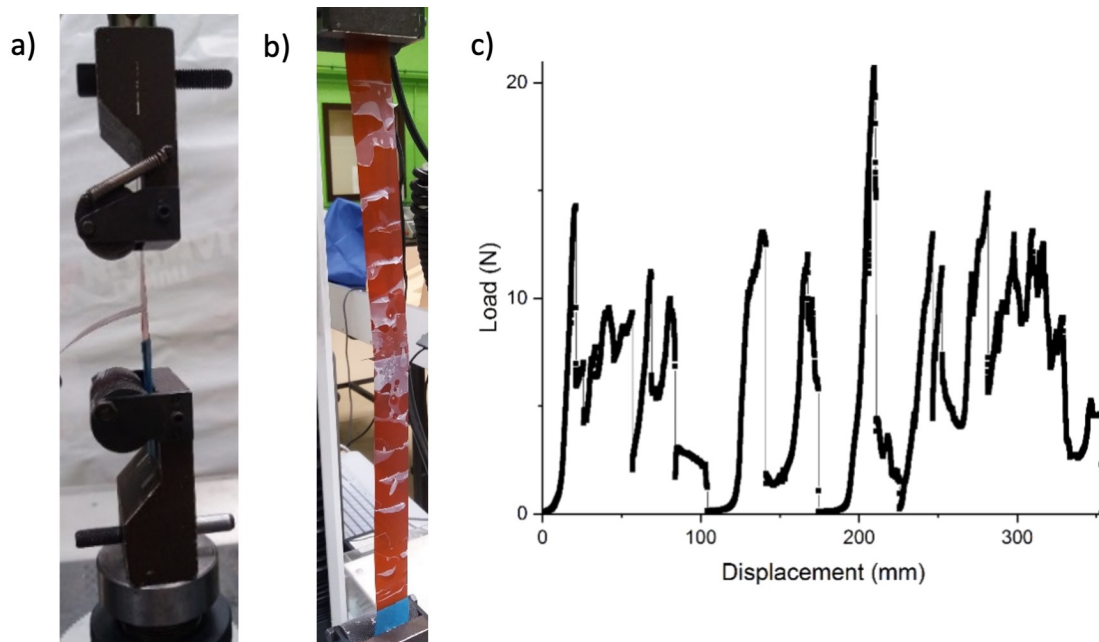


Figure B.3: a) Experimental peeling setup, Peeling results: b) fracture surface and c) peeling force versus displacement.

### B.1.2 Peeling

#### Experimental setup

A T-peel test is implemented on an Instron tensile machine equipped with a 2 kN load cell. Each arm is clamped between the cylinder equipped with springs and a plate surface. As the lower arm tends to slip, paint tape is added around it to improve adhesion, see Figure B.3a. The peeling is performed at 10 mm/min on about 15 cm and 5 cm arms at the load versus displacement curve is recorded.

#### Results

From the T-peel test described above, a fracture surface and the load versus displacement curve are obtained, see Figure B.3b & c. As the welding was not homogeneous, the peeling force is not constant: when a stuck zone is reached, the peel force increases but once it is broken, a not glued zone is reached with a zero-peel force and so on. On the fracture surface picture, at each stuck zone, on both sides a white zone appears characteristic of PTFE under shear. But, between which interface the rupture occurred? Is it between PTFE layers welded or between PTFE and the polyimide matrix? A way to verify this would be to perform infrared measurements on the fracture surface to know the chemical composition of the surface.

Even if we demonstrate that some zones have been well welded together, the welding is clearly not homogeneous; the welding step needs to be improved.

## B.2 Welding part design

The necessity of designing a welding device connecting the jacks not allowed to enter in the oven improving the welding homogeneity has been demonstrated above. A major stake

is how to spread the load coming from the cylindrical jaw homogeneously on a rectangular plate. By priority order, when designing such a structure, we should check:

- if the normal stress distribution at the interface is homogeneous,
- if the Mises strength is not exceeding the steel strength (250 MPa) in every point of the structure,
- that the structure is not bending,
- that the structure is not buckling.

### B.2.1 Flatness adjustment

On the flatness adjustment solution depicted on Figure B.4, the load is applied by the contact surface between the ball (to adjust the flatness of the assembly) and the plate. To check if the load is homogeneously spread on the whole contact surface (the underlying plate), the structure is simplified: it is only two steel plates (30 mm thick, 180 mm wide and 60 mm deep) put in contact allowed to slip tangentially (modeled by the steel-steel friction coefficient of 0.5), on which the load (10 kN force, pressure of 180 MPa) is applied on a disk (the ball of radius 20 mm is 5 mm down in the plate leading to a contact surface radius of 13.23 mm) at the center of the top plate. The disk at the center of the lower plate is fixed in all directions.

All materials are considered as purely elastic (steel young modulus of 210 GPa and Poisson's ratio of 0.3) and a simulation by finite element is run on Abaqus Simulia commercial software. Table B.1 presents other simulation parameters.

Simulation time	1 s
Time step	From 0.00001 to 1 s
Mesh element	C3D10

Table B.1: Table of flatness adjustment Abaqus simulation parameters.

From the simulation, the normal stress distribution in the whole structure is obtained; Figure B.5 shows a cut of the structure. We can see that the normal stress distribution at the interface between the two blocks is very inhomogeneous varying from -7 MPa on the sides to -70 MPa at the center.

### B.2.2 Four points of load application

As the solution presented above does not allow a homogeneous distribution of normal stress at the interface between the two contact surfaces, a new solution has been developed consisting in four points of load application through horizontal cylinders between the plates linked to the cylinders and the contact plates. The goal is now to find the position of the four points of load application allowing the most homogeneous normal stress distribution. In that aim, we simplified the structure in two dimensions: it's only two steel plates (30 mm thick, 180 mm wide) put in contact allowed to slip tangentially (modeled by the PTFE-steel friction coefficient of 0.1), on which 1 kN load (arbitrarily chosen) is applied punctually on the top and bottom plates, see Figure B.6. Considering the symmetries of the problem, we model only the left part of the structure. The cutting edge is fixed in longitudinal direction and its bottom point is fixed vertically. The aim is now to vary the length  $L_t$  and  $L_b$  respectively at the top and at the bottom and to observe the interfacial normal stress

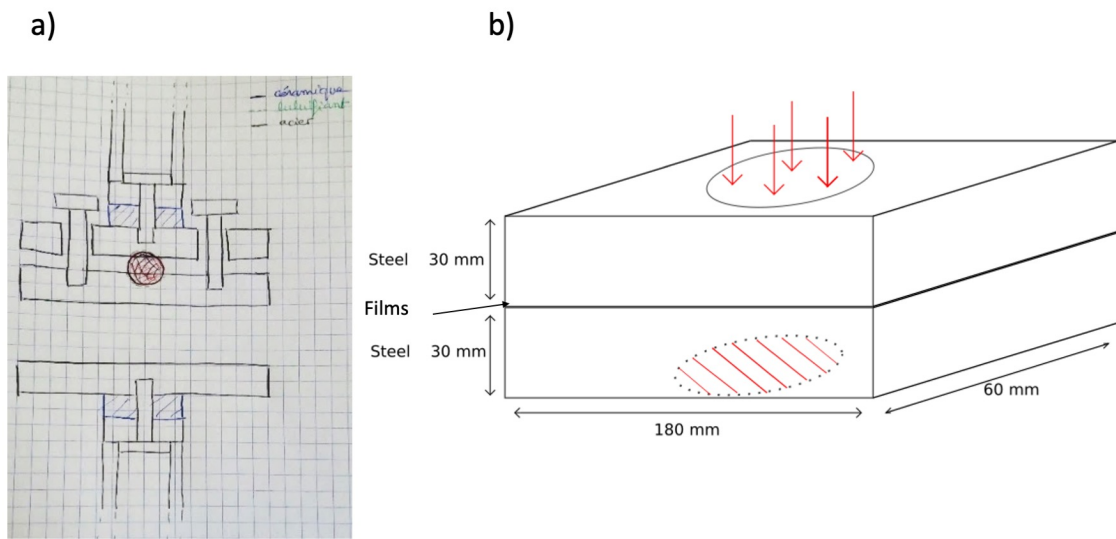


Figure B.4: Scheme of the flatness adjustment welding device and its simplified modelling.

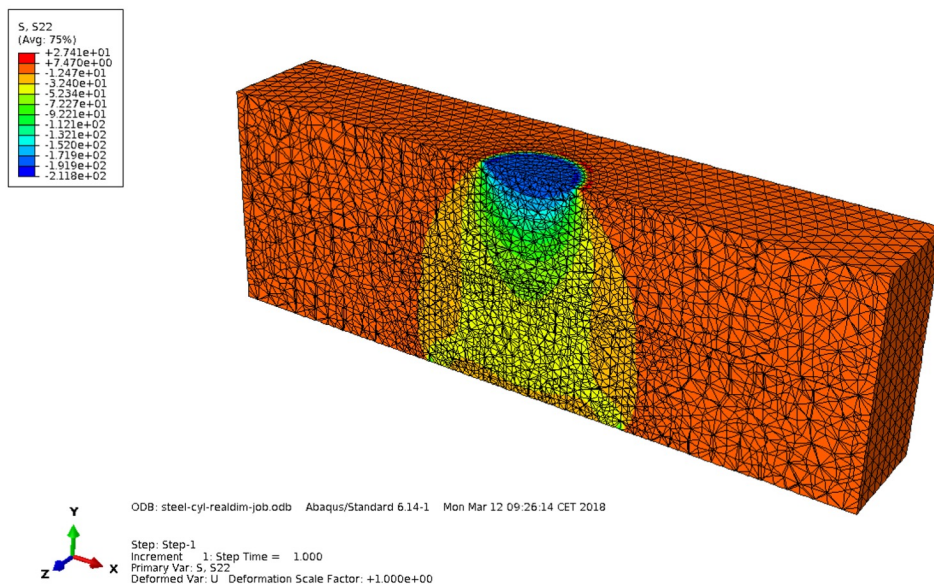


Figure B.5: Normal stress to the contact surface result from Abaqus finite elements simulation.

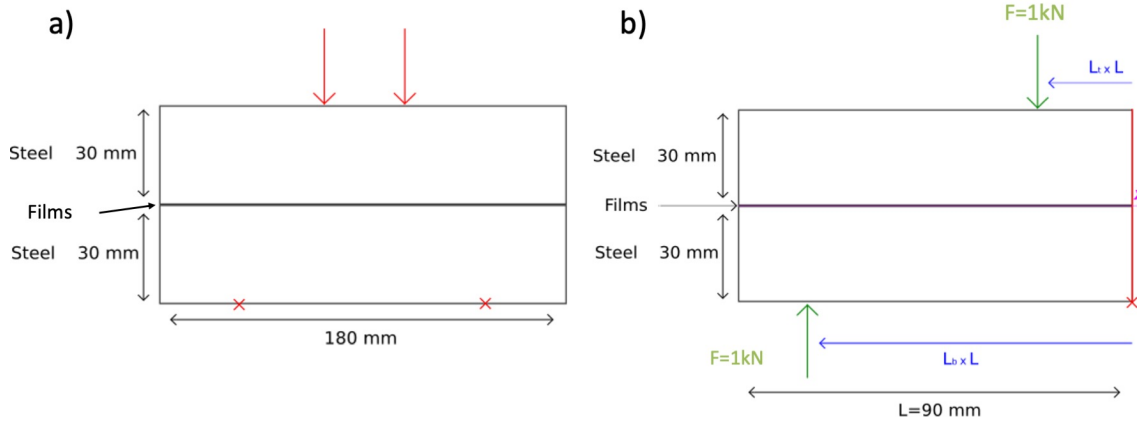


Figure B.6: Scheme of the four points of load application welding device and its simplified modelling.

distribution.

All materials are considered as purely elastic (steel young modulus of 210 GPa and Poisson's ratio of 0.3) and a simulation by finite element is run on Abaqus Simulia commercial software. The modelling is discretized temporally (with a variable time step) because of the strong geometric non-linearity and nonlinear behavior of the interface. Table B.2 presents other simulation parameters.

Simulation time	1 s
Time step	From 0.00001 to 1 s
Mesh element	CPS3

Table B.2: Table of four points of load application Abaqus simulation parameters.

By varying the top force application point from 10 to 40% of the total length (90 mm) and the bottom length by step of 10%, the results on Figure B.7 are obtained. The "best" solution should be allowed to reach a value of zero normal interfacial stress only at the exterior side on the left; only  $L_t = 0.2$  is then acceptable. Moreover, the stress variation should be minimized; the curve should be as flat as possible, so  $L_b$  can be in the range 0.6 to 0.8.

By keeping  $L_t = 0.2$  and looking more precisely at  $L_b$  between 0.6 and 0.8 (Figure B.8a), we deduce that the flattest curve and so the most homogeneous stress distribution is obtained for  $L_t = 0.2$  and  $L_b = 0.68$  (Figure B.8b).

The best solution depicted on Figure B.8b shows a stress variation of about 7 MPa and an unusable zone of about 16 mm at the exterior side; which is not satisfactory.

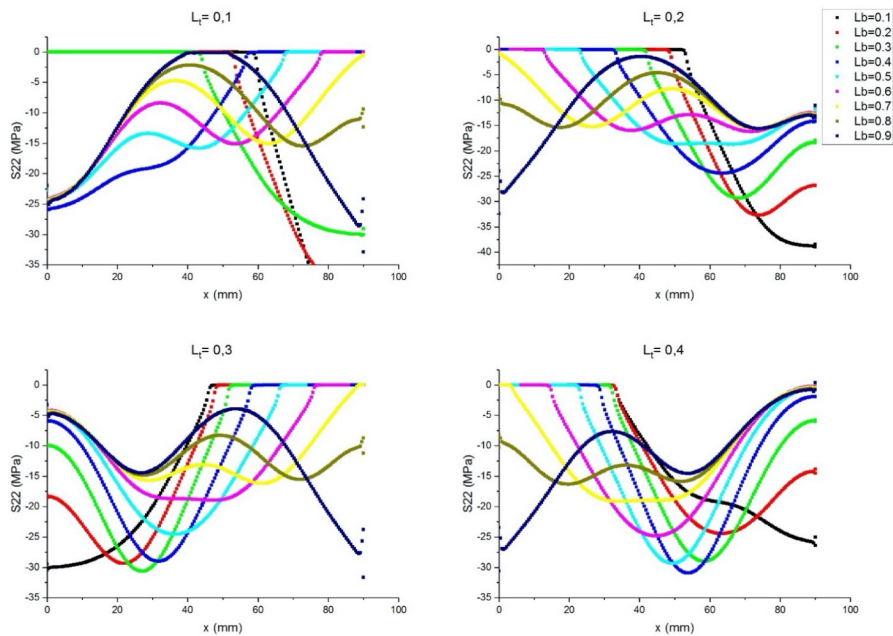


Figure B.7: Normal interfacial stress distribution for different positions of load points application.

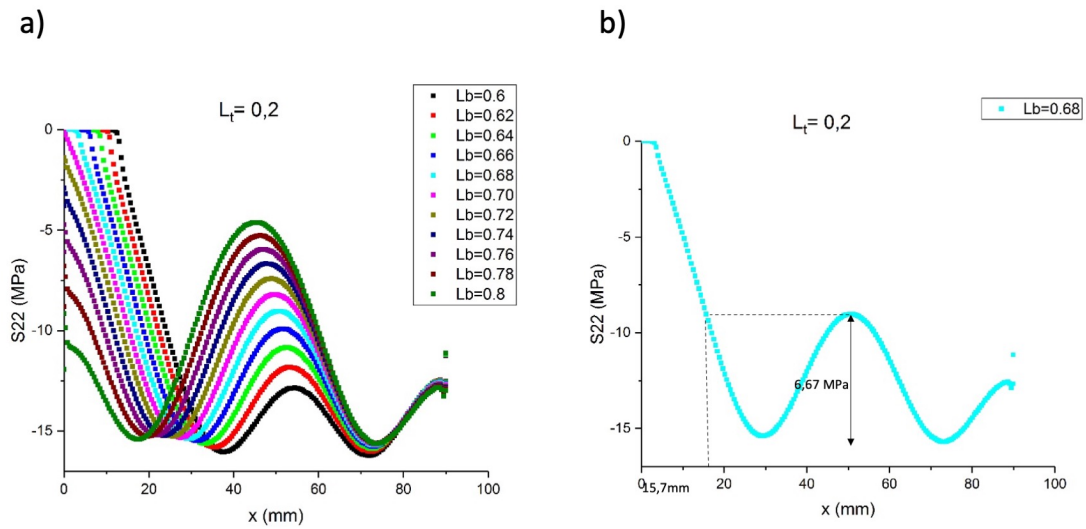


Figure B.8: Normal interfacial stress distribution for a)  $L_t = 0.2$  and  $L_b$  varying from 0.6 to 0.8, b) the best solution  $L_t = 0.2$  and  $L_b = 0.68$ .

### B.2.3 Soft intermediate layer

As the solution presented above does not allow a homogeneous distribution of normal stress at the interface between the two contact surfaces, a new solution has been developed consisting in incorporating a soft but viscous intermediate layer confined between the plate linked to the jaws and the one in contact with the samples. The goal is to check if this solution allows a homogeneous normal stress distribution when the intermediate layer is melted and viscous. In that aim, the structure is simplified: the PTFE soft intermediate layer (10 mm thick, 160 mm wide, 60 mm large) is sandwiched between two steel plates (30 mm thick, 160 mm wide, 60 mm large). The PTFE-steel interaction is modelled as a tangential slip (modeled by the PTFE-steel friction coefficient of 0.1). The load (force of 100 kN, pressure of 80 MPa) is applied on a 2cm radius disk at the center of the top plate, see Figure B.9. The steel plate in contact with the samples is fixed in vertical direction and the soft intermediate layer is not allowed to expand laterally. Considering the symmetries of the problem, only a quarter of the structure is modelled. The cutting faces are fixed in their normal directions.

PTFE has been chosen as a suitable material for the soft intermediate layer because it will not degrade at temperatures reaching its melting temperature and it will be viscous, so able to spread and transfer the load to the other steel plate. All materials are considered as purely elastic: the steel has the same Young's Modulus and Poisson's ratio as before and the PTFE intermediate layer has a Poisson's ratio of 0.48 and a Young's Modulus changing with temperature. At ambient temperature,  $E_{PTFE25^{\circ}C} \approx 500$  MPa [*Polymer data handbook 1999*] but at higher temperature, this value will decrease. Around the PTFE melting temperature, we can estimate the Young's Modulus value by its rubbery modulus:

$$E \approx \frac{3\rho RT}{M_e} \quad (\text{B.1})$$

with  $M_e = 3.7$  kg/mol the molar mass between entanglements [*Polymer data handbook 1999*],  $\rho = 2.16 \times 10^6$  g/m<sup>3</sup> the PTFE density [*Teflon PTFE 2017*],  $R$  the gas constant and  $T \approx 400^{\circ}C = 673.15$  K the temperature in Kelvin, leading to  $E_{PTFE400^{\circ}C} \approx 10$  MPa. A simulation by finite element is run on Abaqus Simulia commercial software. Table B.3 presents other simulation parameters.

Simulation time	1 s
Time step	From 0.00001 to 0.2 s
Large deformations	NLGEOM ON
Mesh element	C3D8R everywhere except on the load application cylinder on the top plate C3D10

Table B.3: Table of soft intermediate layer Abaqus simulation parameters.

From the simulation, the normal stress distribution in the whole structure is obtained and focus is on the normal stress distribution on the bottom surface depicted on Figure B.10. We can see that the normal stress distribution at the interface is quite homogeneous varying from 10 MPa on the left outside side to 10.7 MPa at the center. In the following, focus will be on the normal interfacial stress on the contact surface on the line called "center" depicted on Figures B.9 and B.10.

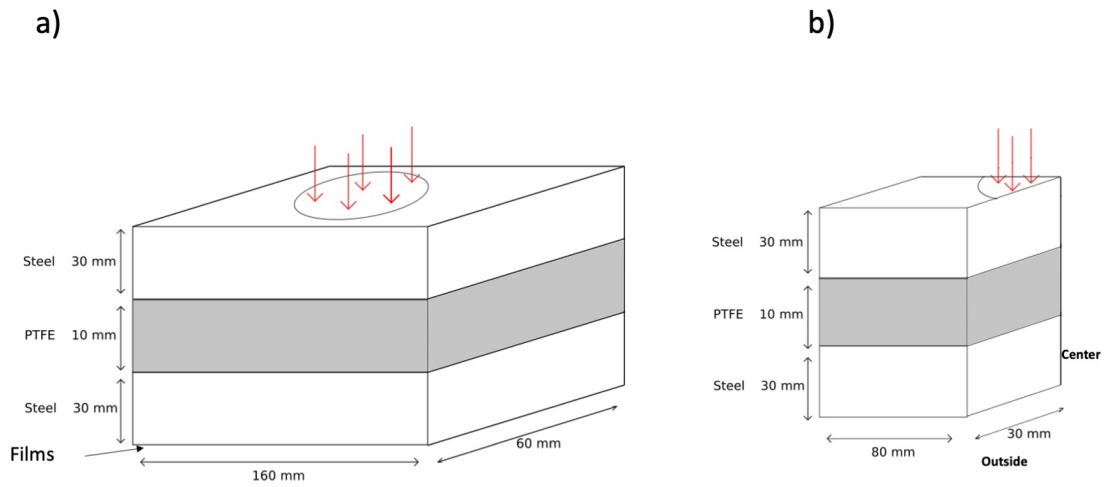


Figure B.9: Scheme of the soft intermediate layer welding device a) drawn and b) its simplified FEM model.

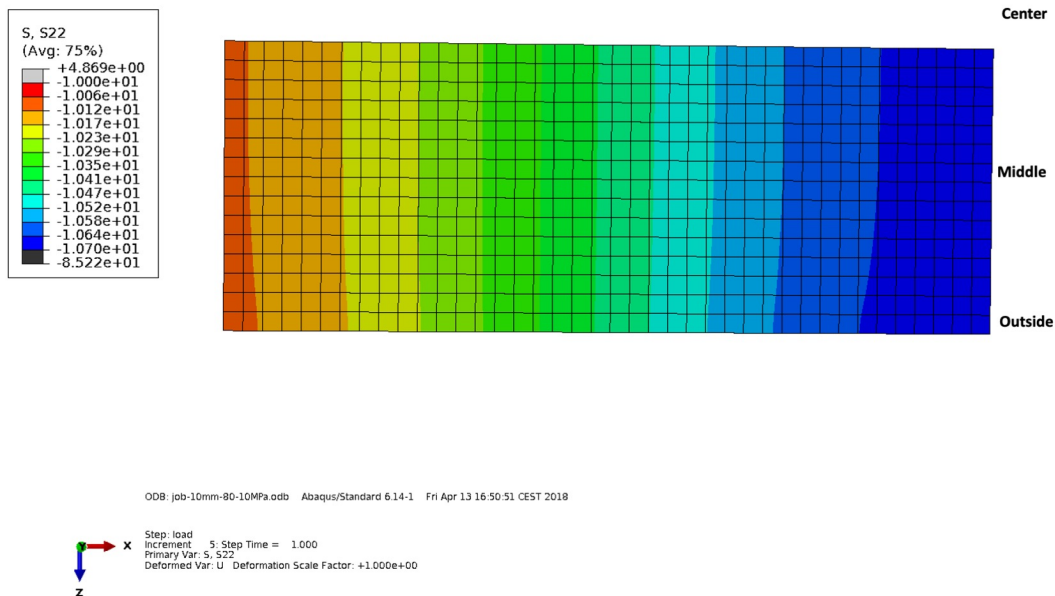


Figure B.10: Normal stress to the contact surface result from Abaqus finite elements simulation on the contact surface.

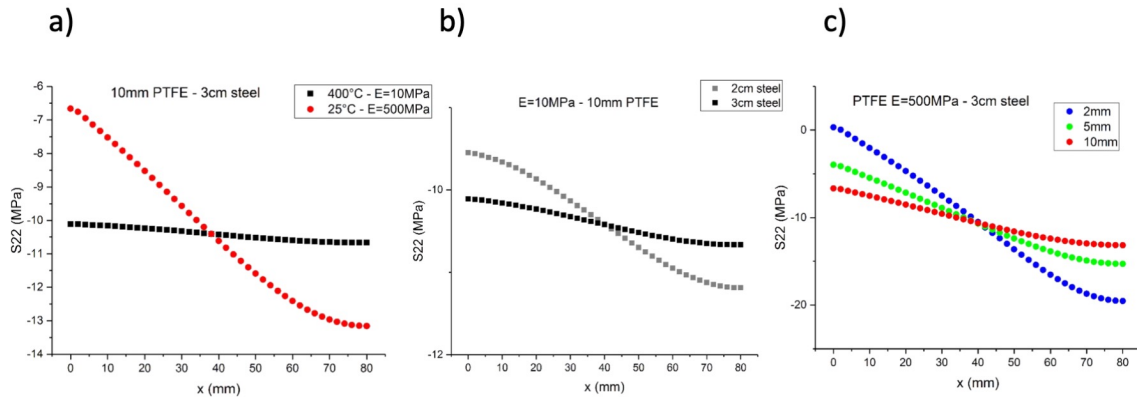


Figure B.11: a) Temperature effect, b) Steel thickness impact, c) PTFE soft intermediate layer thickness impact.

To make sure that the temperature and consequently the physical state of the PTFE intermediate layer is of great importance, the normal interfacial stress distribution on the center line at ambient temperature and 400°C are compared. From Figure B.11a the best homogeneous stress distribution is obtained when the intermediate layer is soft and melted at 400°C. Another parameter of interest is the plate steel thickness impact on the homogeneity of the interfacial stress distribution. From Figure B.11b, 3 cm thick steel plate leads to a more homogenous stress distribution than a 2cm thick steel plate; so, a 3 cm thick steel plate is kept.

After looking at the steel thickness effect, we can look at the PTFE thickness intermediate layer impact. Figure B.11c shows the resulting normal interfacial stress on the center line for 2, 5 and 10 mm thick intermediate PTFE layers.

The most homogeneous stress distribution is observed for the thickest intermediate PTFE layer, but, PTFE is a viscous fluid modeled here as an elastic solid; this means that higher strains than in reality are allowed in the simulation. In fact, PTFE yield stress is around 10 MPa at 23°C [*Polymer data handbook 1999*], and 3 MPa at 250°C [*Polymer data handbook 1999*], and even lower at 400°C. But with the pressure applied, we can consider that the stress in the intermediate PTFE layer is always higher than its yield stress. A perfect elasto-plastic model would probably be more accurate to describe PTFE behavior above its melting temperature and in this case, whatever the PTFE intermediate layer thickness is, the stress distribution would be the same if the material yield stress is exceeded. That's one of the reasons why a 2 mm thick PTFE intermediate layer is chosen; the second one is thermal: as we are interested in having melted PTFE, the thinner it is the shorter the melting time will be. However, the thermal insulation provided by this PTFE layer is reduced: the leaks by the pressure rods are not minimized.

We also check if the cylinder linking the jaws to the plates is not buckling. The critical load that an ideal long slender column can carry without buckling is given by Euler formula:

$$F_c = \frac{\pi^2 EI}{l_k^2} \quad (\text{B.2})$$

with  $E$  the steel Young's Modulus,  $l_k$  the effective length of the column:

- $l_k = 2L$  with  $L$  the unsupported length of column in the worst case of one fixed end and the other end free to move laterally,
- $l_k = 0.5L$  in the best case of both ends fixed,

$I$  the smallest area moment of inertia of the cross section of the column, in the case of a full cylinder  $I = \frac{\pi D^4}{64}$  with  $D$  the column diameter.

In the worst case of the smallest critical force for  $l_k = 2L$ , we obtain for a full steel cylinder, with  $E=210$  GPa,  $L=20$  cm and  $D=27$  mm,  $F_c \approx 340$  kN. This value of the critical load at which the cylinder starts buckling will never be reached: our compression machine cannot reach loads higher than 100 kN. Our design is safe from buckling.

#### B.2.4 Small contact area

To improve the welding homogeneity, all the setup designs proposed here above are trying to reach the most homogeneous normal stress distribution possible. The problem of air bubbles trapped at the two films interface is not solved. In that aim, a new approach consists in reducing the bonded size and applying pressure progressively through the contact zone. This can be done by using cylinders in a crossed configuration equivalent to a sphere on a plane configuration following Hertz theory, see Figure B.12a. Different pressures at the center of the contact zone can be reached with different radii of curvature and different compressing forces applied.

Moreover, to get ride of the identification of the delaminating interface such as in Polyimide-PTFE-FEP composites, the material of interest will be pure PTFE white cast films. To prevent film breakage and be sure of interfacial fracture in the bonded zone, the maximum pull-out force sustainable must be on the plastic plateau at  $\approx 3$  N identified from uniaxial tests, see Figure 3.18. A precise enough load cell has to be found; those available on the tensile test machine equipped with the previously used oven are not suitable. Such load cells are available on universal tensile test machine but not equipped with an oven: in situ heating can be performed thanks to cartridge heaters such as those proposed by Omega company [*Omega - Cartridge Heaters 2019*], see Figure B.12b. A schematic design of such a setup is shown on Figure B.12c. However, such a design is not validated for safety purpose: the heating elements have to be protected such that no one can touch them and get burnt; a closed oven is better. This is why our final choice is implemented on a rheometer equipped with an oven having 50 N load cell.

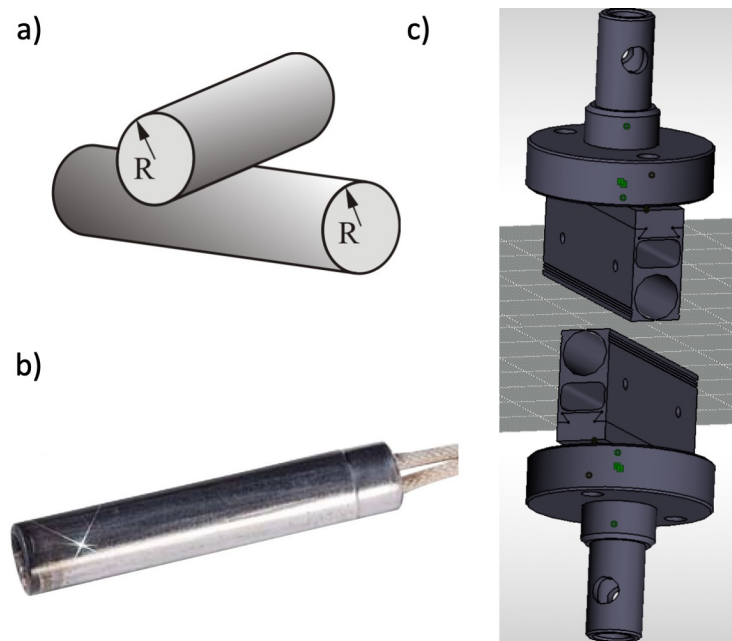


Figure B.12: a) Crossed cylinders configuration equivalent to a sphere on a plane contact, b) Cartridge heater from [*Omega - Cartridge Heaters 2019*], c) Setup design to be implemented on a universal tensile test machine, cartridge heaters can be inserted in the cylindrical spaces on each side.

## Appendix C

# **Mechanical adherence tack test - designs**

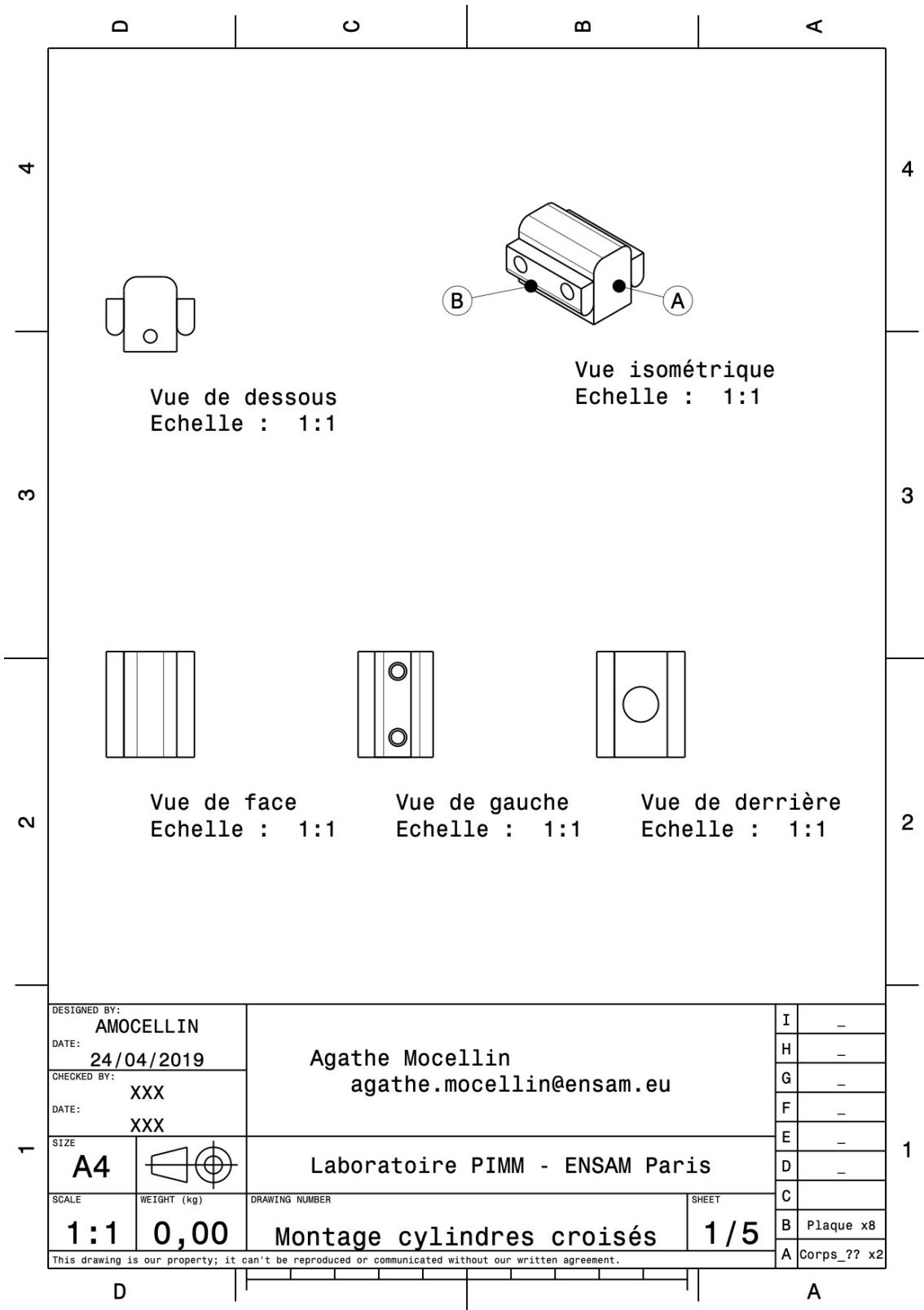


Figure C.1: Design global overview

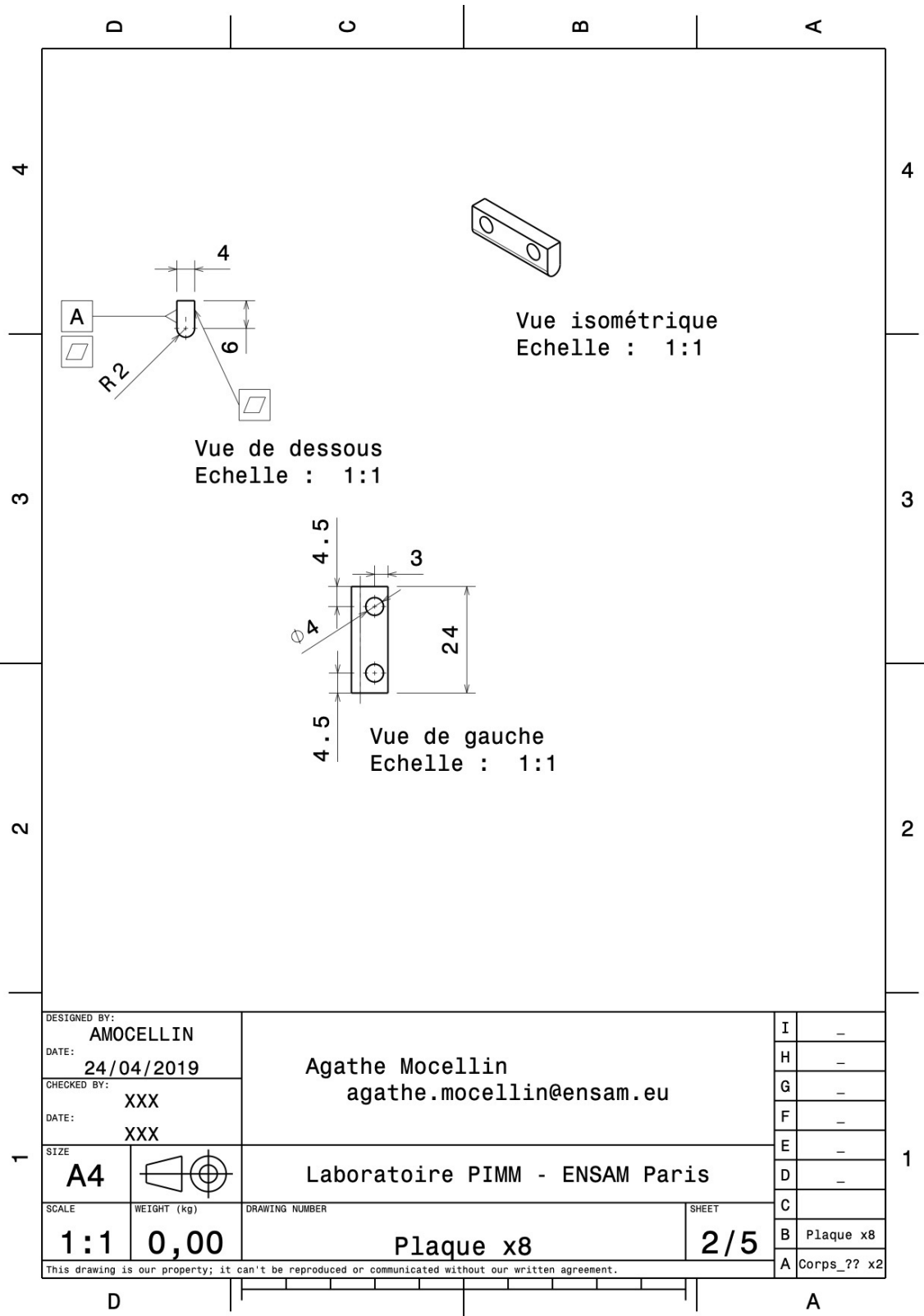


Figure C.2: Design maintaining plate

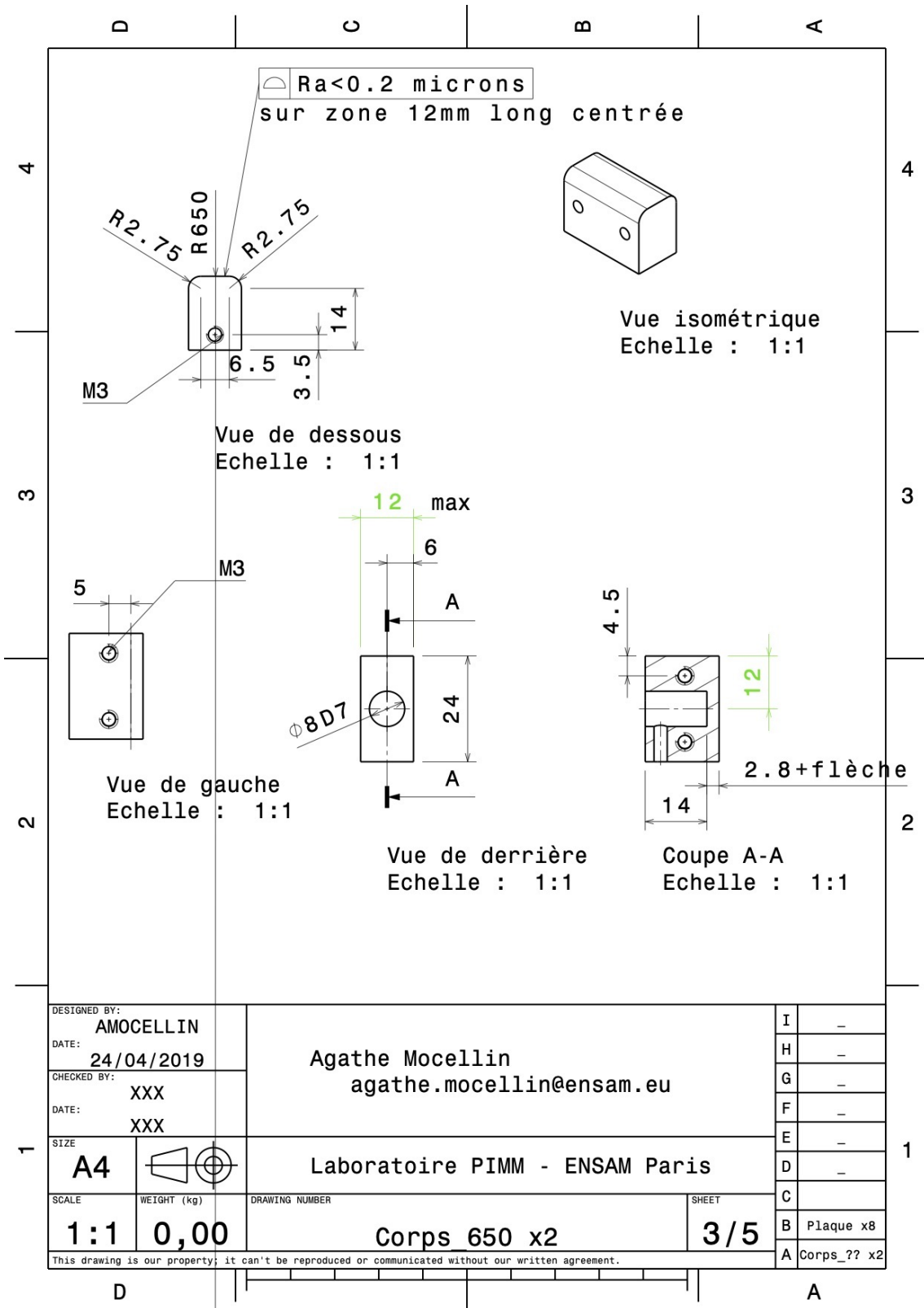


Figure C.3: Design R=650mm

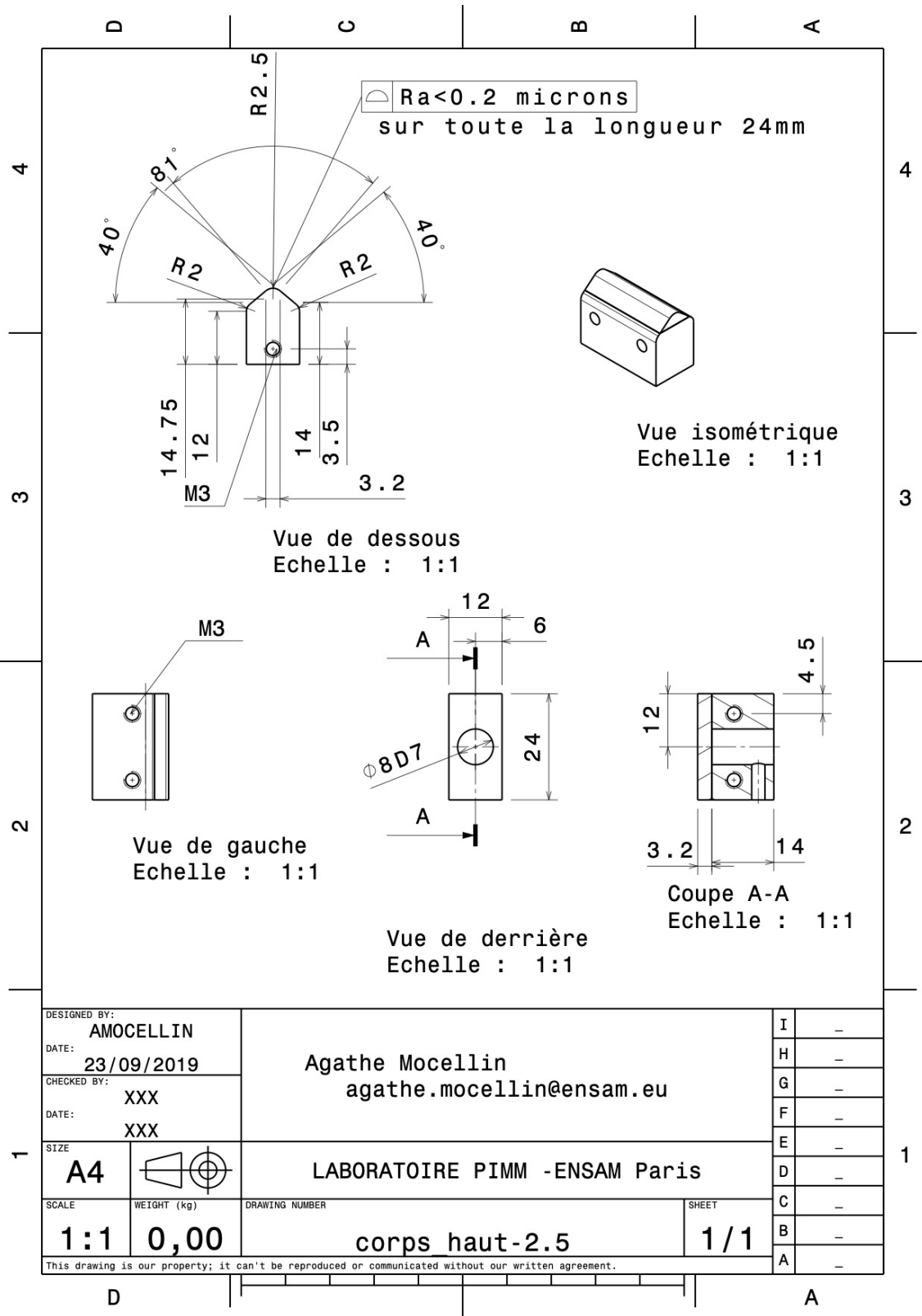


Figure C.4: Design new R=2.5mm



# Secondary crystallization morphology visualization by SEM in temperature

For the crystallization of sintered PTFE, two different mechanisms have been identified by [Guenoun *et al.* 2020]. In section 3.2.3, their experiments are reproduced on our PTFE cast films and their mechanisms are validated on our material. The crystalline structures responsible for the secondary crystallization are supposed smaller and independent from the ones of the primary mechanism [Guenoun *et al.* 2020] which are lamellae of 0.1 to 1  $\mu\text{m}$  thick, see Figure 3.6. In the following, in situ heating and cooling observed by Scanning Electron Microscopy will be performed on PTFE dispersion in order to visualize the crystalline structures related to secondary crystallization mechanism.

### D.1 Experimental setup

Scanning Electron Microscopy (SEM) is an imaging technique giving access to a nanometric resolution. An electron beam scans the surface to analyze; electrons are interacting with atoms and part of them are reflected. The reflected electrons can be collected on different detectors providing different information. Two common types of measured electrons are secondary electrons and backscattered electrons. The secondary electrons are useful for topography inspections and backscattered electrons are more interesting to distinguish phases. A mix of both types of electrons can also be used for imaging.

Environmental SEM (ESEM) is a type of SEM of interest for polymers since it is possible to observe the sample without vacuum chamber. In situ melting and crystallization is followed via ESEM (FEI Quanta 600) equipped with a heating plate available at Laboratoire de Mécanique des Solides, Ecole Polytechnique.

A drop of raw dispersion is deposited on the plate surface of copper supports previously coated with gold and dried in air for at least one night at room temperature. A thin conductive gold coating (1-2 nm) is sputtered on the PTFE surface and the sample is put

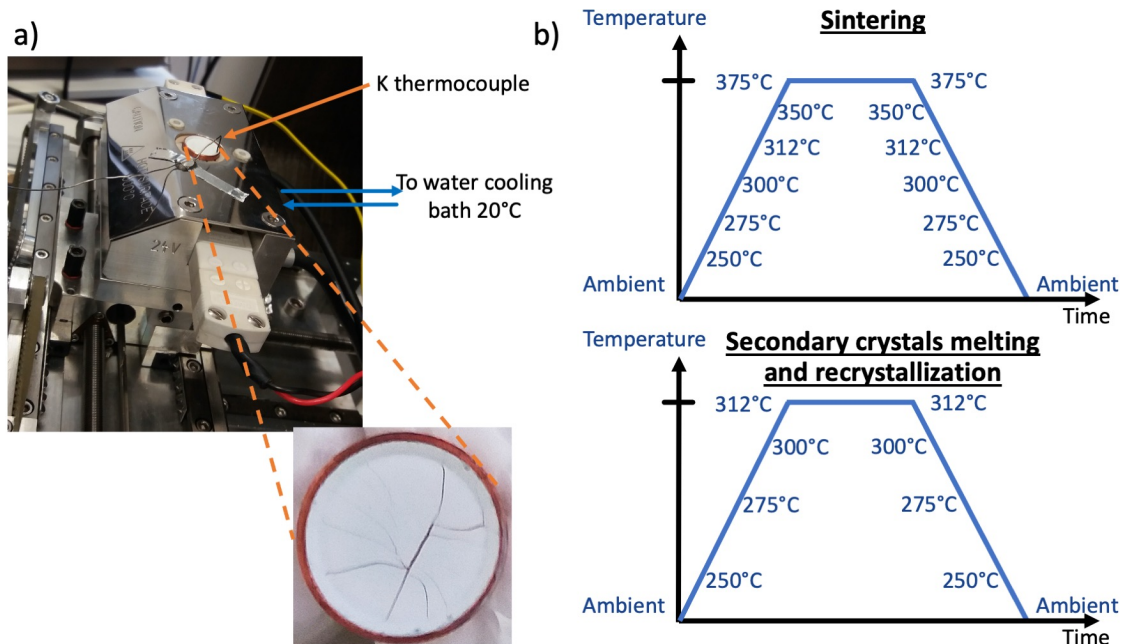


Figure D.1: a) Set up in the SEM chamber: heating stage with sample and thermocouple, the insert is a zoom on the sample surface. b) Proposed thermal cycles to be implemented: top for sintering, bottom for secondary crystals melting and recrystallization.

on the heating plate inside the SEM chamber, see Figure D.1a. A type K thermocouple is placed close to the deposit on the edge of the support, the temperature measured by this thermocouple is the closest one from the real deposit temperature. Two successive thermal cycles are planned to be implemented, see Figure D.1b: a first one up to 375°C to perform PTFE sintering and a second one up to 312°C to follow exclusively melting and recrystallization of the crystalline structures responsible for secondary mechanism. Images are registered at various temperatures during heating and cooling.

## D.2 Results

First the sintering thermal cycle is performed: Figure D.2 depicts the recording of the thermocouple temperature in blue. Different zones of interest are successively imaged - a large view and a crack; their respective temperatures are represented by orange and black points.

In Figure D.3, the width of the large view pictures is 6 mm, so that on the top right corner the border of the copper support is visible. The PTFE deposit is not homogeneous: cracks are noticeable since air drying, see insert Figure D.1a. The deposit thickness is not controlled, the appearance of cracks suggests that the critical mudcracking thickness is exceeded [Drobny 2009]. After a sintering cycle, the cracks are still present, see Figure D.3 last picture.

During the heating up to melting, cracks are progressively closing from the edges: the material is dilating up to 20% as already shown by [Guenoun *et al.* 2019]. During cooling from the melt, cracks are reopening: PTFE is shrinking. Between the two sides of the crack that were in contact, fibrils are formed; during shrinkage, they extend until breakage, see Figure D.4 with magnifications of the red zone highlighted on Figure D.3.

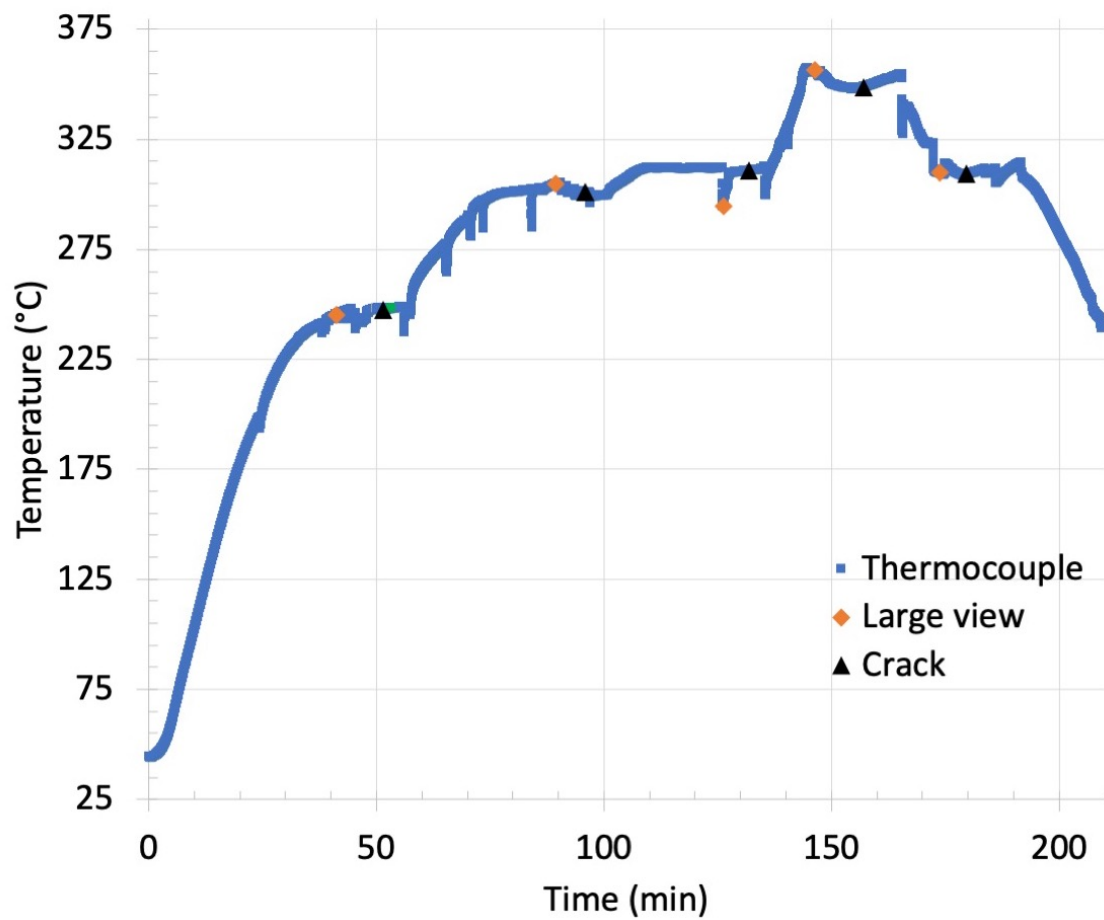


Figure D.2: Temperature profile recorded by thermocouple close to the sample surface on the heating stage.

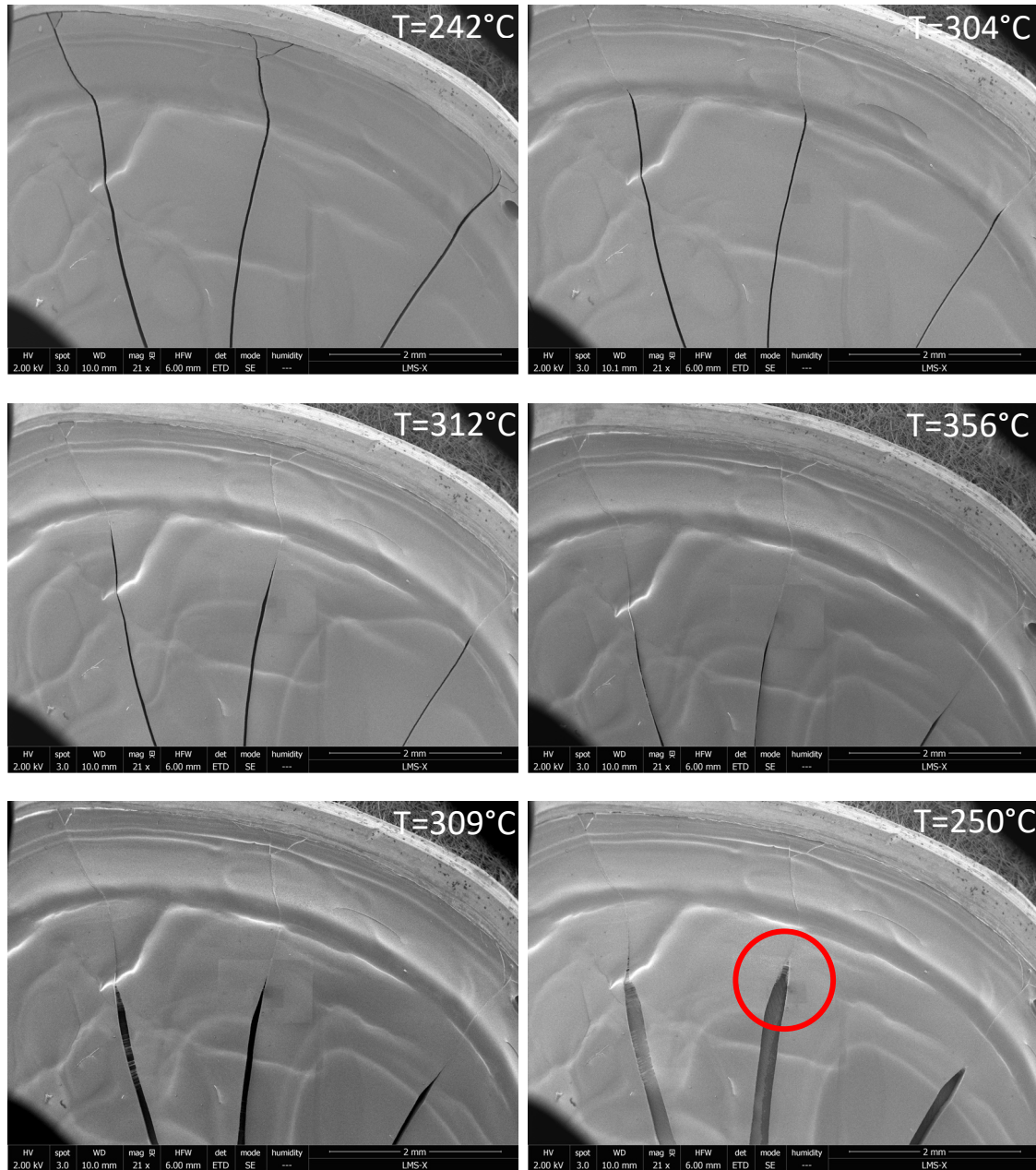


Figure D.3: Large view micrographs along heating and cooling. During heating, PTFE dilates and then shrinks during cooling. The red circle highlight the zone showed on Figure D.4

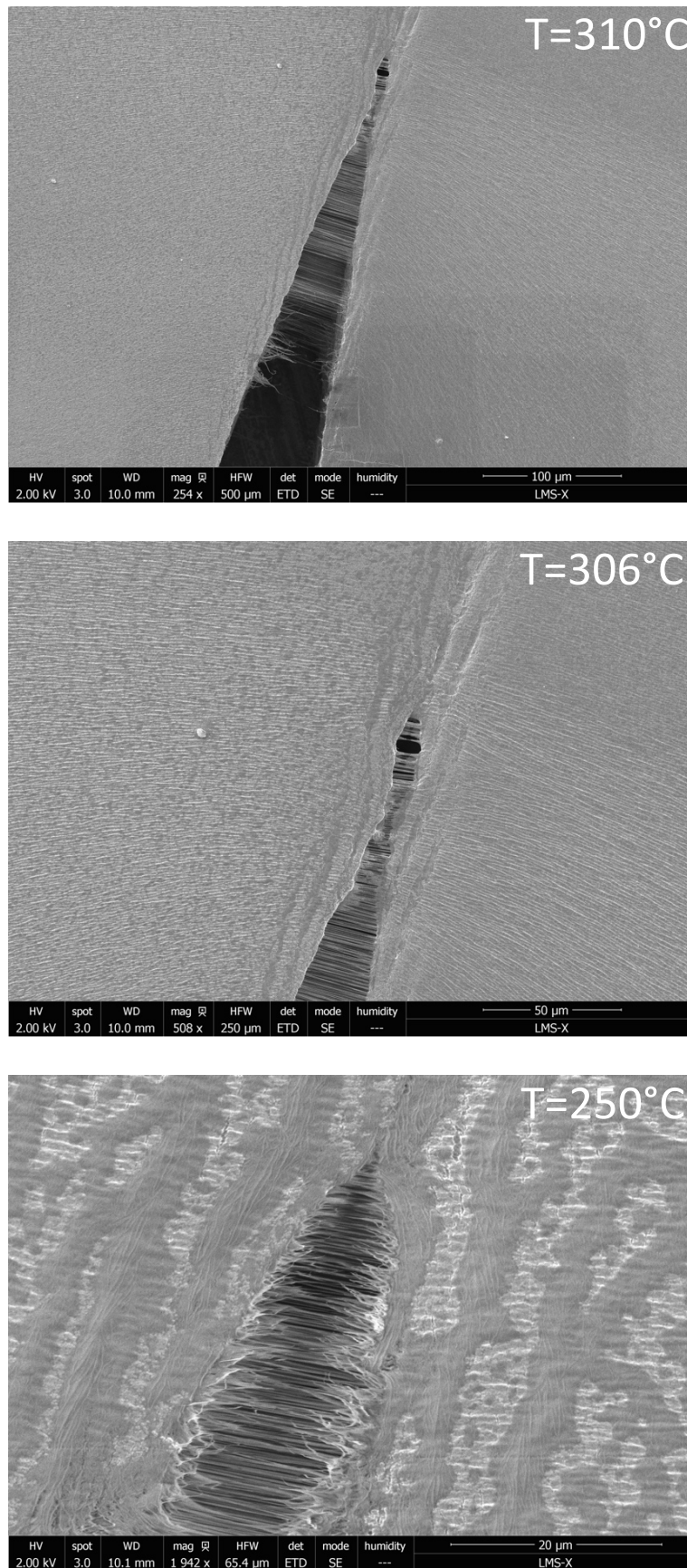


Figure D.4: Crack tip during cooling: fibrils are extended and then broke during material shrinkage.

In an other zone, a crack border is imaged on Figure D.5 where pictures are 10  $\mu\text{m}$  width. The raw dispersion particles are visible all along the sintering cycle: no deformation of these particles is noticeable after melting nor particular change on surface morphology. This behaviour is not expected: at melting, it has already been shown that PTFE dispersion particles lose their spherical shape to form banded structures [Yang *et al.* 2005].

At melting, taking a step backwards, on a 223  $\mu\text{m}$  width image Figure D.6a, a regular pattern of horizontal lines appears. By zooming in, two distinct areas can be identified, see Figure D.6b:

- melt PTFE without metallic coating,
- PTFE dispersion particles still with conductive gold coating.

This pattern is close to the one shown by [Marthelot 2016] concerning the cracking of a rigid thin layer on a soft polymeric substrate and happening with an initial propagation of fragile cracks and then a regularly spaced sinuous pattern. In our case, the cracking of the thin conductive gold coating acting as a rigid shell on a soft PTFE substrate seems a reasonable hypothesis.

At the end of the day, the microscope chamber is opened and the sample looks as depicted on Figure D.7. A black color has been diffusing from the edges. A gold deposit was done on the copper support to avoid such a copper oxide II diffusion with temperature. The raised edge was not well covered and diffusion is starting from there.

To conclude, since melting is not visualized, smaller structures as those expected for the secondary crystallization mechanism would not be possible to distinguish. Thus, the planned second temperature cycle is not performed. Using a different support made of an inert material such as gold or conductive ceramics could help not to deteriorate the PTFE deposit. Observing polymeric materials without conductive coating in a SEM with a low voltage mode could help getting ride of the coating acting as a rigid shell. Another option could be to use an AFM in temperature as the one commercialized by Oxford Instruments compatible with a heating plate up to 400°C.

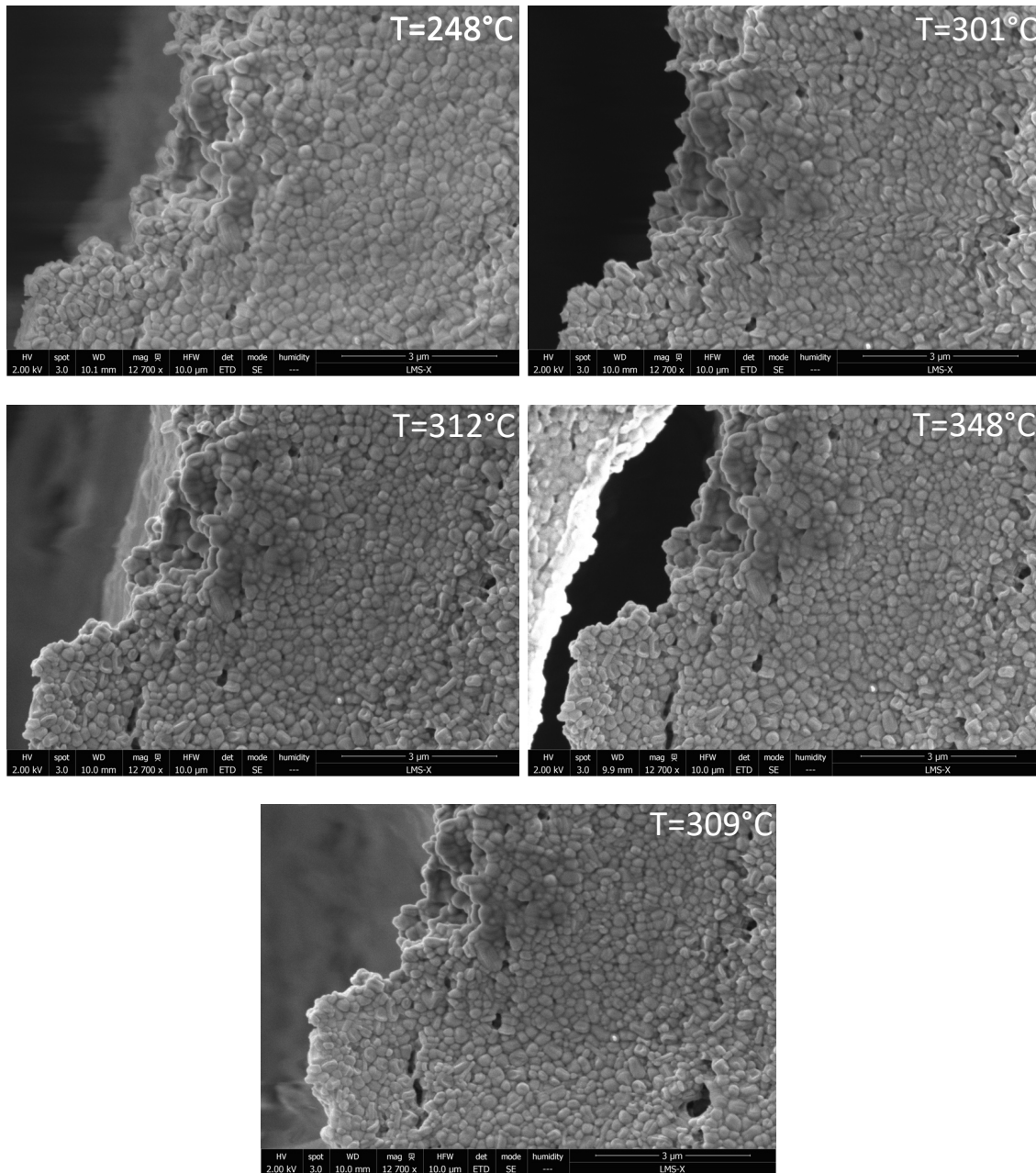


Figure D.5: Crack border zone imaging; no surface morphology change during sintering cycle.

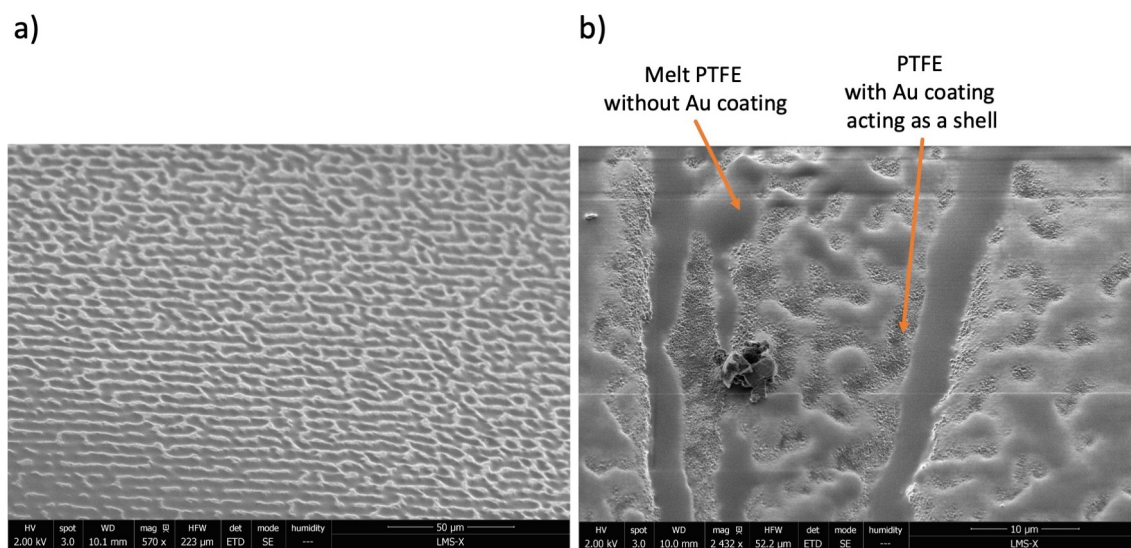


Figure D.6: Cracking at 327°C during heating



Figure D.7: Sample at the end of the experiment. A black color seems to diffuse from the edges.

# Image analysis - supplementary

The mechanical adherence tack test taken as an example all along Chapter 6 has been reproduced. In this appendix, pictures from two reproductions - see Figures E.1 and E.2 - are analysed thanks to the Matlab image analysis code and compared to Figure 6.3. Bonding is performed at 375°C for 6 s and 0.2 N normal force set at 0 N during cooling.

On Figures E.1 and E.2, no image analysis is possible at the beginning (up to 18 s for Figure E.1 and 12 s for Figure E.2): on the recorded pictures films are in contact, it is not possible to differentiate the top and bottom ones and the characteristic sand-glass shape is not yet appearing.

Some parameters of interest can be compared between all these experiments as shown in Table E.1. The time  $t_d$  at which debonding starts is obtained from image analysis when a change in radius of the welded zone  $a$  slope occurs. This time is close to the time at which the measured force is maximum  $t_{F_{max}}$ . Here, the time at which debonding starts  $t_d$  is always larger than  $t_{F_{max}}$ . The largest radius of the welded zone  $a$  is measured both by image analysis at  $t = 0$  s ( $a_{images}$ ) and optical microscopy on the fractured surface ( $a_{OM}$ ). Values are in good agreement with larger values from optical microscopy observation. The sand-glass radius base  $R$  is almost constant in all experiments with a small increasing slope; both start and end values are reported in Table E.1. The two last experiments performed on the same day have  $R$  values close to 1.6 mm whereas for the first one performed a month before,  $R$  value is twice lower. The angle  $\theta$  between the horizontal axis and the film arm is always rapidly increasing until the start of debonding where the slope takes a lower value. All the end angles are close to 35°.

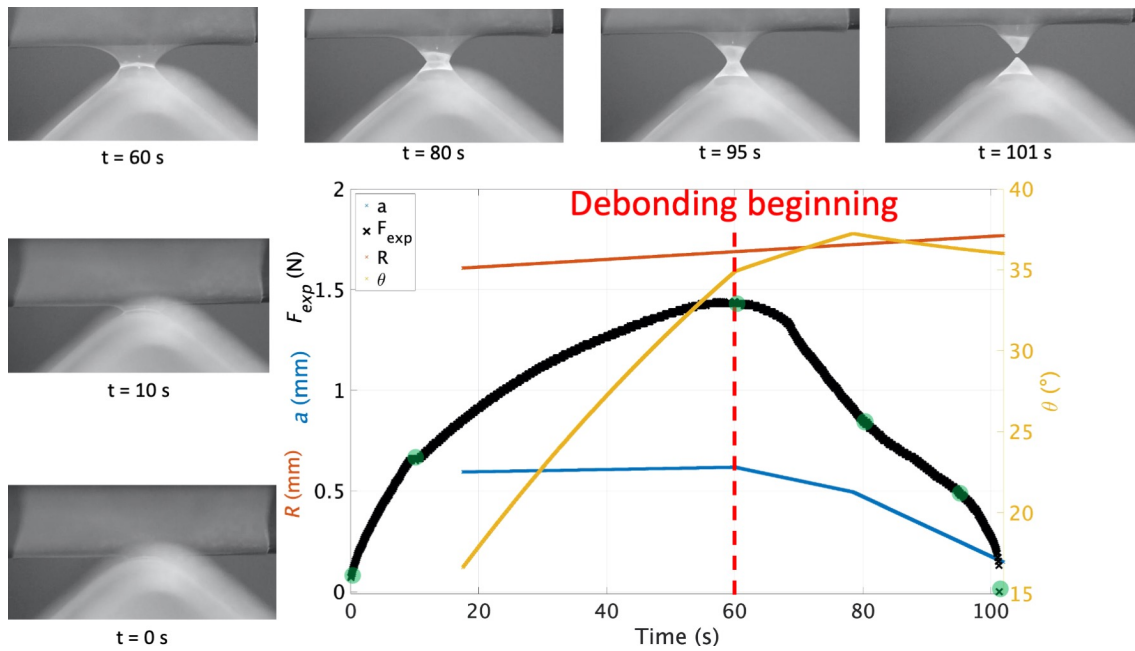


Figure E.1: Experimental results: time evolution of the measured debonding force  $F_{exp}$  and pictures showing the deformation of the two films and their debonding (green points on the black force curve); Image analysis results: time evolution of the radius of the welded zone  $a$ , the contact point  $R$  between film and support and the mean angle  $\theta$  between the film arm and the horizontal axis.

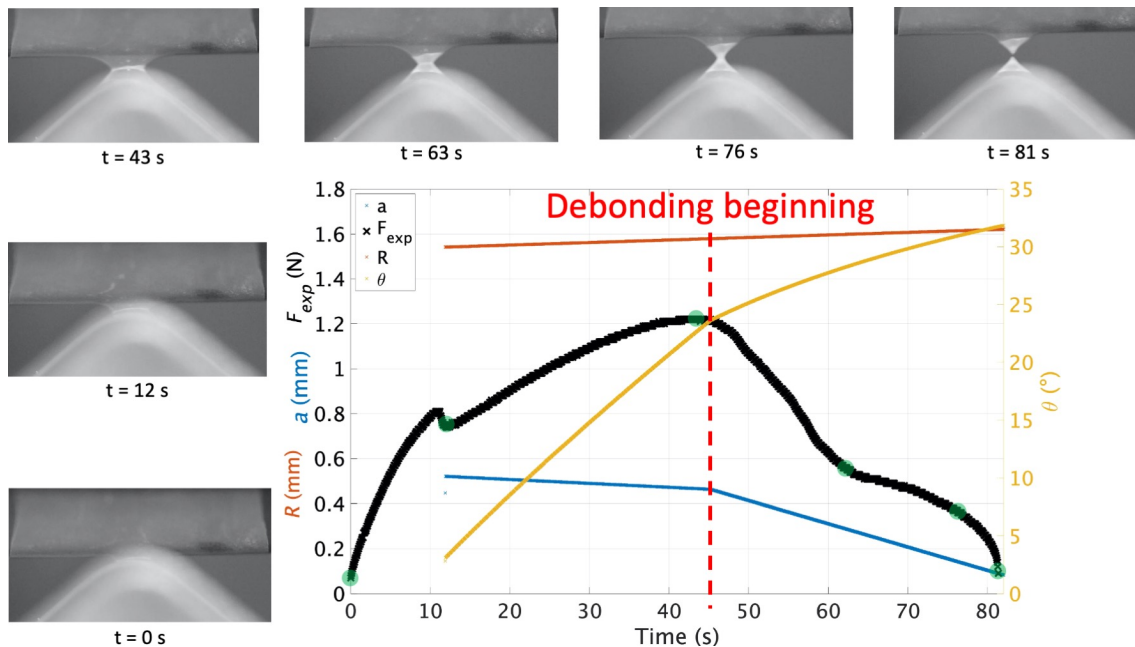


Figure E.2: Experimental results: time evolution of the measured debonding force  $F_{exp}$  and pictures showing the deformation of the two films and their debonding (green points on the black force curve); Image analysis results: time evolution of the radius of the welded zone  $a$ , the contact point  $R$  between film and support and the mean angle  $\theta$  between the film arm and the horizontal axis.

<b>Figure</b>	$t_{F_{max}}$ (s)	$t_d$ (s)	$a_{OM}$ ( $\mu\text{m}$ )	$a_{images}$ ( $\mu\text{m}$ )	$[R_{min}; R_{max}]$ (mm)	$\theta_{end}$ ( $^\circ$ )
<b>6.3</b>	26	38	458	440	[0.84; 0.89]	39
<b>E.1</b>	59	60	618	584	[1.57, 1.77]	36
<b>E.2</b>	43	45	581	542	[1.53; 1.62]	32

Table E.1: Comparative table of three mechanical adherence tack tests reproduction for contact at 375°C for 6 s with 0.2 N normal force.

$t_{F_{max}}$ : time at which the measured force is maximum,  $t_d$ : time at which debonding starts when a change in radius of the welded zone  $a$  slope occurs,  $a_{OM}$  and  $a_{images}$ : respectively the largest radius of the welded zone  $a$  measured by optical microscopy on the fractured surface and image analysis at  $t = 0$  s,  $R_{min}$  and  $R_{max}$ : the sand-glass radius base start and end values,  $\theta_{end}$ : the end angle between the horizontal axis and the film arm.





**Titre :** Adhésion entre films de Polytétrafluoroéthylène (PTFE) : influence des conditions de fabrication

**Mots clefs :** Polytétrafluoroéthylène, PTFE, Adhésion, Adhérence, Science des polymères, Mécanique de la rupture

**Résumé :** Le polytétrafluoroéthylène (PTFE) est un polymère thermoplastique semi-cristallin ayant une très bonne résistance à la corrosion, une forte stabilité thermique, de très bonnes propriétés d'isolation thermique et un très faible coefficient de friction. Par conséquent, ce matériau est utilisé pour de nombreuses applications; une d'entre elles est la fabrication de films et de tissus enduits de PTFE.

En raison de sa masse molaire élevée et de sa haute viscosité à l'état fondu, les films minces en PTFE sont obtenus par dépôts successifs de dispersions sur une matrice qui est ensuite retirée. Des matériaux composites sont fabriqués en soudant ensemble un tissu pris en sandwich entre deux films. Pour des performances optimales, il est crucial de maîtriser au mieux l'adhésion PTFE-PTFE et PTFE-tissu.

Ce travail porte sur un système modèle : deux films de PTFE sans tissu. L'objectif est de comprendre les mécanismes d'adhésion et d'en déduire une optimisation du soudage des films. Un dispositif expérimental origi-

nal de pérosité a été développé et a permis l'analyse de l'influence de la température, du temps et de la pression de contact sur les propriétés d'adhésion à l'interface. Le rôle de l'interdiffusion des chaînes dans la phase amorphe et/ou de la co-cristallisation de la phase quasi-cristalline du polymère dans l'adhésion est étudié.

Une température de contact supérieure à la fusion, facilitant la mobilité des macromolécules, est nécessaire pour obtenir une bonne adhésion. L'augmentation du temps de contact ne montre pas de variation significative de la qualité d'adhésion dans la gamme de temps de contact étudiée. Au-dessus de la fusion, en fonction de la pression de contact, la rupture peut être destructrice ou non. Une pression seuil existe entre ces deux modes de rupture : plus le temps de contact est long, plus la pression seuil est basse. Une première modélisation basée sur un réseau discret à trois dimensions a été construite et une procédure d'identification proposée afin d'estimer le taux de restitution de l'énergie.

**Title:** Adhesion between Polytetrafluoroethylene (PTFE) films: influence of manufacturing process conditions

**Keywords:** Polytetrafluoroethylene, PTFE, Adhesion, Adherence, Polymer science, Fracture mechanics

**Abstract:** Polytetrafluoroethylene (PTFE) is a thermoplastic semi-crystalline polymer, with many outstanding properties such as excellent resistance to corrosion, excellent temperature stability, very high electrical insulation and extremely low friction coefficient. These make it suitable for a large range of engineering applications ; one of them is the manufacturing of PTFE films and coated fabrics.

Due to their high molecular weight and their high viscosity in the melted state, PTFE thin films are obtained by successive deposition of dispersions on a substrate which is finally peeled out. Composite materials are manufactured by welding together a fabric sandwiched between two such PTFE films. Therefore, for optimum performance, PTFE-PTFE and PTFE-fabric adhesion must be controlled.

This work focuses on a model system: two PTFE films without fabrics. The aim is to quantify the adhesion mechanisms and optimize films welding. A specific experimen-

tal setup has been designed to weld PTFE films and perform mechanical adherence tack tests investigating the impact of temperature, contact time and normal pressure on the interfacial adhesive properties. The role of chain interdiffusion in the amorphous phase and/or co-crystallization of the polymer quasi-crystalline phase in the adhesion is investigated.

A contact temperature higher than melting, allowing macromolecular chain or segments mobility, is highlighted as a necessary condition to obtain adhesion. Increasing the contact time shows no significant variation. Above melting, different failure mechanisms are observed according to the contact pressure: the weld fracture is either destructive or not. A threshold pressure exists between these two fracture modes: the longer contact time, the lower the threshold pressure. A model based on a three dimensions discrete network is proposed to obtain an estimation of the characteristic adhesive energetic value.



